Surface nanopatterning by self-assembly techniques: Nanosphere - and block copolymer lithography

Preface

The design of new innovative materials with tailored functionalities attracts huge interest in many fields of research such as bio-engineering, photonics, semiconductor nanotechnology and material science in general. Material design inspired by approaches from different research communities allows for the joining of different material classes into new functional hybrid materials.

In this work, self-assembly processes for the modification of surfaces with regular patterns are introduced, which allow for a subsequent 1-dimensional or 2-dimensional placement of nanoobjects. A novel approach for the hierarchical material surface modification is explored. This allows for the step-wise assembly of different materials and the bridging of different size scales.

Nanosphere lithography (NSL) based on convective self-assembly of colloidal polymer spheres is used for surface patterning with few microns to few hundred nanometer feature sizes. This technique is applied for the modification of large 2-dimensional areas, for the creation of antidot-patterned thin films, as well as for the creation of 1-dimensional chain-like arrangements. The applicability of linear sphere chains as shadow masks in nanosphere lithography for the formation of nanogap electrodes is investigated theoretically and experimentally.

In order to obtain regular patterns with even smaller feature sizes, block copolymer (BCP) lithography as an emerging surface nanopatterning technique for the creation of self-assembled sub-20 nanometer features is established. The formation of nanopores by microphase separation of block copolymers on plane surfaces with different chemical properties is discussed. The created nanopores are shown to be useful topographic traps for the directed assembly of colloidal gold nanoparticles into large 2D arrays.

In order to combine the benefits of both patterning techniques, BCP lithography for the formation of cylindrical nanopores is combined for the first time with antidot formation by NSL. This directed self-assembly approach is shown to result in hierarchical nanopore architectures.

Acknowledgement

Contents

1 Introduction

1.1 Self-assembly

Self-assembly (SA) of micro- and nanometer sized objects is an active and growing field of research. Self-assembly approaches allow for the patterning of surfaces on large areas and are therefore highly interesting for the modification and design of contemporary materials [1-3].

Self-assembly stems from the interactions of small units, which lead to the spontaneous formation of larger periodic structures with new material properties. As this is a very general definition, there exist a great variety of phenomena which are referred to as self-assembly processes. Such phenomena can be found in all disciplines of the natural sciences [4-7]. In chemistry, the spontaneous formation of well-defined structures driven by non-covalent forces, such as known from micelle formation is called self-assembly. In physics, self-assembly is defined as the spontaneous creation of new three-dimensional and temporal structures by a ‚cooperative effect of partial systems‘ [4] as e.g. in ferromagnetism. Biology refers to self-organization, if complex structures are spontaneously build ‚under adequate environmental conditions‘ [4] due to molecular interactions and properties, an example of which is the folding of proteins. However in all definitions self-assembly relates to either the spontaneous packing of individual units into ordered arrangements or pattern formation within one component into ordered domains by phase transitions. Due to the broad range of disciplines the nomenclature may vary [8] and self-assembly may be referred to as self-organization. In this thesis, these the two phrases will be used interchangeably.

In the fields of material science and nanotechnology, self-assembly allows for the bottom-up modification of materials, such as the patterning of surfaces with regular two-dimensional features [9]. Self-assembled objects can be used as lithography masks to produce ordered patterns with nanometer periodicities and feature sizes from a broad range of materials. Such small feature sizes are difficult to obtain by optical lithography [3, 10]. Top-down direct writing techniques are capable of creating high resolution structures but require expensive machinery and are not suitable for large-area patterning. Thus, self-assembly based lithography has the advantage of producing large-area regularly patterned surfaces with nanometer sized features and periodicities in a fast and cost-effective way and at high throughput.

For more pattern flexibility, SA processes can be influenced by directing forces, such as external electric fields, mechanical strain or chemical or topographical pre-patterns. Processes applying such guidance of the self-assembly of units are referred to as directed self-assembly (DSA) [11-14]. DSA can not only improve the pattern regularity [13, 15] but add site-selectivity or allows for tailored pattern morphology, which makes the SA process much more versatile. Thus, DSA allows for the design of new materials with advanced architectures, which extends the field of possible applications of SA enormously.

1.2 Scope of this work

In order to apply SA processes for the controlled modification of surfaces with tailored functionalities, the understanding of the self-organizing systems is indispensable. Thus, this work will focus on the fundamental understanding of SA processes which should give insight allowing for the improvement of SA control, e.g. by DSA. The influence of properties of the single units and their environment, e.g. material surfaces on the self-assembly is investigated. Regularity, arrangement and density of self-arranged patterns on surfaces are

discussed and the work gives perspective on applications of self-assembled nanopatterns, e.g. for new material architectures in bio-engineering, photonics or semiconductor devices. The directed arrangement of nanoobjects into regular 2-dimensional and 1-dimensional arrays as well as the combination of different surface modification techniques will be shown to allow for the creation of hierarchical architectures of functional materials and material hybrids.

This thesis focuses on the modification of surfaces by employing two different self-assembly methods: nanosphere lithography (NSL) and block copolymer (BCP) lithography. Both methods are capable of generating two-dimensional periodic patterns (Fig. 1.1). With NSL feature sizes and periodicities from below 100 nm to about 5000 nm are possible. BCP lithography produces structures in the 5 nm to 50 nm range.
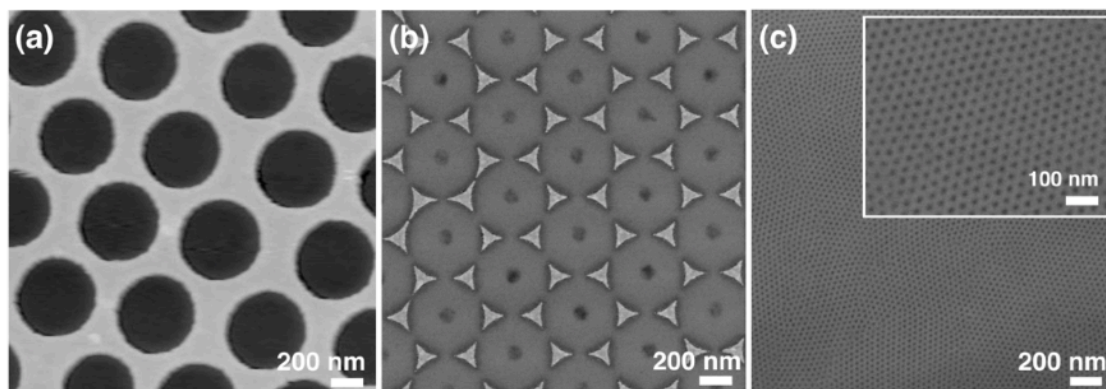
Fig. 1.1: Two-dimensionally nanopatterned surfaces with hexagonally arranged features created by self-assembly techniques. (a) AFM images of a nanopatterned gold thin film with features of 500 nm diameter created by NSL. (b) SEM image of triangular shaped gold nanoparticles with 130 nm edge length by NSL. (c) SEM images of nanopores with diameters of 17 nm in a polystyrene thin film by BCP lithography (inset at higher magnification).

Nanosphere lithography is a well-established technique for the patterning of surfaces with hexagonal arrays of nanoparticles [16-18]. Micro- or nanometer-sized colloidal particles suspended in a liquid medium are deposited onto a surface by convective self-assembly [19, 20] forming close packed mono- or multilayers. As the spheres are not space filling, the voids between them can be used as shadow masks in lithography. This basic NSL procedure has been developed in the 1980s by Pieranski, who first reported the formation of 2-dimensional colloidal crystals [21] and Fischer, who had the idea to use them as lithography masks [22]. In 1982, Deckman and Dansmuir introduced the term ‚natural lithography' [16]. In the 1990s, van Duyne and his team modified surfaces by metal deposition onto sphere monolayers for the creation of 2-dimensional arrays of triangular shaped nanoparticles and investigated their plasmon resonances [17, 23, 24]. In ongoing research different surface modifications through the nanosphere mask openings were shown, for instance by site-selective material removal via reactive ion etching [25] or chemical/ structural surface modification by ion implantation [26]. Modification of the openings prior to their use as masks during NSL allows for the tailoring of the shape of the subsequently created surface patterns [27] for example by thermal treatment [28], plasma treatment [29] or ion beam exposure of polymeric sphere monolayers.

Block copolymer (BCP) lithography is an emerging technique for the self-assembled patterning of surfaces with features in the single- and double-digit nanometer regime [30, 31]. It is based on the microphase separation of polymer chains, which consist of two or more blocks of different polymer species, into ordered homopolymer-enriched domains [31-34]. In the case of BCP consisting of two blocks, the separated domains form periodic structures from lamellar sheets over hexagonally arranged cylinders to cubic body centered spheres. The

motives formed depend on the block length ratio of the polymer species in the BCP and their molecular weight [35]. By selective removal of one polymer species, topographically nanopatterned masks can be obtained on wafer-scale. Even though the microphase separation of polymer mixtures was introduced by Flory [36] and Huggins [37] already in the 1940s, closer investigations of the use of this effect for the nanopatterning of thin films have started only very recently. Mansky first observed in 1995 ordered microdomains in polymer thin films by TEM and had the idea to use them for lithography [38, 39]. Two years later, Park showed first experimental results of BCP thin films being used as lithography mask for pattern transfer into semiconductor surfaces [40]. Since then, the application of microphase separated BCP thin films for lithography is an active research field. The self-arranged polymer domains exhibit a high quality of short-range order within the large-area patterns, however lack of long-range order. Ongoing research faces the use of directed self-assembly to induce a long range order of the patterns by applying electric fields, sheer forces or chemical or topographical surface pre-patterns [13, 15]. This is of current interest as a long-range order is necessary for the pattern use in many applications. Lamella-forming BCP, with lamella being parallel to each other, are for example investigated for their use as templates for the preparation of fin-FET transistors [41].

The content of this thesis is divided into three main parts. The first part is about convective self-assembly of colloids for the two-dimensional surface patterning by nanosphere lithography (NSL). This chapter focuses on the self-assembly process of colloidal polystyrene spheres from aqueous suspension and the doctor blade technique, as an experimental approach for the creation of large area sphere monolayers. The basic principle of nanosphere lithography for nanoparticle array formation is introduced and the creation of antidot patterns by controlled modification of NSL masks is presented. In this context, it is also shown how self-assembled colloids can be used for patterning elastomers with nanoscale tips.

The second part covers the creation of one-dimensional patterns by NSL, i.e. opposing metallic nanotips. To this end, directed self-assembly is employed on chemically and topographically pre-patterned substrates to yield linear chains of nanospheres. These sphere chains are then used in nanosphere lithography for the formation of nanogap electrodes with tunable gap widths. Simulations are performed to characterize the electric properties of the prepared tip pairs for their potential use as nanogap electrodes. This part ends with preliminary experiments on the trapping of nanometric particles by dielectrophoretic forces.

The last part covers block copolymer (BCP) lithography. It is shown how the BCP lithography can be used for the formation of nanopores on different metallic, semiconducting and dielectric material surfaces. The influence of the specific substrate on the polymer self-assembly process is investigated. Results of the pattern formation of home-made block copolymers are presented. As an example of the application of nanopores as topographic traps, the deposition of gold nanoparticles into the pores is investigated. Finally, the combination of the two self-assembly techniques, NSL and BCP lithography, is shown to allow for the formation of hierarchical nanopore architectures.

1.3 Bibliography

[1] G. M. Whitesides, J. K. Kriebek, B. T. Mayers, in: Nanoscale Assembly. Nanostructure Science and Technology, Boston: Springer (2005)

[2] G. M. Whitesides, B. Grzybowski, Science 295, 2418 (2002)

[3] M. Grzelczak, J. Vermant, E. M. Furst, L. M. Liz-Marzán, ACS Nano 4(7), 3591 (2010)

[4] S. Förster, T. Plantenberg, Angew. Chem. Int. Ed. 41, 688 (2002)

[5] P. W. Anderson, D. L. Stein, in: Self-organizing systems, New York: Plenum (1987)

[6] J. Falbe, M. Regitz, Römpp Lexikon Chemie, Stuttgart: Thieme (1996)

[7] Lexikon der Biologie, Heidelberg: Spektrum (2000)

[8] J. D. Halley, D. A. Winkler, Wiley Periodicals 14(2), 10 (2008)

[9] C. Acikgoz, M. A. Hempenius, J. Huskens, G. J. Vancso, Europ. Polymer J. 47, 2033 (2011)

[10] R. A. Farrell, T. G. Fitzgerald, D. Borah, J. D. Holmes, M. A. Morris, Int. J. Mol. Sci. 10, 3671 (2009)

[11] G. A. Ozin, S. M. Yang, Adv. Funct. Mater. 11, 95 (2001)

[12] Y. Xia, Y. Yin, Y. Lu, Adv. Funct. Mater. 13, 907 (2003)

[13] S- J. Jeong, J. Y. Kim, B. H. Kim, H. S. Moon, S. O. Kim, Materials Today 16(12), 468 (2013)

[14] M. Li, C. K. Ober, Materials Today 9(9), 30 (2006)

[15] S. O. Kim, Nature 424, 411 (2003)

[16] H. W. Deckman, J. H. Dunsmuir, Appl. Phys. Lett. 41(4), 377 (1982)

[17] J. C. Hulteen, R. P. VanDuyne, J. Vac. Sci. Technol. A 13(3), 1553 (1995)

[18] C. L. Haynes, R. P. VanDuyne, J. Phys. Chem. B 105, 5599 (2001)

[19] B. G. Prevo, O. D. Velev, Langmuir 20, 2099 (2004)

[20] A. Dimitrov, K. Nagayama, Langmuir 12, 1303 (1996)

[21] P. Pieranski, Phys. Rev. Lett. 45, 569 (1980)

[22] U. C. Fischer, H. P. Zingsheim, J. Vac. Sci. Technol. 19, 881 (1981)

[23] J. C. Hulteen, D. A. Treichel, M. T. Smith, M. L. Duval, T. R. Jensen, R. P. VanDuyne, J. Phys. Chem. B 103, 3854 (1999)

[24] T. R. Jensen, G. C. Schatz, R. P. van Duyne, J. Phys. Chem. B 103, 2394 (1999)

[25] J. Shiu, C.-W. Kuo, P. Chen, C.-Y. Mou, Chem. Mater. 16(4), 561 (2004)

[26] J. K. N. Lindner, B. Gehl, B. Stritzker, Nucl. Instr. and Meth. B 242, 167 (2006)

[27] S.-M. Yang, S. G. Jang, D.-G. Choi, S. Kim, H. K. Yu, small 2(4), 458 (2006)

[28] C. Geng, L. Zheng, J. Yu, Q. Yan, T. Wei, X. Wang, D. Shen, J. Mater. Chem 22, 22678 (2012)

[29] D. Gogel, M. Weinl, J. K. N. Lindner, B. Stritzker, J. Optoelectr. Adv. Mater. 12(3), 740 (2010)

[30] R. A. Puglisi, J. Nanomat. 586458 (2015)

[31] A. Andreozzi, E. Poliani, G. Seguini, M. Perego, Nanotechnology 22, 185304 (2011)

[32] P. G. de Gennes, Introduction to polymer dynamics, Cambridge University Press (1990)

[33] L. H. Sperling, Introduction to polymer dynamics, New Jersey: Wiley (1992)

[34] P. J. Flory Principles of Polymer Chemistry, Cornell Univ. Press (1953)

[35] F. F. Lupi, T. J. Giammaria, G. Seguini, F. Vita, O. Francescangeli, K. Sparnacci, D. Antonioli, V. Gianotti, M. Laus, M. Perego, ACS Appl. Mater. Interfaces 6, 7180 (2014)

[36] P. J. Flory, J. Chem. Phys. 10, 51 (1942)

[37] M. L. Huggins, J. Chem. Phys. 9(5), 440 (1941)

[38] P. Mansky, P. M. Chaikin, E. L. Thomas, J. Mater. Sci. 30, 1987 (1995)

[39] P. Mansky, C. K. Harrison, P. M. Chaikin, R. A. Register, N. Yao, Appl. Phys. Lett. 68, 2586 (1996)

[40] M. Park, C. Harrison, P. M. Chaikin, R. A. Register, D. H. Adamson, Science 276, 1401 (1997)

[41] H. Tsai, H. Miyazoe, A. Vora, T. Magbitang, N. Arellano, C. C. Liu, M. J. Maher, W. J. Durand, S. J. Dawes, J. J. Bucchignano, L. Gignac, D. P. Sanders, E.A. Joseph, M. E. Colburn, C. G. Willson, C. J. Ellison, M. A. Guillorn, Proc. of SPIE 9779, 977910 (2016)

2 Convective self-assembly of colloidal particles

The convective self-assembly of colloidal particles is an attractive bottom-up approach allowing for the creation of nanoscale features on large substrate surface areas. Interactions between colloidal polymer nanospheres at a so-called triple phase boundary can result in the formation of hexagonally close packed monolayers of polymer spheres. This process will be described in detail in Chapter 2.1. By the doctor blade technique, which is introduced in Chapter 2.2, such nanosphere monolayers can be deposited on large areas by moving the triple phase boundary across a substrate surface (Fig. 2.1 (a)).

These sphere monolayers can be used in nanosphere lithography (NSL) for the large-area surface patterning with nanometric features. To this end, the sphere layer acts as a shadow mask in a material deposition step. The thereby created nanopoatterns can be tailored either by modification of the shadow mask morphology, e.g. by thermal, ion beam or plasma treatment of polymeric spheres, or by variation of the material deposition method, e.g. the physical vapor deposition technique or deposition geometry. The NSL technique allows for the creation of hexagonally arranged nanoparticles with triangular basis (Fig. 2.1 (b)) or antidot patterned metal and semiconductor thin films (Fig. 2.1 (c)), which is presented in Chapter 2.3.

This chapter also includes an introduction into the field of soft lithography, where elastomers can be used for pattern transfer. The hexagonally close-packed sphere monolayers are shown to be suitable topographic templates for the preparation of nanopatterned polymeric stamps (Fig. 2.1 (c)).
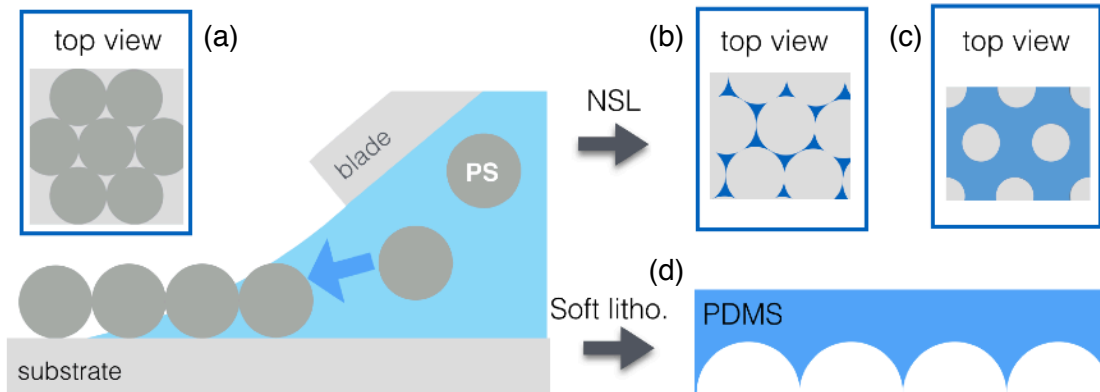
Fig. 2.1: Chapter overview: Hexagonally close-packed monolayers of polymer spheres are prepared by convective self-assembly (a) with the doctor blade technique. They are then used as shadow masks in nanosphere lithography (NSL) for the preparation of large-area nanoparticle arrays (b) or antidot patterns (c). In another approach sphere monolayers act as a topographic template for PDMS stamp patterning for soft lithography (d).

2.1 Colloidal suspensions

The building blocks in a colloidal system are the dispersed particles. The spectrum of nanoparticles which can be dispersed in liquid media is large. Particles differ both with respect to their composition as well as to their shape [1]. Quantum dots from CdSe [2], nanotetrapods from CdTe [3], cubic nanocrystals from perovskite materials [4], micelles or vesicles from polymers and lipids [5] are just a few examples of colloids often found in research as well as in applications. Also core-shell particles are exploited [6,7] and many possibilities for particle modification by functionalization evolve [8].

Colloidal systems are well suitable for the defined deposition of their building blocks onto solid substrate surfaces. While in suspension, particles interact with each other and with the liquid media they are dispersed in, in deposition processes, interaction with the surface need to be taken into account. These interactions strongly depend on surface properties (charges, functionalities, polarities, wettability, …) determining the deposition processes.

This work will focus on the deposition of polymer spheres from aqueous suspensions onto solid semiconductor or metal surfaces by convective self-assembly. Different colloidal suspensions are used:

- In the present chapter polystyrene (PS) spheres with a diameter of 618 nm are arranged in a monolayer on planar silicon substrates. Such polymer spheres are commonly used as they are easy to synthesise in a large range of sizes (few hundred nm - few hundred μm) but with narrow size distributions. The doctor blade technique as one approach for the deposition of such colloids will be described in detail in Chapter 2.2.
- Colloidal PS spheres with a diameter of 2.1 μm are used in Chapter 3, where they are assembled in trenches on pre-patterned silicon substrates for nanosphere lithography.
- Another group of widely used and much investigated colloids are metal nanoparticles. They are of particular interest in catalysis [9] as monodisperse suspensions can be easily created in large amounts with particle

diameters in the single-digit nm regime [10]. In Chapter 4.4 colloidal gold nanoparticles with 5 and 10 nm in diameter are deposited from aqueous suspensions into nanopores on pre-patterned substrates.

2.1.1 Polystyrene spheres

The polymer colloids used in this work are made from polystyrene. Such particles are commonly synthesised by emulsion polymerization [11, 12] (Fig. 2.2).

To this end, (styrene) monomers are dispersed in a water/surfactant mixture forming an immiscible heterophase system. This leads to the formation of large monomer droplets (100 µm - 1 mm diameter) and small surfactant micelles (30 - 500 nm diameter). The emulsion polymerization process is driven by diffusion of monomers from the large droplets into the micelles. Water-soluble initiator molecules are then added, which also diffuse into the micelles where they start the polymerization.

The polymerization process is restricted to the inside of each micelle acting as a nanoreactor. This is ensured by several properties of the system: (a) Both, monomers and initiator molecules show a higher solubility inside micelles. (b) The reservoir droplet has a small surface to volume ratio compared to the micelles. Thus, the diffusion of initiator molecules into the large monomer droplets is unlikely. (c) Coalescence of the micelles is avoided by steric and electrostatic repulsion of the surfactant molecules forming the outer micelle shell.
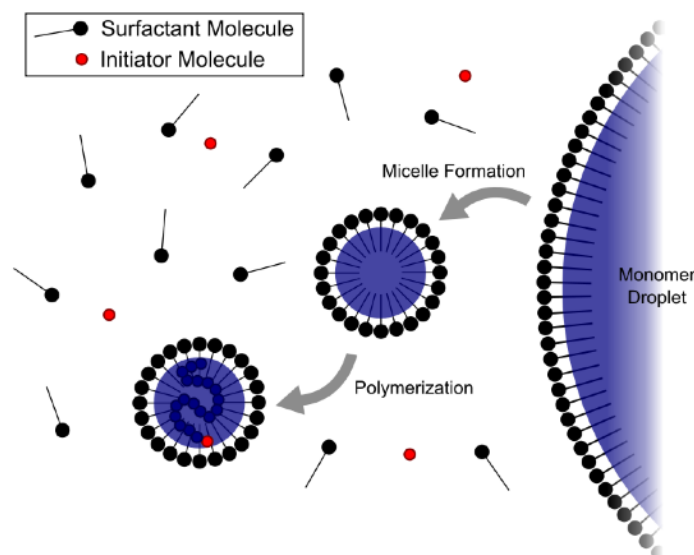
Fig. 2.2: Schematic process of an emulsion polymerization. Smaller micelles form from a monomer droplet. Initiator molecules diffuse into the micelles, where the polymerization takes place [13].

Inside the micelles, radical polymerization of styrene monomers leads to chain growth. Typically few chains per micelle are created, decreasing the probability of chain termination and thus allowing for high molecular weights. The monomer-swollen micelle grows until all the monomer droplets disappear, while the initiator diffuses constantly into the micelles. The polymer chain length thus can be set by control of the monomer and initiator molecule addition. For detailed information on emulsion and polymer particle synthesis by radical polymerizations see e.g. [12] and [14]. By this polymerization process, monodisperse polymer particles with high molecular weight can be prepared in large scale batches at high polymerization rates. Typical colloid particle diameters are 100 nm - 10 µm.

A drawback of this particle synthesis is the need for surfactants (e.g. sodium dodecyl sulfate (SDS)) which will stay on the particle surface and in the suspension medium. The liquid medium is likely to contain residuals such as initiator molecules (e.g. azobis(isobutyronitril) (AIBN)) or styrene monomers. After polymerization, buffer agents, inert salts, preservatives for bacterial growth, and others may be added for better suspension stability and increased shelf life.

2.1.2 Interactions between colloids in suspension

The stability of a colloidal suspension is mainly determined by particle-particle- and particle-liquid interactions. Repulsive and attractive forces between the particles contribute to their behavior in a liquid medium [14]. The DLVO theory (named after Derjaguin, Landau, Verwey and Overbeek) [15,16] combines the forces to an interaction potential. Figure 2.3 shows the interaction energy U_{DLVO} between two colloids as a function of the inter-particle distance d.
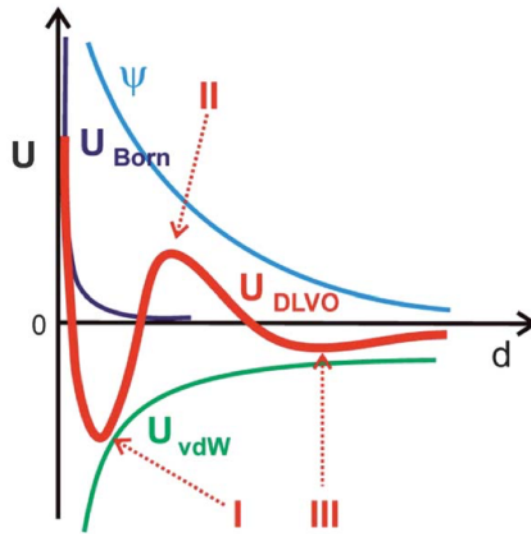
Fig. 2.3: Interaction potential between two particles in dependence of their distance d according to the DLVO theory. Born potential U_{Born}, electrostatic repulsion ψ and van der Waals attraction U_{vdW} sum up to the overall potential U_{DLVO}. Distance I corresponds to particle coagulation avoided by the energy barrier at distance II. Reversible colloid flocculation occurs at distance III [17].

According to the DLVO theory, the total interaction potential U_{DLVO} (Fig. 2.3 marked red, Eqn. 2.1) can be described as the sum of the van der Waals attraction U_{vdW}, the electrostatic repulsion ψ and the Born repulsion U_{Born}:

$$U_{DLVO}(d) = U_{vdW}(d) + \psi(d) + U_{Born}(d) \tag{2.1}$$

The Born repulsion is to be taken into account for particle distances smaller than the particle radius. With the assumption of a hard sphere model, this strongly repulsive potential is typically modelled as a d^{-12} dependence. Overlapping of the particles is prevented by this strong potential. Main contributing forces at particle distances larger than the particle radius result from electrostatic repulsion and van der Waals attraction. At small distances, van de Waals interactions are predominant resulting in a primary minimum (Fig. 2.3, distance I) of the total interaction potential. At this distance colloids will coagulate forming irreversible agglomerates. For stable colloidal suspensions, this state is avoided by dominating repulsive forces creating an energy barrier at larger distances (distance II). The height of this barrier decreases with increasing salt

concentration in the suspension. The salt concentration at which the energy barrier vanishes is referred to as the critical coagulation concentration (CCC). The suspension is then no more stable and irreversible agglomeration occurs. The secondary minimum (distance III) resembles colloid flocculation, i.e. reversible agglomeration [17].

The attractive van der Waals potential U_{vdW} (Eqn. 2.2) evolves from intermolecular dipole interactions at short distances. These interactions can take place between permanent dipoles (U_{Keesom}), induced dipoles (U_{London}) or mixed states (permanent dipole-induced dipole interaction, U_{Debye}).

These van der Waals interactions are proportional to a d^{-6} distance dependency and scale with the distance-independent constant C_{AB}, containing mainly the dipole moment and the polarisability of the particles A and B.

$$U_{vdW}(d) = U_{Keesom}(d) + U_{Debye}(d) + U_{London}(d) = - \frac{C_{AB}}{d^6} \qquad (2.2)$$

The electrostatic repulsion ψ (Eqn. 2.3) is typically defined by the Stern potential ψ_0 (see definition below) in dependence of the distance d between the particles and the Debye length κ^{-1}:

$$\psi(d) = \psi_0 \cdot \exp(-\kappa d) \qquad (2.3)$$

The origin of the electrostatic repulsive forces between the particles is the overlap of the so called electric double layers of two colloids.

In the model of the electric double layer (EDL) formed around a colloidal particle in a suspension, the ζ-potential can be understood as the electrostatic potential at the slipping plane around a colloid [14]. This is illustrated in Figure 2.4. Depending e.g. on their chemical composition, colloidal particles have a certain surface potential, which is in most cases negative. The EDL forms immediately when the particle gets in contact with a liquid medium. In closest distance from the particle surface the dense packed Stern layer of counter ions can be found. Within this layer the electric potential decreases linearly towards the Stern potential ψ_0. In the diffuse layer in larger distance of the particle surface the concentration of the counter ions decreases to the bulk ion density of the electrolyte and the potential decreases exponentially (see plot in Fig. 2.4).
When the particle is in motion another characteristic layer in between the Stern layer and the diffuse layer becomes obvious. This is where counter ions are still strong enough attracted to the particle to follow its motion. A slipping plane evolves as the attracted ions form a stationary layer whereas the bulk liquid will not follow the particle motion. Within this region the potential still decreases linearly. The potential at this slipping plane (white dotted line in Fig. 2.4), where the behavior changes from a linear to an exponential decay, is the ζ-potential.
The thickness of the complete electric double layer is described by the Debye length κ^{-1}, at which the potential reaches 1/e of the surface potential.

For thick electric double layers the particles are electrochemically stabilized. When particles come close to each other, the EDL may overlap but particles will be repelled from each other. If the electrochemical double layers thickness, however, becomes too small, short-range van der Waals attractions become predominant and particles coagulate. This corresponds to the absolute minimum (distance I) in the interaction potential plotted in Figure 2.3. The thickness of the electric double layer is a parameter which can be experimentally adjusted to

influence the suspensions stability, for example by changing the suspensions pH value or the ion density in the bulk suspension. A way to quantify the thickness of the EDL is to measure the ζ-potential.

Describing the repulsive force in dependence of the ζ-potential makes its importance for the suspension stability more obvious. The electrostatic repulsive contribution (Eqn. 2.3) can not only be described in dependence of the Stern potential, but also as potential U_{rep} (Eqn. 2.4), which is a function of the ζ-potential :

$$U_{rep}(d) = 2\pi \cdot R \cdot \varepsilon \cdot \zeta^2 \cdot exp(-\kappa d) \tag{2.4}$$

with distance d from the surface, the colloids geometry (for spherical particles their radius R), the dielectric constant ε of the dispersant, the Debye-Hückel length κ^{-1}.
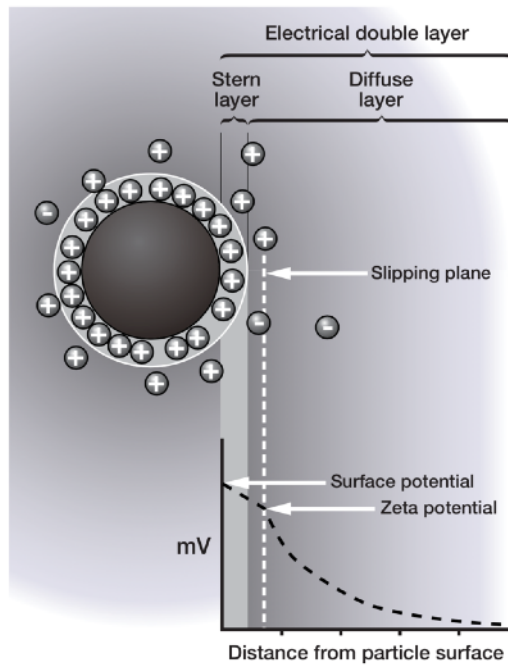
Fig. 2.4: Sketch of the electric double layer formed on a particle surface in a liquid medium and electric potential in dependence of the distance from the particle surface [18].

This ζ-potential is used as a measure for the electrostatic repulsion and the suspensions stability [19]. It relates to the height of the energy barrier marked in Figure 2.3, at distance II.

The ζ-potential can be measured indirectly. The solvent molecules and ions within the sheer plane form a layer around the particle which follows the particles movement. The thickness of this layer thus has an influence on the electrophoretic mobility U_e of the colloidal particle and follows Equation (2.5) [20]:

$$U_e = \frac{2\varepsilon \cdot \zeta \cdot f(\kappa \cdot 2R)}{3\eta} \tag{2.5}$$

with f(κ2R) being the Henry function, R the particle radius, η the dynamic viscosity of the liquid and ε the dielectric constant of the dispersant. Thus, the ζ-potential can be calculated from mobility measurements.

2.1.3 Ultrafiltration of suspensions for ζ-potential control

In this work, the ζ-potential was found to be a measure for the assembly characteristics of colloids onto a solid surface.

For some experiments, e.g. in Chapter 3, two polystyrene (PS) particle suspensions A and B were used. These suspensions have the same specifications (PS spheres in water, 2.1 µm diameter, 10 % w/v solid content, 3% CV) and differ only in the suppliers batch number. However, one of these suspensions (A) shows good assembly properties, i.e. close-packed hexagonal sphere monolayers can be formed by convective self-assembly; the other suspension (B) could not be used for monolayer formation as particles seem to repel each other and only low surface coverage without any order occurred during convective self-assembly experiments (similar to Fig. 2.5(a) left) at otherwise the same self-assembly conditions.

Here, the electrophoretic mobility U_e is measured by dynamic light scattering with a Malvern ZetaSizer Nano instrument [18]. The suspension is filled into a U-shaped test cell with electrodes at the ends of the „U". A voltage is applied, which induces a particle motion. By dynamic light scattering this particle motion can be observed and with an autocorrelation function transferred into the electrophoretic mobility. The ζ-potential is then determined by Equation 2.5.

ζ-potential measurements confirmed the assumption of repulsive forces between particles. The ζ-potential was measured as -56 mV for the suspension B showing no assembly. In contrast, the arranging suspension A has a ζ-potential of -38 mV. Thus, this suspension is less stable, which is more useful for our purpose of particle assembly.
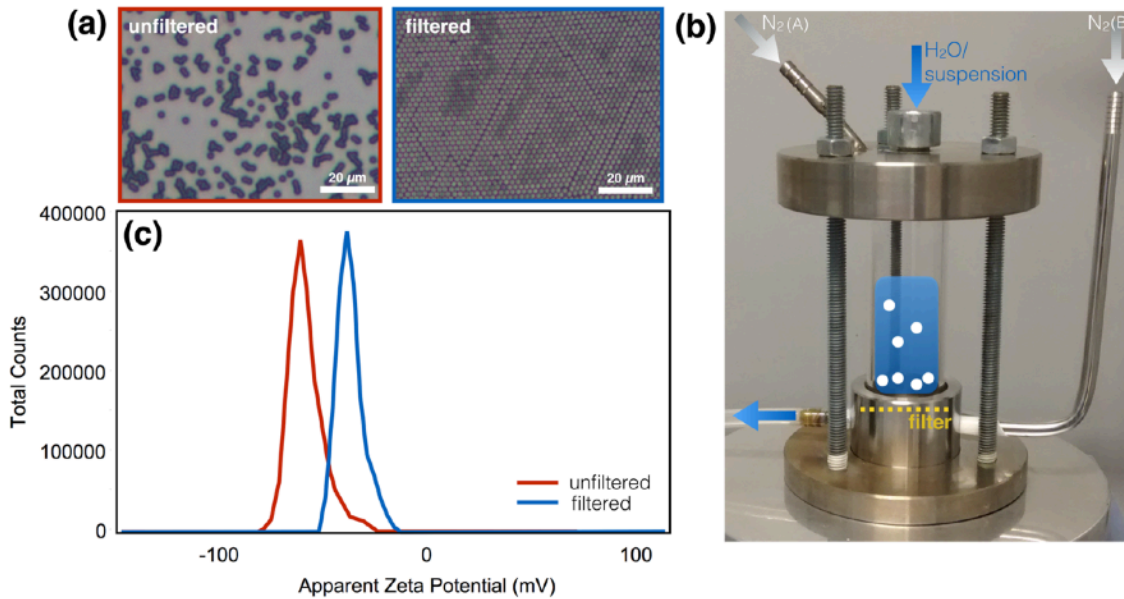
Fig. 2.5: (a) Optical microscope images showing the achievable assembly of spheres before (left) and after (right) filtration. (b) Photography of home-built ultrafiltration system with annotations of the filtration process. The suspension is stored in a glass tube in the center. Water is added from above, nitrogen (N_2(A)) presses the liquid through a filter which prevents spheres from exiting the glass tube, whereas the liquid medium is removed. A nitrogen flux from below the filter (N_2(B)) is used after filtration to release the spheres. (c) Comparison of the measured ζ-potential of filtered (blue) and unfiltered (red) suspension.

As the increased ζ-potential can be expected to result from a higher surfactant concentration in the suspension (added by the supplier), the liquid phase is exchanged by an ultrafiltration with deionized (DI) water. This exchange is performed in a home-built ultrafiltration device as shown in Figure 2.5 (b).

The central element of this tool is a filter made out of polycarbonate (PC) with a pore size of 2.0 µm diameter.[1] The suspension is filled into a tube above the PC foil and filtered and re-dispersed in DI water. To accelerate the filtration process a nitrogen steam (N$_2$(A) in Figure 2.5 (b)) is used to push the dispersing media through the filter. Particle sedimentation and blockage of the filter is avoided by stirring the suspension with a magnetic stirrer right above the filter element. The colloids are trapped above the filter paper, while the liquid is removed. To avoid drying of the spheres and for repeated rinsing, DI water is constantly refilled. After three rinsing repetitions with approx. 20 ml of exchanged water in each step, the filtered suspension is extracted. To minimize the loss of particles sitting on the filter, a nitrogen flux (N$_2$(B) in Figure 2.5 (b)) from below the PC foil is used to flush the colloids back into the suspension.

For suspension B, the ζ-Potential is measured before and after ultrafiltration, as plotted in Figure 2.5 (c). The ζ-potential is decreased from -56 mV before the filtration to -38 mV after the filtration and thus corresponds exactly to the ζ-potential of suspension A.

In order to examine the effect on the ordering behavior of colloids, assembly experiments are performed with both suspensions (B, unfiltered and filtered) under comparable conditions[2]. Results of the sphere arrangement are shown in Figure 2.5 (a). The filtered suspension is able to form close-packed monolayers, indicating that repulsive forces are no longer predominating.

An alternative to the ultrafiltration approach to adjust the ζ-potential is to change the pH value of the suspension [14]. An advantage of the ultrafiltration however is, that one also gets rid of surfactants or at least decreases their concentration. Surfactant residuals may be a problem in subsequent experiments, which are performed with the deposited spheres. The residuals are likely to condense near contact areas between neighboring spheres in close-packed layers or at contact points between spheres and the solid substrate, contaminating the surface.

2.1.4 Convective self-assembly of colloids at the triple phase boundary

In this work, colloidal particles are deposited onto solid surfaces by convective self-assembly. This is an approach for the self-organized creation of close-packed 2-dimensional crystals of colloids. In contrast to other crystallization techniques, all of which mainly rely on the arrangement of particles either on a solid surface or at a liquid interface, the evaporation-induced convective self-assembly shown here allows for the fast, easy and cheap patterning of surfaces.

In convective self-assembly, colloidal particles arrange themselves at the so called triple phase boundary (Fig. 2.6) between the liquid suspension, the solid substrate surface and the surrounding gas phase, when a suspension droplet is placed onto a solid substrate. During evaporation of the liquid phase, particle self-arrangement takes place at this contact line [21, 22].

---

[1] Whatman track edge polycarbonate foils, pore diameter 2.0 µm

[2] Oxygen-plasma cleaned Si wafers at 30 °C substrate temperature in air with 35 % relative humidity. Doctor blade velocity was 7 µm/s. Technique is described in detail in the following chapter.

The behavior of the colloids at a droplets contact line with a solid is different to their behavior in bulk suspension and cannot be described by the DLVO theory as no equilibrium state is emanent and interactions with the surface become predominant. Thus, not only the suspension characteristics influence the behavior, but all the above mentioned contributors (liquid, substrate, gas phase) need to be considered.

The solid substrate can be described by its material, surface free energy, roughness and surface charges. These characteristics mainly determine the shape of the suspension droplet, thus the shape of the triple phase boundary. For the description of the surface interactions with the solvent, the contact angle is a commonly used measure. By contact angle (CA) measurements, the general wettability of the surface with a certain liquid is determined. For convective self-assembly, good wettability (CA < 20°) is an inevitable requirement.

The liquid, i.e. the colloidal suspension, must be described regarding several parameters: the chosen solvent, the dispersed particles (material, size, size distribution, surface charges), the particle concentration, pH values, possible surfactants and many more. Within the description of the colloidal suspension by the DLVO theory discussed above, it was shown that especially the ζ-potential crucially determines the particle-particle interactions, which become even more important at the triple phase boundary than they are in bulk. The control of the ζ-potential was shown to be a requirement for the close-packed colloid assembly.

The surrounding gas phase determines the evaporation flux of the suspensions liquid medium by its relative humidity and the temperature.
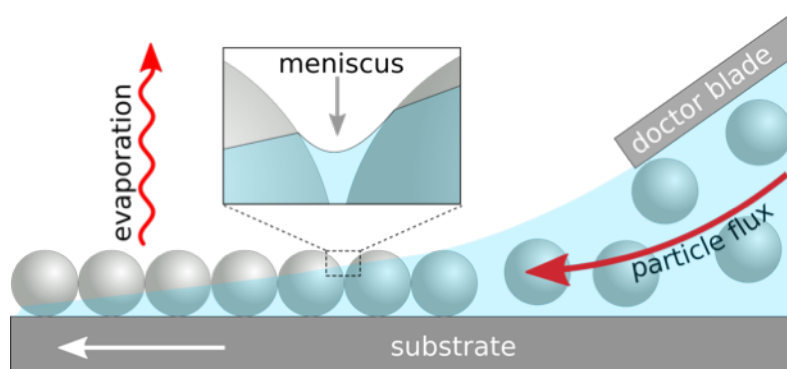
Fig. 2.6: Sketch of triple phase boundary between solid substrate, liquid colloidal suspension and surrounding gas phase. Increased evaporation flux in the evaporation zone induces a liquid flux towards the contact line. This liquid flux leads to a particle flux in the same direction, thus a high colloid concentration at the triple phase boundary. Meniscus formation between the particles (inset) results in capillary forces drawing particles into close-packed layers.

An increased evaporation of the liquid medium occurs at the very boundary. This evaporation leads to a flux of liquid from the bulk of the droplet towards the boundary. This convective liquid flux induces a flux of colloidal particles. The concentration of colloids thus increases drastically in this region and particles need to arrange themselves on the surface. When spheres get in close proximity to each other and the thickness of the liquid reaches/falls below the particle diameter, capillary forces arise. The strongly attractive, long range immersion forces lead to a deformation of the liquid-gas interface (inset Fig. 2.6) [23]. A Laplace pressure then causes the

colloid attraction in order to minimize the interfacial energies. Thus, colloids are drawn together forming hexagonally close packed mono- or multilayers.

Dimitrov et. al [21] found an analytical relation (Eqn. 2.6) describing the colloid crystal growth velocity v in dependence of the conditions at the triple phase boundary:

$$v = \frac{\beta \cdot Q \cdot j_v \cdot \mu}{h_f \left(1-\mu\right)\left(1-\varepsilon_p\right)} \qquad (2.6)$$

The suspensions properties influence the crystal growth velocity v with β as the particle - liquid velocity coupling parameter, μ the particles volume fraction of the suspension, h_f the film height. The evaporation flux j_v is mainly determined by the nature of the liquid medium and the surrounding gas phase (temperature, relative humidity, gas pressure). The solvent evaporation takes place above the length of the evaporation zone Q and ε_p is the layer porosity, which is 0.605 for a hexagonally close-packed arrangement of spherical particles. This relation means that the liquid flux needs to be commensurate with the evaporation flux in order to achieve steady state conditions for a controlled crystal growth.

2.2 Large-area self-assembled nanosphere monolayers by doctor blade technique

To enlarge the area of close packed (mono)layers to a homogeneous large surface area of several cm^2, the triple phase boundary can be moved over the substrate surface. The controlled 2D colloid crystal growth by convective self-assembly can be achieved by several techniques such as dip coating, spin coating or the doctor blade technique [25-27]. The latter is described here.

In order to move the contact line in a controlled way to match with the crystal growth speed as precisely as possible, a home-made doctor blade apparatus [24] is used in this work. The apparatus basically consists of a glass blade which spreads a suspension droplet and draws it over the sample situated on a translation stage. The movement of the sample can be set by a stepper-motor with computer control. Velocities are in the range of 1 µm/s to approx. 250 µm/s. Speed ramps can be set and amount to usually 200 µm/s^2 in the experiments described here.

Besides this, the velocity of the colloidal crystal growth can be tuned indirectly by changing the evaporation rate of the liquid. This is realized by a temperature control of the sample holder with a Peltier-heating system. In addition, the whole setup is situated inside a glove box with dry gas input (N$_2$ or Ar) to control the humidity. The temperature of the sample holder, the temperature of air and air humidity are measured. As the shape of the suspensions meniscus might have an influence on the colloid self-arrangement, the angle between surface and blade is adjustable and the meniscus is observed in-situ with a light microscope.

As a blade to draw the suspension over the sample surface a glass slide or piece of a Si wafer is used, which is functionalized with octadecyltrichlorosilane (OTS) to get a hydrophobic surface. The blade does not touch the sample surface. Capton tapes with 70 µm thickness are used as a spacer as depicted in Figure 2.7.

The experimental procedure is as follows: the substrate surface is cleaned by an RCA process or a plasma treatment (see App. A2) and 2 mm broad stripes of capton tape are placed at two opposing very edges of the sample. A droplet of the suspension with a volume of typically 20-100 µl is placed at one untaped edge of the sample. The blade is then placed onto the droplet. This leads to a spreading of the droplet along the blade between the spacers. The sample is then moved with the translation stage underneath the blade with a defined

velocity. The motion proceeds until the opposite sample edge is reached. The residual suspension is flushed off the sample with nitrogen, to avoid a flow back of the suspension onto the sphere covered areas.
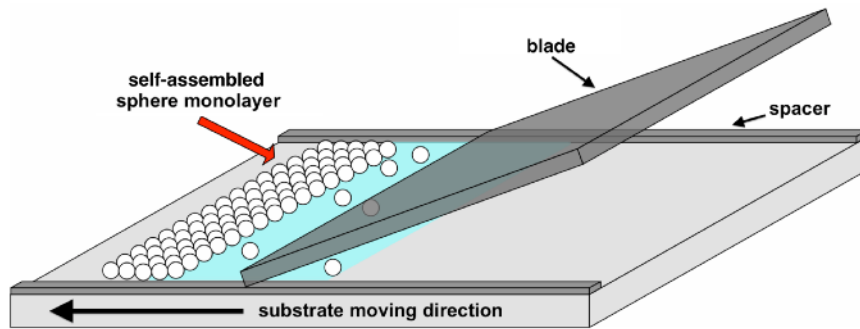
Fig. 2.7: Sketch of the doctor blade technique. A droplet of colloidal suspension is spread between the surface and a blade forming a triple phase boundary. By moving the substrate underneath droplet and blade, the triple phase boundary is moved over large surface areas.

The suspension droplet volume should be large enough so that at least approx. 80 vol% of the droplet are left over after covering the whole sample with a particle layer, as the concentration of particles inside the droplet should be constant throughout the experiment and not increased due to evaporation of the liquid medium or decreased due to sphere deposition. A typical amount of suspension is 20 μl/cm² sample area.

If the velocity of the sample and thus the velocity of the triple phase boundary does not match the particle layer growth rate in Equation 2.6, defects occur within the particle layer. For blade velocities faster than the colloidal crystal growth, particles will arrange themselves into islands leaving blanc substrate areas as particle transport towards the triple phase boundary is not fast enough and not enough particles are available for the formation of close-packed monolayers. If, however, the blade velocity is too slow, more particles are transported towards the triple phase boundary than are needed for colloidal monolayer formation, thus bilayers or multilayers of particles are created.

The most crucial experimental parameters in order to optimize the self-assembled sphere layer quality (few lattice defects, large monolayer fraction) are:
- particle diameter and concentration
- substrate wettability, influencing the length of the evaporation zone
- blade velocity
- substrate temperature and relative humidity of gas phase for evaporation flux control

as they mainly determine the crystal growth velocity.

Experimental parameters for the preparation of hexagonally close-packed sphere layers with high fraction of monolayers with minimal defect density are listed in Table 2.1. Parameters are given for monolayer preparation on silicon wafers with a native oxide layer using plasma cleaning (App. A2) as surface pre-treatment in case of 220 nm or 618 nm spheres, and for monolayers on plasma cleaned glass object slides for 1 and 2 μm spheres.

Tab. 2.1: Best parameters for preparation of the monolayers of different PS spheres on plasma-cleaned Si surfaces. Surrounding temperature is in all cases room temperature. The coefficient of variance (CV) gives the uniformity of the particles and is defined as the standard deviation of particle diameters divided by the actual mean diameter.

Sphere diameter [nm]	Solid content [% w/v]	CV [%]	Supplier [Art. No.]	Relative humidity [%]	Substrate temperature [°C]	Blade velocity [µm/s]
220	10	< 3	Thermo Scientific Inc. [5022A]	50	21	90
618	2	2.7	Microparticles GmbH [PS-ST-B1156]	42	30	22
1000	10	< 3	Duke Scientific [5100A]	50	28	210
2000	10	< 3	Thermo Scientific Inc. [5200A]	40	28	110

For the preparation of monolayers of these PS spheres by convective self-assembly, the wettability of the surface with water is crucial. If the contact angle of water on the substrate is between approx. 10° and 40° the surface is generally suitable for sphere deposition. The monolayer deposition, mostly with 618 nm PS spheres, was successfully conducted on $Si/SiO_{2,nat}$ surfaces, glass, gold and titaniumoxide. Silicon wafers with native oxide are typically cleaned with an RCA process or O_2-Ar plasma treatment (App. A2). As glass surfaces commercially available objective slides were used. They are typically rinsed with water to remove the separating agent and then O_2-Ar plasma cleaned. Gold thin films were prepared by electron beam evaporation of 2 nm Ti as adhesion promoter and 15 nm Au onto $Si/SiO_{2,nat}$ surfaces and used without further treatment. TiOx surfaces were obtained by electron beam evaporation of 15 nm Ti onto $Si/SiO_{2,nat}$ and native oxidation in air. Indium-tin oxide (ITO) and freshly cleaved mica could not be covered with close-packed sphere monolayers, but only with islands of spheres. This is probably due to surface charges in case of mica and bad wettability in case of ITO. For the latter, the contact angle with water is approx. 65° and can not be decreased by surface pre-treatment with a plasma as this leads to damage of the ITO layer.

Choosing the droplet motion velocity and all above mentioned parameters commensurate to the growth velocity of the colloidal crystal (Eqn. 2.6), large area monolayers of self-arranged particles as shown in Figure 2.8 can be created.

The hexagonal arrangement is only disturbed by few defects e.g. originating from (a) surface imperfections which can locally change the shape of the triple phase boundary (meniscus pinning) or (b) spheres with slightly smaller diameter (marked red) leading to voids or dislocations (marked blue). If the particle layers are grown on large areas crystal growth is (c) likely to start at several points along the tripe phase boundary. When these growing domains meet, grain boundaries form (not shown here). For detailed information about the defects and typical defect densities see [28] and [29].
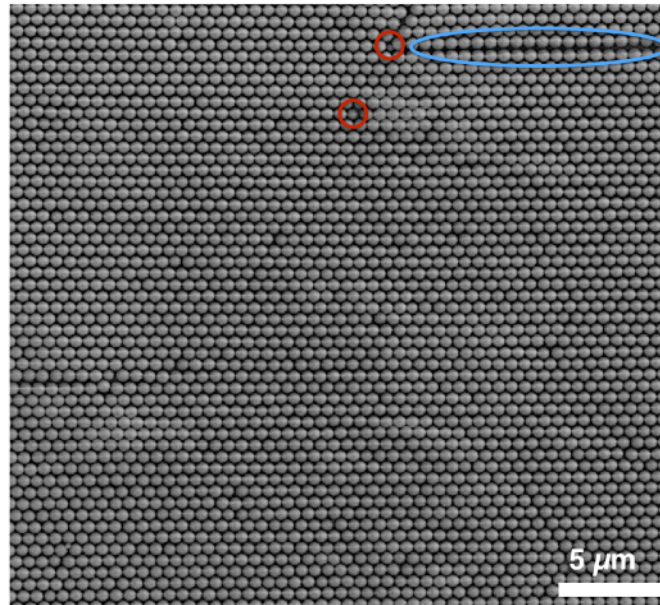
Fig. 2.8: SEM image of a PS sphere monolayer on Si/ SiO$_2$. Sphere diameter is 618 nm. Hexagonal order is only disturbed by spheres which are too small (red circle) which occasionally lead to dislocations (marked blue).

Section summary

Monolayers of nanospheres from colloidal suspensions can be easily created by convective self-assembly, during which the particle concentration is locally increased at a triple phase boundary. Capillary forces then draw the particles into hexagonally close-packed arrangements. By moving the triple phase boundary with the doctor blade technique over a substrate surface, particle monolayers can be prepared at wafer-scale. Suspension characteristics, such as the ζ-potential, need to be taken into account., as strong attractive or strong repulsive forces between colloids can inhibit the formation of close-packed sphere layers.

2.3 Self-assembled nanosphere monolayers as pattern templates

Large-area sphere monolayers can be used as templates for the patterning of surfaces. The general procedure for the creation of triangular shaped nanoparticles by nanosphere lithography (NSL) is described in detail in Chapter 2.3.1, while it is presented in Chapter 2.3.2 how a modification of the nanosphere monolayer allows for the creation of antidot patterned thin films, i.e. thin films with hexagonal cylindrical holes.

The Chapter 2.3.3 gives an introduction into soft lithography. It is demonstrated that the morphology of the sphere monolayers can be replicated by casting PDMS on the surface. This soft lithography approach allows for the patterning of the elastomer with nanosized tips for their use as stamps in micro-contact printing.

2.3.1 Nanosphere lithography for nanoparticle arrays

By nanosphere lithography (NSL) surfaces can be patterned with ordered nano-metric motives on large areas [30, 31]. Monolayers of colloidal polymer spheres can act as a shadow mask during a material deposition step. After this deposition the polymer spheres are removed leaving an array of nanoparticles with the shape of the sphere mask shadow behind [32]. This procedure is sketched in Figure 2.9 (a).

Figure 2.9 (b) shows a SEM image of a polystyrene sphere monolayer on a Si/SiO$_2$ substrate. Polymer spheres are deposited from a colloidal suspension and arrange themselves in a hexagonally close packed layer by convective self-assembly as described in detail in the previous chapter. When arranged in a hexagonally close-packed monolayer mask openings with triangular shape (triangles with concave edges) are formed in between three neighbouring spheres. This gap acts as a mask opening during a material deposition step. The material is deposited onto the whole sample, thus onto the spheres and, through the mask openings, onto the substrate. The polymer spheres are then removed chemically and mechanically by dissolution in tetrahydrofurane (THF) in an ultrasonic bath. As a result, hexagonally arranged nanoparticles with triangular basis are created on the Si surface, as shown in the SEM image in Figure 2.9 (c). The inset shows the metal triangles in larger magnification. However, it must be mentioned, that not only such triangular nanoparticles are formed. Defects in the polymer sphere monolayer are replicated through the metal deposition resulting in e.g. metal lines on the surface, as can also be found in Figure 2.9 (c). Further details on the description and quantification of mask defects can be found in [28].
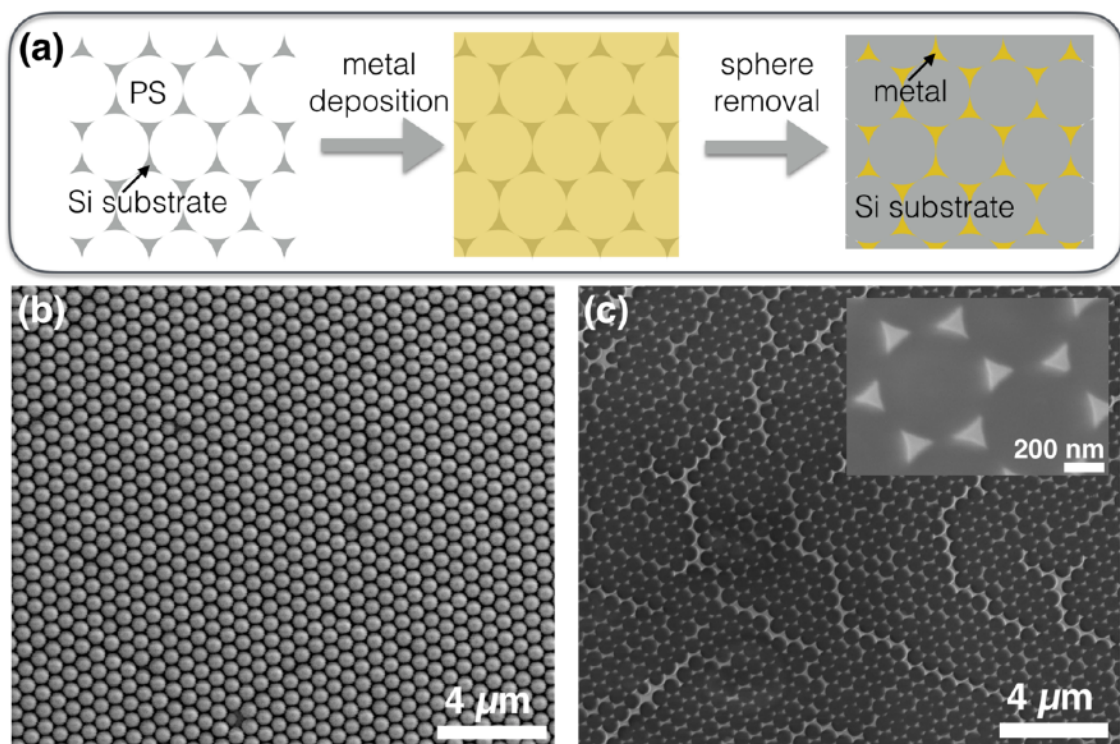
Fig. 2.9: (a) Sketch of the nanosphere lithography procedure. (b) SEM image of a polymer sphere monolayer, here PS spheres with 618 nm diameter on Si/SiO$_2$. (c) Metallic nanoparticle array formed after metal deposition (2 nm Ti adhesion promoter + 10 nm Au) on sphere mask as in (b) and subsequent sphere removal. Inset: Hexagonally arranged nanoparticles with triangular basis at higher magnification.

The variety of motives which can be produced by NSL can be increased by either (i) manipulating the shadow mask [33] or by (ii) modifying the deposition step:

(i) Mask modification. The polymer sphere mask can be e.g. modified by a thermal treatment leading to a sphere sintering which will diminish the mask openings and deform them into a round shape [34]. Treating the sphere layer in an oxygen plasma, however, removes some polymer material resulting in a sphere shrinking, thus spheres do cover less of the surface area and are no longer close-packed [35, 36]. By this for example antidot patterned thin films can be created. This is discussed in detail in the following.

(ii) Deposition step. Different materials can be deposited onto the substrate through the mask openings, such as metals, semiconducting or isolating materials as well as organic materials. Deposition from different angles allows for the creation of nanoparticles with nearly arbitrary shape [32, 37, 38]. The deposition from different angles is further discussed in Chapter 3.3. Instead of adding materials to the defined freely accessible areas, however, the spheres can also act as masks for material removal by etching or material modification by ion implantation processes [39-41].

2.3.2 Antidot patterns by nanosphere lithography with modified sphere masks

Antidot patterns, i.e. material thin films with dot-shaped free substrate areas, can be created by nanosphere lithography if the sphere mask is modified prior to the material deposition step. A plasma treatment by reactive ion etching leads to the shrinking of the polymer spheres to smaller diameters, while maintaining their position in the hexagonal arrangement. Using these non-interconnected spheres as a shadow mask in NSL allows for the creation of these antidot patterns.

Sphere shrinking. In this work, the hexagonally close-packed polymer sphere monolayers are modified by reactive ion etching [35]. Exposure of the polymer spheres to an argon-oxygen plasma results in partial removal of polymer material, changing the shape of the spheres and changing their diameter. This is induced by two effects: chemical modification of the material (here predominantly by the oxygen) and physical sputtering (mainly by the Ar). The extent of these changes can be controlled by defining ion densities, power, pressure and other parameters as further described in [42]. In this work, the exposure time of the spheres to the plasma treatment is adjusted. Figure 2.10 shows the results of polystyrene sphere modification in a plasma of 2 sccm O_2 and 8 sccm Ar at a power of 50 W RF at 75 mTorr for 0.5 - 8 minutes in an *Oxford Instruments PlasmaLab 80plus* apparatus.

The top-view SEM images in Figure 2.10 show polystyrene spheres, which were exposed to the plasma for different treatment times and thus are shrunk to different extends. Sphere diameters decrease with increasing plasma treatment duration.

Plasma treatment of close-packed sphere layers for very short times (< 30 s) results in the deformation of spheres into hexagonally shaped polymer particles. This is probably because of increasing mobility of polymer chains and first breaking of polymer bonds creating chain fragments, which are likely to diffuse towards areas of highest radius of curvature as can be found at contact points between neighbouring spheres. The filling-up of such areas with material is energetically favorable. After this state, for slightly longer plasma treatment times (approx. 1 min), spheres start to shrink. The transition between these early states is shown in Figure 2.10 (b). In the contacting areas of neighbouring spheres, material remains a little longer forming thin connecting wires. These wires can be up to 200 nm long and are very thin (< 20 nm in diameter)[1]. These wires break and disappear after longer exposure to the plasma. Spheres then shrink in diameter nearly linearly with time. In Figure 2.10 (f) the sphere diameters (measured in top-view) are plotted for different plasma treatment times. The data shows the nearly linear shrinking behavior starting with polystyrene spheres with a diameter of 618 nm (blue x) and with polystyrene spheres with a diameter of 220 nm (green triangles) for the plasma parameters used here. In [35] a non-linear behavior for long plasma durations was reported. Figure 2.10 (f) indicates that starting with an appropriate initial sphere diameter, it is possible to adjust the antidot diameter between approximated 550 nm and 80 nm by the plasma treatment time. As one can also see in Figure 2.10

---

[1] Such connecting wires are not shown here as they do not appear during the shrinking of all polymer spheres. This might depend on slightly different polymer densities within the particles or different amount/ species of surfactants in the particle suspensions. Typically connecting wires are more likely to appear during the shrinking of larger particles (initial sphere diameters > 1 µm). Similar wires were also observed after nitrogen plasma treatment of polystyrene spheres [35].

the roughness of sphere surfaces increases over time, which makes it favorable to start with smaller spheres rather than using plasma times larger than 8 min, if small antidot diameters are required.
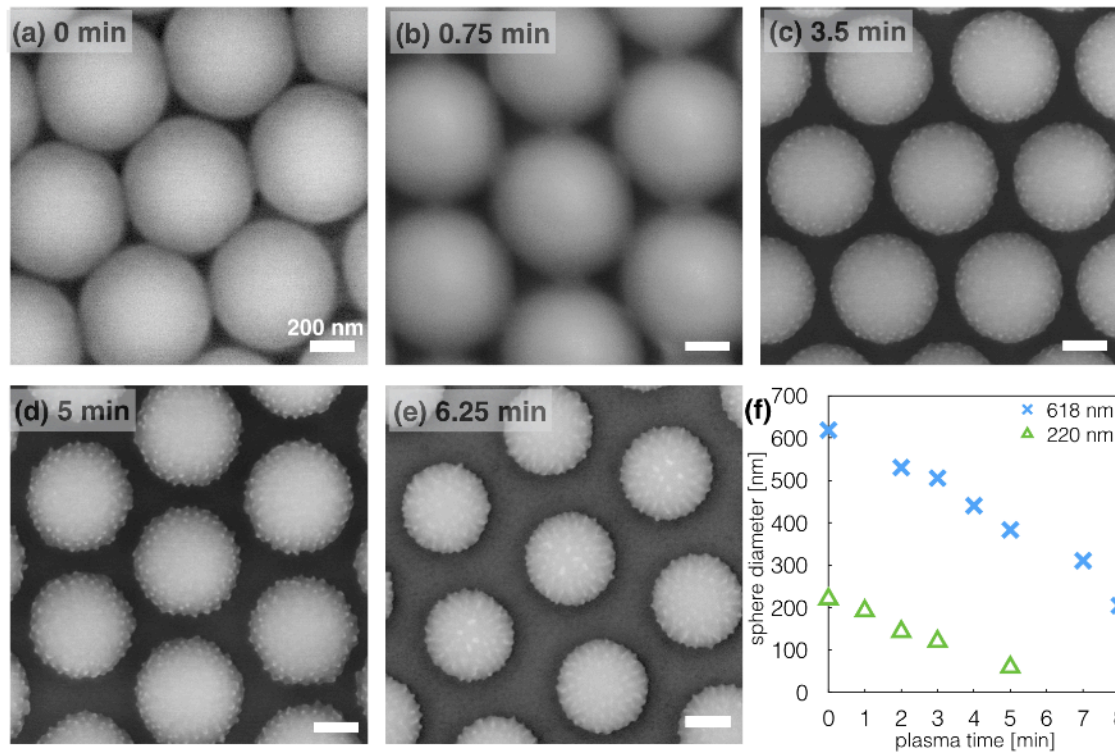
Fig. 2.10: SEM top-view images of polystyrene spheres treated with an oxygen/argon plasma for different treatment times from 0 min to 6.25 min from (a) to (e). All scale bars are 200 nm. (f) Top-view PS sphere diameters as a function of plasma treatment duration. With increasing shrinking time diameters decrease nearly linearly. Graphs show shrinking behavior of two different types of nanospheres with initial diameters of 618 nm (blue crosses) and 220 nm (green triangles).

SEM images in cross-section show the change in shape of the spheres (Figure 2.11). Spheres are etched anisotropically. The top part of the spheres does seem to maintain its round shape while the substrate-near part of the spheres seems to flatten first and diminish in height afterwards. It would have been expected that polymer would be removed from top as the plasma affects the sample mostly from above and is not expected to enter efficiently into the sphere mask openings. This anisotropic shrinking and shape change could be due to a combination of thermal effects and chemical changes induced to the polymer by the plasma. Probably, the top part of the spheres is chemically modified at the beginning of the plasma treatment resulting in a stable globe, which is not affected by the plasma afterwards.

For very long treatment times (> 7 min) the spheres are largely deformed, where the shape change reminds to a melting process on a hot substrate. The amount and thus size of the residuals of the spheres saturates and some part of the polymer remains on the surface for even very long plasma times. Chemical changes of the material during such a treatment are not completely understood. The residuals however are hardly removable from the surface with chemical solvents even in an ultrasonic bath or by additional plasma treatment.
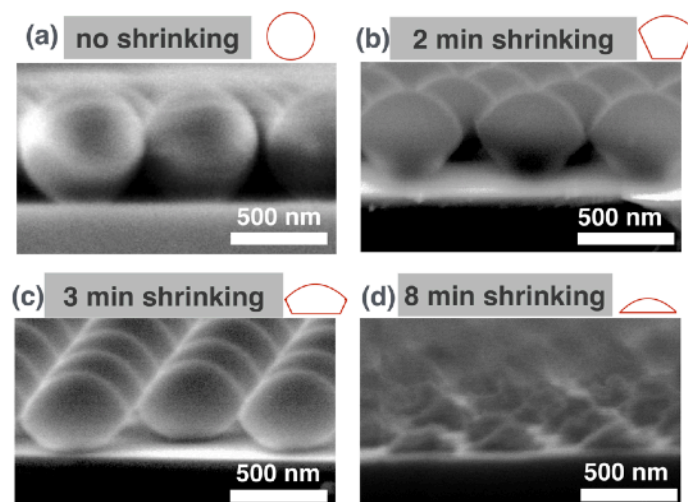
Fig. 2.11: SEM images in cross-sectional view of polystyrene spheres for different plasma treatment durations. (a) Initial PS sphere monolayer. Spheres are round shaped with a diameter of 618 nm. With increasing time in an O_2/Ar plasma (b-d) spheres shrink in diameter as visible in top-view images and change their shape, see cross-section images and sketches. Samples are cut in the center after plasma treatment.

Antidot-patterned thin films. For the creation of antidot patterns, material is deposited onto the shrunk sphere layers as the next step in nanosphere lithography. Physical vapor deposition techniques are suitable for the deposition of different materials such as platinum, gold, titanium or SiO_2 as thin film material. After subsequent sphere removal, this leads to the topographical hole-pattern formation in the thin film. By choice of different substrate and thin film materials, chemical contrasts between antidot film and antidot bottom can be created. The morphology of the antidots, i.e. their shape, thin film roughness and wall slope, is not only determined by the shape of the sphere mask, but also crucially by the material deposition technique used in NSL. Here, the differences in antidot morphology using either electron beam evaporation or sputter deposition are discussed. Specifications of the deposition setups can be found in Appendix A3.

Antidots created by sputter deposition have smaller side wall slopes thus a smaller gradient of the film thickness of deposited material. This is due to the fact that the atoms released from the sputter target hit the substrate surface at a broad angular distribution and with high energies allowing for atom diffusion on the sample surfaces. Thus the surface underneath the sphere equator can be covered with material. This allows for the preparation of antidots with diameters smaller than the top-view sphere diameters. The high energy and therefore mobility of atoms on the surface also contributes to rough material thin films on the plane areas. Figure 2.12 (a) shows AFM images in top-view (grey scale image) and tilted 3D (gold color scale) of antidots prepared by sputter deposition of 15 nm platinum. The cross-section sketch depicts typical feature sizes of such antidots. Side-wall slopes are approx. 10°, peak-to-valley film roughness can be up to 7 nm, the rms roughness is between 1-2 nm.

Electron beam evaporation of a material, in contrast, is directed normal to the substrate with small angular distribution and atoms are less likely to diffuse on the substrate surface. Thus spheres act as a shadow mask leaving antidots with the same diameter as the top-view sphere equator and a sharp contour. The side walls of the antidots are steep and the plane film is smooth. Patterns are well-defined, and the minimum antidot diameters are directly determined by the projections of shrunk spheres. This is shown in Figure 2.12 (b) for the electron beam evaporation of 15 nm Pt. Slopes are steep and plane area surface roughness shows 2 nm peak-to-valley and a rms roughness of 0.4 nm.
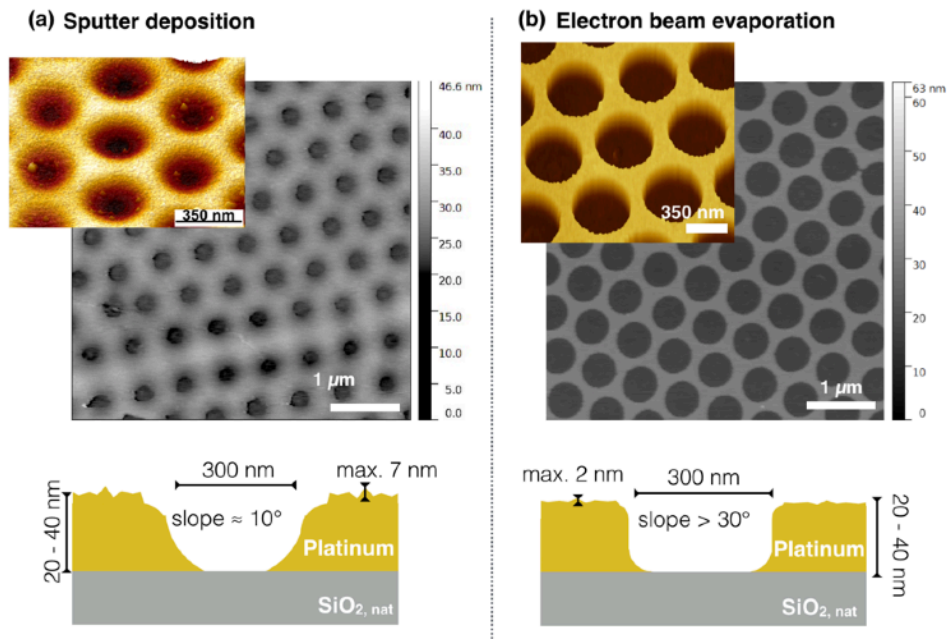
Fig. 2.12: Antidot patterns prepared by nanosphere lithography using (a) sputter deposition or (b) electron beam evaporation of platinum. AFM images in top-view (grey scale) and tilted 3D (gold color scale) and sketches in cross-sectional view show typical morphologies. Sputter deposition leads to lower slopes and smaller free substrate areas with rougher plane films, while evaporation deposition results in steep slopes, smooth films and defined antidot contours.

Applications of antidot patterns. Such antidot patterns can either be used as topographic traps or as chemical pre-patterns in directed self-assembly experiments. In Chapter 4.5 of this thesis, antidot patterns from different materials are created with both material deposition techniques, electron beam evaporation and sputter deposition, and are used for the formation of hierarchical nanopores by performing block copolymer lithography on these pre-patterned surfaces.

Experiments for the site-selective deposition of protein micelles inside the antidots were performed in a collaboration with the ‚Biobased and Bioinspired Materials' group of Dr. Oliver Strube, Dept. of Chemistry, Paderborn University. The material contrast given by an antidot thin film of platinum on a SiO$_2$ surface was exploited in order to perform an ‚enzyme-mediated autodeposition' (EMA) [43] of casein micelles into the antidots (Fig. 2.13 (a)). To this, the enzyme chymosin is covalently bonded to glymo-functionalized SiO$_2$ surface areas inside the antidots. This enzyme immobilization is not possible on the inert platinum thin film. Casein micelles are then deposited from aqueous suspension onto the patterned substrate, where it undergoes a site-selective surface-near cleavage reaction by the immobilized chymosin. This cleavage leads to a change of casein solubility in the suspension allowing for the micelle deposition only into the enzyme-containing antidot nanopatterns (Fig. 2.13 (b-d)). The dip-coating based process allows for the protein micelle deposition at high yields of > 80 % of antidots being filled with at least one protein micelle. Adjusting the antidot diameter commensurate to the protein micelle diameter was shown to result in the selective deposition of single protein micelles into the antidots (Fig. 2.13 (e+f)) [44].
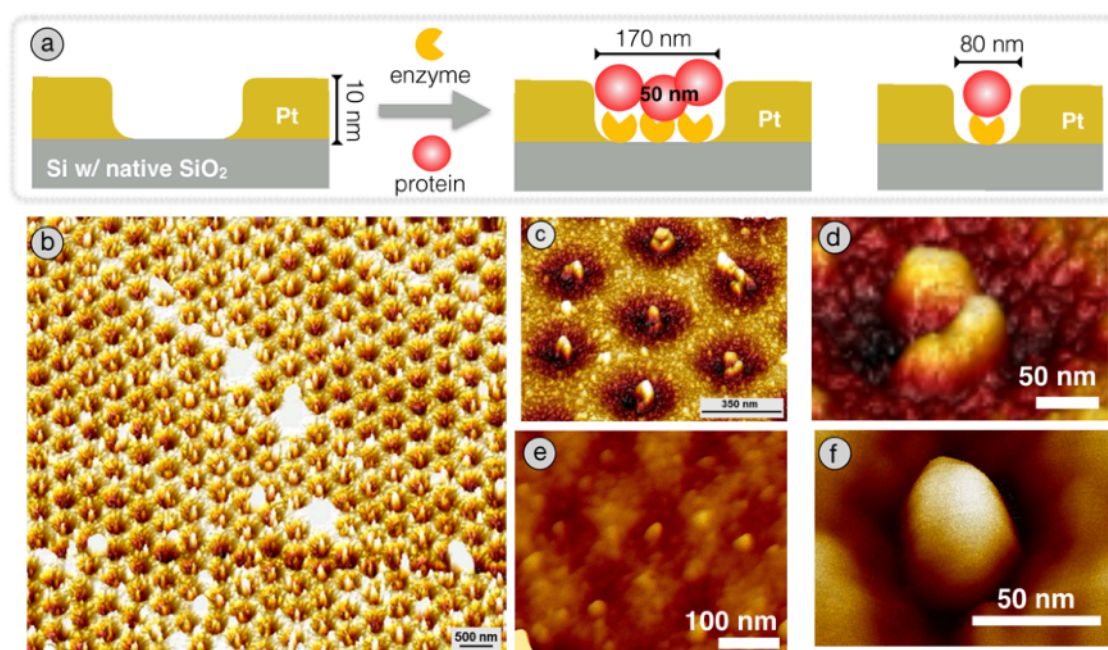
Fig. 2.13: (a) Concept of the site-selective enzyme mediated autodeposition of protein micelles into antidot-patterned Pt thin films sputter-deposited onto Si/SiO$_2$ surfaces. AFM images show the filling of > 80 % of antidots with protein micelles (b-d, height images). Adjusting the antidot diameter commensurate to the micelle diameter allows for the selective deposition of single micelles (e+f) [44].

In another collaboration with the group of Prof. Kitzerow, Dept. of Chemistry, Paderborn University, gold antidot thin films on glass substrates were used to build two-dimensional liquid crystal (LC) phase gratings (Fig. 2.14 (a)) [45]. To this end, the structured gold substrate and a plane ITO substrate form the electrodes of a liquid crystal cell. The cell is filled with a special liquid crystalline phase, the blue phase. The blue phase has unique properties such as fast response times (<1ms), optical anisotropy in the field-off state and a Kerr response in the presence of electric fields. The latter property makes modelling of the macroscopic optical properties of this liquid crystalline phase much more facile compared to standard nematic liquid crystals. Under the application of an electric voltage, the structured substrate leads to an inhomogeneous electric field across the LC cell (Fig. 2.14 (b)). The Kerr response to the field leads to a locally varying index profile which results in an optical phase grating. The diffraction efficiency changes with the applied voltage (Fig. 2.14 (d)). The diffraction pattern and the diffraction angle is determined by the antidot pattern, hence they can be controlled by changing the size of the employed spheres in the structuring process. The discussed device exhibits a large diffraction angle of 21.4° (Fig. 2.14 (c)), which corresponds to a sphere diameter or lattice parameter of 2.1 μm. The fillet size, however, is only a few 100 nm, which is not achievable with standard UV-lithography. Further, the fillet size can be easily varied by changing the shrinking ratio of the sphere, which influences the inhomogeneity across the cell.
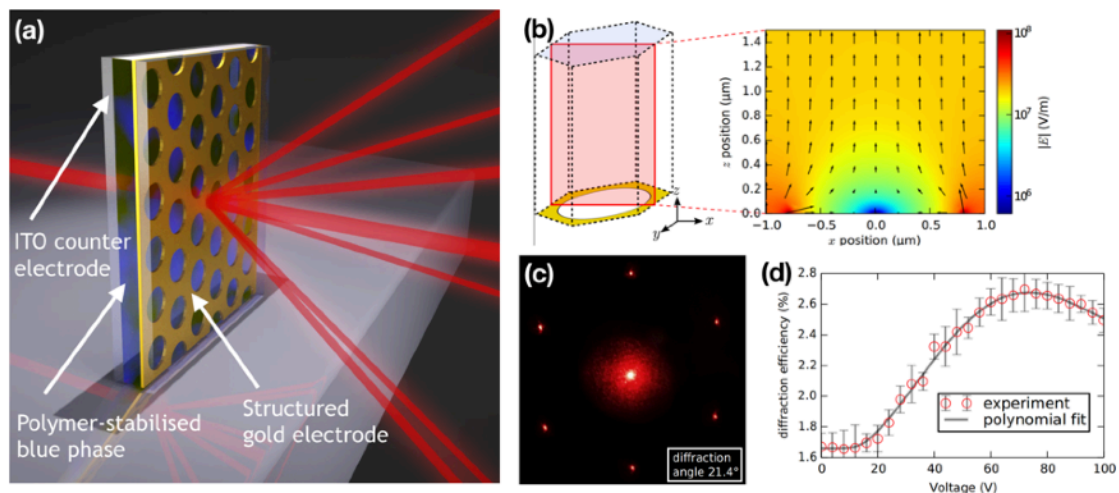
Fig. 2.14: (a) Concept of the use of an antidot-structured Au film as electrode in a LC blue phase cell. (b) Finite-element simulation of the electric field distribution across the antidot-patterned Au film. (c) Diffraction pattern of the hexagonally patterned LC cell showing a large diffraction angle of 21.4°. (d) Switchable diffraction efficiency with voltage. [45]

Section summary

Nanosphere lithography allows for the large-area patterning of surfaces with nanofeature arrays using sphere layers as shadow masks in a material deposition step.

The use of polymer spheres allows for an easy modification of the shadow mask, e.g. by thermal or plasma treatment, prior to material deposition. The shape of the mask openings and thus the shape of the resulting material nanofeatures can be tailored.

It is shown, that polymer spheres can be shrunk by reactive ion etching. This allows for the creation of antidot-patterned thin films with round shaped free substrate areas with adjustable diameter in metal, semiconductor or insulating thin films. Such antidot-patterns are used as templates for the site-selective deposition of protein micelles or as nanopatterned electrodes in liquid crystal cells for the creation of a 2D phase grating.

2.3.3 Nanosphere monolayers as mold in soft lithography

Soft lithography is a low-cost surface patterning technique, where structured elastomers act as re-usable templates. The elastomers are typically patterned by pouring them in their unbranched liquid state onto a topographic mold where they are cured. In their solid state, they can then be released maintaining the replica of the topography of their mold. These patterned elastomers are used as transfer medium of micro- and nanopatterns, for example by using them as stamps to print different inks site-selectively onto different surfaces. Produced feature sizes are typically in the range of few hundred micrometer down to nanometric motives. The use of such a patterned elastomer allows for an easy-to-use, fast and cheap way of prototyping. An overview of soft lithography and its different applications is given in [46], where microcontact printing, replica molding, microtransfer molding, micromolding in capillaries and solvent-assisted micromolding are described in detail.

Principle of soft lithography

In microcontact printing (μCP), the patterned elastomer is used as a stamp [47-49]. The typical experimental procedure of μCP is depicted in Figure 2.15. Typically, an optical or electron beam lithography resist patterned by these techniques with the desired structure is used as a topographic mold (Fig. 2.15 (a)). Typical feature sizes are depicted in the sketch on the right. Lateral dimensions range from few 100 μm down to few hundred nanometers, even though it was shown that (under ideal conditions) sub-10 nm sized features could be replicated into an elastomer [50]. The aspect ratio of the patterns plays a major role in their use as stamps, as explained below. Pattern heights therefore need to be adjusted, but typically account to few μm to few hundred μm.

The unbranched, liquid elastomer, mostly polydimethylsiloxane (PDMS), is then poured onto the mold, where it covers the whole surface. The amount of added elastomer relates to the thickness of the stamp, which determines its flexibility and mechanical robustness and can range from 0.1 to 10 mm. The elastomer is then cured and the solid elastomer can be released from the mold after complete polymerization (Fig. 2.15 (b)).

The patterned polymer can then be used as a stamp for μCP as it is flexible, easy to clean and thus re-usable. To this end, an ink is deposited onto the patterned stamp surface. The ink needs to be chosen regarding good wettability on the elastomer. Usually, a solvent is used, which allows for diffusion into the elastomer, where it builds an ink reservoir. Residual ink on top of the stamp is removed and the stamp can be pressed onto a solid surface. The ink will only be released onto the surface in areas of direct contact between substrate surface and elastomer, thus creating patterned ink areas transferring the pattern of the initial mold. An advantage of this process is, that it can be repeated several times and that roughness or planarity of the surface to which the pattern is transferred does not play a major role.
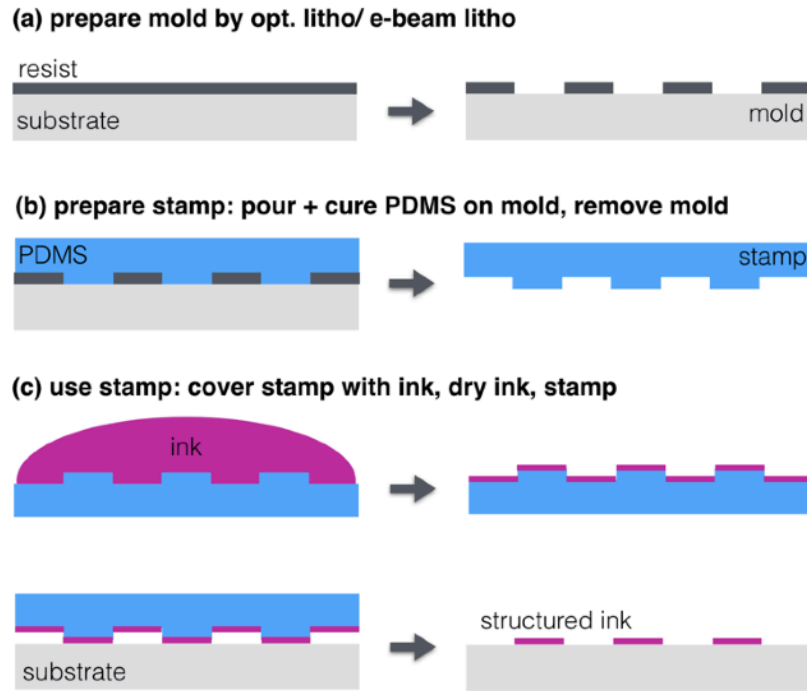
Fig. 2.15: Sketch of experimental procedure in µCP. (a) Molds are typically prepared by spin casting and patterning of a resist as common sense in optical or electron beam lithography. This patterned resists then acts as a topographic mold. (b) Unbranched PDMS is poured onto the mold and cured. After peeling the stamp off, a topographic pattern remains. (c) This patterned PDMS can be used as a stamp for site-selective application of a ink onto a substrate.

Polydimethylsiloxane (PDMS)

Polydimethylsiloxane (PDMS) is often chosen as elastomer for µ-contact printing as it is a nontoxic, biodegradable, flexible elastomer which is stable to many solvents. Because of its convenient properties, the optically transparent PDMS is used as LED lighting encapsulations, in sensors, as adhesive or encapsulation for solar cells or in life science applications as additive to body lotions, shampoos, etc. In (academic) research it is most commonly used for the preparation of microfluidic devices.

In this work, „Dow Corning Sylgard 184" [51] is used, which is commercially available and very common in literature. This two-component kit contains the unbranched colorless silicon oil and a curing agent. The base is dimethylsiloxane (dimethylvinylized and trimethylized silicondioxid) and as curing agent dimethyl-methylhydrogen siloxane copolymer containing Si-H bonds is added. The crosslinking is catalysed by a Pt compound. Usually hexachloro-platinate is used. Branching of the PDMS then follows a hydrosilylation [52].

The viscous components are mixed in a ratio of 1:10 crosslinker:silicon oil (viscosities 100:5100 cP) [51]. An increase of the crosslinker fraction leads to a faster polymerization and a stiffer polymer after complete curing, whereas a lower crosslinker concentration results in a soft PDMS stamp. Polymerization at the recommended ratio of 1:10 results in a Durometer Shore 43 stiffness [51].
The polymerization starts immediately after mixing of the components. At room temperature, the reaction velocity is very low and the PDMS mixture can be used for several hours (1.5 h according to the data sheet [51], up to 4 h from experience). The mixture needs to be degased in a vacuum before being poured onto a topographic mold to remove air and ensure a homogeneous wetting of the mold at a defined height (typically 0.2 - 10 mm). The mold with the still viscous PDMS on it should be degased in vacuum again to increase the

achievable pattern quality/ resolution. The resolution limit achieved in literature so far is down to 6 nm [50]. The curing time at room temperature (25°C) is 48 h, at 100 °C 35 min, at 125 °C 20 min and at 150°C 10 min [51]. Best results are achieved by curing the polymer in a vacuum furnace at a pressure of 20 mbar and a temperature of 90 °C for 1 h. After complete curing, the stiff PDMS can be peeled off from the mold and the structured part can be cut out with a scalpel.

Experimental procedure

The preparation of the micro- or nanostructured mold is typically a bottleneck in soft lithography. Usually, resists on silicon structured by electron beam lithography or optical lithography are used. Here however, it is shown that the use a self-assembled polymer sphere monolayer as a topographic mold is a cheap and easily available alternative. Large stamps with nanoscale features on squarecentimeters of patterned area can be created. A sketch of the experimental procedure is depicted in Figure 2.16.
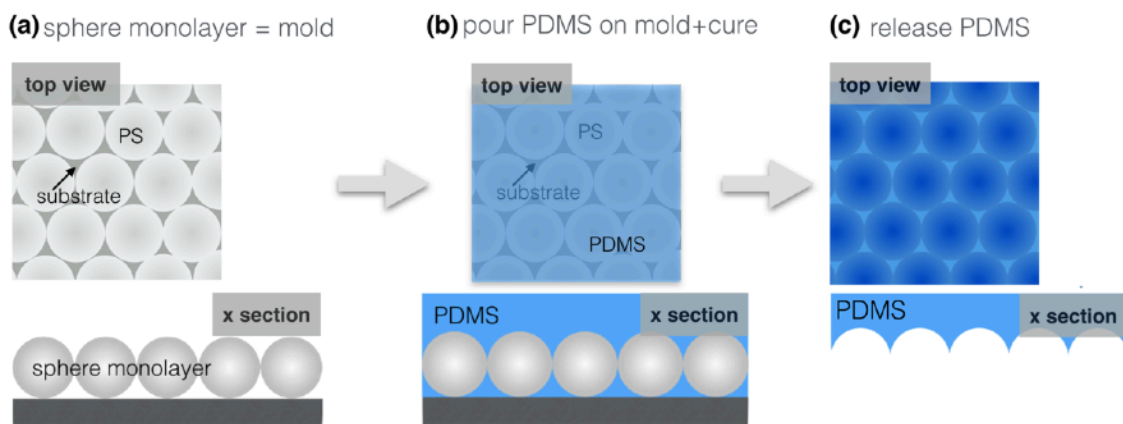
Fig. 2.16: Sketch of the PDMS stamp preparation by nanosphere lithography. (a) Polystyrene nanosphere monolayer acts as template. (b) PDMS is poured onto the template and cured. (c) PDMS is released from the template and shows the replicated hexagonal sphere arrangement.

In the first step (Fig. 2.16 (a)) the topographic mold is prepared: Monolayers of polystyrene spheres (2 wt.% solids, CV < 3 %, Microparticles Inc.) with a diameter of 618 nm are deposited from an aqueous suspension onto an oxygen-plasma cleaned Si(100)/ $SiO_{2,nat}$ surface by convective self-assembly with the doctor blade technique as stated above (Chap. 2.2).

The PDMS is prepared as follows: Dow Corning Sylgard 184 is mixed with the cross linker at a ratio of 9.5:1. The mixture is degased for approx. 15 min in a desiccator at $2x10^{-2}$ mbar until the polymer is bubble-free and then poured onto the sphere monolayer. The sample with PDMS is degased again for 5 min and cured in a furnace at 90 °C for

1 h at ambient atmosphere (Fig. 2.16 (b)). The solid PDMS stamp is released from the sphere layer by peeling the elastomer off (Fig. 2.16 (c)).

Results and discussion

The photograph in Figure 2.17 shows the result of the PDMS stamp patterning with a nanosphere monolayer used as mold. The patterned PDMS stamp (Fig. 2.17 (a)) shows selective reflections after being cured and peeled off from the mold. This selective reflection, which is visible with the naked eye, indicates the successful replication of the spheres' periodically curved surface structure into PDMS. Figure 2.17 (b) shows the mold, i.e. the silicon surface with the nanosphere monolayer, from which the PDMS in (a) was just removed. Again, the

selective Bragg reflections of the sphere layer is visible. This shows, that the spheres remained on the Si surface and were not removed by the PDMS proving the successful stamp release and patterning. Defects in the sphere monolayer, such as the drying edge in the lower center of the image or stripes of sphere multilayers, can be found both in the initial sphere template as well as in the replicated pattern in the PDMS.
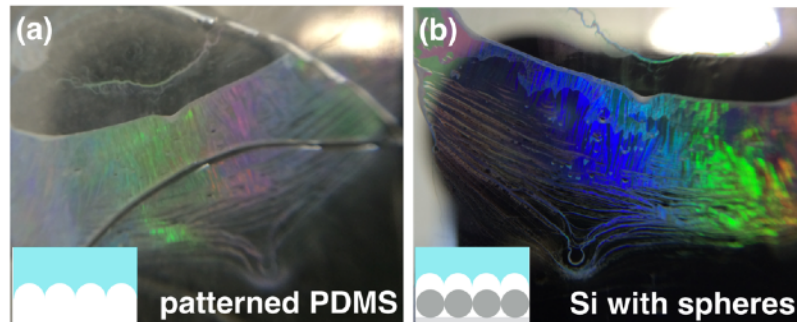
Fig. 2.17: Photographs of (a) patterned PDMS stamp after release from Si wafer with polymer sphere monolayer in (b). Both images show selective reflections of the periodic sphere monolayer structure. This proves the successful pattern transfer into the PDMS and also ensures that the spheres remain on the Si surface. Image area is approx. 1 cm^2.

SEM and AFM investigations of the PDMS stamp shown in Figure 2.18 allow for a more detailed characterization of the replicated patterns. The top-view SEM image in Figures 1.4 (a) show the hexagonally arranged bowls replicated from the sphere layers. In between the bowls, elevated PDMS walls can be identified. At interconnects of the walls, in between 3 neighboring bowls PDMS tips with triangular basis can be seen giving a slightly different contrast. The periodicity, i.e. the mean distance from bowl center to bowl center, is with 620 nm commensurate with the diameter of the spheres of the template, which was 618 nm. Cross-section SEM in Figure 2.18 (b) gives a better proof of the topographic patterning. The size and height of the hexagonally arranged elevated tips can be determined by AFM imaging of the structured PDMS surface (Fig. 2.18 (d)). The height of these separated tips is measured to 240 nm. The tips arrangement in the AFM image in Fig. 2.18 (d) appears slightly asymmetric. This is a measurement artifact: the PDMS is quite soft, therefore in AFM cantilever gets pinned on the highest sample points and the resolution in scanning direction (left to right) suffers.

This tip height is found to be tunable by changing the viscosity of the PDMS prior to pouring onto the sphere monolayer [53]. This can be achieved by increasing time between mixing of the unbranched PDMS with the curing agent and pouring the mixture onto the mold, as during this waiting time the PDMS starts to cure, decreasing its viscosity. The PDMS viscosities plotted in Figure 2.18 (c) are obtained by curing at room temperature for 22 - 69 min after mixing. Viscosities are measured by cone-plate viscometry [54].

The maximum tip height of 230 nm is prepared with PDMS of a viscosity of 2.8 Pa s. The tip height decreases for higher viscosities. This is most likely due to the fact that the PDMS is too stiff to penetrate into the openings in between the spheres. For very low viscosities < 2.8 Pa s, tip height decreases again. This is most likely due to the fact that PDMS enters further into the openings and has contact to the substrate. During stamp release, the tips get ripped off the surfaces and thus have a smaller height than expected. For very low viscosities (2.5 Pa s) spheres can be embedded into the PDMS as shown in Figure 2.19 (a, b): the stamp can not be released from the templates surfaces without removing the spheres too. Cross-section SEM images (Fig. 2.19 (b)) show that the spheres are completely covered by the PDMS. Only the contact areas of the spheres with the former silicon substrate surface are free of PDMS and stick out of the stamp (also visible as bright dots in top-view SEM Fig. 2.19 (a)). This sphere embedding obviously prevents the formation of a PDMS stamp with elevated, separated tips.
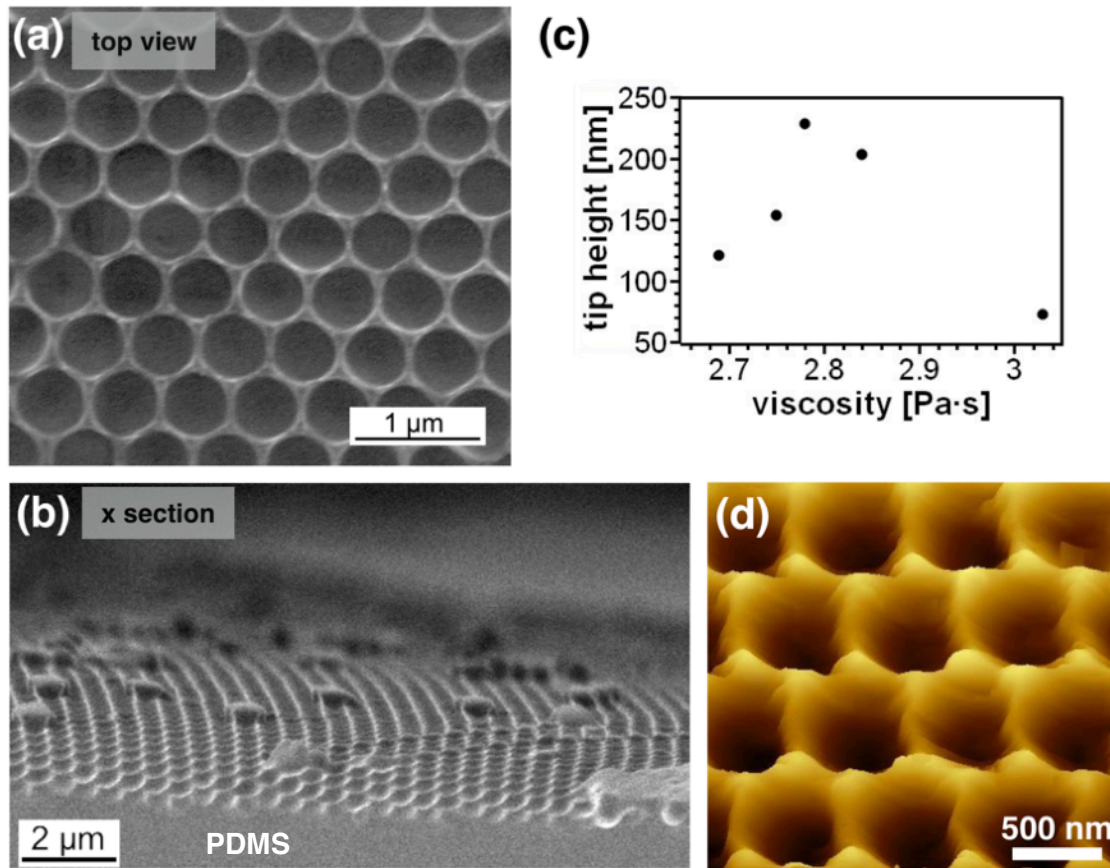
Fig. 2.18: SEM image of a structured PDMS stamp showing the sphere replica after curing on a sphere monolayer (diameter 618 nm) and peeling off the template, (a) in top-view and (b) in cross-sectional view. (c) Height of hexagonally arranged PDMS tips depends on the viscosity of PDMS before pouring over template. The ratio between PDMS and cross-linker is here 10:1. (d) Topography of structured PDMS measured by AFM (tilted 3D image).

However, from geometrical considerations the maximum tip height without sphere embedding into the PDMS should be the sphere radius. If this is the case, then the PDMS covers the sphere monolayer up to the sphere equator. Thus, the maximum tip height should be tunable by using monolayers of spheres with different diameters as a mold.

Along with the creation of a maximum tip height, it is important to consider the stamp aspect ratios. For extreme aspect ratios, stamp failure mechanisms can occur (Fig. 2.20). Stamp features with a very high aspect ratio can suffer lateral collapse; very low aspect ratios can lead to a sagging.

This means for the shown viscosity-tip height dependence that stamp failure can be overcome by choosing appropriate PDMS viscosities and thus stamp feature geometries. Typically the stamps with maximum tip height patterned with 618 nm sphere monolayers as mold have height-to-length aspect ratios H/L of about 1 and height-to-distance H/D > 0.4 and are therefore within the range of stable feature geometries, thus stamp failure due to sagging or lateral collapse is unlikely.
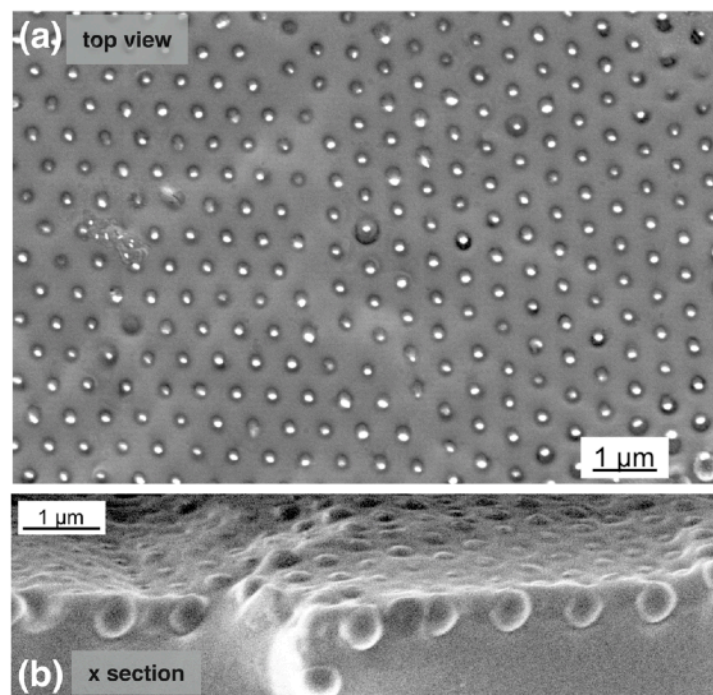
Fig. 2.19: SEM images of PDMS stamps with embedded polymer spheres. After stamp release from the template, spheres are removed from the template surface and remain in the PDMS if PDMS viscosity prior to curing was with 2.5 Pas too low.
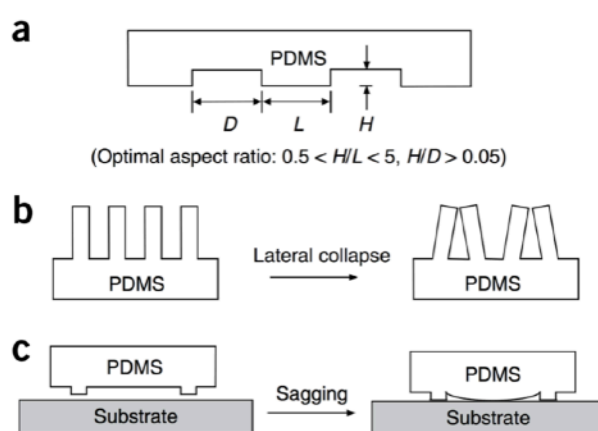
Fig. 2.20: Sketch of (a) optimum stamp feature aspect rations and stamp failure mechanisms: (b) lateral collapse and (c) sagging. [after 47]

If such patterned PDMS surfaces are discussed to be used as stamps in µ-CP, their wetting properties must be known in order to chose appropriate inks. Here, surface properties of the structured PDMS surface were investigated by contact angle measurements (Fig. 2.21). Contact angles with water, diiodomethane and ethanol were measured as described in Appendix A1 and surface energies are calculated following the OWRK-method. For comparison, a flat PDMS surface is analysed similarly.

Both PDMS surfaces, structured and flat, are water repelling showing water contact angles of 117° and 105°, respectively. For unpolar solvents, here diiodomethane, however, the structure induces a dewetting: contact angles of diiodomethane on the planar surface is with 72° significantly lower than 112° on the patterned PDMS. Thus, the total surface energy of the patterned PDMS is decreased to 7 mN/m, which makes the surface repellant to most liquids. For μ-CP applications, inks on basis of solvents with very low surface energy should be used. An example is ethanol, which shows reasonable wetting with contact angles of 40° and 46° on planar and patterned PDMS, respectively.

An alternative way to improve the wetting probabilities with other solvents is an air plasma treatment of the stamp surface. The treatment was performed in a „Harrick Plasma Cleaner" at 10.5 W RF power and 0.1 mbar. This results in a hydroxy-termination of PDMS dangling bonds at the surface [55], increasing the total surface energy from 7 mN/m to 64 mN/m. The drop of contact angles with water to 21°, as well as with diiodomethane to 35°, directly after plasma treatment is significant. This state however is only stable for few minutes as the hydroxy-terminated polymer chains diffuse back into the bulk of the PDMS material [55]. Thus, the stamps surface returns to being hydrophobic.
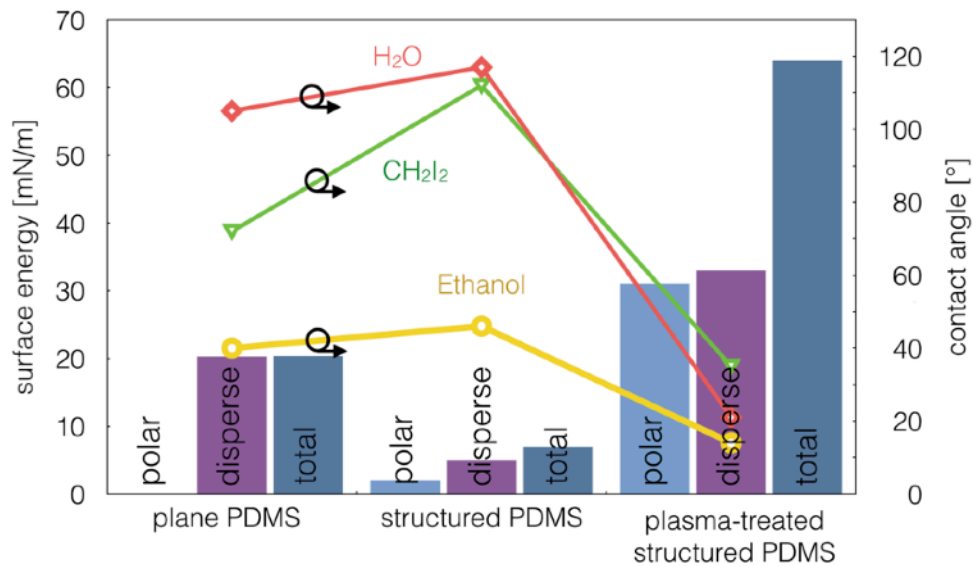
Fig. 2.21: Contact angle measurements and calculation of surface energies with the OWRK method on planar PDMS, structured PDMS and structured PDMS after an O_2/Ar plasma treatment. Data point correspond to contact angles (right y-axis) with water (red), diiodomethane (green) and ethanol (yellow). Surface energies (left y-axis) are calculated by the OWRK method and plotted in the bar chart: polar (light blue) and disperse (purple) fractions of the surface energies sum up to the total surface energy (dark blue).

Section summary

Soft lithography allows for an efficient transfer of micro- or nanoscale patterns onto different surfaces using a patterned elastomer as transfer agent. In μ-contact printing, the patterned elastomer is used as a stamp for the site-selective deposition of an ink, which can contain nanoparticles or (macro-) molecules.
Here, the elastomer polydimethylsiloxane (PDMS) was patterned with hexagonally arranged nanotips by using a nanosphere monolayer as a mold. It was shown that the height of these tips can be tailored by adjusting the viscosity of the unbranched PDMS. The surface patterns determine the wetting characteristics of the PDMS surface, which can be further tuned by plasma treatment.

2.4 Conclusions

In this Chapter, the principle of convective self-assembly for the creation of polymer sphere monolayers from aqueous suspensions onto solid substrates was introduced. Liquid fluxes and evaporation of the liquid lead to a colloid transport from a bulk suspension droplet deposited onto the substrate towards the contact line of this droplet, named the triple phase boundary. Here, colloid concentration is increased and evolving capillary forces draw particles into close packed arrangements. By moving this triple phase boundary over the sample surface, the doctor blade techniques allows for the deposition of such monolayer on areas as large as several cm^2. The quality of the monolayers regarding defect densities (voids, grain boundaries, …) is determined by experimental parameters such as the blade velocity or the control of the evaporation flux, as well as by characteristics of the colloidal suspension. The ζ-potential of colloids in the suspension medium was shown to be a good indicator for their ability to form close packed assemblies and that an exchange of the liquid medium with an ultrafiltration technique allows for the ζ-potential adjustment. The doctor blade technique introduced in this Chapter is exploited for the directed self-assembly of colloids on topographically pre-patterned surfaces, i.e. for the deposition of polymer spheres into trench structures in Chapter 3.2 and for the placement of Au nanoparticles into block copolymer-created nanopores in Chapter 4.4.

By means of nanosphere lithography (NSL), which is a well-established technique for large-area surface patterning, sphere layers created by convective self-assembly act as shadow masks during a material deposition step. In the simple case, when using the sphere monolayer directly as mask, hexagonally arranged triangular nanoparticles of the deposited material are created on the surfaces after sphere mask removal. By modification of the polymer spheres prior to a material deposition, the shape of the resulting nanoparticles can be tailored. Polymer spheres were shrunk in a reactive ion etching process to diameters which can be chosen by adjusting the duration of the plasma treatment. Deposition of material on these modified masks results in the formation of materials thin films with hexagonal antidot patterns. Different material deposition techniques, i.e. sputter deposition or electron beam evaporation, lead to characteristic antidot pattern morphologies.

The antidot pattern exhibits a topography on the surface as well as a chemical pattern due to the material contrast between thin film and free substrate inside the antidots. By choosing substrate materials for sphere deposition and deposited material during NSL a large variety of material combinations can be prepared allowing for a large flexibility for possible applications. Three exemplary applications of antidot-patterned thin films were shown in this chapter: (a) Inert platinum thin films with free silicon oxide dots were used for the site-selective deposition of protein micelles by means of enzyme-mediated autodeposition (b) Antidot-patterned gold thin films on glass were used as electrodes for the creation of switchable 2-dimensional liquid crystal phase gratings. (c) In Chapter 4.5 of this work, antidots of free SiO_2 or $TiOx$ in gold, platinum, $TiOx$ and SiO_2 thin films are used as templates in the directed self-organization of block copolymers for the creation of hierarchical nanopores. These examples show, that self-assembly allows for the advanced hybrid-material surface design with tailored nanofeatures.

The sphere monolayers can also be used as topographic templates for the patterning of elastomers. Such patterned elastomer can be used as a stamp for easy pattern transfer. This is known as micro contact printing in soft lithography. An advantage of this technique is the large flexibility in motives on different size scales and the high throughput in the preparation of re-usable stamps. However the preparation of the molds is typically the bottleneck in soft lithography. Especially if nanosized features are desired electron beam lithography is often the technique of choice, even though it is a comparably slow and expensive method, which is not suitable for large-area patterning. The use of self-arranged nanosphere layers as a mold offers a fast and easy alternative if regular stamp patterns on large areas are needed.

The elastomer used as stamp material is PDMS. It is poured onto sphere monolayers where it is cured by thermal treatment. It was shown, that by choice of suitable parameters, hexagonally arranged nanosized tips are found on the stamp after stamp release from the sphere mask. Such a stamp could be used e.g. for the formation of ordered nanoscale self-assembled monolayer (SAM) islands on large areas of planar or even curved surfaces, which is not possible by most other top-down or bottom-up patterning techniques.

2.5 Bibliography

[1] G. Schmid (ed.), Nanoparticles, Weinheim: Wiley VCH (2010)

[2] M. L. Landry, T. E. Morrell, T. K. Karagounis, C.-H. Hsia, C.-Y. Wang, J. Chem. Educ. 91, 274 (2014)

[3] D. N. Dirin, R. B. Vasiliev, M. S. Sokolikova, A. M. Gaskov, Inorganic Materials 47(1), 23 (2011)

[4] L. Protesescu, S. Yakunin, M. I. Bodnarchuk, F. Krieg, R. Caputo, C. H. Hendon, R. X. Yang, A. Walsh, M. V. Kovalenko, Nano Lett. 15, 3692 (2015)

[5] C. G. Palivan, R. Goers, A. Najer, X. Zhang, A. Car, W. Meier, Chem. Soc. Rev. 45, 377 (2016)

[6] J.-Z. Ma, Y.-H. Liu, Y. Bao, J.-L- Liu, J. Zhang, Adv. Colloid and Interf. Sci. 197, 118 (2013)

[7] T. Taniguchi, T. Inada, T. Kashiwakura, F. Murakami, M. Kohri, T. Nakahira, Colloids and Surfaces A 377, 63 (2011)

[8] A. Ezhova, K. Huber, Macromolecules 49, 7460 (2016)

[9] F. Tao, Metal Nanoparticles for Catalysis: Advances and Applications, RCS Catalysis Series No. 17, Cambridge: The Royal Society of Chemistry (2014)

[10] J. Turkevich, P. C. Stevenson, J. Hillier. J. Phys. Chem. 57(7), 670 (1953)

[11] W. D. Harkins, J. Am. Chem. Soc. 69, 1428 (1947)

[12] G. Odian, Principles of Polymerization, New York: Wiley (2004)

[13] https://commons.wikimedia.org/wiki/File:Emulsion_Polymerization_Cartoon_3.svg (01.08.2017)

[14] H.-J. Butt, K. Graf, M. Kappl, Physics and Chemistry of Interfaces, Weinheim: Wiley-VCH (2003)

[15] B. Derjaguin, L. Landau, Acta Physicochimica URSS 14, 633 (1941)

[16] E. W. Verwey, J. T. G. Overbeek, Theory of the stability of lyophobic colloids, Amsterdam: Elsevier (1948)

[17] N. Vogel, C. K. Weiss, K. Landfester, Soft Matter 8, 4044 (2012)

[18] Malvern ZetaSizer Nano User Manual, MAN0485, Issue 1.0 (2012)

[19] M. Larsson, A. Hill, J. Duffy, Ann. Transact. Nord. Rheol. Soc. 20, 209 (2012)

[20] M. Kaszuba, J. Corbett, F. M. Watson, A. Jones, Phil. Trans. R. Soc. A. 368, 4439 (2010)

[21] A. Dimitrov, K. Nagayama, Langmuir 12, 1303 (1996)

[22] B. G. Prevo, O. D. Velev, Langmuir 20, 2099 (2004)

[23] Q. Li, U. Jonas, X. S. Zhao, M. Kapp, Asia-Pacific J. of Chem. Engin. 3, 255 (2008)

[24] O. Driesner, B. Sc. Thesis, Analyse und Weiterentwicklung einer Rakeltechnik zur selbstorganisierten Herstellung großflächiger Nanomasken, Paderborn University (2012)

[25] P. Born, S. Blum, A. Munoz, T. Kraus, Langmuir 27, 8621 (2011)

[26] M. Yoldi, C. Arcos, B.-R. Paulke, R. Sirera, W. Gonzalez-Vinas, E. Görnitz, Mater. Sci. Engineering C 28, 1038 (2008)

[27] X. Ye, L. Qi, Nano today 6, 608 (2011)

[28] D. Drude, B. Sc. Thesis, Quantitative Bestimmung von Defektdichten in kolloidalen Masken, Paderborn University (2015)

[29] V. Canalejas-Tejero, M. Ibisate, D. Golmayo, A. Blanco, C. Lopez, Langmuir 28(1), 161 (2012)

[30] H. W. Deckmann, J. H. Dunsmuir, Appl. Phys. Lett. 41, 377 (1982)

[31] P. Colson, C. Henrist, R. Cloots, J. Nanomaterials, DOI: 10.1155/2013/948510 (2013)

[32] C. L. Haynes, R. P. VanDuyne, J. Phys. Chem. B 105, 5599 (2001)

[33] S.-M. Yang, S. G. Jang, D.-G. Choi, S. Kim, H. K. Yu, small 2(4), 458 (2006)

[34] C. Geng, L. Zheng, J. Yu, Q. Yan, T. Wei, X. Wang, D. Shen, J. Mater. Chem. 22, 22678 (2012)

[35] D. Gogel, M. Weinl, J. K. N. Lindner, B. Stritzker, J. Optoelectr. and Adv. Mater. 12(3), 740 (2010)

[36] M. Manso-Silvan, M. A. Hernandez, V. T. Costa, R. J. M. Palma, J. M. M. Duart, Europhys. Lett. 76, 690 (2006)

[37] A. Kosiorek, W. Kandulski, P. Chudzinski, K. Kempa, M. Giersig, Nano Lett. 4(7), 1359 (2004)

[38] C. Brodehl, S. Greulich-Weber, J. K. N. Lindner, MRS Proc. 1748, mrsf14-1748-ii11-25 (2015)

[39] J. K. N. Lindner, B. Gehl, B. Stritzker, Nucl. Instrum. Methods B 242, 167 (2006)

[40] J. K. N. Lindner, D. Kraus, B. Stritzker, Nucl. Instrum. Methods B 257, 455 (2007)

[41] J. K. N. Lindner, C. Seider, F. J. C. Fischer, M. Weinl, B. Stritzker, Nucl. Instrum. Methods B 267, 1397 (2009)

[42] U. Hilleringmann, Silizium-Halbleitertechnologie, Wiesbaden: Springer View EG (2014)

[43] A. A. Rüdiger, W. Bremser, O. I. Strube, Macromol. Mater. Eng. 301, 1181 (2016)

[44] A. A. Rüdiger, K. Brassat, J. K. N. Lindner, W. Bremser, O. I. Strube, submitted (2017)

[45] M. Wahle, K. Brassat, J. Ebel, J. Bürger, J. K. N. Lindner, H.-S. Kitzerow, Optics Express 25(19), 22608 (2017)

[46] Y. Xia, G. M. Whitesides, Annu. Rev. Mater. Sci. 28, 153 (1998)

[47] D. Qin, Y. Xia, G. M. Whitesides, nature protocols 5(3), 491 (2010)

[48] D. B. Weibel, W. R. DiLuzio, G. M. Whitesides, Nature Reviews Microbiology 5, 209 (2007)

[49] P. Kim, L. D. Zarzar, X. He, A. Grinthal, J. Aizenberg, Curr. Opin. Solid State Mater. Sci. (2011)

[50] S. Y. Chou, P. R. Krauss, W. Zhang, L. Guo, L. Zhuang, J. Vac. Sci. Technol. B 15(6), 2897 (1997)

[51] Dow Corning Product Information: http://www.dowcorning.com/DataFiles/090276fe80190b08.pdf (21.08.2017)

[52] B. Marciniec (ed.), Advances in Silicon Science, Springer Science (2009)

[53] J. Bürger, B.Sc. Thesis, Abformung komplexer Oberflächen mit PDMS, Paderborn University (2016)

[54] R. McKennell, Analytical Chemistry 28(11), 1710 (1956)

[55] D. Bodas, C. Khan-Malek, Sensors and Actuators B 123, 368 (2007)

3 Nanogap electrodes by directed self-assembly and nanosphere lithography

The precise positioning of single nanoobjects is of crucial importance for many applications. In the field of optics for example, regular assemblies of nanoparticles exhibit new functionalities in ensembles due to plasmonic interactions [1, 2]; in electronics, device miniaturisation depends on perfect nanoobject positioning [3]; paving the way towards bioelectronics, the exact positioning of bio units such as single molecules is necessary for the investigation of their characteristics [4, 5].

An established technique for the trapping of objects is dielectrophoresis (DEP) in inhomogeneous electric fields [6]. It is well-known in the field of biological research on lab-on-a-chip devices, as it allows for the non-destructive particle separation, positioning and analysis. The electrodes used on these devices match the typical sizes of biological cells, thus are round about a few hundred micrometer in size. Decreasing the electrodes dimension to the few ten nanometer scale would allow for the use of DEP for the positioning of nanoobjects, such as quantum dots or single biological units.

In this chapter, an approach for the formation of electrodes with nanosized gaps for the creation of inhomogeneous electric fields required in DEP is investigated.

The self-assembly properties of colloidal polymer spheres explained in the previous chapter are exploited in this chapter for the preparation of self-assembled nanogap electrodes (NGEs). Silicon surfaces are pre-patterned topographically by optical lithography and chemically by surface modification with self-assembled monolayers (SAMs) (of molecules) (Fig. 3.1 (a)) and then used for the directed self-assembly of the colloids [7]. The preparation of the SAMs is described in detail in Chapter 3.2. It is shown that the surface patterning and functionalization allow for the site-selective deposition of spheres inside the trenches (Chapt. 3.3). The sphere rows are used as shadow masks in nanosphere lithography (Chapt. 3.4). By this, linear rows of nanogap electrodes inside the trenches are created (Fig. 3.1 (b)) [8]. The gap width between the electrodes can be tuned by oblique metal deposition during nanosphere lithography. Ray trace like simulations allow for the prediction of gap widths. Finite element simulations of the electric field distributions between such NGEs with different geometries are presented. An extended outlook in Chapter 3.5 discusses preliminary results on the NGEs use for particle trapping in dielectrophoretic experiments (Fig. 3.1 (c)).
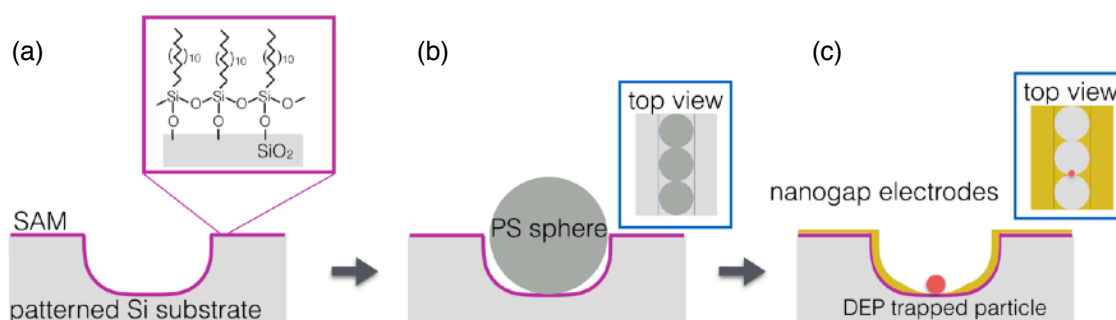
Fig. 3.1: Overview of nanogap electrode preparation by directed self-assembly. Chemical and topographical pre-patterning of the surface (a) allows for the directed assembly (b) of rows of polymer spheres selectively inside a trench. (c) By nanosphere lithography nanogap electrodes with tunable gap width are created, which can be used for particle trapping in dielectrophoretic experiments.

3.1 Directed self-assembly

The convective self-assembly of colloids for the creation of monolayers of spheres was shown in the previous chapter. Large-area 2D colloid assemblies were deposited and used in nanosphere lithography (NSL) for the creation of 2D arrays of nanoobjects and antidot patterns. This approach can be transferred to pre-modified surfaces e.g. for the formation of different motives such as linear arrangements. To this end, surfaces can be pre-patterned chemically and/ or topographically. Such surface modifications can then favor or suppress colloid assembly site-selectively. This allows for the assembly of colloidal particles into of a large variety of motives, which can be used as shadow masks in NSL for the creation of material nanoobjects with tailored shapes.

The principle of interfering into the assembly process by pre-treatments of the substrate is referred to as directed or template-assisted self-assembly (DSA or TASA) [9-11]. Directed self-assembly is the more general term, comprising all kinds of manipulation of the assembly process, such as by electric or magnetic fields, host-guest interactions, capillary forces and convective flows [12-15]. Template-assisted self-assembly however directly refers to techniques by which topographic or chemical surface pre-patterns are used to induce forces, which drag colloidal particles into desired arrangements [16].

The topographical surface modification is further discussed in the following: (i) in Chapter 3.2, polymer spheres will be deposited in topographic trenches on silicon surfaces for the preparation of nanogap electrodes and (ii) in Chapter 4.4, nanopores created by block copolymer lithography will be used as topographic traps for gold nanoparticles.

The arrangement of colloids into topographic traps is based on capillary assembly and convective flows. The convective self-assembly mechanism was introduced in the previous chapter for the creation of colloid monolayers on planear surfaces. High particle concentrations at a triple phase boundary with liquid film thicknesses commensurate to the particle diameter led to capillary forces drawing the particles into close-packed arrays. If the surface is topographically patterned, additional forces act on the colloids: the long-range convective flow then leads to the increased particle concentration at the assembly sites, where additional short-range capillary forces drag the particles into the pre-patterns. Wolf et al. [17] differentiate between the capillary assembly mechanism and convective assembly into topographic patterns (Tab. 3.1 and Fig. 3.2).

Tab. 3.1: Difference between capillary assembly and convective assembly.

	Convective assembly	Capillary assembly
Contact angle regime	< 20°	> 65°
On plane surface	assembly (Chap. 2.2)	no assembly
On patterned surface	2D assembly	1D assembly
Mechanism	vertical confinement of particles on surface by flat mensicus	capillary forces draw particles into pattern when meniscus is disturbed by structure

The convective self-assembly mechanism, described before on planar surfaces (Fig. 3.2 (a)), occurs if the surface is well wettable with contact angles < 20° by the colloidal suspension on the surface. For well wettable patterned surfaces with shallow structures (with lateral dimensions much larger than the colloid diameter), a triple phase boundary forms too. Again, the colloid concentrations increase locally at this triple phase boundary and particles are deposited into the patterns, analogous to the particle deposition on the planar surface (Fig. 3.2 (b)). 2D assemblies are created by this mechanism forming colloid arrays with distinct shape, order and periodicity inside pre-patterns.

Capillary assembly, in contrast, occurs on poorly wettable surfaces which exhibit contact angles with water of 65° or higher. Here, the meniscus' shape is very different compared to wettable surfaces. Due to the large contact angle, no flat meniscus is formed and consequently on plane surfaces colloid deposition is completely suppressed (Fig. 3.2 (c)). On pre-patterned surfaces however, the meniscus shape is distorted by the topography of the surface, which can lead to a site-selective colloid deposition. The forces acting on the colloid at the disturbed meniscus are depicted in Figure 3.2 (d). The confinement of particle movement, necessary for particle deposition, can be created by the pre-pattern: the capillary force F_{cap} (as well as an adhesive force F_{adh}), overcome the electrostatic force F_{e-stat}, leading to an effective force drawing the particle into the topographical pre-pattern. This mechanism allows for the colloid deposition into complex patterns [12] and 1D structures.
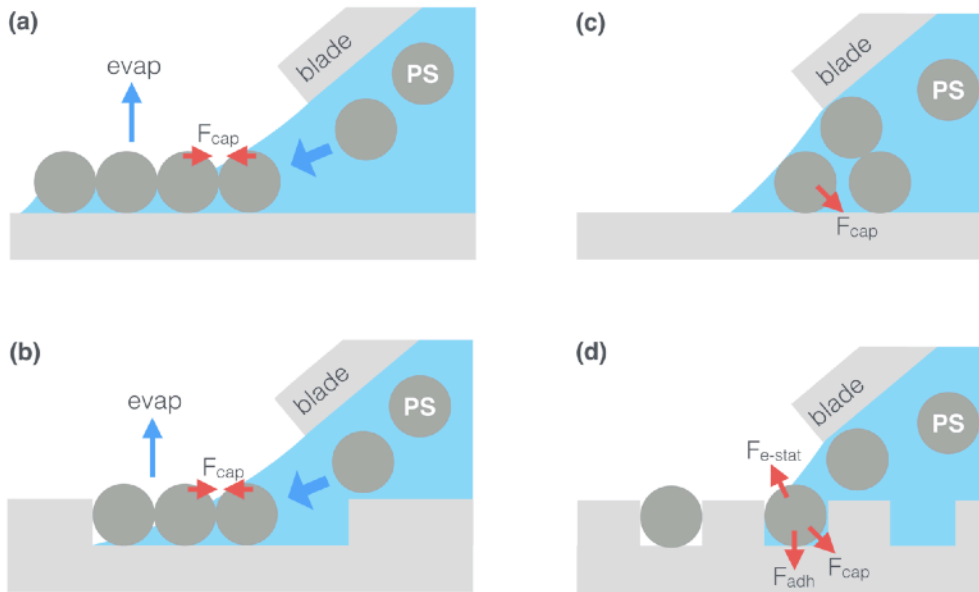
Fig. 3.2: Principles of convective assembly valid for small contact angles and capillary assembly for larger contact angles for colloid deposition on pre-patterned surfaces, where adhesive forces F_{adh} and capillary forces F_{cap} overcome electrostatic forces F_{e-stat} and draw the colloid into the topographic pattern (after [17]).

In this work, capillary assembly is applied to create 1D colloidal sphere rows inside trench structures. The surface wetting is adjusted by functionalization of a silicon surface with a self-assembled monolayer (SAM). The aim to suppress particle assembly on planar surface areas following Figure 3.2 (c), while colloids should be deposited inside the pre-patterns as in Figure 3.2 (d).

3.2 Self-assembled monolayers (SAMs)

In this section the preparation of self-assembled molecular monolayers (SAMs) will be discussed. Self-assembled monolayers are spontaneously formed, ordered, dense-packed molecular assemblies created by the specific affinity of a molecules head group towards a surface, while the molecule tail consisting of a spacer and end group is forced to stretch away from the surface [18].

The choice of molecular building blocks (Fig. 3.3), meaning head group, tail group and spacer, will dictate the nature of the resulting self-assembled order and the monolayer properties. Changing the head- and tail group of the molecules or its spacer chain length, the conformation, binding properties, density, thickness and functionality of the thin film on a chosen substrate material can be designed.

Such monolayers of organized molecule networks are typically deposited on surfaces by Langmuir-Blodgett techniques, vapor deposition, solution deposition or organic molecular beam epitaxy [19, 20]. SAMs are used in many applications as their preparation is easy, cost-effective, applicable on large areas and allows for an immense flexibility regarding the choice of molecules and substrates resulting in tailored surface properties and functionalizations. SAMs are used for wetting control, i.e. making surfaces hydrophilic or hydrophobic, for adhesion control, as protective coating in corrosion protection or mechanical protection, as building blocks in heterostructures, as systems for tailored surface chemistry or as bio-coating for biomolecule immobilizations [21-25].
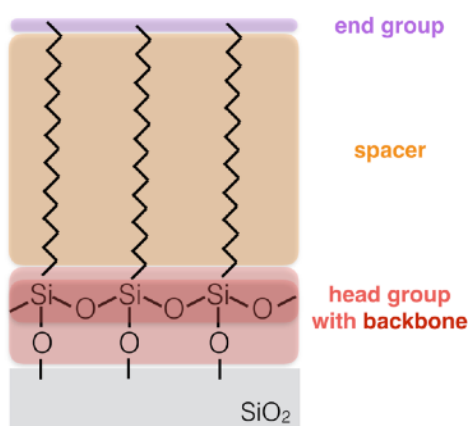
Fig. 3.3: Sketch of a SAM with characteristic molecular building blocks on the example of octadecyltrichlorosilane (OTS) on a SiO_2 surface.

3.2.1 SAM formation process

Formation process

The formation process of self-assembled molecular monolayers is described in Figure 3.4. The molecule concentration on the surface is plotted for different temperatures at which the formation process can take place, while passing through different stages of increasing molecule density, from a vapor-like state through a disorder regime into a solid-like state. Two different formation processes valid for different formation temperatures T1 and T2 are shown. They can be explained [26] by following the two different paths through the phase diagram in Figure 3.4 (a) below and above a critical temperature T_{triple} above which an additional low density liquid-like state occurs. The molecules configurations within these different stages are depicted in Figure 3.4 (b).

One path is described for a low formation temperature T1 $<$ T_{triple} (T1 in Fig. 3.4 (a), molecule sketch in Fig. 3.4 (b), case A). For very low surface concentrations the molecules behave vapor-like without orientational order. As the molecule density is low, they do not interact with other molecules. This is also called the striped phase, where molecules are oriented parallel to the surface and have a high mobility on the surface. With increasing concentration, within a disordered state, islands of SAMs are forming at several sites on the surface. Islands grow, molecules crosslink and start forming a so-called backbone (Fig. 3.3). In between these islands, molecules are in the vapor-like state. At this point, the film thickness is typically lower than in the ordered state. When the surface concentration increases further a dense ordered phase forms. In this solid-like phase the mobility of the molecules is very low as they are bound to the surface and the backbone is formed, comparable to a crystallization. Islands merge forming a closed film on the surface and SAM formation is complete. As the molecule density is as high as possible, the tails of the molecules are forced to configure in all-trans and arrange themselves parallel to their neighboring molecules. In areas, where previously build islands meet, tail orientation can misfit and grain boundaries are formed.

At a temperature higher than a critical temperature T_{triple} (T2 in Fig. 3.4 (a), molecule sketch in Fig. 3.4 (b), case B) another stable phase occurs, which is liquid-like. Again, starting at low surface concentrations molecules are stripped and in a vapor-like state. With increasing concentration the liquid phase is entered. Here, molecules

form a closed, but unordered film on the surface, either by lying stretched on the surface (case B on the left) or by forming a low density SAM with molecular tails being unstretched and randomly oriented (case B on the right). In both cases, upon further increase of the surface concentration, molecules start to from SAM islands with tails being stretched and upright. At even higher surface concentrations the dense packed, ordered solid-like phase is entered.

In contrast to the low temperature route, at higher process temperatures the island formation occurs at a point of higher surface coverage. Thus, the SAM islands form in a simultaneous and homogeneous way. Therefore the grain sizes are usually larger [26]. A more detailed SAM formation mechanism is proposed in [27] distinguishing in addition between island growth at higher or lower temperatures.
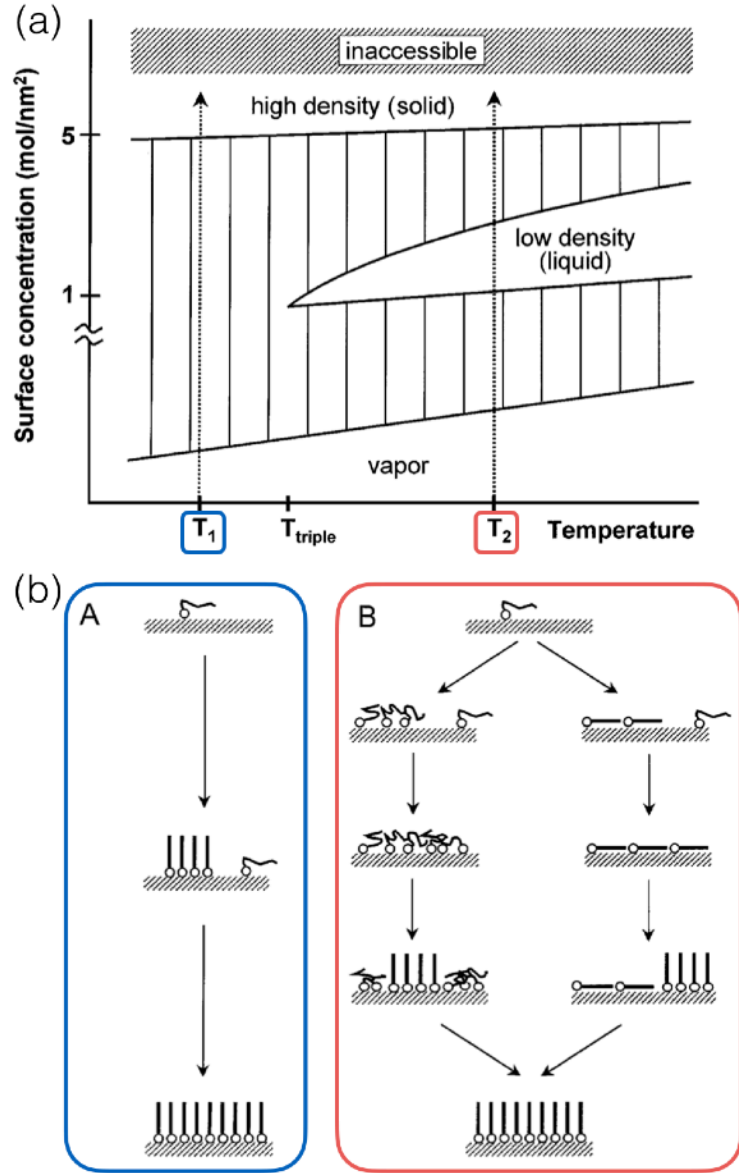
Fig. 3.4: Formation process of SAMs. (a) Phase diagram of states during SAM formation. Phase transitions from vapor through liquid-like to solid-like state with increasing molecule concentration on the surface. Paths for exemplary temperatures $T_1 < T_{triple} < T_2$ are marked. (b) Sketches of molecule conformation during SAM formation, following path T_1 in case A and T_2 in case B [26].

Defect formation

The model of SAM formation explained above is an idealized concept. Especially the binding of molecules to the surface can result in defect formation. This is discussed in the following for typical SAM-forming molecules with three binding sites, which will also be used in the experimental part of this work. Sketches in Figure 3.5 show possible miss-arrangements for the example of silanes on SiO_2-surfaces.

For the optimum SAM formation with molecules which have three binding sites the horizontal polymerization (Fig. 3.5 (a)) [28, 29] of molecules is the desired outcome. One binding site covalently binds to the surface whereas the other two binding sites interconnect neighboring molecules. This builds a 2D network that increases the SAM density by increasing domain sizes and stabilizing the thin film. For silanes, this stabilizing backbone is formed by strong lateral siloxane bonds, here SAM densities can reach 5 groups/ nm^2 [28, 29]. Typical for the horizontal polymerization is the formation of all-trans conformations, especially for molecules with a long tail groups. The tail groups arrange themselves parallel to each other due to sterical hindrance and van der Waals forces between the alkyl chains. When all molecules arrange themselves parallel, large domains can be achieved and the surface is homogeneously terminated.
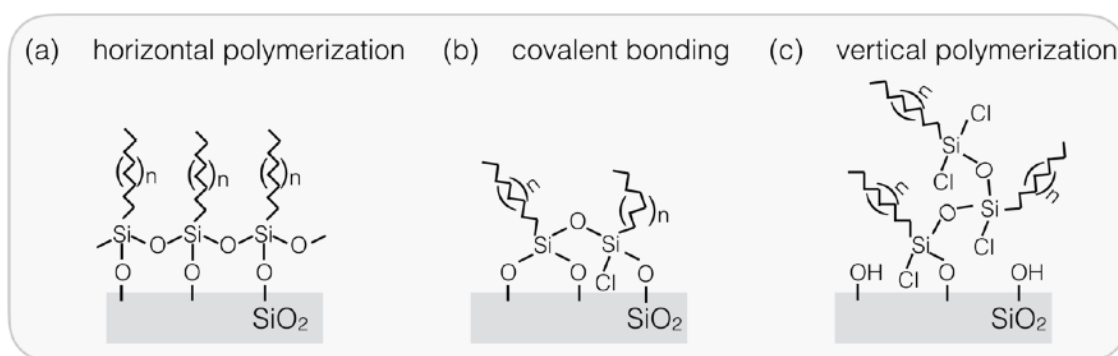
Fig. 3.5: Sketch of possible polymerization processes during SAM formation. (a) Horizontal polymerization: one binding site of the head group covalently binds to the surface while the other two sites interconnect and build a backbone with neighboring molecules. (b) Covalent bonding: two binding sites of the head group bind to the surface, no backbone can be formed, therefore the SAM is not dense packed. (c) Vertical polymerization: Cross-linking between molecules leads to 3D polymerization, no SAM is formed. [after: 28]

If the SAM formation process is disturbed, molecules can covalently bond to the surface with two binding site (Fig. 3.5 (b))[1]. This usually occurs in the presence of too much surface-near water (for siloxane-building head groups). Tail groups can not arrange themselves parallel to each other and no SAM-backbone develops. This leads to a lower SAM density with lower film thickness and the surface functionalization is more inhomogeneous.

In case of vertical polymerization SAM formation is largely suppressed (Fig. 3.5 (c)). This occurs when molecules polymerization starts within the solvent far away from the surface or when one site of the head group of single molecules binds to the surface, lacking neighboring molecules. Random cross-linking of surface-approaching molecules from the bulk then leads to the formation of 3D instead of 2D networks. Molecules aggregate and are likely to sediment onto the surface, where they disturb the formation process by blocking the surface. This

---

[1]All three binding sites can not bind to the surface due to sterical hindrance.

typically takes place due to the presence of water in the solvent (in case of silanes). The water leads to early hydroxylation of the head group making it more reactive whereby the oligomerization of molecules is likely to happen before the molecules reach the surface. The film thickness is very inhomogeneous and tends to be much larger than expected for the horizontally polymerized SAM. The modified surface properties will not be homogeneously developed.

3.2.2 SAM properties: experiment and results

In this work self-assembled monolayers are deposited on silicon surfaces in order to change the surface wetting and reactivity by the tail groups of the SAM molecules.
The SAM formation of octadecyltrichlorosilane (OTS) on silicon dioxide surfaces is investigated. As the OTS tail is highly unpolar, the surface properties of the SiO_2 can be tuned from being hydrophilic to hydrophobic. With mercaptopropyltrimethoxysilane (MPTMS) SAMs, a silicon dioxide surface gains reactivity due to the terminating thiol groups. The latter allows to form covalent bonds to gold.

Different vapor- and solvent deposition techniques are explored and resulting SAM properties are compared. The self-assembled molecular monolayers are investigated regarding their thickness by ellipsometry, their homogeneity and domain sizes by AFM and the new surface properties by contact angle measurements. Specifications of the measurement setups can be found in Appendix A3.

Octadecyltrichlorosilane (OTS)

Octadecyltrichlorosilane (OTS) $CH_3(CH_2)_{17}SiCl_3$ is a molecule consisting of a polar $SiCl_3$ head group and an unpolar CH_3 end separated by a long alkyl chain $((CH_2)_{17})$ (Fig. 3.6). The polar chlorosilane head offers 3 reactive binding sites. By hydroxylation one binding site forms a covalent bond to the silicon oxide surface, the other 2 binding sites build a backbone by crosslinking with neighboring molecules.
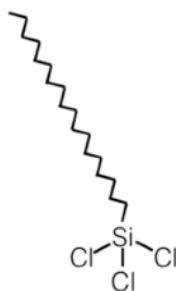
Fig. 3.6: Molecular structure of octadecyltrichlorosilane (OTS).

When the molecule head binds to a surface, the unpolar spacer and tail, consisting of an alkyl chain terminated with CH_3, will stretch away from the surface forming a new interface towards the atmosphere. The termination with methyl groups results in unpolar surface properties.
For the sterically most favorable conformation all tail groups arrange themselves parallel to each other. For OTS, the tilting angle of the all-trans chain conformation with respect to the surface normal is 30°. The molecule length for the fully stretched all-trans conformation is 2.81 nm [30], thus the SAM thickness is expected to be 2.43 nm.

Results and discussion. OTS SAMs are deposited on RCA-cleaned silicon substrates with native SiO$_2$ layer (see App. A2) by means of different deposition techniques. Recipes A and B are solution-based deposition techniques, whereas C is an ambient pressure chemical vapor deposition technique (Fig. 3.7).

Tab. 3.2: Preparation processes of OTS SAMs on silicon dioxide surfaces. A + B: solution deposition techniques, C: chemical vapor deposition. Process parameters: solvent, temperature (T), reaction time (t). SAM properties: contact angles (CA) with water.

recipe	solvent	T [°C]	t [min]	CA (H$_2$O) [°]
A	toluene	RT	20	56 - 109
A.1	toluene + CHCl$_3$	RT	20	105°
A.2	toluene	RT	20	80 - 110°
A.3	toluene	RT	50	110°
B	CCl$_4$ + hexadecane	RT	10	103 - 119°
C	(OTS vapor)	150	300	105 - 108°

Experimental procedures are described in the following and parameters are compiled in Table 3.2.

A Si substrates are stored in toluene with 5.1x10^{-3} mol/l OTS for 20 min at room temperature. After short rinsing of the samples with toluene they are stored for another 20 min in pure solvent. Afterwards, surfaces are dried in nitrogen flux.

Recipes A.1-A.3 are basically the same as in Recipe A, with slight variations:

A.1 The same recipe as in A. During the SAM formation step in OTS/toluene solution, samples are removed every 5 minutes and rinsed with CHCl$_3$ to remove aggregates from the surface.

A.2 Same recipe as in A, but with an OTS concentration of 8x10^{-2} mol/l.

A.3 Same recipe as in A.2 but with an increased SAM formation time of 50 min instead of 20 min. After SAM preparation, the samples are cleaned in an ultrasonic bath in CHCl$_3$ for 5 min.

B Samples are stored in a solution of 2.4 ml CCl$_4$, 0.6 ml hexadecane and 0.5 mol/l OTS at room temperature for 10 min. After that, the samples are rinsed and treated in an ultrasonic bath with CHCl$_3$.

C Chemical vapor deposition is performed by positioning a bottle with 0.25 ml of pure OTS and the RCA cleaned silicon substrates next to each other in a Teflon beaker (Fig. 3.7). The closed Teflon beaker is then heated to 150 °C for 5 h. After cooling down to room temperature, samples are removed.
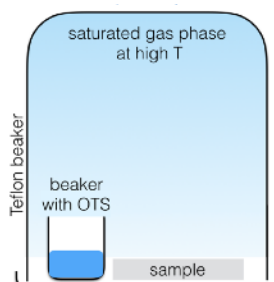
Fig. 3.7: Sketch of setup for SAM vapor deposition.

For recipe A contact angles with water vary from 56° on aggregates to 109° on smooth surface areas. Due to the use of wet/hydrous solvents and the humidity of the surrounding air, water is dissolved in the reaction mixture and vertical polymerization between OTS molecules occurs. The silane is hydroxylated and oligomerization of the OTS leads to 3D aggregate formation in the bulk solution. These aggregates sediment onto the surface of the sample leading to a highly inhomogeneous surface coverage. By rinsing the samples stepwise during the SAM formation with $CHCl_3$ sedimented aggregates can be removed from the surface (recipe A.1). This leads to more homogeneous surfaces with water contact angles of 103-107°. However, the vertical polymerization of molecules bonded to the surface with one binding site of the molecule head can not be suppressed and aggregates are still present.

A higher OTS concentration (recipe A.2), which might lead to a filling-up of areas which were covered with aggregates before rinsing with $CHCl_3$, do not result in a better SAM quality. An OTS concentration of 5 mmol/l is sufficiently high for full substrate coverage. After treating the surface with recipe A.2, the surface still is inhomogeneous. The contact angle with water varies at different positions on the sample between 80° to 110°. An extension of the treatment time (recipe A.3) improved the result slightly.

With a different choice of solvent (hexadecane and CCl_4) in recipe B obtained surfaces are macroscopically completely inhomogeneous as one can see with the eye. Nevertheless, contact angles with water vary between 103° and 119°.

SAM formation by vapor deposition (recipe C) results in a very homogeneous surface coverage, which is confirmed by contact angle measurements showing water contact angles of 107° all over the surface. This significant improvement in homogeneity could result from the absence of water during the SAM formation, since the evaporation takes place at 150 °C. Siloxane groups are not reactive before reaching the surface, thus vertical polymerization is suppressed and no 3D aggregates are formed. However, the difference can also result from the higher substrate temperature during the vapor deposition. As stated above the formation mechanism can follow two different paths in the phase diagram, where for higher temperatures a liquid-like state is passed. This phase is expected to improve the continuity of islands formed in the beginning of the SAM formation process. The critical temperature T_{triple} for OTS separating the temperature regions of different phase transition (Fig. 3.4) could not be found in literature. Works from others [27] suggests, that the critical temperature could be slightly above room temperature. Experiments in [27] show that the quality of OTS SAMs prepared at 40 °C is significantly better than the quality of those prepared at 20 °C or lower at otherwise the same experimental conditions.

SAMs made by recipes A.3 and C, as most promising deposition techniques, are further investigated by means of AFM, ellipsometry and contact angle measurements in the following. Results are summarized in Table 3.3.

Tab. 3.3: Characteristics of OTS SAMs on silicon dioxide surfaces. A.3: solution deposition, C: chemical vapor deposition. SAM properties: contact angles with water CA, surface roughness R_{rms} and peak-to-valley-distance p-to-v as domain sizes measured by AFM, and SAM thickness measured by ellipsometry.

recipe	CA (H_2O) [°]	R_{rms} [nm]	p-to-v [nm]	domainsize [nm]	thickness [nm]
A.3	110°	0.44 - 98.4	14.26 - 839	5-20	inhomogeneous
C	105 - 108°	0.25	5.15	10-30	2.30 ± 0.25

The results for a surface functionalization by recipe A.3 are shown in AFM images in Figure 3.8 (a+b): On wet-chemically prepared samples, the SAM formation is inhomogeneous. In smooth regions (Fig. 3.8 (b)), horizontal SAM polymerization occurred: the R_{rms} roughness is measured to 0.44 nm with a peak-to-valley roughness of 14.26 nm. At rough sites however (Fig. 3.8 (a)), the R_{rms} roughness is 98.36 nm, the peak-to-valley roughness 839.2 nm. Large 3D aggregates of cross-linked OTS are formed by vertical polymerization.

The vapor deposition, in contrast, leads to more homogeneous surfaces. Figure 3.8 (c+d) show AFM measurements at different scan sizes of a SAM prepared with recipe C. The R_{rms} roughness is 0.25 nm, peak-to-valley roughness 5.15 nm.

The domains themselves seem flat and with 10-30 nm lateral size comparable to values from literature, which range from 30-50 nm [29]. This good SAM order probably results from the slow deposition rate during CVD, the absence of water which could lead to cross-linking of the molecules and the elevated SAM formation temperature, most likely above T_{triple}.

For this sample ellipsometry measurements were performed using an refractive index of OTS at the used wavelength of 523 nm of n(OTS) = 1.5 [31], the OTS film thickness is determined to (2.30 ± 0.25) nm, which is in good agreement to literature, which is 2.43 nm for all-trans conformation of OTS [30].
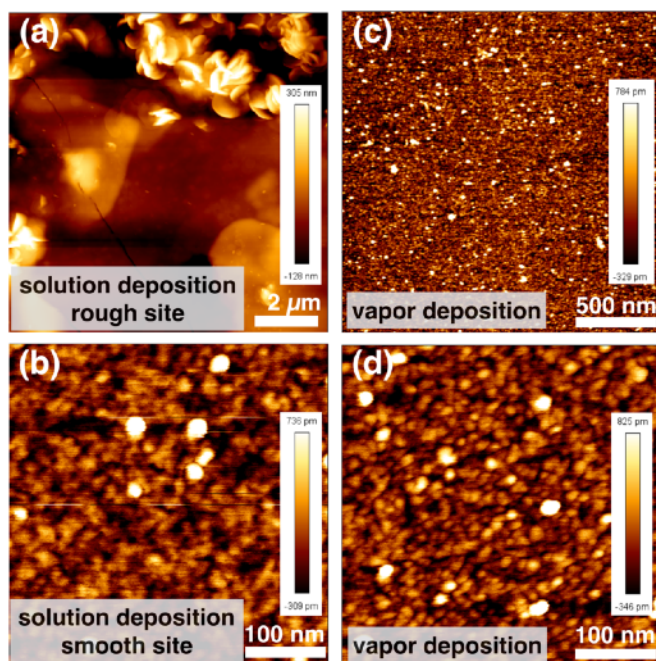
Fig. 3.8: AFM images of OTS SAMs. (a+b) Solvent deposited OTS fabricated by recipe A.3 forms inhomogeneous film on the SiO2 surface. (a) shows a rough area on the sample, where micrometer sized 3d aggregates are formed, while (b) shows a monolayer on the same sample with OTS domains of 10-40 nm. (c+d) Vapor deposited OTS using recipe C. SAMs are build homogeneously all over the sample surface.

Contact angle measurements with different solvents by the sessile drop method (details in App. A2) allow for the calculation of the surface free energy (SFE) by the OWRK method. For the vapor deposited OTS SAMs the surface free energy was determined to (25.23 ± 1.63) mN/m with nearly total dispersive character, which is in accordance to the CH_3-termination of the SAM-air interface. The contact angles are listed in Table 3.4.

Tab. 3.4: Contact angles (CA) and surface free energy (SFE) of a vapor deposited OTS SAM on Si/SiO$_2$.

	CA [°]		SFE [mN/m]
water	105.63 ± 0.53	polar	0.05 ±0.16
n-hexadecane	32.21 ± 1.18	disperse	25.18 ± 1.46
ethanol	1.52 ± 0.32	total	25.23 ± 1.63
diiodomethane	61.35 ± 0.44		

3-Mercaptopropyltrimethoxysilane (MPTMS)

3-Mercaptopropyltrimethoxysilane (MPTMS) SH(CH$_2$)$_3$Si(OCH$_3$)$_3$ has a trimethoxysilane head group, offering three binding sites (Fig. 3.9). The spacer is a propyl chain terminated with a thiol end group. The molecule length is 0.8 nm.
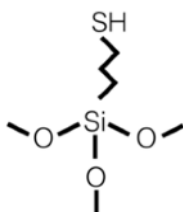
Fig. 3.9: Molecular structure of 3-mercaptopropyltrimethoxysilane (MPTMS).

MPTMS can form SAMs in two different configurations: (a) with the trimethoxysilane as a head group binding with one site to an oxide surface and the thiol group pointing towards the atmospheric interface. The other two binding sites form a backbone. Or (b) with the opposite orientation to the surface: with the thiol binding to the surface as head group and the Si(OCH$_3$)$_3$ stretched away and terminating the SAM. The orientation (b) is formed e.g. on Au surfaces, which form covalent bonds to the thiol, while not offering binding sites to the silane [18].

In this work, the SAM configuration formed on a SiO$_2$ surface with trimethoxysilane as a head group and the thiol terminating the interface to air is investigated.

Results and discussion. Three different approaches (Tab. 3.5) are used to create self-assembled monolayers of MPTMS on oxygen plasma cleaned silicon substrates with native SiO$_2$ (sample size 2 cm^2, cleaning procedure in App. A2). Recipes A and B are solution deposition, while C is a vapor deposition approach.

A   Substrates are stored in a mixture of 2 % (v/v) MPTMS in water for 7 h at room temperature. Samples are afterwards rinsed with water and dried in a nitrogen flux.

B   Si substrates are stored in a solution of 10 ml 2-propanol, 250 µl MPTMS and 10 µl water for 7 h at room temperature. Samples are then rinsed with pure 2-propanol and dried in a nitrogen flux.

C   200 µl of pure MPTMS and Si samples are annealed at 140 °C for 7 h in a sealed Teflon container (see sketch OTS vapor dep.). After cooling down, the samples are removed.

Tab. 3.5: Approaches for MPTMS SAM preparation on silicon dioxide surfaces. A+B: solution deposition, C: chemical vapor deposition. Preparation parameters: process: solvent, temperature T, time t. SAM properties: contact angles with water CA, surface roughness R_{rms} and peak-to-valley-distance p-to-v measured by AFM.

	process	T [°C]	t [h]	CA (H$_2$O) [°]	R$_{rms}$ [nm]	p-to-v [nm]
A	water	RT	7	56	0,13	1,14
B	isopropanol	RT	7	55	0,24	1,36
C	vapor	140	7	79	0,22	1,70

All techniques allow for the formation of very homogeneous surfaces, which is obvious from AFM and contact angle measurements. Contact angles are measured on three different spots on each surface, showing no differences.

AFM investigations show that for all three SAM deposition processes very smooth surfaces are produced. The water-based solution process A leads to a SAM with a R_{rms} roughness of 0.13 nm with a peak-to-valley distance of 1.14 nm. The isopropanol-based solution process B leaves a film with a R_{rms} roughness of 0.24 nm with a peak-to-valley distance of 1.36 nm. For both wet-chemical deposition techniques however, no domain formation can be determined. The molecules seem to arrange randomly in a monolayer without conformational order.

Figure 3.10 shows AFM images of the SAMs deposited by vapor deposition C. Their roughness is with $R_{rms} = 0.22$ nm in the same range as on the solvent deposited SAMs, the peak-to-valley distance is 1.70 nm. But in contrast to the other techniques large orientational domains with lateral sizes of 40-70 nm (mean value 55 nm) are formed.
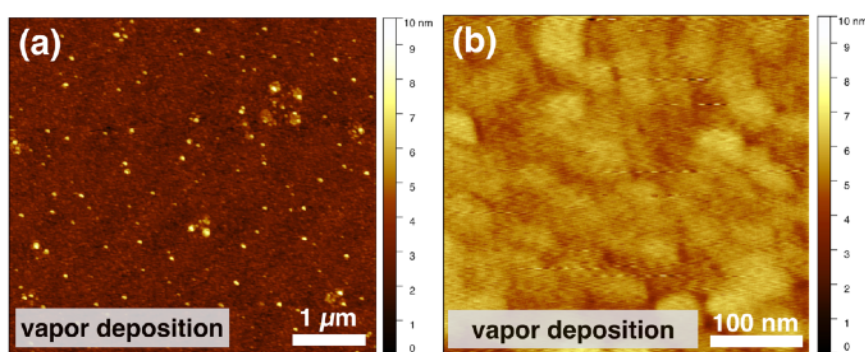
Fig. 3.10: AFM images of MPTMS SAMs prepared by vapor deposition. (a) Very homogeneous surface coverage. (b) Zoom-in showing SAM domains of lateral sizes between 40 nm and 70 nm.

Contact angle measurements are performed on samples prepared by all three approaches and surface free energies are calculated by the OWRK method. The results are plotted in Figure 3.11. The two solvent deposition techniques show quite similar results. Contact angles with water and diiodomethane are 55° and 37°, respectively. The surface free energy is about 55 mN/m with a polar fraction of 14 mN/m and a disperse fraction of 41 mN/m. The vapor deposition approach, however, shows different results: higher contact angles with water occur for the vapor deposited MPTMS as the polar contribution of the surface energy is with 3.4 mN/m much smaller than for the solution deposited SAMs. This could be due to the fact that the molecules arranged themselves more densely, the outer surface is more homogeneously covered with the thiol. The contact angle

measurements also confirm the molecule orientation towards the surface: contact angles with water of 68° are reported in literature for the termination with the thiol group towards the air interface, while a termination with the silane group would show hydrophobic surface properties with contact angles of 103° with water [32].

It can be expected that with longer assembly times, the SAMs qualities will increase. Solvent- and vapor-based deposition both lead to high quality MPTMS SAMs.
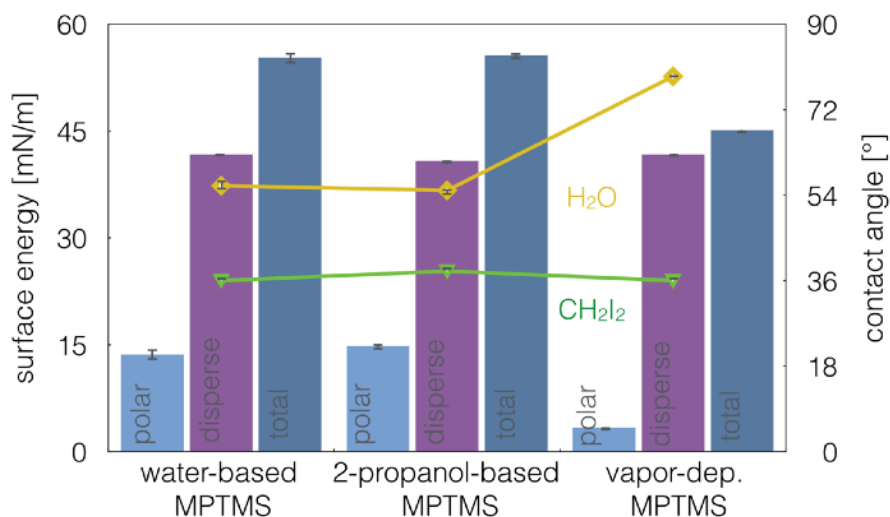
Fig. 3.11: Contact angles and surface free energies of MPTMS SAMs on SiO$_2$ surfaces prepared by different deposition techniques. Data point show contact angles with water and CH$_2$I$_2$, respectively. Bar chart corresponds to polar part, disperse part and total sum of surface energies.

3.2.3 Conclusions

In this chapter, the formation of self-assembled molecular monolayers (SAMs) on solid substrates is explained. SAMs of octadecyltrichlorosilane (OTS) and 3-mercaptopropyltrimethoxysilane (MPTMS) are investigated in the experimental section.

For OTS, difficulties can occur due to the high reactivity of the molecules with water. Moisture leads to an oligomerization of OTS molecules far away from the substrate, if the SAM formation is performed in a solvent deposition approach. Agglomerates form and suppress the formation of a large-area uniform SAM. As the homogeneity of the SAMs is crucial for subsequent experiments (Chap. 3.3), a vapor deposition technique is used to create high quality large area SAMs of OTS. The CVD approach leads to homogeneous SAMs with a surface free energy of (25.23 ± 1.63) mN/m with water contact angles of 107° at a measured film thickness of (2.30 ± 0.25) nm with domain sizes of up to 70 nm. Thus, homogeneous hydrophobic surfaces are prepared.

MPTMS SAMs are produced on Si substrates in order to create a thiol termination of the surface. Solvent-based as well as vapor deposition approaches show homogeneous SAM formation, however, by vapor deposition the polar contribution to the surface energy is significantly lower than in case of the solvent deposition. Domain sizes are large on SAMs prepared by the vapor deposition. In case of solvent deposition, molecules do not seem to have build a backbone network leading to conformational order.

SAMs are applied in the next chapter (Chap. 3.3), where OTS SAMs are used for hydrophobization of a silicon surface to avoid wetting with polymer particle suspensions and suppress particle assembly onto the surface.

Section summary

Self-assembled monolayers (SAMs) can be used for the chemical functionalization of surfaces. They consist of single molecules with functional head groups, spacers and tail groups, which arrange themselves on interfaces forming a close-packed monolayer.

In this work, SAMs from octadecyltrichlorosilane (OTS) are investigated, as they are suitable for the hydrophobization of silicon oxide surfaces. Different solution and vapor deposition techniques are studies for OTS SAMs as well as for 3-mercapto-propyltrimethoxysilane (MPTMS) SAMs.

3.3 Topographically & chemically directed self-assembly for polymer sphere chains in trenches

The topographical patterning of trenches on silicon surfaces is realized by photolithography and reactive ion etching; the surfaces are then chemically functionalized with a self-assembled monolayer (SAM). The homogeneity of this chemical surface modification was found to be a crucial step for the subsequent sphere deposition. The SAM quality was therefore optimized by investigation of different solution- and vapor-based deposition techniques. This was explained in detail in Chapter 3.2.

It is shown that these surface modifications can result in the ordered arrangement of spheres exclusively inside topographic patterns while sphere deposition on plane surfaces is suppressed. The experimental procedure is explained in detail and the influence of pre-pattern geometry, surface wettability and parameters during the colloid deposition are investigated.

3.3.1 Topographic pre-patterning: trenches on silicon surfaces

Two basic structures are investigated (Fig. 3.12): (a) long freestanding trenches are used for experiments concerning the colloid deposition. Trenches have widths d between 1 μm and 6 μm. The distances D between neighboring trenches vary from 75 μm to 300 μm. Trench lengths L are 1 and 5 cm. The influence of trench width d and distance D between neighboring trenches on trench filling with colloids is investigated in the following. (b) Short trenches, which end in square reservoirs, are prepared for the use in nanogap electrode applications. Here, trenches are d = (2 ± 0.2) μm wide corresponding to the diameter of spheres to be used and have varying lengths of L = 50 - 1000 μm. At each end trenches enter into a square reservoir with edge lengths of 1 mm.
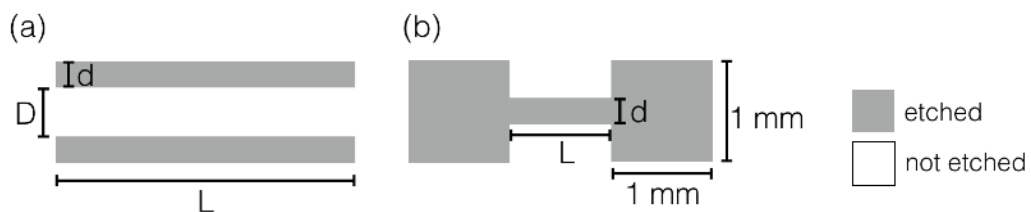
Fig. 3.12: Sketch of trench structures for topographic pre-patterning of Si substrates by photolithography. (a) Trenches with width d, length L and distance D. (b) Trenches with width d and length L ending in 1 mm^2 large reservoirs.

The technical drawing of the photolithography mask, which contains these and additional structures, and further details of the mask can be found in Appendix A4. The aimed structure depth after pattern transfer into the Si substrate is 2 μm.

Photolithography procedure. 4″ Si wafers are cleaned in piranha etch (H_2SO_4:H_2O_2, 4:1) and coated with hexamethyldisilazane (HMDS, Sigma Aldrich) as adhesion promoter by vapor deposition. The Photoresist AZ5214E (MicroChemicals GmbH) is then spin coated at 4000 rpm for 45 s resulting in a resist thickness of 3 μm. During a soft-bake at 100 °C for 60 s at air the solvent is evaporated. The exposure is done in mask contact mode with a Hg lamp (Osram HBO350w/s, 350 W) at a wavelength of 365 nm for 2.7 s. A reverse-bake for 60 s at 120 °C is followed by a flood exposure for 45 s. The resist is developed in diluted NaOH for 45 s. Last, a post-bake for 60 min at 130 °C is done in air.

Pattern transfer. For pattern transfer into the Si substrate by reactive ion etching a Plasma Technology PlasmaLab u80P is used. Etching is performed in 100 sccm SF_6 at 150 mTorr and 100 W RF for 1 min. This results in a structure depth of about 2 μm in the silicon substrate (with native SiO_2). The resist is removed afterwards in an oxygen plasma.

The final structure sizes and etch profiles are investigated by confocal laser scanning microscopy with an Olympus Lext 4000. A typical trench profile is shown in Figure 3.13. The slope of the trench walls is approx. 68°. Prior to use, surfaces are either cleaned in a RCA process or by additional plasma cleaning, as described in Appendix A2.
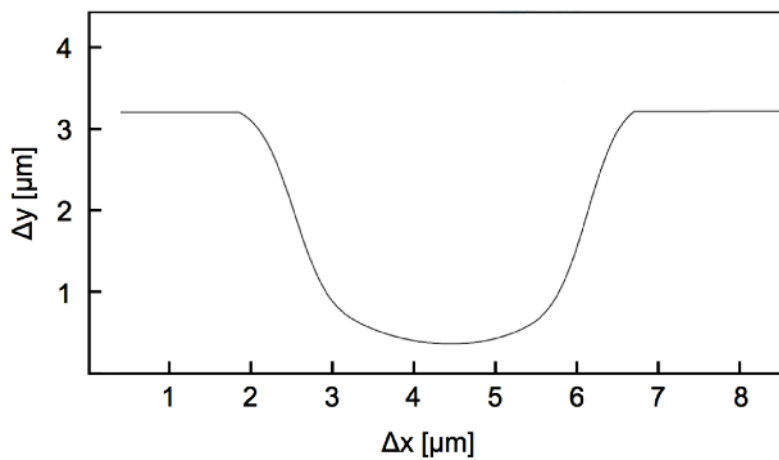
Fig. 3.13: Trench profile after photolithography and reactive ion etching into Si as measured by CLSM. The slope of trench sidewalls is representative for all samples and amounts to 68° on average.

3.3.2 Chemical functionalization of silicon surfaces with SAMs

The chemical surface modification is applied in order to change the surface wettability with water. To this end, a self-assembled monolayer (SAM) of octadecyltrichlorosilane (OTS) is created, following the results discussed in Chapter 3.2.

3.3.3 Directed self-assembly of colloids

As a next step, the pre-patterned surfaces are used as substrates for the directed deposition of polymer spheres from colloidal suspensions. For all experiments in this chapter polystyrene spheres with a diameter of 2.1 µm[1] are used and deposited onto the surface by the doctor blade technique explained in Chapter 2.2. The triple phase contact line of the suspension is always kept parallel to the trench long-axis.

In order to determine the influence of both topographical and chemical surface treatment, first, the solely topographically pre-patterned surfaces are used as substrate. Figure 3.14 (a) shows the result of the sphere deposition on such patterned surfaces, here with two parallel trenches (marked in red), if the doctor blade procedure is performed analog to sphere deposition onto plane surfaces, here at a velocity of 115 µm/s at room temperature and a relative humidity of 25 %. The trench is filled with spheres, however, a non-continuous monolayer of spheres is also visible on the plane surface areas next to the trenches.

As the patterned substrate $Si/SiO_{2,nat}$ is treated with an RCA cleaning, the surface is terminated with hydroxy groups. This hydrophilic nature of the surface is confirmed by contact angle measurement showing small contact angles of 17° (see inset) [7]. Thus, the polymer sphere suspension forms a flat meniscus on the substrate and convective self-assembly of spheres occurs on the whole sample (Chap. 3.1).
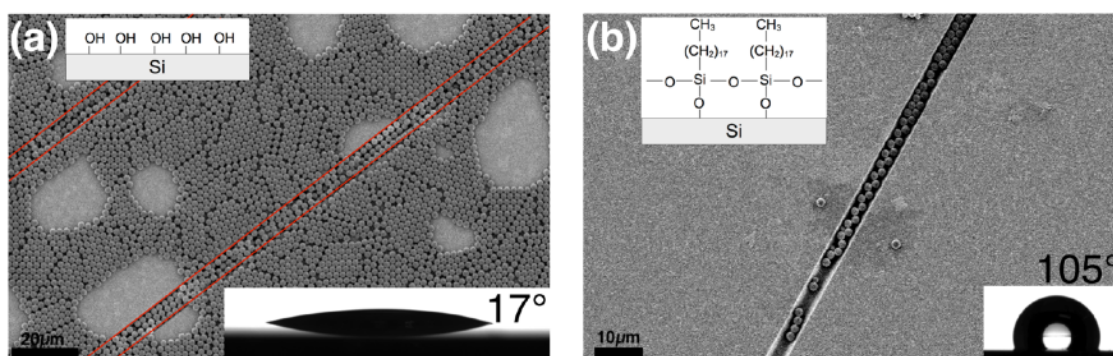
Fig. 3.14: SEM images of topographically pre-patterned silicon substrates after self-assembly of polymer spheres without (a) and with (b) chemical surface functionalization. (a) Non-functionalized, RCA cleaned hydrophilic surface with an contact angle with water of 17°. (b) OTS treated hydrophobic surface with a contact angle with water of 105°. The insets in the upper left show schematically the surface terminations [7, 33].

In order to achieve site-selective polymer sphere deposition inside the trenches while suppressing the deposition of polymer spheres on the silicon top surface, topographically pre-patterned surfaces are chemically functionalized with an octadecyltrichlorosilane (OTS) SAM (Chap. 3.2.2). This leads to a hydrophobization of the surface, now showing contact angles with water of 105°, which changes the sphere deposition mechanism from convective self-assembly to capillary assembly, as discussed in Chapter 3.1. Figure 3.14 (b) confirms this change showing the drastic effect of the surface functionalization on the deposition of polymer spheres during

---

[1] Polystyrene spheres, 2100 nm diameter, 10 % w/v solid content, CV < 5%, Thermo Scientific Inc. [Art. No. 5200A]

the doctor blade procedure. Sphere deposition on the plane silicon surface is largely suppressed, while the trenches are filled (at otherwise same experimental conditions in the doctor blade process: RT, RH = 25 %, v = 115 µm/s, triple phase contact line parallel to trench). Following the assumptions of the concept of capillary assembly (Chap. 3.1), a state of capillary assembly on plane surfaces preventing sphere deposition (Fig. 3.2 (c)) is created due to the chemical surface modification, while capillary assembly in the topographic patterns, following Figure 3.2 (d) takes place. However, it should be noted that the reason for particles being deposited inside the trenches is not trivial, as the trenches are also covered with the OTS SAM, thus are also hydrophobic. Figure 3.15 illustrated a possible model explaining the largely preferential deposition of spheres in trenches based on a pinning of the triple phase boundary at a trench. In this model the contact line is pinned at the trench rim leading to a meniscus deformation, allowing for the capillary sphere assembly inside the trench. Again, in general no sphere assembly occurs on the hydrophobic surface as no flat meniscus is formed, which would result in convective self-organization (Chap. 3.1). At some point, however, when the suspension droplet is moved further across the surface the contact line hits a trench and gets pinned at its rim. The meniscus deforms due to this pinning, forming a smaller contact angle to the substrate and thus capillary assembly of spheres inside trench occurs as explained before. After some time with further movement of the droplet, the contact line gets detached off the rim of the trench. The meniscus' shape recovers back to a large contact angle and again no spheres are deposited [7].
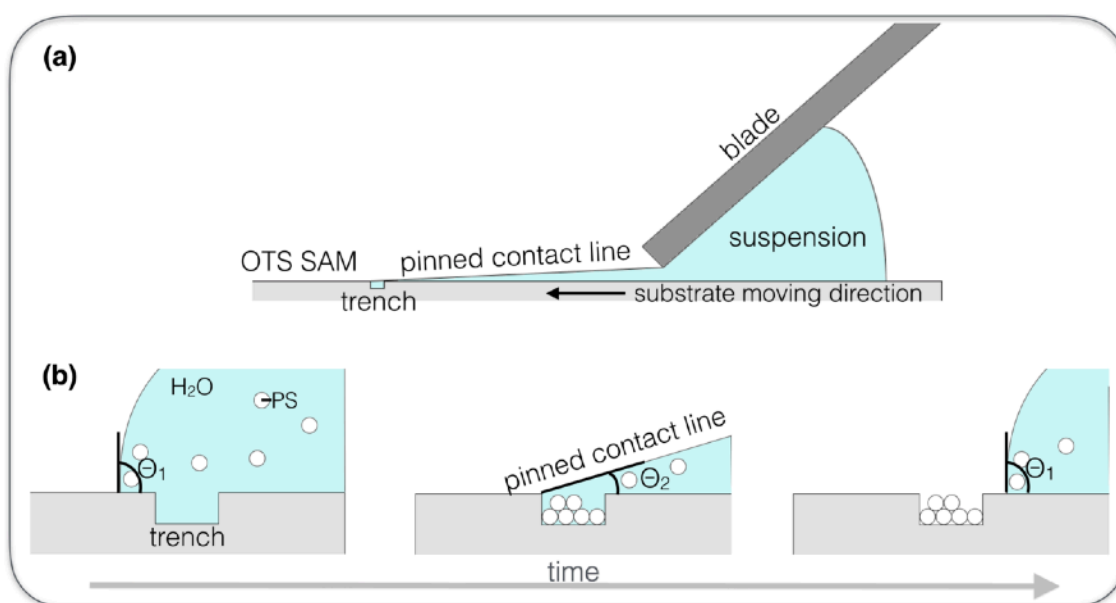
Fig. 3.15: Model of suspension meniscus pinning at a trench edge. (a) Meniscus is pinned at a trench while the sample is moving to the left. State as assumed in middle image of (b) at lower magnification.(b) Time line of meniscus shape at trench edge during doctor blade technique. Left: No sphere assembly occurs on plane substrate next to the trench due to large contact angle prior to hitting the trench. Middle: Contact angle gets smaller, when the meniscus in pinned at the trench edge, thus capillary assembly of colloids into the trench takes place. Right: After further sample movement, the meniscus is ripped off and states back to the large contact angle, suppressing sphere deposition.

The reason for the contact line pinning at the trench edge could either be explained by the topographic change of the surface or a chemical discontinuity. However, a pinning at the topographic edge is expected to have less impact on the pinning process, as the trench edges are rather smooth, as shown in the trench profile measurements by CLSM (Fig. 3.13). It is therefore assumed that the SAM is locally not densely packed at trench

edges. Thus, due to a decreased density, the hydrophobicity is not that distinct and the contact line of the aqueous suspension pins in the less hydrophobic area.

The local defect in the SAM order could result from the following three possible molecule behaviors at a topographic edge as depicted in Figure 3.16: (a) Emanating from strong van der Waals interactions between the alkyl chains of neighboring molecules a gap in the SAM could be formed at the edge. (b) A limitation of binding sites on the substrate surface could just allow for a sparse coverage with the SAM at the edge, i.e. the density of alkyl chains could be smaller. (c) The SAM backbone formation could be interrupted at the edge so that molecules do not arrange in all-trans conformation but are unstretched. The behavior of SAMs on topographic edges is not well investigated in literature. However, a proposal of Whitesides et al. [34] is made for topographic edges with radii of curvature of opposite sign (compared to the edges in Fig. 3.16). According to this proposal, local disorder similar to case (c) in Figure 3.16 would be expected. In any case, a defect in the SAM at the trench edge leads to a decreased dynamic contact angle and enables the contact line pinning of the aqueous suspension.

(a) gap **(b)** sparse **(c)** no order
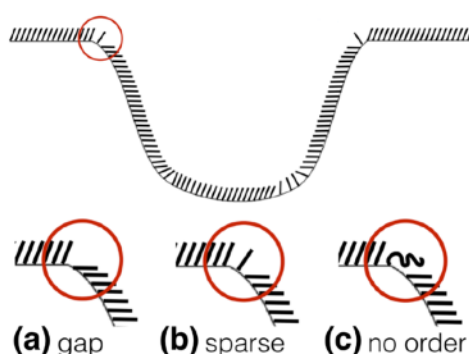
Fig. 3.16: Sketch of possible OTS molecule arrangements at trench edges. Trench profile is as measured by CLSM of prepared samples, but for sake of visibility OTS molecules are not in scale. (a) Strong van der Waals forces between alkyl chains lead to gap formation at the edge. (b) Molecules are stretched, but sparsely arranged due to the radius of curvature. (c) Molecules have no all-trans conformation at the edge, but lie unstretched and unordered on the substrates surface. In all cases the wettability properties are different at edges in comparison to planar surfaces as substrate coverage is reduced. Edges are likely to be less hydrophobic.

3.3.4 Sphere deposition inside trenches

So far, it was shown that by combined topographical and chemical surface pre-patterning, polymer spheres can be self-selectively assembled inside the trenches, while no spheres are deposited on the plane surface areas.

The way, the spheres arrange themselves inside the trenches however is mainly affected by two other aspects: the geometry of the pre-pattern, i.e. trench width, depth and trench density on the substrate; and the parameters during the doctor blade experiment, i.e. especially the velocity of the moving triple phase boundary. These parameters will be discussed in the following. The triple phase contact line is in all cases moved parallel to the trenches, experiments are performed at room temperature and at relative humidities of $(50 \pm 5)\,\%$. The trench depth is 2 μm if not stated otherwise.

Obviously, the width of the trench limits the number of spheres deposited inside. Figure 3.17 displays SEM images of trenches of different widths filled with polymer spheres. Commensurate with the ratio between sphere diameter d_s and trench width d_t, the trenches are filled with 1 to 4 spheres next to each other. For trench widths matching a full multiple of the sphere diameter, spheres arrange themselves quadratically packed. For

trenches slightly larger than a full multiple of the sphere diameter the spheres arrange themselves hexagonally (not shown). For $d_t = 2.2\ d_s$, this resembles e.g. a zick-zack-chain of spheres. As the trenches do not have vertical walls but a profile as shown in Figure 3.13, this arrangement does also occur for a trench width of 0.5 x multiples of d_s, as shown in Figure 3.17 (a) on the left. If the trench width is commensurate with the sphere diameter, a single row of contacting spheres can be created as in Figure 3.17 (a) on the very right (the trench width decreases towards the lower part of the image; thus the zick-zack row of the spheres changes to a linear chain).
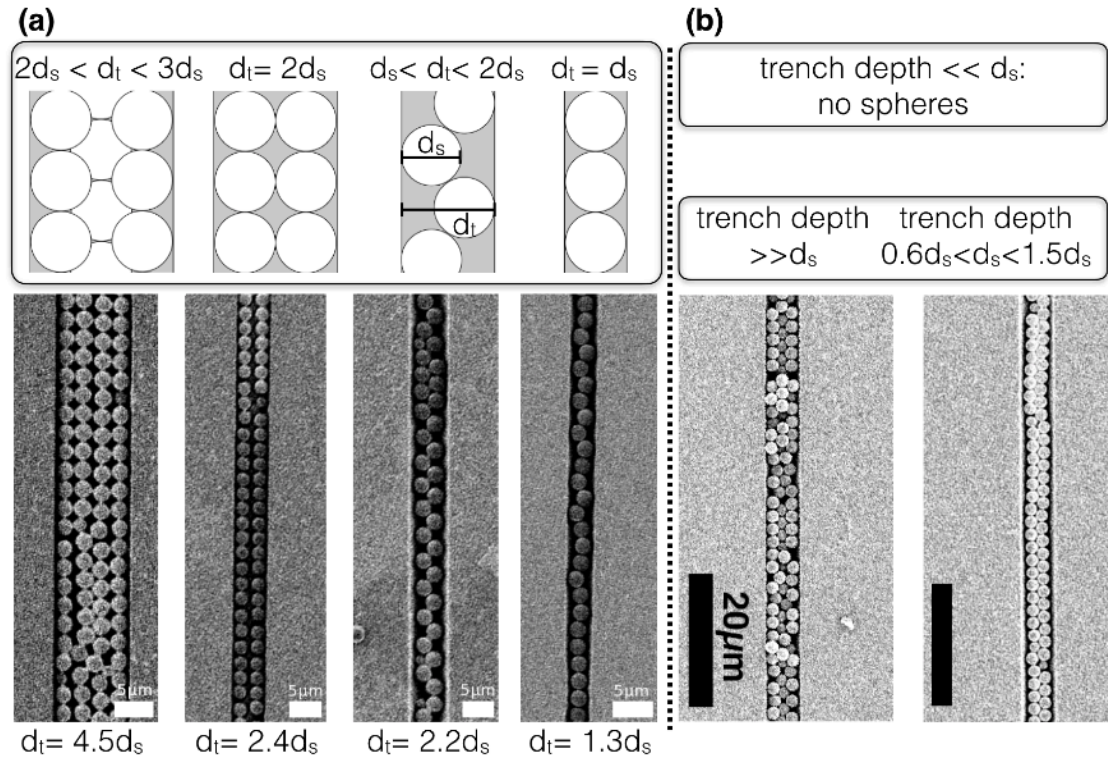
Fig. 3.17: SEM images (bottom) and sketches (top) of sphere assembly inside trenches with respect to the size ratio of (a) trench width to sphere diameter and (b) the trench depth to sphere diameter. (a) Multiple spheres arrange themselves quadratic or hexagonal arranged next to each other for trench widths D larger than twice the sphere diameter d_k. For trench width equal to sphere diameter, linear chains of sphere are formed. Zick-zack chains appear for trench width between one and two sphere diameters [33].

The trench filling also depends on the trench depth (Fig. 3.17 (b)). If trenches are too flat ($<< d_{sphere}$) no filling occurs. Spheres are neither deposited in the trench nor on the plane substrate surfaces. This is probably due to the fact that spheres, deposited in the trench while the contact line is pinned, are removed when the contact line gets detached off the trench rim. For a trench depth between $0.6\ d_{sphere} < d < 1.5\ d_{sphere}$ the trenches are filled as desired (Fig. 3.17 (b), right). A monolayer of spheres is deposited into the trench and capillary forces arrange the spheres close packed commensurate to the lateral space available. If the trench depth is much larger than the sphere diameter the trench is filled up with particles and multilayers are formed. Due to the small slope of the trench walls, the trench width changes strongly in deep trenches and no ordered sphere assembly can occur. Thus, trenches are filled randomly with particles as visible in Figure 3.17 (b) on the left.

As stated above, the wettability of the surface is crucial for the site-selective assembly of polymer spheres inside the trenches. The wettability of structured surfaces depends strongly on the pattern density [8, 13,14]. Contact

angle measurements with water, displayed in Figure 3.18 (a), confirm this effect on surfaces with different trench area fractions S. This trench area fraction is defined as the ratio of the area occupied by the trenches to the total sample area. Here, silicon surfaces with native oxide, patterned by photolithography with trenches of 2 µm depth as explained above and functionalized with an OTS SAM are studied. The sphere deposition is performed at a blade velocity of 100 µm/s, RT and 50 % relative humidity with the triple phase contact line being parallel to the trenches. For the patterning of silicon surfaces with high pattern densities, special photolithography masks (different to the one described in Appendix A4) were used. In some cases, beamer lithography or electron beam lithography are used. The preparation of these structures is explained in [33]. Plane OTS-covered surfaces show a contact angle with water of 107°, for a low trench area fraction as e.g. for single trenches with a distance of 100 µm to the next neighboring trench, the contact angle increases slightly towards 115°. Such trenches are filled with ordered sphere arrangements as shown before and in Figure 3.18 (c) for a fraction of S = 0.025. However for large trench area fractions, i.e. high pattern densities as in Figure 3.18 (b) (S = 0.67), the wettability decreases drastically towards superhydrophobicity (contact angle of 146°) and spheres are poorly deposited into the trenches. This is shown in Figure 3.18 (b). Small sphere islands are formed inside trenches as well as next to the trenches on plane Si surfaces and are randomly distributed.
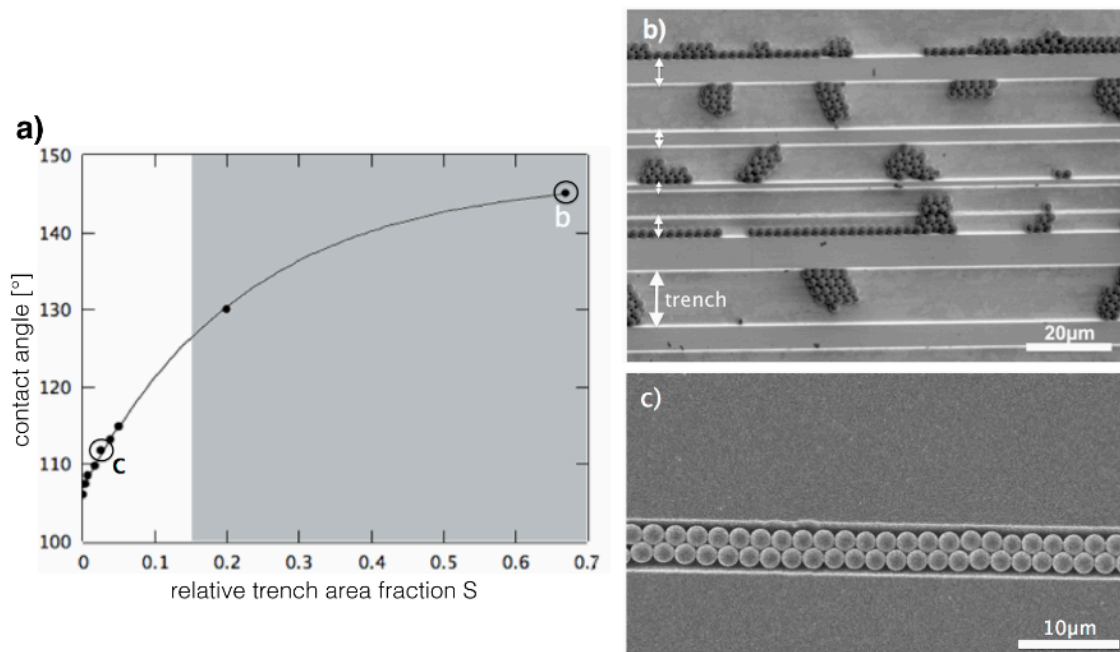
Fig. 3.18: (a) Contact angles with water in dependence on the relative trench area fraction S. The grey area marks the region of high trench densities where ordered sphere arrangement inside trenches is not observed but occurs randomly as in (b). For lower trench area fractions the desired ordered site-selective sphere arrangement as in (c) is possible [8].

Additionally to these geometrical requirements for the defined sphere assembly inside the trenches, experimental conditions of the doctor blade process need to be considered.

As explained in more detail in Chapter 2.2, the formation of a large-area dense-packed polymer sphere monolayer at a triple phase boundary is only possible if the crystal growth velocity is in accordance with the motion velocity of the triple phase boundary. This crucial dependence on the blade velocity, i.e. the velocity of the triple phase boundary, is also found for the site-selective sphere assembly into trenches as shown in Figure 3.19 (a). Too slow movement of the contact line leads to sphere assembly not only inside trenches but also next to them, too fast movement leads to incomplete trench fill-up. At optimum velocity, the trenches are completely

filled with close-packed ordered sphere arrangements, while the plane areas between different trenches are free of spheres. This optimum velocity v_{opt} can be calculated for the formation of sphere layers by Equation 2.6 and depends on parameters given by the sphere suspension, the evaporation flux and the surface coverage with spheres. This coverage is for a monolayer of hexagonally arranged close-packed spheres given by the layer porosity ε_p in Equation 2.6. For a pre-patterned surface with site-selective sphere assembly, the relative trench area fraction S needs to be includes as a factor to this porosity [8]:

$$v = \frac{\beta \cdot Q \cdot j_v \cdot \mu}{z \cdot d_K (1-\mu)(1-\varepsilon_p S)}$$

(3.1)

Again, v is the velocity of crystal growth, β the velocity coupling constant between particle and liquid, Q the length of the evaporation zone, j_v the evaporation flux, μ the particle volume fraction, z the number of formed particle layers, d_k the sphere diameter.
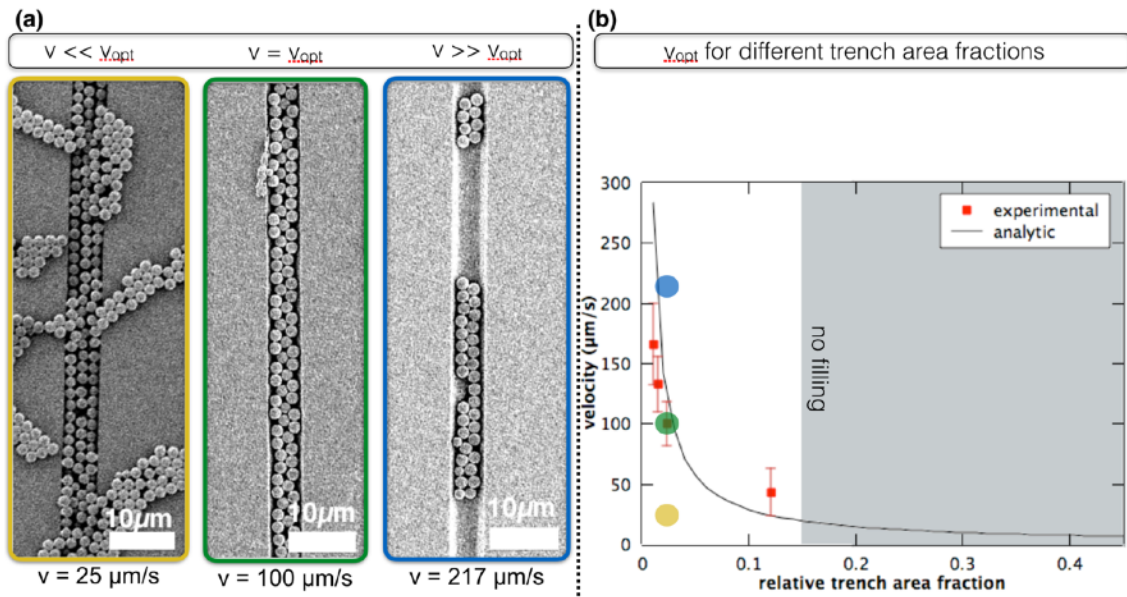
Fig. 3.19: (a) SEM images of the state of trench fillings for different blade velocities in the doctor blade experiment. Trenches are 2 μm in depth and correspond to a trench area fraction of S = 0.025. For slow movement spheres are not site-selectively deposited in trenches but also on the Si surface, for fast movement trench filling is incomplete. Only for an optimum velocity a perfect site-selective trench fill-up is possible. (b) The optimum velocities for different trench area fractions can be calculated by the extended Dimitrov equation (Eqn. 3.1) and are in good agreement to experimental data [8, 33]. The blue, green and yellow points refer to the images in (a) for a constant S = 0.025.

By this new relation, the optimum velocities for different trench area fractions can be calculated and are shown in Figure 3.19 (b). The experimental data points give the velocities at which trenches could be site-selectively filled with close-packed sphere arrangements. For a low trench area fraction experimental data (red points) fit quite well to the calculated velocities (black line), for large trench area fractions however, no experimental data is available as trenches can not be filled with spheres due to wettability problems as explained in Figure 3.19. The error bars for the experimentally found velocities indicate a region of velocities in which site-selective trench filling is obtained.

At optimum conditions, concerning both the trench geometry and the parameters in the doctor blade experiment, a single line of contacting spheres on a length of 0.5 mm as shown in Figure 3.20 can be created.

Spheres were deposited into 2 μm deep trenches with a width of 2.5 μm and a distance of 100 μm to the neighboring trench at a velocity of 100 μm/s at room temperature and 55 % relative humidity with the triple phase contact line moved parallel to the trench direction. Only few defects in the sphere row occur, typically due to the size distribution of spheres within the suspension or trench irregularities caused by the photolithography and reactive ion etching.
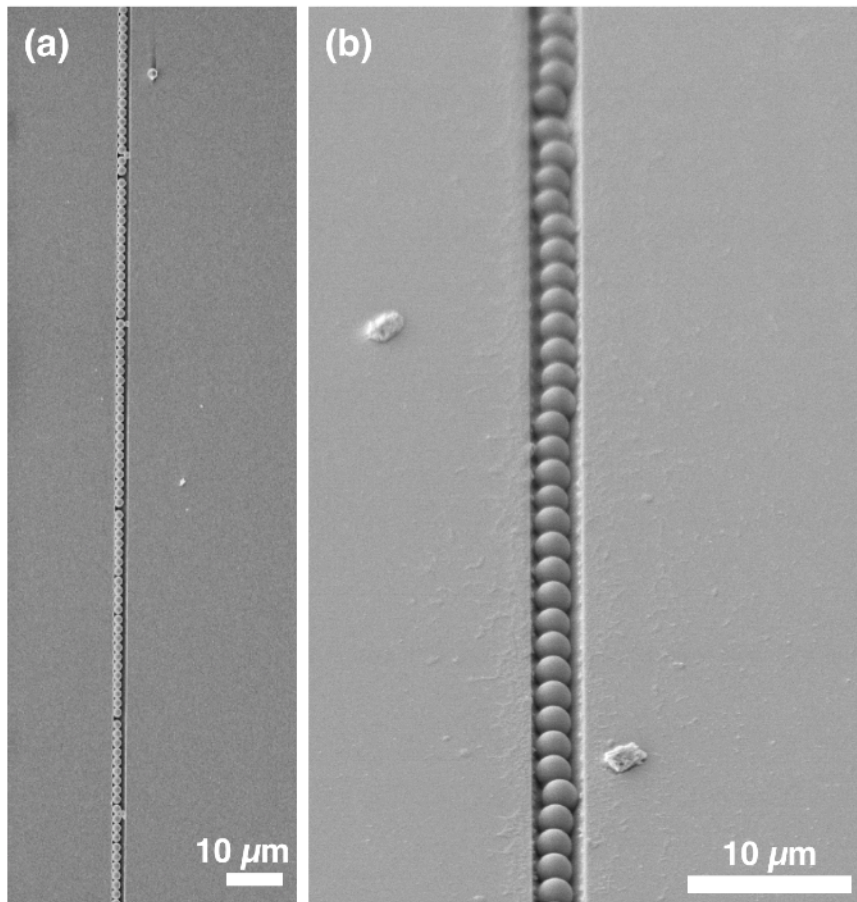
Fig. 3.20: SEM images of single line of contacting polymer spheres in a trench obtained at optimum conditions in (a) top-view and (b) tilted view.

Section summary

The directed self-assembly of colloidal nanospheres is exploited on pre-patterned surfaces. Topographic trench patterns are created on silicon surfaces by conventional photolithography and reactive ion etching.
A subsequent chemical surface functionalization with an OTS SAM allows for the site-selective deposition of nanospheres inside the trenches while sphere deposition on plane substrate areas is suppressed. Adjusting the trench geometry and parameters during the nanosphere deposition by the doctor blade technique, millimetre long single chains of polymer spheres inside trenches are created.

3.4 Nanogap electrodes

In this chapter it is shown how the directed self-assembly of colloidal polymer spheres allows for the effective and flexible creation of nanogap electrodes (NGEs), i.e. pairs of electrodes with a gap width in the nanometer range.

Such NGEs can be applied for the analysis and characterization of materials at the nanoscale [36, 37]. Single nanoparticles can be precisely positioned in between the NGEs. For such applications, the gap width between the NGEs needs to be adjustable to the nanoobject dimensions. They then can be used for e.g. single molecules trapping or DNA contacting [38-41].

For better applicability, the NGEs need to be integrated into e.g. microfluidic devices for lab-on-a-chip applications, where particles can be trapped by dielectrophoresis in inhomogeneous electric fields. For sufficient statistics it is desirable to investigate many nanoparticles in parallel.

The controlled fabrication of large numbers of electrodes with such small gaps in the range of (10 - 100) nm is demanding. Most conventional lithography techniques reach their limit in the sub-μm feature size regime. Thus, nanogap electrodes are most commonly created by direct writing techniques such as by electron beam lithography or with focused ion beams [42], by which small gap widths of a few nm can be achieved. However, only a small numbers of typically < 10 NGE pairs are written [37]. Others use different approaches such as electrowetting [43] or arrange carbon nanotubes which are subsequently cut [44]. There, the prediction of the gap width is a problem.

In this work, it is presented that by means of the directed self-assembly of nanospheres and nanosphere lithography (NSL), NGEs can be created inside microfluidic channels in large numbers of thousands of metallic tip pairs per centimetre channel length. The gap width between the electrodes can be tuned precisely by oblique metal deposition during the NSL preparation process and is predictable by ray-trace simulations. The NGE characterization is supplemented by finite element simulations of the electric fields.

3.4.1 Nanosphere lithography for the preparation of nanogap electrodes

The principle of nanosphere lithography [45, 46], where spheres acts as a shadow mask during a metal evaporation step, was explained earlier (Chap. 2.3.1) for 2D planar nanoparticle arrays. Here, a linear single chain of spheres is used as shadow mask in order to produce rows of opposing nanotips as depicted in Figure 3.21 (a).

Figure 3.21 (b) shows a SEM image of a close-packed chain of polymer spheres with a diameter of 2.1 μm in a trench with commensurate width prepared by capillary assembly as discussed in detail in the previous chapter. 50 nm Ti were deposited by PVD and the spheres were removed subsequently. By this, a row of opposing metallic nanotip pairs inside the trench as shown in Figure 3.21 (c) is obtained. These tip pairs leave a gap of (393 ± 12) nm (measured for 30 tip pairs) in between (see inset). As the macroscopic plane silicon surface next to the trench was free from spheres prior to metal deposition, the Ti film remains unpatterned and connects the individual tips on each side.
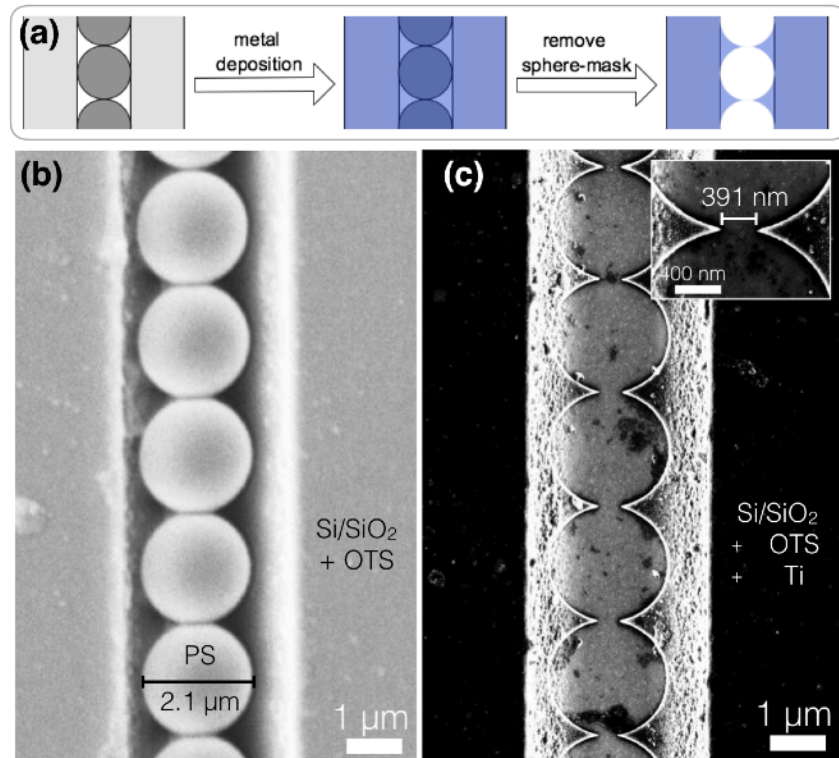
Fig. 3.21: (a) Sketch of the nanotip pair preparation by nanosphere lithography with polymer spheres in a trench. (b) SEM image of a close-packed single linear chain of polymer spheres in a trench. After Ti deposition and subsequent polymer sphere removal a row of opposing metallic tips is obtained as a shadow of the sphere mask. The gap between the tips is about 391 nm (inset).

The formation of the gap between the tips evolves from the fact, that the polymer spheres are not ideal hard spheres, but fuzzy spheres. The difference is shown in Figure 3.22 (a) from a top-view on spheres (grey). Hard spheres would only contact in one point. After NSL this would result in an infinitesimal small gap between the electrodes. The real polymer spheres however are fuzzy and can be drawn together by capillary forces. Thus, they deform and a contact area occurs. There is evidence from EFTEM imaging of assembled PS spheres that materials, most likely monomers and surfactants dissolved in the liquid phase of the colloidal suspension, condenses at the contact points of spheres upon self-assembly, contributing to the deformation of contact areas. Figure 3.22 (b) shows a SEM cross section view of a sphere monolayer after metal deposition. The sample was cleaved into 2 pieces, this image shows the edge where the sample pieces were separated. The capping with Titanium (yellow) makes the former contact areas (red circles) with neighboring spheres visible. In these areas, metal atoms were deposited first, starting to fill up the contact points with highest radius of curvature, leading to a mask clogging effect. The diameter of these contact areas between spheres of a diameter of 2.1 µm is 468 nm on average, thus 22 % of the sphere diameter. This is in good agreement with the obtained gap widths between the metal tips after NSL which is 391 nm. The gap width is expected to be a little smaller than the contact area, as the metal tips prepared by NSL are not the direct projection of the spheres: Diffusion of deposited metal atoms on the surface, slightly oblique deposition of metal atoms underneath the spheres and mask clogging occur during the metal deposition step leading to deviations of the gap width from the geometrically expected one. A similar effect is discussed and used for surface patterning by NSL with modified sphere masks in [47], where the contact area between PS spheres is even enlarged by thermal annealing.
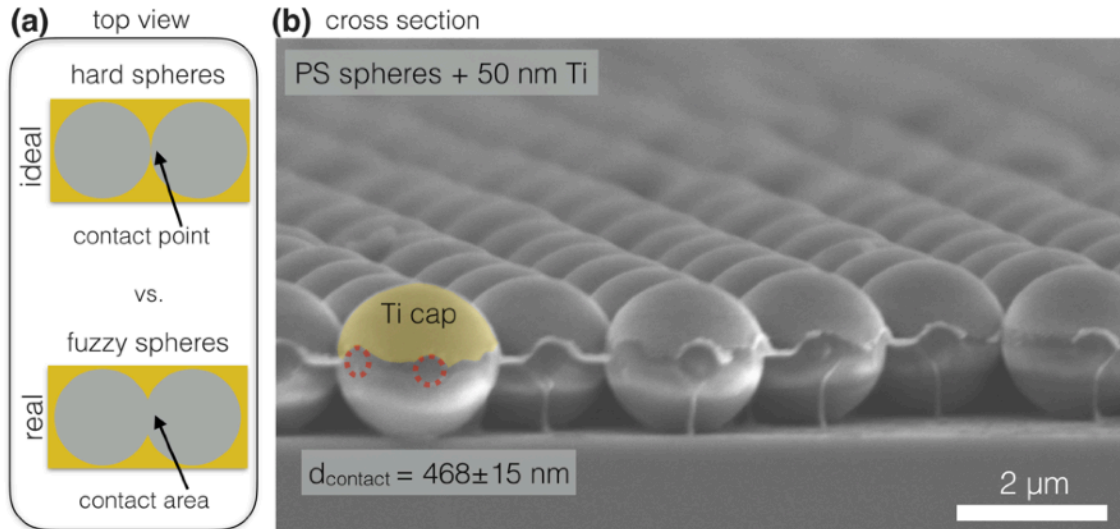
Fig. 3.22: (a) Sketch of contact points or areas between neighboring hard spheres or fuzzy spheres, respectively. (b) Cross sectional SEM image of PS sphere monolayer after Ti deposition (one Ti cap marked in yellow). At this sample edge, the contact areas towards formerly neighboring spheres are visible (red circles).

3.4.2 Oblique metal deposition for tunable nanogap electrode gap width

The width of the gap between the opposing metal nanotips can be changed by using polymer spheres with a different diameter. However, for this, the trench width needs to be adjusted and especially for very small sphere diameters the pre-patterning is more difficult.

Here, an easy approach to tune the gap width continuously at a constant sphere diameter is presented. The nanosphere lithography procedure is modified by applying oblique metal deposition onto the sphere mask [48-50].

To this end, the sample with a row of spheres deposited inside the trench is tilted towards the evaporation source during metal deposition as depicted in Figure 3.23 (a) using a home-built electron beam evaporation setup (App. A3). The sample can be tilted (with the trench as tilt axis) by a variable deposition angle α measured with respect to the surface normal. For a metal deposition angle $\alpha \neq 0°$ the position of the tip gap is shifted away from the trench center towards one of the trench walls. Performing this oblique metal deposition twice at the angles $+ \alpha$ and $- \alpha$ as marked in Figure 3.23 (b) two superimposed tip pairs which are both displaced from the trench center are produced. The result of such a 2-step metal deposition of 2x 20 nm Ti from $+12.8°$ and $-12.8°$ and subsequent sphere mask removal is shown in the SEM images in Figure 3.23 (c). The tip pairs produced in each single deposition step are highlighted in blue and pink, respectively. The final gap between opposing tips is formed between the inner tips. By variation of the deposition angles the gap width can be tuned, for this $\pm 12.8°$ deposition a final gap width of 29 nm can be created. It should be mentioned that the gap widths between the tip pairs produced within each single metal deposition step differ from each other. The mean gap width of tips from the first deposition step is, here with 418 nm, always smaller than the gap width between the tips created in the second step, here with 518 nm. This difference in the gap widths between the tip pairs results from mask clogging effects [51] during the metal depositions. Material is not only deposited through the mask openings onto the substrate, but also onto the spheres. This leads to a diminished size of the mask opening in the second evaporation step compared to the first step, an effect which is dealt with in the next section (Chap. 3.4.3).
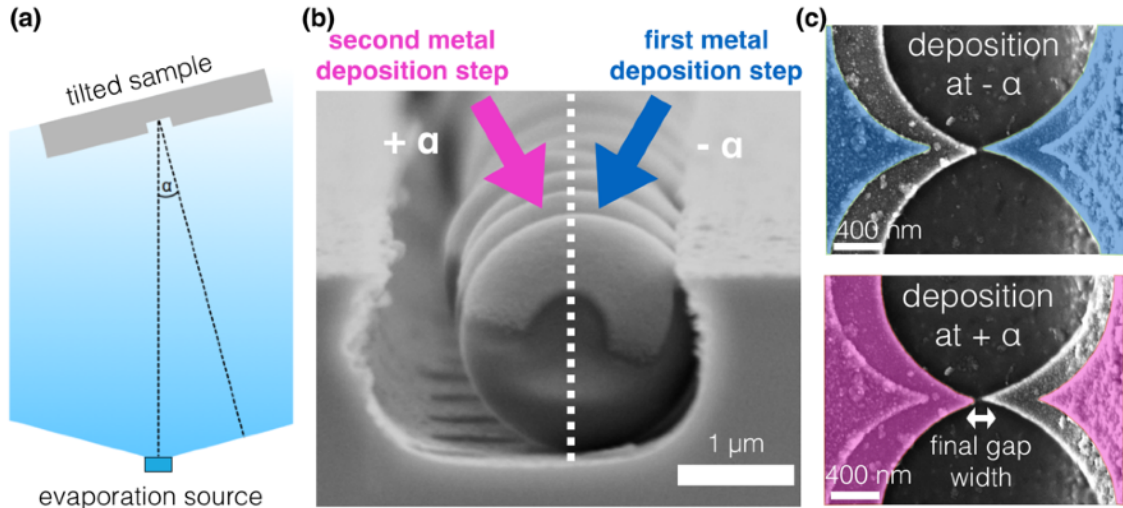
Fig. 3.23: (a) Sketch of the oblique metal deposition procedure. The sample is tilted by an angle α towards the evaporation source. (b) Cross-sectional SEM image of a linear chain of PS spheres inside a trench in a Si substrate. Two metal deposition steps from angles $\pm \alpha$ are indicated. (c) Resulting metal tips after NSL from two directions from $\pm 12.8°$ (first deposition highlighted in blue, second in pink). In the two subsequent metal deposition steps two tip pairs slightly dislocated from the trench center are created. The final gap width evolves between the inner tips, here 29 nm.

Figure 3.24 shows SEM images of tip pairs with different gap widths prepared by tilting the samples by different angles $\pm \alpha$ during the metal deposition. 50 nm titanium are deposited in each step at 0° (a), $\pm 6.4°$ (b), $\pm 12.8°$ (c) and $\pm 16.0°$ (d), respectively. Normal deposition at 0° results in a gap width of (393 $\pm$ 12) nm. By deposition at $\pm 6.4°$ and $\pm 12.8°$ as shown in Figure 3.24 (b) and (c) the gap width between the inner tip pairs can be set to (201 $\pm$ 7) nm and (29 $\pm$ 9) nm, respectively. However for larger angles such as $\pm 16.0°$ the gap vanishes, i.e. the inner tips overlap as shown in (d).
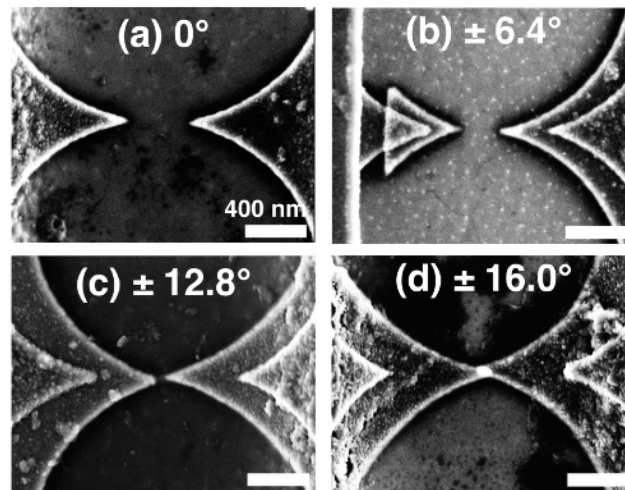
Fig. 3.24: SEM images of tip pairs with tunable gap width by (a) vertical metal deposition of 50 nm Ti; or oblique metal deposition of 50 nm Ti each at (b) $\pm 6.4°$, (c) $\pm 12.8°$ and (d) $\pm 16.0°$ during nanosphere lithography, respectively. The resulting gap width between the inner tip pairs decrease with increasing deposition angle.

3.4.3 Gap width prediction by ray trace simulations

To predict the gap width between the nanogap electrodes resulting from oblique metal deposition during nanosphere lithography (NSL) a ray trace simulation is performed. The ray trace simulation calculates the shadow projection of the polymer spheres onto the substrate [48, 49, 52]. This projection can be calculated for different angles between ray source and objects. The algorithm thus allows to estimate the required deposition angle to create a desired gap width prior to the experimental NGE preparation.

As two ideal hard spheres would only contact in a point resulting in an infinitesimally small gap width, the ray trace simulation of two ideal spheres shows this exact projection. As this is not compatible to the experiment, a metaball [53] with a radius r_{meta} slightly larger than the radius of the real polymer sphere is introduced (Fig. 3.25 (a)). Within this larger sphere an interaction potential is defined, which decreases with increasing distance from the sphere center and reaches zero at r_{meta}. If two of such metaballs are placed side by side their potentials will overlap (Fig. 3.25 (a), dotted lines). In the calculation this resembles a sphere necking as formed between two real fuzzy polymer spheres. This leads to a contact area instead of a contact point between the spheres and thus a broader gap width between the nanogap electrodes as existent in the experiment.

Applying now the ray trace simulation at different angles, the oblique metal deposition during NSL can be simulated. The results of such a simulation with an assumed meta ball radius of $r_{meta} = 1093$ nm $= 1.041$ x r_{real} is shown in Figure 3.25 (b) ($r_{real} = 1050$ nm). With the assumption of sphere necking the gap between the NGEs would disappear at a deposition angle of 11°. The experimental results, however, show an open gap of 29 nm at 12.8° deposition. The metaball radius is adjusted to match with the experimental results as calibration. Figure 3.25 (c) shows the calculated gap width for different metaball radii in dependence of the sample tilt angle α. The simulation results are compared with the experimental values for the gap widths at different metal deposition angles. The angle dependence of the gap width is nearly linear in the angle interval considered. The experiment however shows a dependence with a different slope than the simulation. This is due to the fact that the mask openings between the polymer spheres get smaller during the metal evaporation (mask clogging). Thus for high deposition angles and a large amount of deposited material, the forming gap between the NGE will get larger than predicted without taking into account dynamical mask clogging effects. Nevertheless, the ray trace simulation allows for a good estimation of the NGE gap width after metal deposition at different angles.
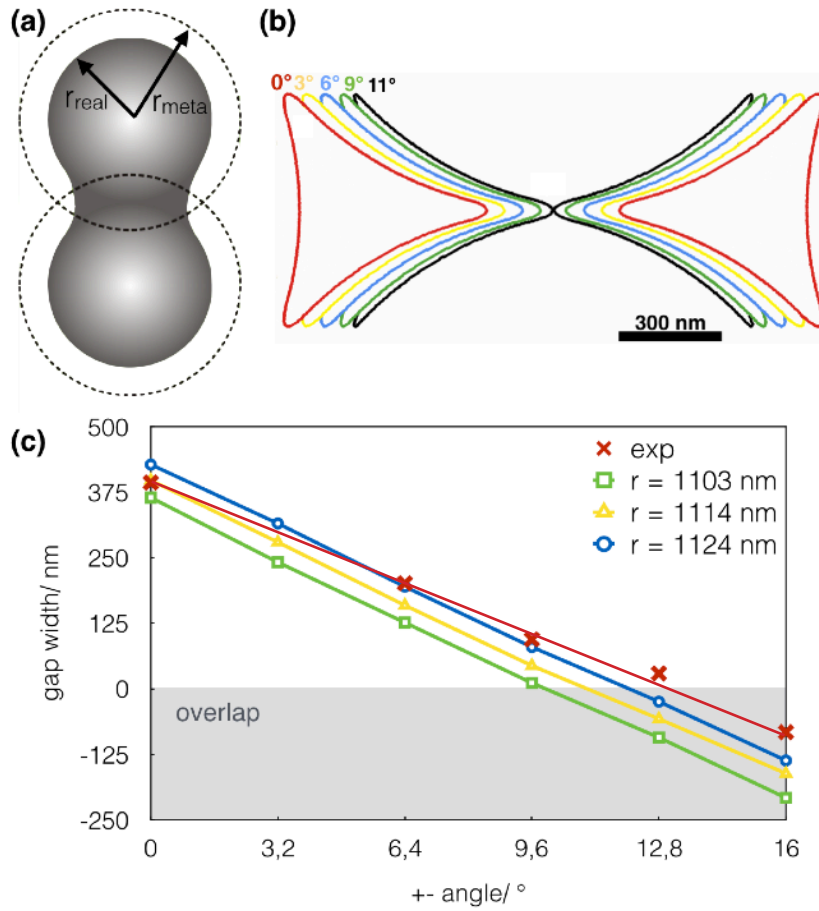
Fig. 3.25: (a) Sketch of sphere necking described by meta ball overlap. (b) Ray trace calculation of nanogap electrodes formed in a two-step deposition process at different deposition angles $\pm\alpha$ for a meta ball radius r_{meta} of 1.041 x real radius r_{real}. (c) Calculated gap widths for different meta ball radii in comparison with experimental data. (r_{real} = 1050 nm, r_{meta} = 1.051 (1103 nm), 1.061 (1114 nm), 1.071 (1124 nm))

3.4.4 Finite element simulations of electric field distributions between nanogap electrodes

The nanotip pairs with tunable gap width prepared by nanosphere lithography could be used as nanogap electrodes. The sharp metallic nanotips are expected to be suitable for their use as electrodes to create locally high electric fields, as it is well known that electrically addressing such sharp metallic tips results in a strong field enhancement [54-56].

Finite element (FE) simulations are performed in order to estimate the field enhancement at metal nanotips with geometries as created in the experiments presented above. COMSOL Multiphysics [57] is used for these simulations. The assumed tip geometry is shown in Figure 3.26. Two spheres are positioned contacting each other in one point. The area not covered by these spheres (blue) forms the tip shape. The zoom-in shows the detailed tip shape in the center with the radius of curvature r and the gap width d between the NGEs. All simulations are performed in 2D, tip material is titanium and the surrounding is SiO_2 as is the substrate surface of the trenches. The reduction to two dimensions is justified by the fact that the trench bottom of 2 μm wide trenches is almost flat over the distance of NGE gaps. For the simulation of a patterned trench of infinite length with a row of tip pairs, periodic boundary conditions are used. The black lines in Figure 3.26 show the adaptive free simulation mesh.
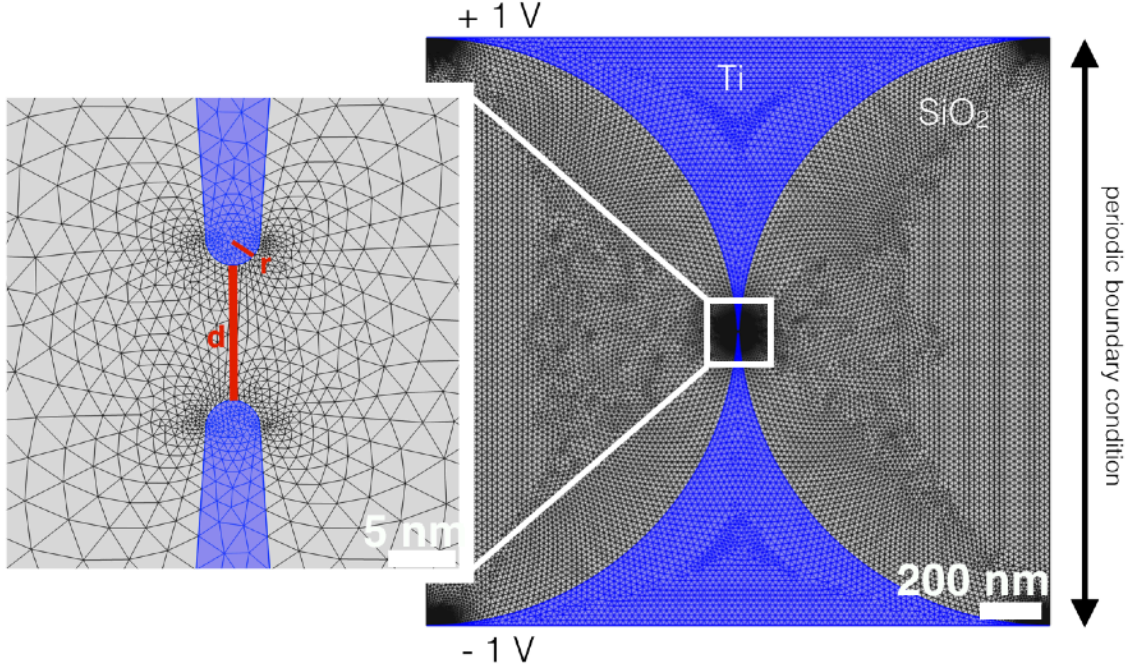
Fig. 3.26: Right: The tips geometry (blue shaded areas) evolves from two contacting spheres. Black lines: adaptive FEM mesh. Left: Zoom-in. r is the tip radius, d the distance between the tips.

In the following, the electric field distribution between the tips in dependence of the tip geometry, i.e. the tip radius r and their distance d, are investigated.

As the field strength is proportional to the applied voltage, a field enhancement factor FE (Eqn. 3.2) is introduced, giving the electric field relative to the field of an infinite parallel plate capacitor E_{cap} with plate distance of 2 μm, corresponding to the trench width.

$$FE = \frac{|E|}{E_{cap}} \tag{3.2}$$

Figure 3.27 shows the result of the FEM calculations of the electric field distribution between the NGEs. The surface plot in the center shows an image section with the two tips in dark blue (|E| = 0 V/m). The graphs show the electric field at line cuts through the structure at x = 0 and y = 0 for y-cut and x-cut, respectively. In this simulation, the tips have a radius of 10 nm and a distance of 400 nm, which are typical values for the tip pairs prepared in the experiments. The electric field is highest at the very tips reaching a maximum value of 1.9×10^7 V/m (for an applied voltage of 2 V), decreasing with increasing distance to the tips. The lowest field strength is with 0.13×10^7 V/m half way between the tips. The latter value is in good agreement with the field evolving in a parallel plate capacitor with a width of 2 μm, which is the trench width assumed in the calculations. The field enhancement at these tips of FE = 19 is quite low.

The tip radius (2 nm, 10 nm, 25 nm) and the tip distance (10 nm, 50 nm, 100 nm) are systematically varied in oder to evaluate the effect of the tip geometries on the maximum electric field for further field enhancement. The results of these geometry combinations are shown in Figure 3.28. These feature sizes are chosen according to the experimentally obtained nanotip pairs by NSL with oblique metal deposition as shown in the previous chapter.
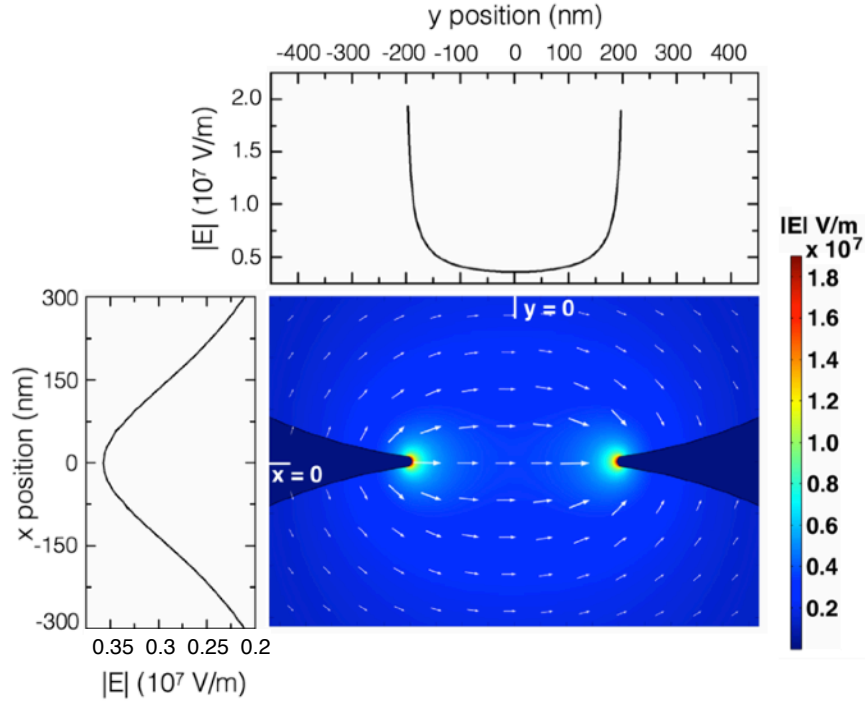
Fig. 3.27: Calculated field distribution |E| for the NGE geometry (tips: dark blue) displayed as a colour plot. 10 nm tip radius and 400 nm tip distance. Graphs show line cuts of the distribution of |E| in y-direction (graph on top, line cut at x = 0) and x-direction (left, cut at y = 0). White arrows represent the electric field lines.

Simulations show that a reduction of the tip radius and decrease of tip distance lead to the maximization of the field strength. The combination of the smallest tip radius and the smallest distance (Fig. 3.28 upper left) results in the highest fields with a maximum field enhancement of FE = 338 (3.4×10^8 V/m). In contrast, the largest tip radius with broadest distance (Fig. 3.28 lower right) only exhibits a field enhancement of FE = 31.

Plotting the line cuts (as described for Fig. 3.27) as different visualization of these field distributions, it becomes clear, that a tip distance variation has a stronger influence on the electric field than a change in tip radius has. Figure 3.29 shows the field distribution along the y-cut (a) and x-cut (b) for all geometries shown in Figure 3.28. In both plots, the different tip distances define a regime of field strengths that can be reached, while a change in tip radii influence the fields distribution locally in closest proximity to the tips. The line cut in y-direction in (a) shows highest fields directly at the tips, decaying when moving away from the tip and then increasing again when approaching the opposite tip. The maximum field strength is smaller for larger distances and the field is more homogeneous between the tips. A change of tip radius affects the field distribution close to the tips. For small gap width the effect becomes significant, e.g. for radius of 2 nm (black line at d=10 nm) allowing for highest fields at the tip and drastic decay towards the area in between the tips, while this decay is less distinct for tip radii of 10 nm or 25 nm (red and green lines at d=10 nm).
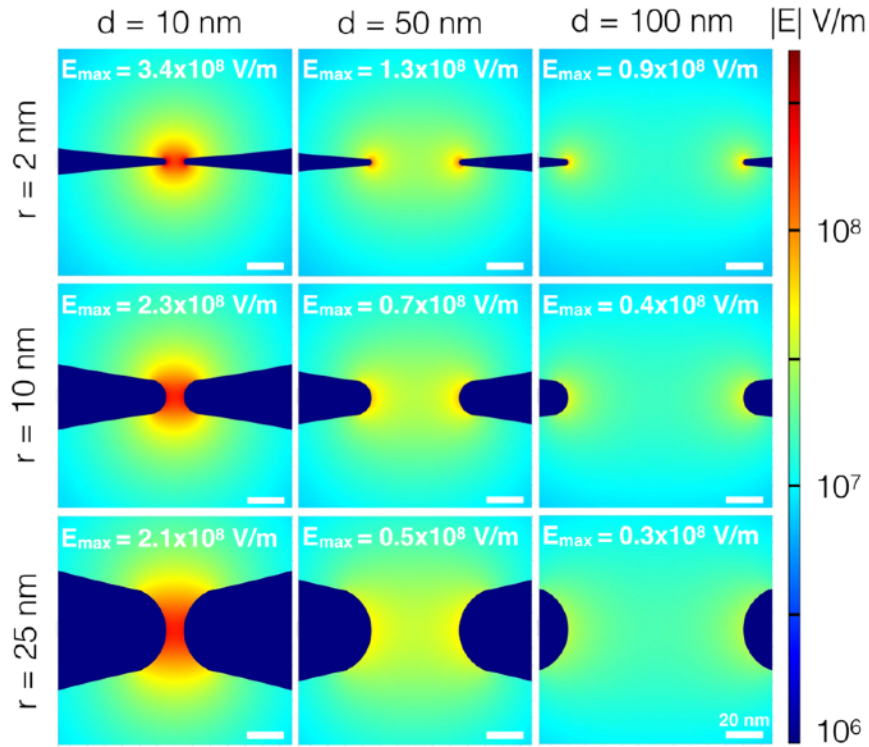
Fig. 3.28: Investigation of NGE geometry on the electric field distribution at an applied voltage of 2 V. Color plots of |E| for tip radii varying between r = 2, 10 and 25 nm (increasing from top to bottom) and tip distances between d = 10, 50 and 100 nm (increasing from left to right). Scale bar is 20 nm for all images.

The x-cut (b) shows the field distribution through the center of the gap between the tips along the trench long axis. The fields are strongest between the tips decaying towards the areas of largest distance to the tips. Here the field strength approaches a field enhancement of 1, i.e. it matches the field in a capacitor.

Again, comparison of the effects of tip radius and tip distance show a larger impact of the NGE gap width on the maximum fields in the middle of the gap. A decrease of the radius from 25 nm to 2 nm (at a constant distance of 10 nm) leads to an max. electric field increase of 20%, while a decrease of the tip distance from 100 nm to 10 nm (@ 2 nm radius) increases the max. field by 60 %.
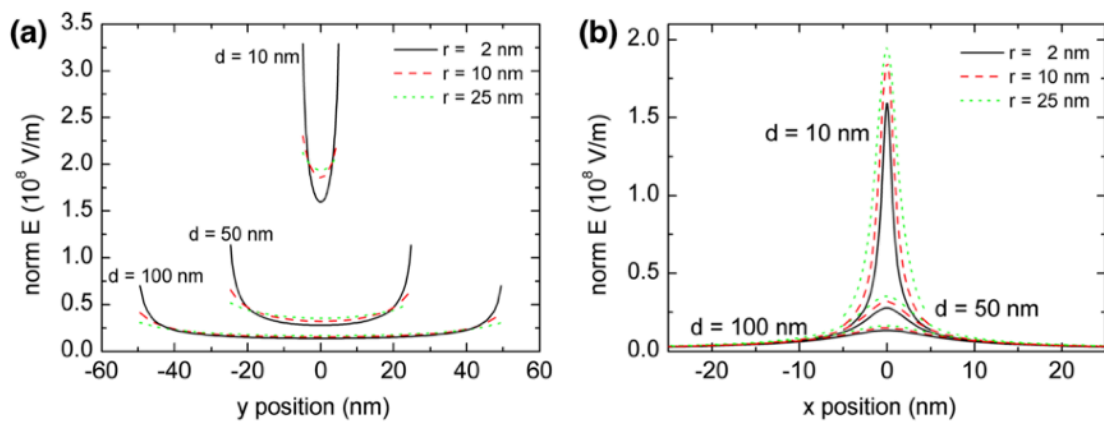
Fig. 3.29: Electric field distribution along line cuts in y-direction (a) and x-direction (b) in Fig. 3.28 for different tip radii and tip distances. Solid black lines are related to a tip radius of 2 nm, dashed red lines to r = 10 nm and dotted green lines to r = 25 nm. The different tip distances d are marked at the corresponding curve groups.

Calculation for experimentally obtained NGEs. The simulation of electric field distributions in dependence of the tip geometry allows for the valuation of the suitability of the experimentally obtained nanotip pairs as nanogap electrodes. Figure 3.30 shows a plot of the obtained tip distances, i.e. nanogap electrodes gap widths, for different deposition angles in the nanosphere lithography preparation procedure (red circles and linear fit). The corresponding expected max. field strength, in this plot the gradient of the squared field strength giving the field gradients, for these gap width (at a constant tip radius of 10 nm) were simulated (blue squares). By changing the deposition angle in NSL from 0° to 12.8°, thus decreasing the gap width from 400 nm to 30 nm, the electric field can be enhanced by 260 %.
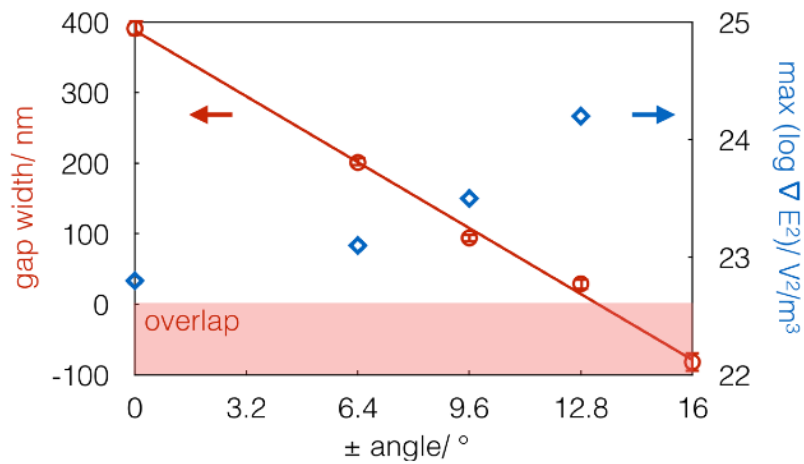
Fig. 3.30: Red circles: Gap width plotted over deposition angle. Error bars show the distribution for 20 tip pairs, solid red line: linear fit. Shaded red area indicates tip overlap. Blue squares: Corresponding calculated maximal field gradients ∇E^2 for tip pairs with different gap width. Assumed tip radius is 10 nm.

Section summary

The nanosphere chains inside the trenches are used as shadow masks for nanosphere lithography. By this, rows of opposing metallic nanotip pairs are created, which can be used as nanogap electrodes.

By oblique, instead of vertical, material deposition during nanosphere lithography, the gap width between the opposing nanotips can be tuned between 400 nm and 29 nm. The gap width can be predicted by ray-trace simulations.

Finite element simulations are performed to investigate the electric field distribution between the sharp nanotips. The influence of the tip diameter and the gap width between the tips on the field distribution is determined, predicting, that the electric field can be enhanced by 260% between the created nanogap electrodes with 29 nm gap width.

3.5 Particle trapping by dielectrophoresis using NGEs

Dielectrophoresis (DEP) [58] is a well-known technique applied in lab-on-a-chip devices for cell isolation, molecular analysis and sensing [59-61].

Basically, in a DEP-cell small electrodes are positioned inside a microfluidic device creating electric field strength variations throughout the flow-direction of a liquid medium through a channel, e.g. on micro total analysis systems [62-64]. Particles to be analyzed are suspended in a liquid and travel along the channel with the electric field inhomogeneities (Fig. 3.31). Passing by the electrodes, dipoles are induced in the particles, which then interact with the fields. Due to different permittivities of the particles and their surrounding liquid medium, the interactions of these two materials with the field differ and thus particle movement can be guided towards areas of either highest or lowest electric field gradients. This is referred to as positive or negative DEP, respectively.
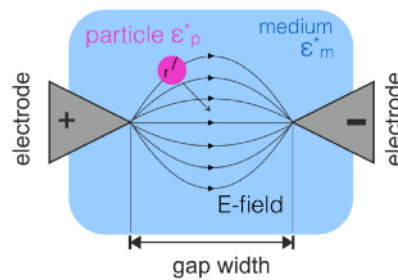
Fig. 3.31: Sketch of principle of dielectrophoresis.

Thus, particles can be trapped and further investigated, separated from unequal particle species, counted or collected. In lab-on-a-chip devices, living cells can e.g. be distinguished from dead cells [65, 66].

The main advantages of the particle trapping by DEP are its applicability to different kinds of uncharged particles (many other techniques rely on electrical interactions only apparent with charged particles), it is non-destructive (important in biological experiments allowing for the investigation of living cells), and low particle concentrations are sufficient, which is in particular important for sensing [59].

Besides, the experiment is scalable: As biological cells have typical sizes of few ten to few hundred micrometers, the electrodes on lab-on-chip devices for the creation of the inhomogeneous fields are designed accordingly with gap widths of few hundred μm [65].

For the trapping and investigation of smaller particles, however, smaller electrodes with gap widths in the nanometer range are necessary. This is interesting for the exact positioning of nanoobjects for future-devices in nanotechnology and molecular electronics [67]. Particles such as nanowires with small diameters but larger length e.g. could be positioned, oriented and contacted between electrodes with a gap width of few hundred nm in between. Nanoparticles such as quantum dots or single macromolecules, such as proteins, typically are only few nm in diameter, thus for trapping of such single particles, the gap width needs to be commensurate with the size of particles to be trapped.

It was shown in the previous chapter that NGEs with tunable gap width can be created by directed self-assembly of nanospheres and nanosphere lithography. In the following first preliminary considerations and results of using these NGE in DEP experiments are shown.

3.5.1 Basics of dielectrophoresis

The dielectric force F_{DEP}, which acts on particles in an inhomogeneous electric field, is given by Equation (3.3) [60]:

$$F_{dep} = 2\pi \cdot r^2 \cdot \varepsilon_m \cdot Re\{\kappa\} \cdot \nabla|E^2| \qquad (3.3)$$

with the radius r of (spherical) particles, $\varepsilon_{m,p}(\omega)$ the complex permittivity of the medium or particle, respectively, E the external electric field and $K(\varepsilon_m, \varepsilon_p)$ the Clausius-Mosotti factor. This factor describes the dependency of the DEP-force on the frequency ω. Its real part $Re\{K\}$ is defined by

$$Re\{\kappa\} = (\varepsilon_p - \varepsilon_m)(\varepsilon_p + 2\varepsilon_m) + \frac{\omega^{-2}(\sigma_p - \sigma_m)(\sigma_p + 2\sigma_m)}{(\varepsilon_p + 2\varepsilon_m)^2 + \omega^{-2}(\sigma_p + 2\sigma_m)^2} \qquad (3.4)$$

with $\varepsilon_{p,m}$ as the real part of the permittivity and $\sigma_{p,m}$ the conductivities of particle and medium. The relation between ε_p and ε_m determines the sign of the DEP force, which becomes negative if the Clausius-Mosotti factor is negative (negative DEP). In this case particles move into regions of lowest field gradients. In positive DEP, particles are drawn towards highest field gradients, if the Clausius-Mosotti factor is positive.

As the conductivities of particle and medium $\sigma_{p,m}$ depend on the frequency, the sign of the Clausius-Mosotti factor can be changed by applying different frequencies and it is possible to switch between positive and negative DEP.

Typically, when working with metal or semiconductor particles in aqueous media, the permittivity and conductivity of particles is larger than that of the solvent and positive DEP is predominant for large frequency regimes.

The dielectrophoretic force is not the only force acting on the particles. Besides convective flows e.g. due to evaporation of the solvent or capillary forces, the probably most problematic counteracting force is due to thermal fluctuations. This force $F_{thermal}$ can be estimated by Equation (3.5) [60]:

$$F_{thermal} = \frac{k_B T}{2r} \qquad (3.5)$$

with r being the particle radius. Figure 3.32 shows the dielectrophoretic force F_{DEP} for SiO_2 particles with a diameter of 50 nm suspended in ethanol for different applied field gradients ∇E^2 (a) and the characteristics of the Clausius-Mosotti factor K in a frequency regime (b). This is a system used later for first experiments. The permittivity of SiO_2 is $\varepsilon_p = 3.9\varepsilon_0$, and of EtOH $\varepsilon_m = 24.5\varepsilon_0$ [68]. Conductivities are for SiO_2 $\sigma_p = 3.5\times10^{-5}$ S/m and for EtOH $\sigma_m = 2.5\times10^{-5}$ S/m [69].

In this example the dielectrophoretic force is expected to overcome the thermal fluctuations for field gradients $\nabla E^2 > 10^{20}$ V^2/m^3 (for $\omega = 10^6$ Hz). However other forces acting on the particles are neglected here.

Figure 3.32 (b) shows that for the particle/ solvent system SiO_2/ ethanol the Clausius-Mosotti factor is positive for $< 10^7$ Hz, showing a drop at this frequency to close to zero. A negative sign is reached only at frequencies $> 10^{16}$ Hz. Positive DEP, i.e. particles being always drawn into regions of highest field gradients, is thus expected over a large frequency regime with stronger forces $< 10^7$ Hz.
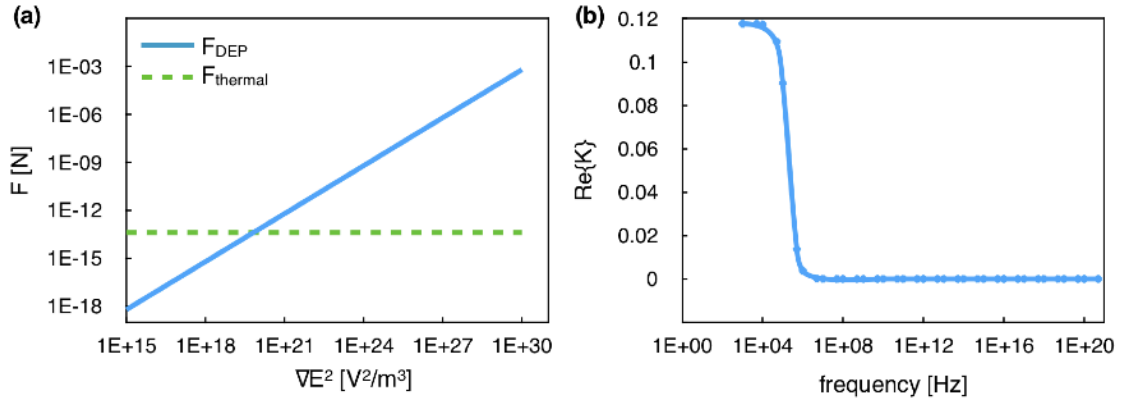
Fig. 3.32: Calculated characteristics of spherical SiO_2 nanoparticles with radius of 50 nm in ethanol at room temperature in a dielectrophoretic experiment. (a) Dielectrophoretic force F_{DEP} (blue solid line) and force on particles due to thermal fluctuations $F_{thermal}$ (green dashed line) as a function of field gradients ∇E^2. Dielectrophoretic force overcomes thermal fluctuations at field gradients larger than $\nabla E^2 = 10^{20}$ V^2/m^3 (for $\omega = 10^6$ Hz). (b) Frequency-dependence of the real part of the Clausius-Mosotti factor Re{K}.

3.5.2 Dielectrophoretic experiments

Field gradients between nanogap electrodes formed by nanosphere lithography

Figure 3.33 and 3.34 give an overview of the distribution of electric field gradients at different positions of the experimentally prepared NGE. Figure 3.33 shows the distribution in x-y direction. A FEM contour plot (for 2 V and tip radius r = 10 nm) is overlayed to an SEM image of the NGE structure. The minimal dielectrophoretic force needed for SiO_2 @ EtOH particle trapping overcoming the thermal fluctuations, as stated above, is at $\nabla E^2 = 10^{20}$ V^2/m^3. Higher field gradients are obtained close to and in between opposing tips (orange + red).
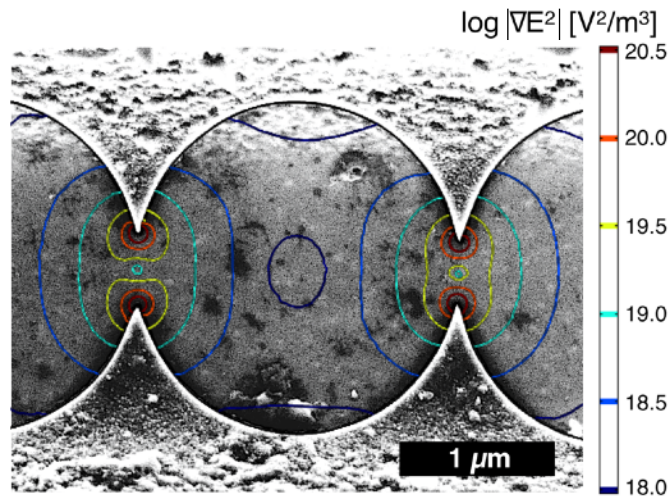
Fig. 3.33: Simulated iso-field gradient lines in x-y view as an overlay to a SEM image of experimentally obtained nanogap electrodes with a gap width of approx. 400 nm. Assumed tip radius is 10 nm. The field gradients are oriented perpendicular to the lines and point to the tips of NGEs on both sides

78

Figure 3.34 (a) shows color plots of FEM calculations indicating additionally the field gradient distribution in z-direction. The corresponding values, including different applied voltages, are plotted in Figure 3.34 (b) in dependence of the z-position, i.e. measured height from the trench bottom.

The volume in which the fields are strong enough for particle trapping depends on the strength of the applied field. Field gradients $> 10^{20}$ V^2/m^3 are reached in heights of 500 nm, measured from the trench bottom, at 2 V up to 1.3 µm at 10 V. Thus, the available trapping volume within the trench can be estimated.
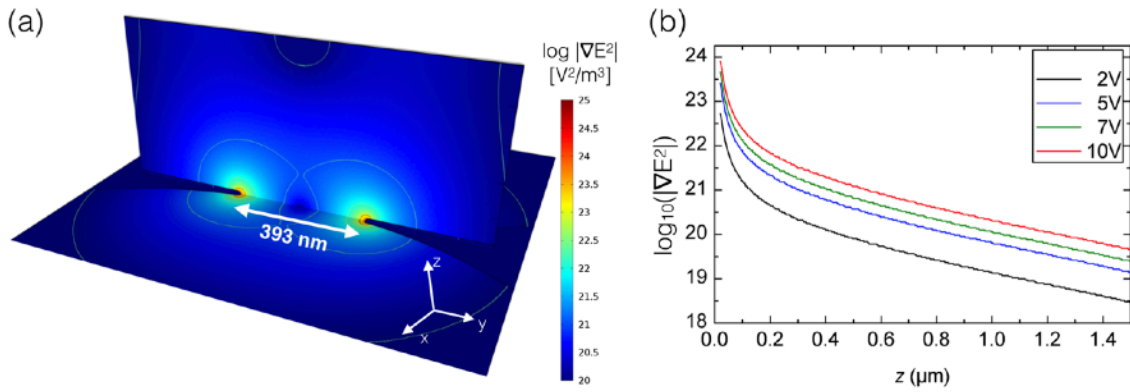
Fig. 3.34: (a) FEM color plot of field gradient in x-y-z direction. (b) Simulated decay of field gradient $\nabla|E|^2$ with increasing height from electrodes at bottom of the trench (z-position) at the tip (y = 0, x = 196.5 nm) for different applied voltages.

Dielectrophoretic experiments

Device. For the preparation of the DEP-test-cell, the NGE need to be addressable by macroscopic contacts. To this end, contact pads are created by using an additional shadow mask during the metal evaporation step in NSL. The additional shadow mask leaves a slit between the reservoirs open for metal deposition onto the trench with spheres and some plane sample surface around. This allows for the creation of separated contact pads and the nanogap electrodes within one preparation step. 2 nm Ti as adhesion layer and 30 nm thick layers of Au were evaporated as chemically inert contacts. After removal of both masks, PS spheres and macroscopic shadow mask, the nanogap electrodes are now addressable.
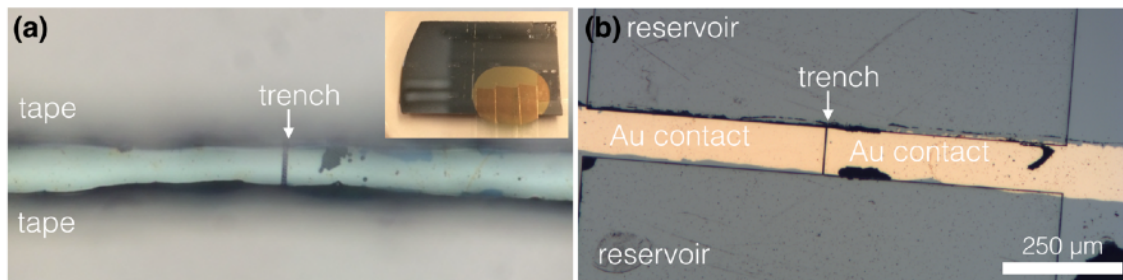
Fig. 3.35: Optical microscope images of the DEP-test structure. (a) Reservoirs covered with adhesive tape acting as macroscopic shadow mask for preparation of separated contacts. Inset: Photograph with lower magnification: sample with 4 tapes for preparation of 2 DEP test cells. Sample size is approx. 2x1.5 cm². Yellow spot: evaporated gold. (b) Sample after Au deposition and shadow mask removal. Trench with nanogap electrodes inside ends in 2 reservoirs. The NGEs can be addressed by macroscopic Au contacts.

As additional shadow mask for contact creation small (approx. 3 mm broad) strips of adhesive tape are used, which can be positioned precisely with a x-y-z micrometer stage while inspected with an optical microscope. The positioned tape on the sample with the freely accessible trench is shown in the optical microscope image in Figure 3.35 (a). The inset shows a photograph of the whole sample (approx 2x1.5 cm²) with two masked structures, thus four tape stripes. Figure 3.35 (b) shows an optical microscope image of the resulting macroscopic Au contact pads, appearing as a yellow stripe, after metal deposition and removal of the masks.

Particles. As test particles for the trapping by dielectrophoresis fluorescent FITC-SiO$_2$ core-shell particles in ethanol are synthesised in a two-step sol-gel Stöber process. In a first step, the fluorescent cores are prepared by stirring 20 mg fluorescein isothiocyanate (FITC) and 43 mg 3-aminopropyltriethoxysilane (APTES) in 5 ml ethanol over night at room temperature. To add a silica shell, these cores are used within a standard Stöber process [70]. 7.7 ml ammonium, 7.7 ml tetraethoxysilane, 4.6 ml water and the cores are stirred for 6 h at room temperature in 140 g EtOH. FITC-SiO$_2$ particles with diameters between 100-160 nm are obtained. Figure 3.36 shows an SEM image of the synthesized nanoparticles. The excitation wavelength of the fluorescein is 495 nm, the maximum of the emission at 519 nm [71]. The initial concentration of particles in EtOH after synthesis is not known. For DEP, the inital concentration and diluted solution with 20 % and 0.1 % of the initial one are prepared. The suspension at initial concentration is very oblique, for 0.1% concentration no scattering from particles is visible at all with naked eye.
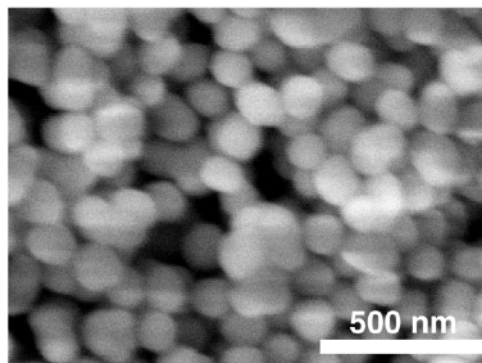
Fig. 3.36: SEM image of FITC-SiO$_2$ core-shell nanoparticles synthesized in a two-step sol-gel Stöber process.

Setup. Figure 3.37 (a) shows the setup for the DEP experiments. A voltage is applied to the NGEs by a Keithley source measure unit. The NGE are contacted via their macroscopic Au contact pads on which Au needles are positioned as in Figure 3.37 (b). Positions are controlled with an optical microscope with large working distance. Prior to the DEP experiment electrical characteristics of the structures are measured and the DEP cell is conditioned (Fig 3.38). During the NGE preparation, polymer spheres in the trench occasionally do not arrange themselves in a close-packed line, contacting each other, but can leave a gap to the neighboring sphere, for example due to variations in sphere diameters. This results in a defect in the nanogap electrode formation in form of a metal bridge that will lead to a short-circuit when applying a voltage. In order to avoid such a short-circuit during the DEP experiment, a voltage is applied to the device without adding the FITC-SiO$_2$ particle suspension. The current-voltage characteristics are recorded. At the beginning a low resistance of about 135 Ω is typically measured. With increasing applied voltage the current increases linearly, showing the expected behavior of an ohmic resistance. The current drastically drops at a certain break-down voltage. In this moment the metal bridges allowing for the short-circuit current to flow break, probably due to dewetting of the metal as a result of heating. The resistance after this break-down is > 20 MΩ. To check whether the contacts are now separated I-U characteristics are recorded again, showing that with an increase of the applied voltage, no current is measurable (< 1 nA).
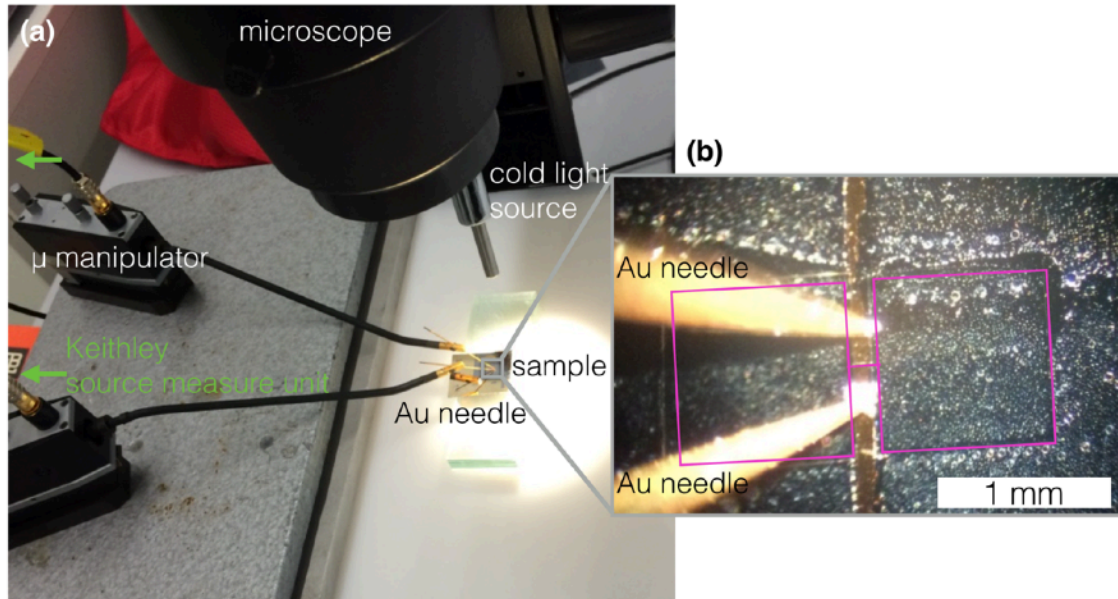
Fig. 3.37: (a) Photograph of the DEP-test structure. Sample is contacted with Au needles. The position of the needles is adjusted by micro-manipulators and checked with an optical microscope with large working distance, shown in (b) Position of DEP test structure is marked in pink. Current-voltage characteristics are recorded with a Keithley source measure unit, that is connected through the micro-manipulators.
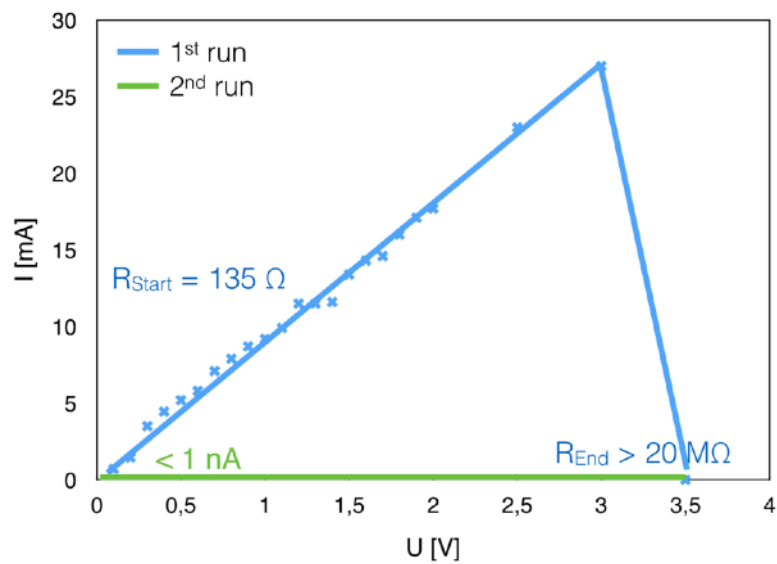
Fig. 3.38: Electrical DEP cell conditioning: current-voltage characteristics of a DEP test structure with nanogap electrodes recorded with a ‚Keithley source measure unit'. Initially, a low resistance of 135 Ω is measured due to defects in the NGE arrangement. At a certain voltage these defects break and the current drops. Resistance then is > 20 MΩ. A second run assures contact separation.

Trapping experiments. Experiments for the trapping of the FITC-SiO$_2$ particles between the nanogap electrodes were performed with the setup described above. A 2 µl droplet of the suspension was added into one reservoir (Fig. 3.39 (a), right reservoir). Due to capillary forces the suspension is drawn into the trench with the electrodes. A small amount of arriving suspension is visible in the reservoir on the opposite site (appearing dark in the left reservoir). Due to good wettability of the Au contact pads, the suspension also wets those. Thus after the experiment and complete drying particle agglomerates are visible as dark spots in the initially filled reservoir as well as on the contact pads. 2 V were applied at 1 - 10 kHz during the DEP experiment[1] for different times (i) between 5 s and up to 20 min (until all liquid suspension medium evaporated) and with different particle concentrations (ii).
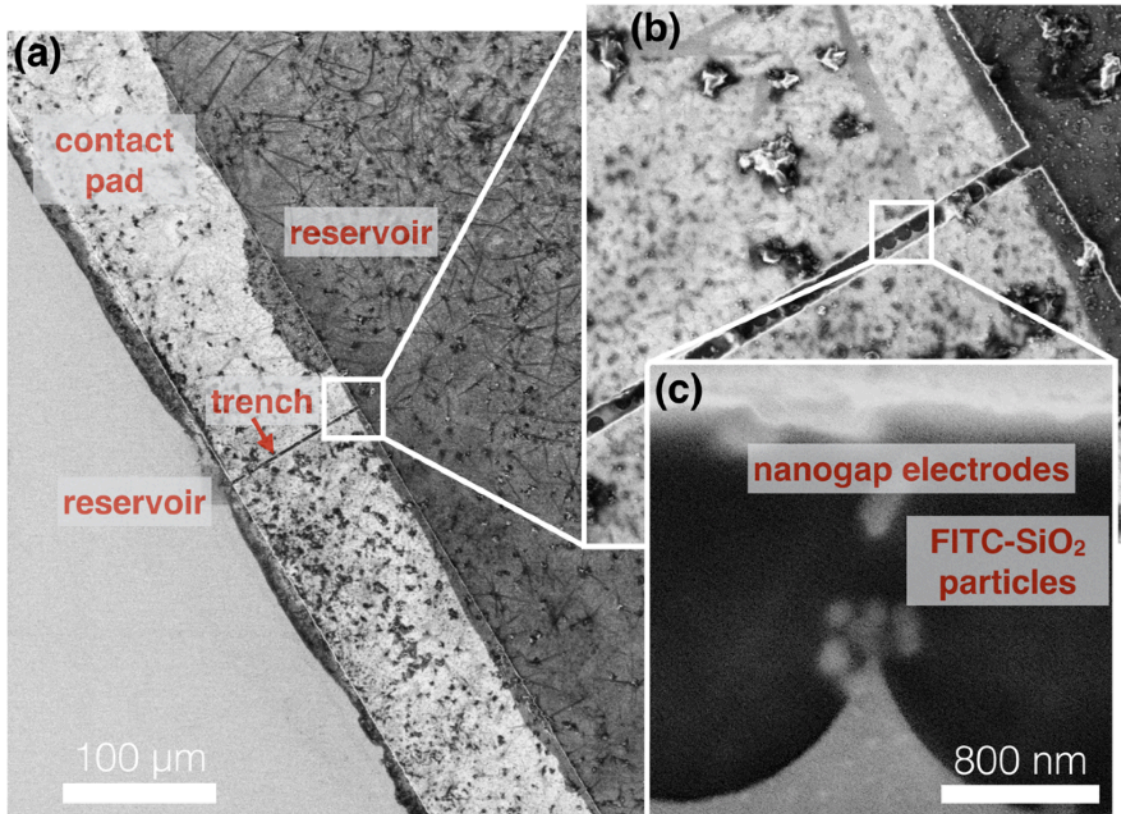
Fig. 3.39: SEM images of the result of a DEP trapping experiment of SiO$_2$ nanoparticles at different magnifications.

(i) In case of short voltage application (5-10 s) no site-selective particle deposition was observed. The results of the particle guiding probably get lost after turning the voltage off due to evaporation fluxes and thermal fluctuations. In case of voltage application until complete drying of the sample (20 min), particle deposition could be observed in between the NGEs but also in the areas around them. The dielectrophoretic field is probably not strong enough to trap all particles, thus untrapped particles just sedimented during drying at undefined positions. For a better selectivity, the particle concentration was varied. (ii) High particle concentrations led to the formation of large agglomerates, which precipitated onto the trench or the contact areas. Single particles were likely to be found everywhere. Lower particle concentrations were expected to result in less agglomeration and sedimentation. However, in experiments with concentrations of 0.1 % of the initial suspension resulted in almost no particle trapping. Trenches were nearly particle free, only few agglomerates

---

[1] The voltage was applied either before or after suspension deposition. Both procedures show similar results.

remained on the gold surfaces. For a medium concentration (20% of initial concentration), as used in the experiment shown in Figure 3.39, agglomeration was minimized and few particles could be trapped at the nanogap electrodes tips (Fig. 3.39 (c)). However, many particles are still found on the contact pads, some agglomerates were deposited onto the trench (e.g. visible in Fig. 3.39 (b)), while many nanogap electrodes were empty.

Improvements. A major problem is the excellent wettability of the gold contacts by the aqueous or EtOH suspensions of the particles. This leads to a favored wetting of the macroscopic contact pads (visible as grainy sample coverage in Fig. 3.39) avoiding a controlled flux through the channel. To add the test suspension to the cell in a more controlled way the channel could be covered with a PDMS sheet. This PDMS sheet could be bonded to the DEP-test-cell, if both surfaces are treated with an oxygen plasma (e.g. 10.5 W, 0.2 mbar, 1 min) and bonded together immediately after. Preliminary results show that the plasma treatment does not have any visible influence on the nanogap electrodes structure.

Besides, it is not possible to control directly whether the single NGEs are really contacted to the contact pads. A proper connection to the contact pads can be disturbed e.g. by trench profiles showing too sharp edges. This can happen if underetching occurs during the pattern transfer with RIE after photolithography as exemplarily observed (Fig. 3.23). At sharp edges, the Au film connecting the NGE and the macro contact pads could be very thin and thus more likely to dewet. Besides, a strong underetching could lead to a shadowing of the trenches themselves such than trench side walls are not covered with metal during the evaporation process.

A flux of liquid through the channel due to capillary forces, and probably more problematic, fluxes in the liquid due to evaporation of the liquid medium could also occur and disturb the particle trapping. As the trenches are small and contact pads next to the trench are wetted due to electrode materials characteristics, the liquid film thickness is low and surface is large, thus a high evaporation flux can be expected. This effect would also be better controllable by covering the whole cell with a PDMS lid.

The application of an external field of 2 V produces fields strong enough to overcome thermal fluctuations only up to a height in the channel of approx. 500 nm, which is only 20% of the trench height. Thus particles travelling through the channel at larger distance to the electrodes are not affected by the electric field. Applying a voltage of 7 V should result in fields strong enough for particle trapping up to 50% of trench height (1 µm). However, if applying this voltage, the Au film forming the NGE and their contact pads seems to dewet due to heating. Thicker gold films and lower trench side-wall slopes could resolve this problem.

Section summary

Dielectrophoresis is a method for the trapping of uncharged particles in inhomogeneous electric fields. Matching the size of electrodes with the size of target-particles allows for the trapping of single particles. The nanogap electrodes created by nanosphere lithography are shown to be suitable for trapping of single nanoobjects as the electrode gap width can be tailored. Preliminary results of dielectrophoretic trapping of FITC-SiO$_2$ core-shell nanospheres are presented.

3.6 Conclusions

Directed self-assembly of colloidal polymer spheres allows for the creation of advanced colloid arrangements other than close-packed 2D monolayers as shown in the previous chapter. Topographic and chemical surface pre-patterns interact with the colloidal particles at the triple phase boundary and capillary assembly can result in site-selective colloid deposition.

Here, capillary assembly was shown to allow for the deposition of polymer spheres into trench structures created by photolithography and reactive ion etching. By additional chemical functionalization of the surface with a self-assembled monolayer (SAM), spheres arrange themselves site-selectively inside the trenches, while sphere deposition on the plane substrate surface is suppressed. The creation of such SAMs was discussed in detail. Different SAM formation techniques were presented and the SAM quality was evaluated by AFM and contact angle measurements.

The deposition mechanism of the colloids on the topographically and chemically pre-treated surfaces was discussed. Trench geometries are shown to guide the sphere arrangement, trench densities determine the surface wettability and thus sphere deposition. By appropriate choice of trench geometry and sphere deposition parameters with the doctor blade technique, trenches are filled with single sphere chains. These sphere rows are used as a shadow mask in nanosphere lithography (NSL). By this, rows of opposing nanotip pairs are prepared. An oblique deposition of material during nanosphere lithography is shown to allow for the creation of nanotip pairs with tunable gap widths. These gap widths can be predicted by ray trace simulations. Nanotip pairs with gaps between 400 nm and 29 nm are prepared.

Such tip pairs can be used as nanogap electrodes e.g. for particle trapping or nanowire orientation. When applying electric fields to such sharp tips, fields are strongly enhanced. Finite element simulations are performed in order to estimate this field enhancement and the electric field distribution between nanotips as created in the experiment. The influence of the tip geometry, i.e. tip radius and gap width, on the field distribution is discussed.

With this, an easy and fast preparation process for the creation of rows of thousands of nanogap electrodes was introduced. Most preparation techniques described in literature allow for the creation of only few tip pairs (< 10) and depend on expensive methods as electron beam lithography or focussed ion beams for direct writing or modification of patterns. However for better signal quality or better statistics it is desirable to measure large amounts of test objects at once.

In the last section of this chapter, the principle of dielectrophoresis was introduced, where inhomogeneous electric fields are used for trapping of polarizable particles. It was shown how the nanotip pairs prepared by NSL can create such inhomogeneous fields along the flow direction in a microfluidic trench. An approach for the easy addressing of the nanotips with an electric field by creating macroscopic contact pads with an additional shadow mask during metal deposition in NSL was shown. First preliminary results show, that the nanotips could be used for the dielectrophoretic trapping of fluorescent core-shell silica particles.

As the presented preparation process allows for the adjustment of the gap width between the tips with respect to the dimensions of target-objects, single particle trapping of nanoobjects with dimensions of few hundred to few or few ten nanometers should be possible.

3.7 Bibliography

[1] N. J. Greybush, M. Saboktakin, X. Ye, C. della Giovampaola, S. J. Oh, N. E. Berry, N. Engheta, C. B. Murray, C. R. Kagan, ACS nano 8(9), 9482 (2014)

[2] N. J. Greybush, I. Liberal, L. Malassis, J. M. Kikkawa, N. Engheta, C. B. Murray, C. R. Kagan, ACS nano 11, 2917 (2017)

[3] Y. Cui, M. T. Björk, J. A. Liddle, C. Sönnichsen, B. Boussert, A. P. Alivicatos, Nano Lett. 4(6), 1093 (2004)

[4] A. Cerf, H. C. Tian, H. G. Craighead, ACS nano 6(9), 7928 (2012)

[5] A. Zhang, C. M. Lieber, Chem. Rev. 116, 215 (2016)

[6] A. Kuzyk, Electrophoresis 32, 2307 (2011)

[7] K. Brassat, F. Assion, U. Hilleringmann, J. K. N. Lindner, Phys. Stat. Sol. A 8, 1485 (2013)

[8] K. Brassat, J. K. N. Lindner, MRS Proceedings 1663, mrsf13-1663-ww04-09 (2014)

[9] T. Kraus, H. Wolf, Templated Self-Assembly of Particles. In: Handbook of Nanotechnology. Berlin: Springer-Verlag, 187 (2010)

[10] G. A. Ozin, S. M. Yang, Adv. Funct. Mater. 11, 95 (2001)

[11] Y. Xia, Y. Yin, Y. Lu, Adv. Funct. Mater. 13, 907 (2003)

[12] N. J. Gleason, C. J. Nodes, E. M. Higham, N. Guckert, I. A. Aksay, J. E. Schwarzbauer, J. D. Carbeck, Langmuir 19, 513 (2003)

[13] V. Mahalingam, S. Onclin, M. Peter, B. J. Ravoo, J. Huskens, D. N. Reinhoudt, Langmuir 20, 11756 (2004)

[14] S. M. Yang, H. Miguez, G. A. Ozin, Adv. Funct. Mater. 12, 425 (2002)

[15] Y. Xia, B. Gates, Y. Yin, Y. Lu, Adv. Mater. 12, 693 (2000)

[16] N. V. Dziomkina, G. J. Vancso, Soft Matter 1, 265 (2005)

[17] L. Malaquin, T. Kraus, H. Schmid, E. Delamarche, H. Wolf, Langmuir 23, 11513 (2007)

[18] F. Schreiber, Prog. Surf. Sci. 65, 151 (2000)

[19] A. Ulman, An introduction to ultrathin organic films, Boston: Academic Press (1991)

[20] S. R. Forrest, Chem. Rev. 97, 1793 (1997)

[21] J. Scherer, M. R. Vogt, O. M. Magnussen, R. J. Behm, Langmuir 13, 7045 (1997)

[22] S. Kim, G. Y. Choi, A. Ulman, C. Fleischer, Langmuir 13, 6850 (1997)

[23] G. B. Sigal, C. Bamdad, A. Barberis, J. Strominger, G. M. Whitesides, Anal. Chem. 68, 490 (1996)

[24] K. L. Prime, G. M. Whitesides, Science 252, 1164 (1990)

[25] R. Singhvi, A. Kumar, G. P. Lopez, G. N. Stephanopoulos, D. I. C. Wang, G. M. Whitesides, D. E. Ingber, Science 264, 696 (1994)

[26] D. K. Schwartz, Annu. Rev. Phys. Chem. 52, 107 (2001)

[27] C. Carraro, O. W. Yauw, M. M. Sung, R. Maboudian, J. Phys. Chem. B 102, 4441 (1998)

[28] A.Y. Fadeev, T.J. McCarthy, Langmuir 16, 7268 (2000)

[29] J. Dong, A. Wang, K.Y. Ng, G. Mao, Thin Solid Films 515, 2116 (2006)

[30] M.-H. Jung, H.-S. Choi, Korean J. Chem. Eng. 26, 1778 (2009)

[31] Y. Wang, M. Liebermann, Langmuir 19, 1159 (2003)

[32] M. Hu, S. Noda, Y. Tsuji, T. Okubo, Y. Yamaguchi, H. Komiyama, J. Vac. Sci. Technol. A 20(3), 589 (2002)

[33] K. Brassat, M. Sc. Thesis, Selbstorganisierte Anordnung von Nanokugeln auf vorstrukturierten Siliziumoberflächen, Paderborn University (2012)

[34] J. Aizenberg, A. J. Black, G. M. Whitesides, Nature 394, 868 (1998)

[35] A. Dimitrov, K. Nagayama, Langmuir 12, 1303 (1996)

[36] T. Li, W. Hu, D. Zhu, Adv. Mater. 22, 286 (2010)

[37] A.Kuzyk, Electrophoresis 32, 2307 (2011)

[38] H. Park, J. Park, A. K. L. Lim, E. H. Anderson, A. P. Alivisatos, P. L. McEuen, Nature 407, 57 (2000)

[39] G. Maruccio, P. Visconti, V. Arima, S. D'Amico, A. Blasco, E. D'Amone, R. Cingolani, R. Rinaldi, S. Masiero, T. Giorgi, G. Gottarelli, Nano Lett. 3, 479 (2003)

[40] R. V. Seidel, A. P. Graham, J. Kretz, B. Rajasekharan, G. S. Duesberg, M. Liebau, E. Unger, F. Kreupl, W. Hoenlein, Nano Lett. 5, 147 (2005)

[41] C. Joachim, J. K. Gimzewski, A. Aviram, Nature 408, 541 (2000)

[42] K. Horiuchi, T. Kato, S. Hashii, A. Hashimoto, T. Sasaki, N. Aoki, Y. Ochiai, Appl. Phys. Lett. 86, 153 (2005)

[43] Q. Qing, F. Chen, P. Li, W. Tang, Z. Wu, Z. Liu, Angew. Chem. Int. Ed. 44, 7771 (2005)

[44] D. C. Wei, Y. Q. Liu, L. C. Cao, Y. Wang, H. L. Zhang, G. Yu, Nano Lett. 8, 1625 (2008)

[45] H. W. Deckmann, J. H. Dunsmuir, Appl. Phys. Lett. 41, 377 (1982)

[46] C. L. Haynes, R. P. VanDuyne, J. Phys. Chem. B 105, 5599 (2001)

[47] Z. Li, L. Zhang, Q. Li, J. Hu, P. Liu, S. Feng, W. Chen, Y. Li, RSC Adv. 3, 14829 (2013)

[48] C. Brodehl, S. Greulich-Weber, J. K. N. Lindner, MRS Proc. 1748, mrsf14-1748-ii11-25 (2015)

[49] C. Brodehl, Ph. D. Thesis, Paderborn University.

[50] J. Zhao, B. Frank, S. Burger, H. Giessen, ACS Nano 5(11), 9009 (2011)

[51] S. Syrenova, C. Wadell, C. Langhammer, Nano Lett. 14, 2655 (2014)

[52] A. Kosiorek, W. Kandulski, P. Chudzinski, K. Kempa, M. Giersig, Nano Lett. 4(7), 1359 (2004)

[53] J. F. Blinn, ACM Trans. Graph. 1, 235 (1982)

[54] U. Herr, B. Kuerbanjiang, C. Benel, G. Papageorgiou, M. Goncalves, J. Boneberg, P. Leiderer, P. Ziemann, P. Marek, H. Hahn, Beilstein J. Nanotechol. 4, 306 (2013)

[55] Z. G. Dai, X. H. Xiao, Y. P. Zhang, F. Ren, W. Wu, S. F. Zhang, J. Zhou, F. Mei, C. Z. Jiang, Nanotechnology 23, 335701 (2012)

[56] W. Zhang, X. Cui, O. J. F. Martin, J. Raman Sprectrosc. 40, 1338 (2009)

[57] COMSOL Multiphysics 4.3a (2013)

[58] H. A. Pohl, J. Appl. Phys. 22, 869 (1951)

[59] N. M. Jesus-Perez, B. H. Lapizco-Encinas, Electrophoresis 32, 2331 (2011)

[60] A. Kuzyk, Electrophoresis 32, 2307 (2011)

[61] H. Moncada-Hernandez, B. H. Lapizco-Encinos, Anal. Bioanal. Chem. 396, 1805 (2010)

[62] P. Chen, X. Feng, W. Du, B. F. Liu, Front. Biosci. 1, 2464 (2008)

[63] G. M. Whitesides, Nature 442, 368 (2006)

[64] J. Mairhofen, K. Roppert, P. Ertl, Sensors 9(6), 4804 (2009)

[65] H. Shafiee, M. B. Sano, E. A. Henslee, J. L. Caldwell, R. V. Davalos, Lab Chip 10, 438 (2010)

[66] J. Regtmeier, R. Eichhorn, M. Viefhues, L. Bogunovic, D. Anselmetti, Electrophoresis 32, 2253 (2011)

[67] V. Linko, S. T. Paasonen, A. Kuzyk, P. Törmä, J. J. Toppari, small 5(21), 2382 (2009)

[68] Y. Xie (ed.), The Nanobiotechnology Handbook, Boca Raton: CRC Press, Taylor & Francis Group (2013)

[69] Y. Shin, D. Lee, K. Lee, K. H. Ahn, B. Kim, J. Industr. Engin. Chem. 14, 515 (2008)

[70] W. Stöber, J. Colloid and Interface Sci. 26, 62 (1968)

[71] http://www.fluorophores.tugraz.at/substance/252 (14.08.2017)

4 Block copolymer lithography: large-area nanopore patterns, placement of Au nanoparticles and hierarchical nanopores

Block copolymer (BCP) lithography is an emerging technique for the large area surface patterning with single digit nanoscale features [1], based on the microphase separation of block copolymers into ordered motives (Chap. 4.1). Using the behavior in thin films, the self-organized motives can be used as lithography masks. Standard thin film processing makes this technique easily up-scalable to wafer scale. This combination of small feature sizes and diverse motives accessible by simple preparation routes makes the BCP lithography interesting for technological miniaturisation processing. Current research investigates the use of BCP lithography to create patterns for magnetic storage media [2, 3], fin-field effect transistors [4], seeds for nanowire growth [5, 6], or quantum dots [7, 8]. For the controlled creation and tailoring of nanopatterns, the detailed understanding of the self-organized phase separation process is fundamental.

In this work, the microphase separation of polystyrene - polymethylmethacrylate block copolymers (PS-*b*-PMMA) is investigated, which forms hexagonally arranged PMMA cylinders embedded in a PS matrix as depicted in Figure 4.1 (a). By selective removal of the PMMA, nanoporous polystyrene with pores of less than 20 nm diameter are obtained. The influence of the substrate surface properties on the pattern creation are investigated for various materials surfaces (metal surfaces, semiconducting and insulating oxide surfaces) and

with different home-made polymers (changing block length ratios, molecular weight and polydispersity) (Chap. 4.2). The patterned polymer thin films can be used as a lithographic mask for the pattern transfer into the substrates (Chap. 4.3).

Chapter 4.4 gives an application of such nanopores in a silicon surface as topographic traps for the directed self-assembly of colloidal gold nanoparticles (Fig. 4.1 (b)). These ordered arrays can be used as seeds for the catalytic growth of semiconductor nanowires. In Chapter 4.5, directed self-assembly is applied to confine the phase-separation of BCPs site-selectively into topographic and chemical pre-patterns. The pre-patterns are created by nanosphere lithography, as explained in the previous chapters (Chap. 2.3). The combination of these two self-assembly techniques is shown to be suitable for the creation of periodical hierarchical nanopores on large areas (Fig. 4.1 (c)).
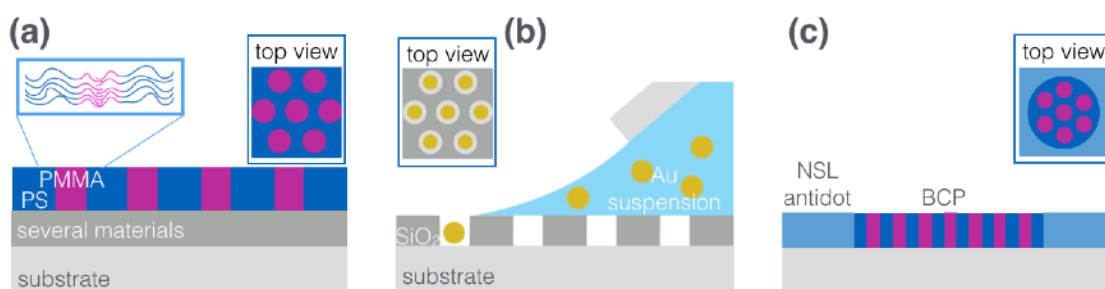
Fig. 4.1: The outline of Chapter 4 is illustrated schematically. (a) Sketch of phase separated BCP thin films forming self-assembled PMMA cylinders in a PS matrix on a surface with feature sizes of 13-20 nm. (b) The BCP nanopores can act as a lithography mask to transfer the nanopores in SiO_2. Nanopores can then act as topographic traps for the directed self-assembly of colloidal Au nanoparticles. (c) The BCP lithography can be performed on nanosphere lithography pre-patterned antidot surfaces for the creation of hierarchical nanopores.

4.1 Basics of (block-) copolymers

Polymers are macromolecules composed of many repeating units, the monomers, which are covalently bonded to each other in classical polymers [9-11]. The properties of polymers are determined by the monomer species and the arrangement of the monomers in a polymer chain.

Polymers containing one type of monomer are referred to as homopolymers. Polymers, which are composed of a mixture of different monomer species are called copolymers. The monomers are bonded to each other in polymerization reactions. Many different synthesis routes are available, suitable for different monomer species and resulting in polymers of different configurations and properties. Commonly used chain-growth polymerization methods are the free radical polymerization or living polymerization [12].

The configuration of the polymer chain is determined by their (i) architecture, (ii) chain length and (iii) monomer composition *(For the sake of brevity, specifics for block copolymers (BCP) as used later are noted in italic font).*

(i)   Architecture. The polymer architectures describes the general polymer shape. Linear chains of monomers can be created, as well as branched polymers with one or more branch points, forming star polymers, dendrimers or even polymer networks. The polymer architecture determines physical properties such as viscosity, solubility or the glass transition temperature.

(ii) Chain length. The chain length can be tailored during the polymerization and is a basic characteristic of the polymer, determining most physical properties of the macromolecule. The chain length and size of unbranched, linear polymers is usually characterized by the following measures:

- The polymerization degree N is the total number of monomer units building the polymer chain.
- The size of the polymer is typically given by the, usually very large, molecular weight. The number-average molecular weight M_n of the polymer is defined as

$$M_n = \frac{\Sigma M_i N_i}{\Sigma N_i} \tag{4.1}$$

with the number of moles N_i of the polymer chain of species i with the molar mass M_i.
The mass-average molecular mass M_w (Eqn. 4.2) is

$$M_w = \frac{\Sigma M_i^2 N_i}{\Sigma M_i N_i} \tag{4.2}$$

The total (number-average) molecular weight of a BCP A-b-B is the sum of the molecular mass $M_{n,A}$ of the polymer block of type A and the molecular mass $M_{n,B}$ of the polymer block of type B.

- The polydispersity index PDI quantifies the width of the distribution of the polymer chains molecular weight. It is defined as the quotient of the number-average molecular mass M_n and the mass-average molecular mass M_w:

$$PDI = \frac{M_n}{M_w} \tag{4.3}$$

If all polymer chains are equally long the PDI equals 1, the larger the value of PDI the broader is the molar mass distribution. *A small distribution of the chain length is crucial for the homogeneity of the nanopatterns formed during BCP phase separation. Therefore small PDI ≈ 1 are desired.*

- The size or occupied volume of the macromolecule depends strongly on its environment (good solvent, poor solvent, theta solvent, melt), but can be estimated by the radius of gyration R_g. Based on a random walk of a freely-jointed polymer, the polymer chain forms a coil with the radius:

$$R_g = a \sqrt{\frac{1}{6} N} \tag{4.4}$$

with the polymerization degree N and the Kuhn length a [13, 14].
The Kuhn length of polystyrene and polymethylmethacrylate, used in this work, are 0.68 nm and 0.69 nm, respectively [15]. This length is typically much shorter than the so called contour length, which is the length of the polymer chain in its fully stretched state.

(iii) Polymer composition. The arrangement of monomers along the polymer chains of copolymers (CPs) can be very versatile and determines intermolecular interactions. One differentiates between alternating copolymers, periodic CPs, statistical CPs, also referred to as random CPs, grafted CPs and block copolymers. *Random copolymers and block copolymers are used for the block copolymer lithography and will be described in detail in the following.*

Characteristic temperatures for the phase transitions of polymers are the glass transition temperature, the melting temperature and the degradation temperature. At the glass transition temperature the polymer undergoes a transition from an amorphous solid glassy state to a viscous, rubber-like state. Above the melting point, the polymer behaves liquid-like. However, many polymers do not reach this state and degrade before. Typical phase transition temperatures for polystyrene (PS) and poly(methylmethacrylate) (PMMA) are listed in Table 4.1. However, the phase transition temperatures depend on the molecular weight of the polymers, the tacticity, architecture, compositions and synthesis method. The phase behavior of polymer mixtures is complex. This is described in more detail for the phase-separation of block copolymers in the following.

Tab. 4.1: Phase transition temperatures for polystyrene (PS) and poly(methylmethacrylate) (PMMA). T_g: glass transition temperature, T_m: melting temperature, T_{deg}: degradation temperature.

	PS	PMMA
T_g [°C]	90 [16]	105 [18]
T_m [°C]	270 [16]	200-230 [19]
T_{deg} [°C]	> 295 [17]	> 340 [19]

4.1.1 Copolymers

(Di-)Copolymers consist of two monomer species A and B, which form a mixed polymer chain during polymerization. As stated above, monomers A and B can be added to a polymer chain in more or less ordered manner, forming alternating copolymers, periodic copolymers, statistical copolymers or block copolymers. In the following, the two latter types will be described in more detail, as they are used in block copolymer lithography.

Statistical copolymers, also referred to as random copolymers (RCP), consist of randomly distributed monomers A and B forming the polymer chain. The amount of monomer A and B forming the chain can be set during polymerization by adjusting the monomer concentrations during synthesis, the sequence of monomers in the chain is however always statistical.

(Di-) Block copolymers (BCP) consist of two homopolymer blocks linked to each other by a covalent bond. Suitable synthesis routes for the preparation of BCPs are living polymerization techniques [12] such as reversible addition fragmentation chain transfer (RAFT) polymerization or atom transfer free radical polymerization (ATRP). The total molecular weight of the polymer and the block length ratios between polymer block A and B are set during synthesis.

A characteristic measure to describe a copolymer consisting of A and B is the moluecular weight fraction f_x of one species $M_{n,A}$ on the total molecular weight M_n. For a RCP the fraction f_x refers to the probability to find a type A monomer in the sequence, for a BCP it is the ratio between the block lengths, e.g. $f_{PS} = 0.5$ if PS and PMMA blocks have the same molecular weight or $f_{PS} = 0.7$ if 70 % of M_n is PS and the PMMA block is shorter with 30 % of M_n. This value is important in BCP lithography as the motives formed during microphase separation are determined by this fraction.

All used copolymers, BCP and RCP, in this work consist of the monomers styrene and methylmethacrylate. BCP are referred to as Polystyrene-b-Polymethylmethacrylate (PS-b-PMMA) (Fig. 4.2), RCP as Polystyrene-co-Polymethylmethacrylate (PS-co-PMMA).
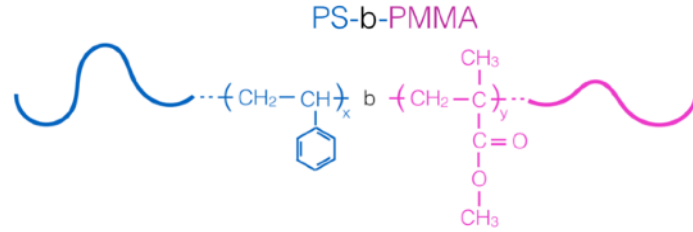
Fig. 4.2: Sketch and molecular structure of the block copolymer Polystyrene-b-Polymethylmethacrylate (PS-b-PMMA).

4.1.2 Phase separation of block copolymers

The coexistence of two different polymer species, A and B, in a (di-) block copolymer leads to a complex phase behavior of the BCP. The different polymers A and B can interact predominantly repulsively or attractively to each other. If the species A and B in a BCP are immiscible, a phase separation will occur. However as the blocks from the incompatible species are covalently bonded to each other, they can not phase separate macroscopically, but micro-phase separate forming periodic nanopatterns with A- or B-rich domains.

The micro-phase separation results in a decrease of the free energy of the system by minimization of the interfacial area between the different blocks and a maximization of the chain conformational entropy within each block [14, 20, 21].
The change of the free energy ΔG_{mix} during mixing of polymers is given by

$$\Delta G_{mix} = \Delta H_{mix} - T\Delta S_{mix}$$

(4.5)

with the change in enthalpy ΔH_{mix} and the change in entropy ΔS_{mix} dependent on the temperature T. P. Flory and M. Huggins [20, 21] found the solution

$$\Delta G_{mix} = RT(n_A \ln(\phi_A) + n_B \ln(\phi_B) + n_A \phi_B \chi_{AB})$$

(4.6)

with $n_{A,B}$ the number of moles of the components A and B, respectively, $\phi_{A,B}$ their volume fractions and χ_{AB} the Flory-Huggins parameter. R is the ideal gas constant.
The Flory-Huggins parameter χ_{AB} is a measure, describing the interactions between two species A and B [22, 23] and can be split up into an entropic and an enthalpic component χ_S and χ_H:

$$\chi_{AB} = \chi_S + \frac{\chi_H}{T}$$

(4.7)

If mixing of same polymer species, A - A or B - B, is energetically favorable, the mixing of A - B is endothermic, Flory Huggins parameter is $\chi > 0$, the Gibbs free energy G_{mix} decreases. For exothermic mixing of A and B, the

Flory Huggins parameter becomes negative (X < 0). Figure 4.3 shows the Flory-Huggins parameters of different polymer combinations in dependence on the temperature [24]. The Flory-Huggins parameter can be measured e.g. by small angle neutron scattering [22]. For the mixing of polystyrene with polymethylmethacrylate (PS-PMMA), the Flory-Huggins parameter is given [22] by:

$$X_{PS/PMMA} = (0.028 \pm 0.002) + \frac{(3.9 \pm 0.6)}{T} \qquad (4.8)$$
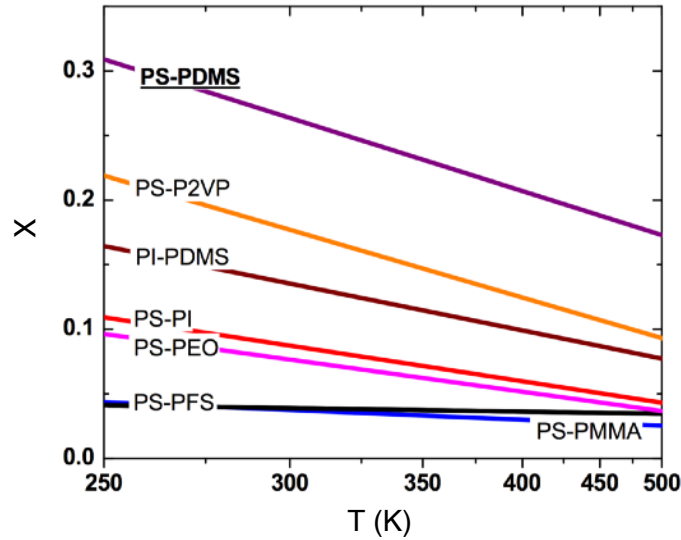
Fig. 4.3: Dependence of the Flory-Huggins parameter X on the temperature T for different copolymers [24].

For the polymer combination PS-PMMA, the Flory-Huggins parameter is positive, X > 0, the entropic contribution X_S is much greater than the enthalpic contribution X_H and the Flory-Huggins parameter shows a weak temperature dependence. This means that a mixture of PS and PMMA will segregate at suitable temperature.

For repulsive forces matching the strong segregation criterion XN > 10.5 polymers separate into ordered phases [25]. Separation here means that the polymer chains rearrange within the polymer mixture and form A-rich and B-rich areas. In a PS-b-PMMA BCP a macroscopic segregation is suppressed as the blocks A and B are still covalently bonded to each other. Thus, a microphase separation occurs into A- or B-rich areas which form regular patterns with defined shapes. A typical phase diagram [26] of this microphase separation of block copolymers is shown in Figure 4.4. The Flory-Huggins parameter weighted by the polymerization degree N is plotted over the fraction of polymer A of the BCP.

Depending on the ratio of the block-lengths the self-arrangement can lead to different phase-separation motives. The possible motives are shown in Figure 4.4 in the order of increasing fraction of polymer type A and correspond to marked areas in the phase diagram. For small fractions of polymer A, e.g. f_A = 0.2 and low polymerization degrees N at a given Flory-Huggins parameter X, phases separate forming spherical areas of polymer A in a matrix of polymer B. These spherical A areas arrange themselves in a body-centered cubic cell. Increasing the A-fraction the energetically favorable separation of blocks results in cylinders of A in a B matrix with the cylinders being hexagonally arranged. This is the structure which will be discussed in detail within this

work. Increasing the fraction f_A further, a gyroidal phase is formed until the ratio of blocks is 0.5 and the polymers arrange themselves in a lamellar phase where equal layers of blocks A and B alternate. For even higher fractions of A ($f_A > 0.5$), the same phases are formed, but with A and B exchanged.
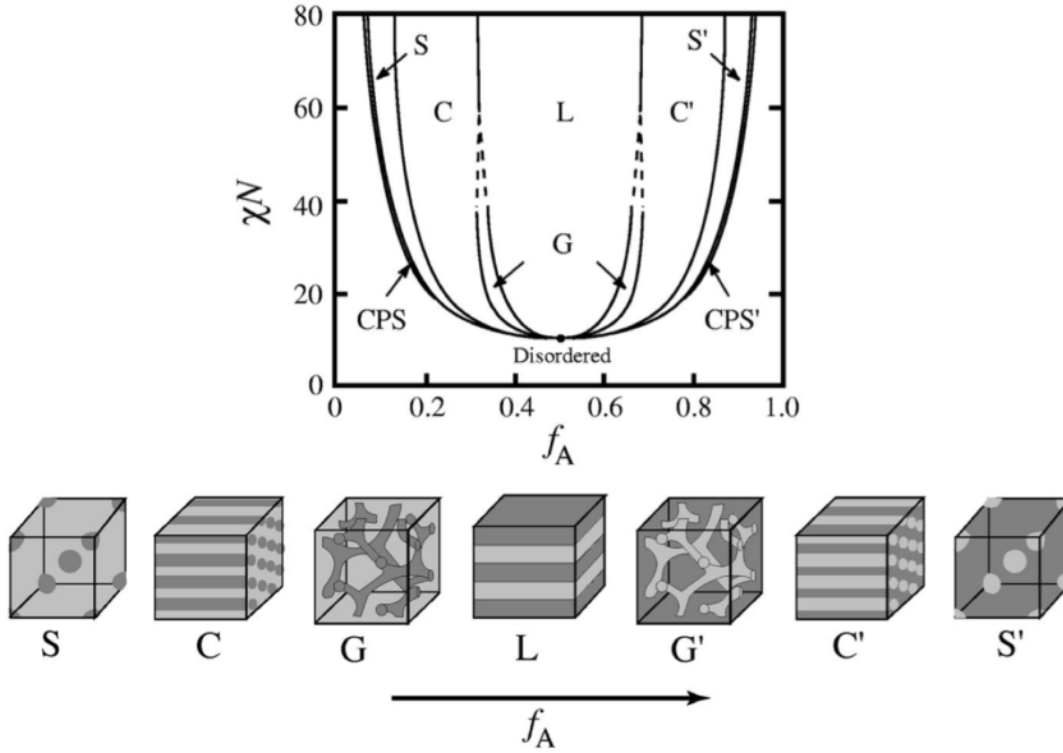
Fig. 4.4: Phase diagram of the phase separation of a block copolymer A-b-B. Depending on the polymerization degree N and the polymer fraction f_A for a given polymer system with the material specific repulsion characteristic described by the Flory-Huggins Parameter X, the BCP can separate into different shapes. These characteristic shapes for the phases are shown in the sketches below. S = spherical phase, C = cylindrical, G = gyroidal, L = lamellar [26].

4.2 Nanopores by block copolymer lithography

The effect of microphase separation of block copolymers as described previously for bulk structures can also be applied to thin films. This allows for the use of the self-arranged patterns as templates for a lithographical nanostructuring of solid surfaces. In bulk phase separation the intra- and intermolecular polymer interactions described by the Flory Huggins parameter, the polymerization degree and the block length ratio were shown to be the most important parameters. However in thin films additional factors become crucial, such as the polymer film thickness, the thin film interfaces and solvents used for the deposition.

The free energy F for the BCP thin films can be expressed in a phenomenological description (Eqn. 4.9) as the sum of the elastic free energy F_{elast} of the stretched polymer chains, the mixing free energy of the polymers F_{mix}, described above, and the interfacial energy $F_{interface}$ [27]

$$F = F_{elast} + F_{mix} + F_{interface}$$

(4.9)

The mixing energy F_{mix} includes polymer characteristics such as the block length ratio, polymerization degree and polymer species determining the size and shape of the self-organized nanostructures as stated above. In the following, this energy will be considered as constant, as the same PS-b-PMMA BCP will be used. The elastic energy F_{elast} is determined by the polymer chain conformation and can vary if the BCP gets stretched. This can result in changes of the characteristic dimensions of the microphase separated BCP, i.e. the diameter of PMMA cylinders in a PS matrix. For thin films, surface effects can become predominant. The interfacial energy $F_{interface}$ determines the intermolecular forces between the polymer species A and B within the film, leading to an orientation of the microphase separated domains towards the thin film interfaces to substrate s or air a (Eqn. 4.10). Thus, two effects evolve from this energy consideration: the wettability of the polymer on the surface and the interfacial interactions, which can result in a preferential wetting of the substrate with one polymer species on the BCP. Ham et al. [28] summarize all interface energies including those of blocks A-B as

$$F_{interface} = f(\gamma_{A,B\text{-}s},\ \gamma_{A,B\text{-}a},\ \gamma_{A\text{-}B},\ \gamma_{s\text{-}a}) \qquad (4.10)$$

with γ the interfacial energy between block A or block B, substrate s or air a [28]. Two interfaces need to be considered in particular: (i) the interface between the polymer and the substrate surface and (ii) the polymer-air/ vacuum interface.

(i) Polymer-substrate interface. The interfacial energies with the substrate are crucial for the orientation of polymer domains formed during microphase separation. Figure 4.5 shows the two possible extrema of orientation for cylinders of PMMA in a PS matrix: the cylinders can be either perpendicular or parallel to the substrate surface.

PMMA cylinders are formed perpendicularly oriented to the surface (Fig. 4.5 (a)) only if the surface is ,neutral' to both BCP polymer species. In literature, this is commonly explained by an equal interfacial energy $\gamma_{PS\text{-}s}$ between the surface and PS and interfacial energy $\gamma_{PMMA\text{-}s}$ between the surface and PMMA, i.e. $\gamma_{PS\text{-}s} \approx \gamma_{PMMA\text{-}s}$. In this case no block preferentially wets the surface. If the surface is not neutral towards both polymers but shows a higher affinity to e.g. PS, i.e. $\gamma_{PS\text{-}s} < \gamma_{PMMA\text{-}s}$, the interfacial area between surface and PS is maximized, thus with PMMA is minimized, resulting in a PMMA cylinder orientation parallel to the substrate surface, as depicted in Figure 4.5 (b). For small deviations from the equality $\gamma_{PS\text{-}s} = \gamma_{PMMA\text{-}s}$, the elastic free energy F_{elast} is assumed to balance interactions, allowing for a perpendicular cylinder orientation with adjusted domain dimensions, e.g. an adjusted cylinder diameter.

This direct correlation between interfacial energies and polymer domain orientation is controversially discussed in literature [29], however it offers a proper estimation of the polymer behavior.

Fig. 4.5: Schematic orientation of polymer domains with respect to the substrate for the example of PMMA cylinders in a PS matrix. (a) Cylinder orientation perpendicular to the surface, usually valid for ,neutral' surfaces. (b) Parallel PMMA cylinder orientation due to preferential wetting of the surface with PS.

(ii) Polymer-air interface. The interface to air, or vacuum (since the phase separation is done at low pressures), is kept constant during the experiments and assumed to be ‚neutral', i.e. it does not determine the orientation of polymer domains towards air/ vacuum.

The discussion of interfacial energy effects on the domain orientation is valid for a certain film thickness window [30]. The energy F within the film and the wetting of the polymer on the substrate surface can lead to a local adjustment of the film thickness commensurate with the characteristic polymer domain repeating unit L_0, which is for the PS-b-PMMA BCPs discussed here as the center-to-center distance between PMMA cylinders, and typically in the range of few ten nanometers. If a polymer thin film with a non-commensurate film thickness is deposited onto the surface (e.g $1.2 \times L_0$ in Fig. 4.6 (a)), the microphase separation leads to an adjustment of the polymer film thickness towards a majority surface coverage with a film, whose heights are commensurate with a full or half integer multiple of L_0. In the example in Figure 4.6 (b), this results in the formation of a film of $1.0 \times L_0$ which contains islands with the thickness $2 \times L_0$ and holes of $0.5 \times L_0$. The holes/islands have typical lateral dimensions in the range of few micrometers and heights of few to few ten nanometers.
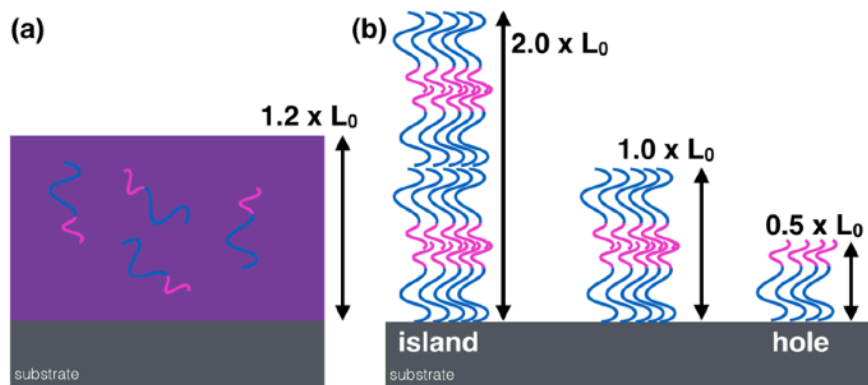
Fig. 4.6: Schematic representation of the adjustment of the film thickness. (a) A polymer thin film with non-commensurate thickness $1.2 \times L_0$ is deposited onto a substrate surface. (b) During microphase separation the majority of the surface will be covered with ordered BCP in the commensurate film thickness $1.0 \times L_0$ while locally islands with a full integer of $2.0 \times L_0$ and holes with half integer $0.5 \times L_0$ can be formed.

The island/hole formation on the surface can go along with a change of domain orientation in films of non-commensurate thickness within the region of gradual thickness transition. Different models concerning this change of orientation (alternating orientations, mixed states of orientation, …) are presented in literature [23, 28, 31-33]. An example of the changing orientation along the edge of an island is shown in the next chapter (Fig. 4.10), where the optimization of the film thickness along with other experimental parameters is discussed.

Besides this island/hole formation mechanism as a way of the system to adjust a non-commensurate film thickness, a mixed orientation state is discussed in the literature [32]. Theoretical simulations [34, 35] suggest a slight preference of surfaces for the polymer species forming the smaller block of the BCP at otherwise ‚neutral' surface conditions. It is claimed that this is an entropic effect as an increasing number of polymer chain ends arrange towards the substrate surface in the cylinder orientation parallel to the substrate. Thus, at non-commensurate film thickness, which mediate defect formation, mixed states with partial cylinder orientation parallel to the surface in otherwise perpendicular oriented patterns can be formed.

Both thickness effects, i.e. hole/island formation and mixed orientation states, are observed in this work and shown in Figure 4.7. Mixed cylinder orientation states (Fig. 4.7 (a+b)) are distributed homogeneously over the polymer film. Defects induced by island formation (Fig. 4.7 (c-e)) usually form larger domains with ordered patterns in perpendicular orientation, here on the islands, while the area around is covered with patterns oriented parallel to the surface. AFM measurements (Fig. 4.7 (e)) confirm the local film thickness adjustment. Here, islands are elevated by 30 nm with respect to the plane polymer film around.
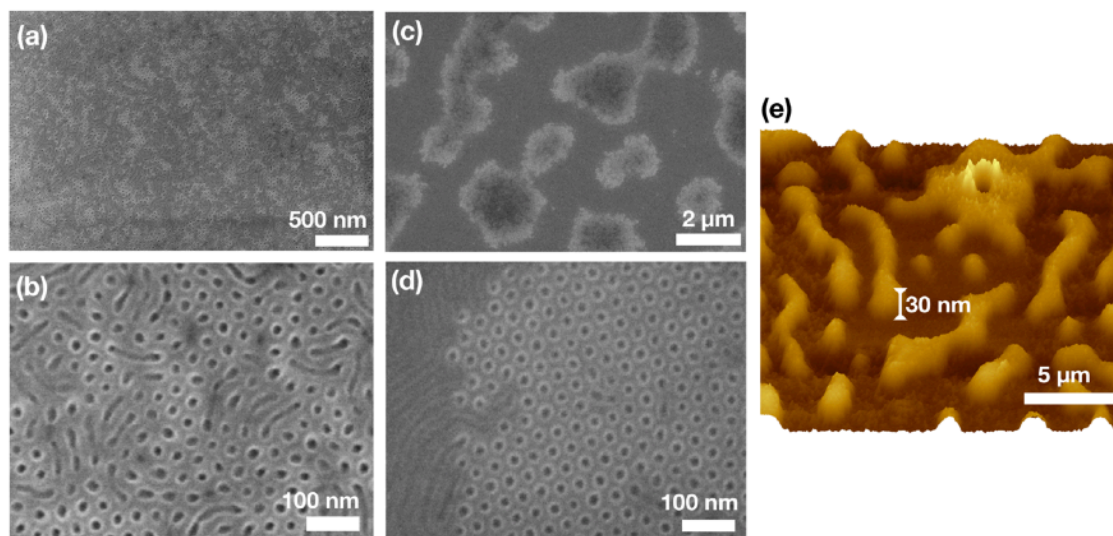
Fig. 4.7: SEM images of (a+b) mixed orientation state and (c+d) island formation in polymer thin films of non-commensurate thickness. (e) AFM image in tiled 3D view of islands on sample (c). The elevation of islands is 30 nm.

Thus, modification of either the interfacial energies between polymers and surface or the film thickness, the orientation of the polymer domains with respect to the substrate surface can be guided. Examples will be shown in Chapter 4.2.4.

This work will exclusively discuss the phase separation in PS-b-PMMA block copolymers with block length ratios and polymerization degree resulting in the formation of PMMA cylinders in a PS matrix. For lithography purposes, the cylinders must be vertically oriented with respect to the surface. Thus, by selective removal of the PMMA cylinders, PS thin films with regularly arranged cylindrical nanopores are created.

In this chapter, the general experimental procedure for the preparation of nanopatterned thin films is presented. The interface interactions with different substrate materials are investigated in Chapter 4.2.4-5. Finally, the phase-separation of home-made BCPs is demonstrated in Chapter 4.2.6.

4.2.1 Experimental procedure

The general experimental procedure for the nanopatterning of surfaces by block copolymer lithography is depicted in Figure 4.8. BCPs are suspended in a solvent and a thin film with defined thickness is deposited onto the substrate by spin coating. The thickness can be set by adjusting the polymer concentration in the solvent (typ. 0.5-2 wt.%) and by the rotation velocity. It is controlled by ellipsometry. Different substrate materials were used. The prerequisites concerning their wettability by the polymer suspension and interactions with the BCP are discussed in detail in Chapter 4.2.4 and 4.2.5. The example in Figure 4.8 shows a SiO$_2$ surface on a Si wafer functionalized with a random copolymer, as will be discussed later. The thin film is then annealed in vacuum at a defined temperature for microphase separation. The BCP shown here forms a PS matrix with

cylinders of PMMA which are oriented perpendicularly to the substrate surface. One polymer type can then be selectively removed in order to create a topographic pattern on the surface. In this case, the PMMA cylinders are removed by UV exposure and development in acetic acid.
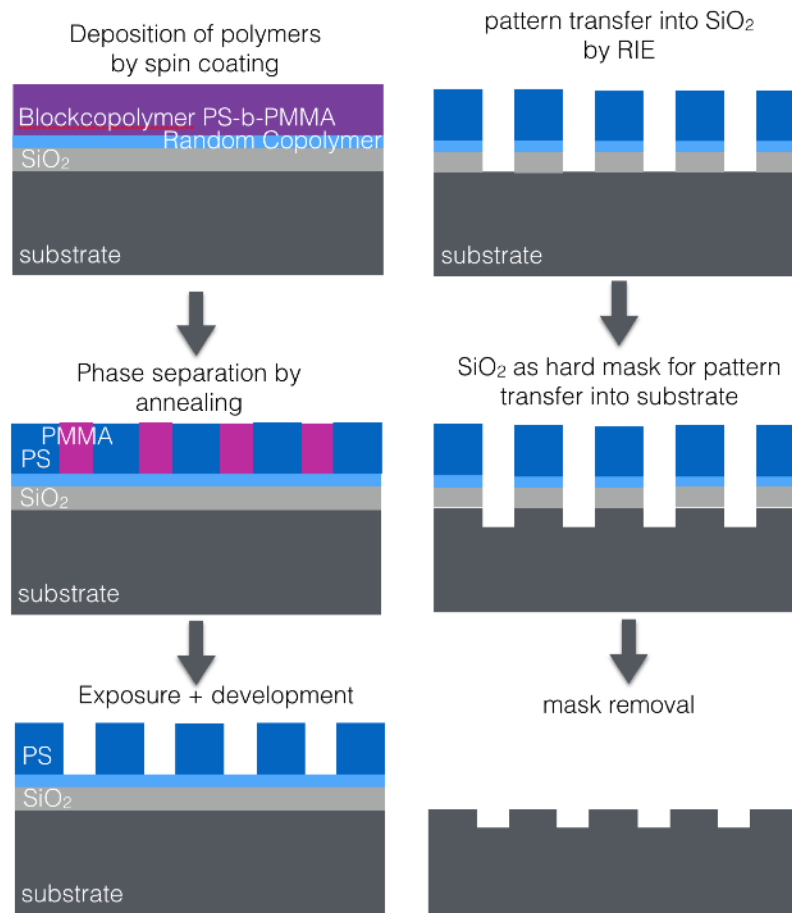
Fig. 4.8: Schematic experimental procedure of block copolymer lithography (left) and pattern transfer into substrate (right).

The resulting nanoporous PS thin film can then act as a shadow mask for pattern transfer into the substrate. The depicted procedure in the right column shows one possible approach to transfer the pattern from the polymer into a SiO_2/Si substrate: by reactive ion etching the polymer pattern is transferred into the SiO_2 which can then act itself as a hard mask for pattern transfer into the Si. By this, nanopatterned Si surfaces exhibiting a hexagonal array of vertical pores can be obtained after final mask removal.

In the following, the left column of Figure 4.8 will be discussed in detail. The experimental parameters need to be optimized for a homogeneous large-area phase separation into well-ordered patterns: the influence of changes in film thickness of the spin casted BCP, the annealing conditions, i.e. annealing temperature, time and chamber pressure, and the substrate surface properties such as wettability and surface polarity are discussed concerning their influence on the nanopore formation [26, 36].

4.2.2 SEM image analysis for nanopattern characterization

For an objective comparison of the nanopores formed during microphase separation at different experimental conditions, scanning electron microscopy (SEM) images of the nanoporous PS matrix are taken and evaluated with a home-made image analysis software based on a Delaunay triangulation. Details regarding this software can be found in [37]. Pore density, pore size, center-to-center distance between pores, coordination numbers, defects and domain sizes are determined.

SEM images are converted into 1-bit images. As BCP nanopores appear in SEM images darker than the surrounding polystyrene matrix (Fig. 4.9 (a)), pores are found and marked as white areas when setting an appropriate gray scale threshold value (Fig. 4.9 (b)). Defining a minimum number of pixels to form an area avoids the program to interpret single bright pixels or image artifacts as pores. The pore size is then evaluated by the number of pixels forming the white areas. By setting thresholds of pixel numbers, pores of average size (green) and significantly larger pores (typ. > 20%)(red) are color-marked as shown in Figure 4.9 (c). The total pore density is calculated as the sum of both, large and average pores, per sampling area.

In a next step the centroids of the white areas in the 1-bit image are calculated. These centroids then are evaluated with a Delaunay triangulation algorithm [38, 39]. Within this calculation step three neighboring datapoints, here pore centroids, are connected with lines forming a triangle, fulfilling the requirement that no additional datapoint is embedded. From the lengths of the triangle sides, center-to-center distances of the pores can be read and averaged. This value is in literature also referred to as the lattice constant or correlation length L_0.

The number of centroids within the distance of a certain cut-off radius corresponds to the coordination number of pores (Fig. 4.9 (d)). By evaluation of the orientation of the triangle sides, pore domains with different crystal orientations can be analyzed concerning their orientation to each other, their sizes and crystal defects at grain boundaries. To make this orientation visible, a color wheel with six-fold symmetry is introduced, marking the same orientations within the hexagonal arrangement with the same colors (Fig. 4.9 (e)).
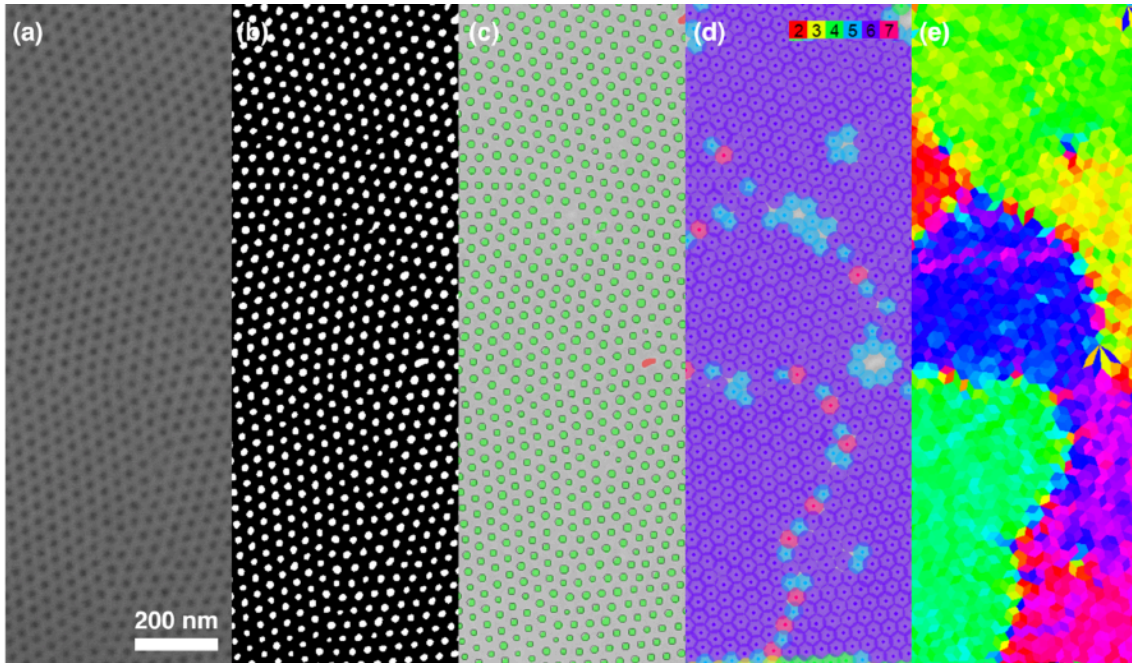
Fig. 4.9: Evaluation of BCP nanopore SEM image (a). This image is converted into 1-bit image (b). Pore sizes are classified and marked by colors (green = average pores, red = larger pores) (c). Pore positions are calculated and the coordination number is determined (d). Pore domains are determined according to their orientation (e). (a) - (e) show the same image section.

The pore sizes and center-center distances are determined by the molecular weight and block length ratios of the BCP. For the used BCP67 with a molecular weight of $M_n \approx 67$ kg/mol and a block length ratio of approx. 70:30 PS:PMMA the average pore diameter is 17 nm, the center-to-center distance $L_0 = 35$ nm. These values are confirmed in literature [1]. The pore density is an indicator for the phase-separation quality as it decreases with increasing number of defects in the arrangement. A good value for the pore density, such as for the image in Figure 4.9, is 8.3×10^{10} cm^{-2}. The geometrical maximum for the pore density of this BCP is 9.43×10^{10} cm^{-2}. For the evaluation of coordination numbers, a cut-off radius of $(1.2 - 1.25) \times L_0$ is used. Pores are color marked corresponding to their coordination. In Fig. 4.9, 81% of the pores have a coordination number of 6, thus are hexagonally arranged. Coordinations < 6 are found near larger pores and when the microphase separation is not finished. Coordination numbers > 6 are also possible, as the pores (or more precisely the PMMA cylinders which later turn into pores) are no hard objects but a soft medium with possible deformations. They are mainly found at dislocations. At grain boundaries between domains of different pore orientations, 5-fold and 7-fold coordinated pores typically alternate. Domains sizes are usually in the range of several hundred nm^2.

4.2.3 Influence of film thickness and annealing conditions on nanopore formation of BCP67

The commercially available BCP67 (Polymer Source P2400SMMA, M_n = 46.1-b-21.0) is a well-known Polystyrene-b-Polymethylmethacrylate (PS-b-PMMA) block copolymer for BCP lithography. The polystyrene fraction is 68.7 %, the polydispersity index is with PDI = 1.09 very narrow, the molecular weight is 67.1 kg/mol (datasheet App. A5). Therefore a phase separation in form of hexagonally arranged PMMA cylinders in a PS matrix is expected. In the following, this BCP is deposited onto a ‚neutral' surface, in order to minimize surface-effects on the microphase separation and to provide constant conditions for a parameter study on the influence of film thickness, annealing temperature and annealing time. To this end, a PS-co-PMMA random copoolymer (RCP) on a Si/SiO$_2$ surface is used as substrate, which promotes a cylinder orientation perpendicular to the substrates surface [40]. The influence of different substrate surfaces (RCP brushes, different materials, different surface roughnesses) on the microphase separation is discussed later on.

Silicon surfaces with native oxide layer functionalized with a PS-co-PMMA random copolymer brush (deposition procedure see below) are spin coated with the BCP dissolved in toluene at 1 wt%. Film thicknesses, controlled by ellipsometry (App. A3), are varied between 16 nm and 50 nm, in order to optimize the quality of the subsequent phase separation. Samples are then annealed for different times between 2 and 24 h at different temperatures between 170 °C and 190 °C at pressures of 1-3 x 10^{-3} mbar for parameter optimization. The phase separated films are afterwards exposed to UV light from a Hg discharge tube with a spectral maximum at 254 nm with a power of approx. 50 mW/cm^2 at a distance of 18 cm for 20 minutes. During this exposure, the PMMA is selectively degraded. After exposure the samples are developed at acetic acid, which dissolves the degraded PMMA. For this purpose, concentrated acetic acid is flushed with nitrogen to remove water from the acid preventing oxidation of the polymer film. Samples are then treated with the acid at room temperature for 30 min. The development is stopped in a water bath, the samples are dried in nitrogen flux.

The parameter optimization was performed as follows: The annealing times were initially set to 4 hours for practical reasons. It is shown later, that the annealing time is not crucial for the phase separation, but allows for an improvement of the pattern order with increasing annealing time. A crucial parameter is the film thickness. As a rule of thumb, the optimum film thickness is in the range of the correlation length L_0. Thus, this is adjusted first. Start annealing temperatures are estimated from comparable literature results and due to the fact that a correspondence between the polymers molecular weight and the appropriate annealing temperature is apparent. Film thicknesses are optimized regarding the appearance of cylinders perpendicular to the substrate surface.

Film thickness. Film thicknesses of a half or full integer multiple of the pattern correlation length L_0 result in microphase separation into the motives predicted by the phase diagram and with an orientation given by the surface characteristics. For film thicknesses deviating from $(1/2 \times n$ or $n)$ L_0 pattern orientation can be influenced [31] or formation of ordered patterns can be completely suppressed.

Experiments were performed with different deposited polymer film thicknesses between 16 nm and 50 nm, as listed in Table 4.2. Pore densities as well as pore size homogeneity are determined by SEM image analysis with the Delaunay software outlined above, and are good measures for the overall quality of the nanopattern formation. For the BCP67 a film of 16 nm, annealed at otherwise optimum temperature of 180 °C for 24 h at a pressure of 1×10^{-3} mbar, is too thin to enable pore formation. Only few single pores are formed similar to the left region in Figure 4.9. Films with thicknesses of 27.5 nm, 30 nm and 35 nm show quite similar nanopore formation. For the thickness of 35 nm pore densities are slightly higher as well as the degree of 6-fold coordination, i.e. the hexagonal arrangement of pores is more homogeneous. At 37.5 nm film thickness, about 37% of pores are elongated implying a mix of parallel and perpendicular cylinders. 50 nm thick films, however, show again a poor phase separation with only single pores being formed within a rough polymer film. Films as thick as $2 \times L_0$ could not be prepared due to technical reasons.

....

Tab. 4.2: Nanopore characteristics after phase separation at different polymer film thicknesses, determined by Delaunay triangulation (see Chap. 4.2.2). „Larger pores" means the fraction of much too large pores on the total number of pores found on the sample. These pores have dimensions significantly larger (> 20%) than the mean pore diameter, mainly caused by a local cylinder orientation parallel to the surface. BCP thin films were annealed for 24 h at 180 °C. The pore densities are comparatively small, which is probably due to a slightly higher chamber pressure of 3×10^{-3} mbar (same for all samples) during the annealing.

film thickness [nm]	pore density [$\times 10^{10}$ cm^{-2}]	larger pores
16.0	no pores	no pores
25.0	4.57	29 %
27.5	6.70	7 %
30.0	6.92	4 %
35.0	7.09	2 %
37.5	4.88	37 %
50.0	0.89	only single pores

The thickness dependence of cylinder ordering can be nicely observed on samples exhibiting a thickness gradient of the BCP film, like in Figure 4.10. Such thickness gradients occasionally occur due to dewetting of the BCP film, most likely due to unstable pressure during the annealing. The thickness difference in the sample of Figure 4.10 was determined by AFM to be 15 nm.

Experiments with film thickness gradients (Fig. 4.10) show, that for very thin polymer films, microphase separation does not result necessarily in the formation of defined motives. For films with a thickness $d < 0.7 \times L_0$ no motives are formed, films may only increase roughness after complete BCP lithography and PMMA removal. This region is visible at the left side in Figure 4.10, where some roughness might be visible and only single pores can be found. At thicknesses $0.7 \times L_0 < d < L_0$ the phase separation into ordered patterns takes place and e.g. nanopores on RCP-functionalized SiO_2 are perpendicularly orientated to the surface, as in the middle of Figure 4.10. For larger film thicknesses $L_0 < d < 2 \times L_0$ orientation of PMMA cylinders change to parallel orientation (Fig. 4.10 right). It is reported in [32] that at thicknesses of a full multiple of L_0 the orientation changes back to being perpendicular.
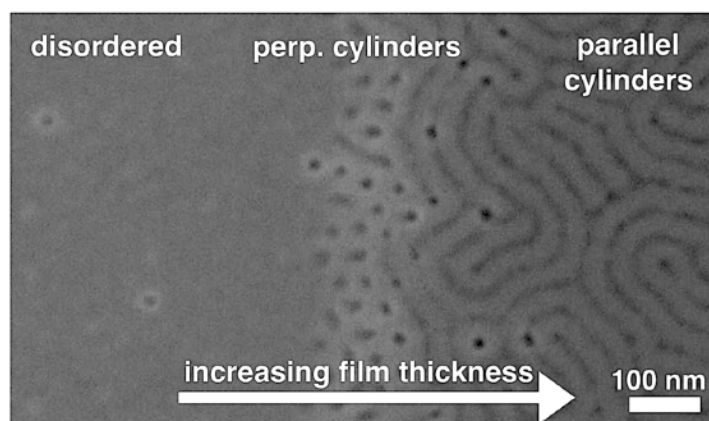
Fig. 4.10: SEM image of BCP67 with increasing film thickness after dewetting of polymer. No order is visible in the thin film (left), perpendicular cylinders at a medium thickness (middle) and cylinders parallel to the surface in thick films (right).

The direction of increasing film thickness in Figure 4.10 is determined by AFM. The height difference between the disordered region and the area with parallel cylinders is 15 nm. The sample is a result of a polymer dewetting probably due to annealing at an unstable pressure between 3.5×10^{-3} mbar and 1×10^{-4} mbar. The initially deposited polymer film was 30 nm in thickness, thus the disordered region is probably about (10-20) nm thick. The experiments with the BCP67 show an optimum film thickness of 30 nm, however the correlation length L_0, which is the center-center distance between hexagonally arranged nanopores, is 35 nm. Thus the disorder region is $d < 0.8 \times L_0$, the area with perpendicular pores $d \approx 0.8 \times L_0$ and the region with parallel cylinders $d > 0.8 \times L_0$ with a total difference of 15 nm.

Such a change of motive orientation with increasing film thickness is also reported for triblock terpolymers in [31], where many different orientations and surface interactions can occur, resulting in a more complex behavior.

Annealing temperature. For the optimized film thickness the annealing temperature was varied. The temperature regime is framed by the glass temperature of the polymer, below which polymer chains have no mobility and do not phase separate, and the degradation temperature, above which polymers decompose. Typical phase transition temperatures for PS and PMMA were compiled above in Table 4.1. The glass transition temperatures for the BCP67 is $T_g(PS) = 105$ °C, $T_g(PMMA) = 128$ °C. DSC data for the polymer BCP67 can be found in Appendix A5.

Figure 4.11 shows SEM images of the nanopores in the PS matrix created by phase separation at a constant film thickness of 30 nm at different temperatures of 170 °C to 190 °C for 4 h. Too low annealing temperatures, i.e. for BCP67 170 °C, lead to a more frequent appearance of cylinders parallel or oblique to the substrate surface as shown in Figure 4.11 (a). The mobility of polymer chains depends strongly on the temperature, thus for low temperatures the phase separation seems to be unfinished after short annealing times. With longer annealing times the order will probably improve. At the optimum annealing temperature of 180 °C (Fig. 4.11 (b)), in contrast, completed phase separation resulting in well-ordered patterns can be achieved within short times. Too high temperatures leads to polymer degradation. Figure 4.11 (c) shows starting degradation of BCP67 at 190 °C. Table 4.3 summarizes the corresponding pore densities.
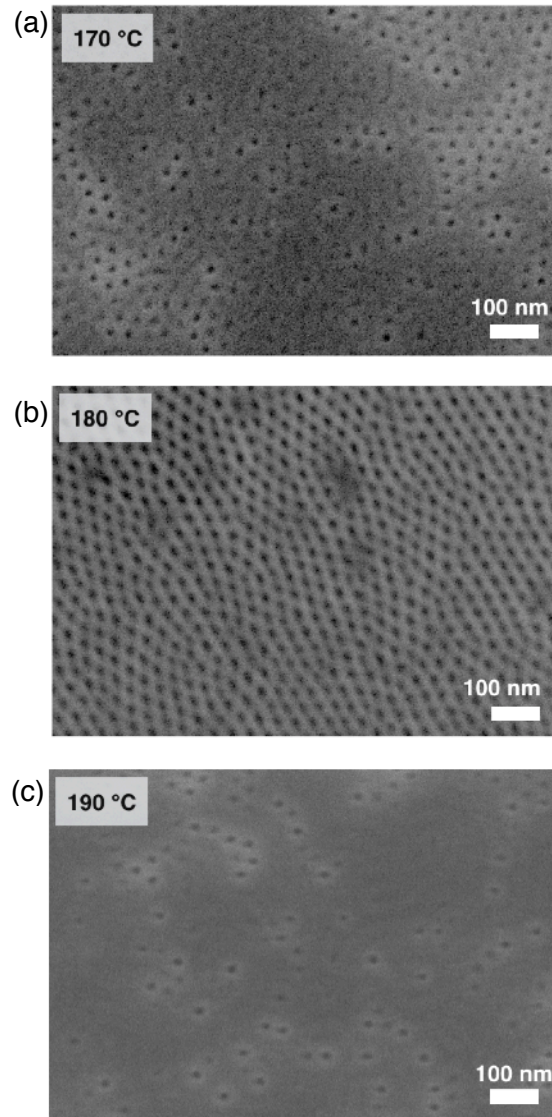
Fig. 4.11: Effect of annealing temperature on the microphase separation of BCP67. Too low temperatures (170 °C) result in unfinished phase separation, while too high temperatures (190 °C) lead to degradation of the polymer. Only at medium temperatures (180 °C) well defined cylinders are formed. (BCP 67, d = 30 nm, t = 4h)

Tab. 4.3: Nanopore characteristics after phase separation at different annealing temperatures, determined by Delaunay triangulation (see Chap. 4.2.2). Larger pores mean pores with dimensions significantly larger (> 20 %) than the actual pore diameter, mainly caused by cylinder orientation parallel to the surface. BCP thin films have a thickness of 30 nm and were annealed for 4 h at 3×10^{-3} mbar.

temperature [°C]	pore density [$\times 10^{10}$ cm^{-2}]	larger pores [%]
170	4.27	3.4
180	9.34	0.5
190	0.90	-

Annealing time. With optimized film thickness and annealing temperature, the annealing time is increased for defect minimization and domain size maximization. Detailed information about the used furnace and specifics about the temperature ramps are shown in Appendix 3. For a polymer annealing at otherwise optimum conditions (30 nm thickness, 180 °C) the pore density can increase from 9.0×10^{10} cm^{-2} to 9.2×10^{10} cm^{-2}, accompanied with a decrease of the number of very large pores from 5.1% to 4.7%. Very long annealing times (>> 24 h) can lead to polymer degradation similar to the effect at high temperatures as in Fig. 4.11 (c).

However, annealing time t and annealing temperature T both influence the polymer chain diffusion length L_D by the relation described by Equation 4.11. While the diffusion length is directly related to the annealing time, an increasing annealing temperature T increases the polymer diffusivity D

$$L_D = \sqrt{Dt} \propto e^{-C/T}\sqrt{t} \tag{4.11}$$

where C is a material dependent constant [41]. Due to the exponential dependence of L_D on the temperature, a small increase of the temperature enhances the chain diffusion length drastically. This is important as for practical reasons, it is desirable to keep the annealing time as short as possible. As a higher temperature is expected to be most efficient for the microphase separation, it is desirable to choose the highest possible temperature not showing any signs of degradation.

One has to keep in mind that the chain diffusion length also scales with the degree of polymerization: for high polymerization degrees N along with increasing chain entanglement, as apparent in the block copolymers used here, the diffusivity is proportional with $D \propto N^{-2}$ [41] and thus the chain diffusion length can be expressed by Equation 4.12

$$L_D \propto N^{-1}e^{-C/T}\sqrt{t} \tag{4.12}$$

This allows to estimate, that a higher annealing temperature/ time needs to be chosen for PS-b-PMMA BCP with higher molecular mass in order to reach similar microphase separation.

Section summary

Block copolymer lithography is an emerging techniques for the patterning of thin films with self-assembled nanoscale features. Microphase separation of PS-b-PMMA block copolymers with a block length ratio of 70:30 can be induced by thermal annealing and results in the formation of hexagonally arranged PMMA cylinders with diameters of 17 nm in a PS matrix at pore densities of up to 9.2×10^{10} cm^{-2}.

The homogeneity of resulting nanopores and their arrangement can be optimized by adjusting annealing temperature, annealing time and polymer film thickness and amount for BCP67 used here to 180 °C, 24 h and 30 nm, respectively.

4.2.4 Nanopores on random copolymer brushes

As stated above, the surface needs to be ‚neutral' to both polymer species of the block copolymer in order to promote perpendicular pattern orientation during microphase separation. To create this neutrality, surfaces can be functionalized chemically with SAMs [42] or polymer brushes [40] or modified by X-Ray or UV exposure [43, 44] avoiding an enhanced affinity of one polymer type with the substrate.

An established way to neutralize the surface is to use a polymer brush as a mediating grafting layer on the surface [27, 32]. This polymer brush is commonly built by a random copolymer (RCP) containing similar polymer species as in the BCP used. This RCP has an end group that can selectively bind to the surface, e.g. a hydroxy group for binding to oxide surfaces. The polymer chain will stretch away from the substrate surface building a dense brush layer that is, regarding its chemical composition, neutral to the BCP. The brush formation mechanism is in principle comparable to the formation of a self-assembled monolayer (SAM) [45], which is described in detail in the Chapter 3.2.

If the RCP layer is referred to as a ‚grafting layer' the RCP is covalently bonded, not adsorbed, to the substrate. The grafting density Γ_g [chains/nm^2], i.e. the number of bonded RCP molecules per surface area, is a typical measure for the RCP brush. It reaches its maximum for a molecule distance of their radius of gyration R_g (Fig. 4.12).
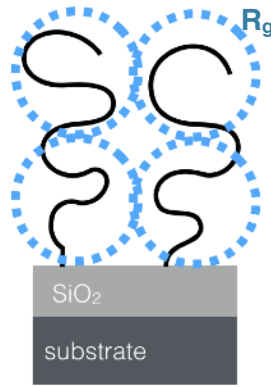
Fig. 4.12: Sketch of random copolymer (RCP) brush on SiO$_2$ surface with marked maximum grafting density determined by the radius of gyration R_g.

One typically distinguishes between a low grafting density ($\Gamma_g < 1/R_g^2$) and a high grafting density ($\Gamma_g > 1/R_g^2$). A polymer brush is defined as a grafted layer with high Γ_g [46]. The grafting density apparent in a created grafting layer can be determined [15] by:

$$\Gamma_g = \frac{H \, \rho \, N_a}{M_n}$$

(4.13)

with H the height of the layer, ρ the RCP density (commonly assumed to match the bulk density of the polymer species [15]), N_a the Avogadro constant and M_n the molecular mass of the RCP. The height of the layer is measured in the dry state. The addition of a good or poor solvent can result in polymer swelling which can induce a change from a low to a high grafting density state [47].

In this work, the polymer brush is created in a ‚grafting to' -approach, i.e. polymer chains are deposited from solution onto the surface. In contrast, in ‚grafting from'-approaches the brush molecules are created on the

surface by surface-initiated polymerization [46]. The ‚grafting to' approach is easy, however does not allow for grafting densities as high as possible in ‚grafting from' approaches, as deposited molecules from solution may hinder deposition of other molecules (analog to the defect formation in SAMs, Chap. E2). Surface characteristics, such as wettability [48] and the homogeneity of the chemical surface termination as well as of the brush thickness are strongly influenced by the grafting density and thus need to be adjusted to neutralize the surface for the following BCP lithography properly [15, 49]. Also the RCP composition, i.e. fraction of polymer species, need to be considered [50]; especially it is discussed in literature [29] that a RCP brush can adjust its conformation underneath the BCP layer in order to modulate inhomogeneities in the interfacial energies.

Experimental procedure. In this work, silicon surfaces with native oxide are functionalized with the random copolymer Polystyrene-co-polymethylmethacrylate (PS-co-PMMA) (Fig. 4.13) with a α-hydroxy and ω-TEMPO termination. The molecular weight of the RCP is $M_n = 5.3$ kg/mol with a PDI = 1.44 at a PS-content of 74 mol% (purchased from Polymer Source, Art-Nr. P19014D-SMMAranOHT, for data sheet see App. A5).
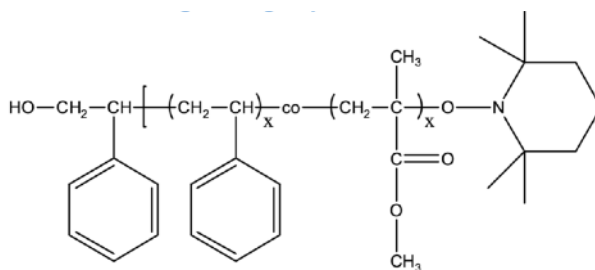
Fig. 4.13: Molecular structure of the random copolymer Polystyrene-co-polymethylmethacrylate (PS-co-PMMA) used as grafting layer.

An approximately 60 nm thick layer of the RCP solved in toluene with a concentration of 2 wt% is spin casted onto a substrate. Film thickness is controlled by ellipsometry. The sample is annealed at a temperature of 140 °C at a pressure of $1\text{-}3\text{x}10^{-3}$ mbar for 48 h. Within this annealing time the surface-nearest RCP molecules bind to the surface and form the polymer brush of a thickness of approx. 7 nm (measured by ellipsometry). The brush density increases with increasing annealing time and the grafting layer gets more homogeneous, however approaches a saturation, which should be reached in the present procedure [15]. After the annealing the samples can be stored at room temperature and at ambient atmosphere for several days. Before using the samples for the spin coating with the BCP and its annealing, the unbonded RCP is removed from the surface by rinsing the sample with toluene. This additional polymer film acts as a protective layer against oxidation of the polymer brush during storage. The unprotected brush should be covered with the BCP within several minutes.

Corresponding to Equation 4.4, the RCP used here has a radius of gyration of $R_g \approx 2.01$ nm. With Equation 4.13, the grafting density of the created grafting layer can be determined to 0.88 chains/nm^2, for the measured brush height of 7 nm and the molecular weight of 5.3 kg/mol a density of 1.11 g/cm^3 assuming that the density of the brush is equal to that of PS and PMMA in bulk [15]. Thus, the created layer matches the high grafting density criterion $\Gamma_g > 1/R_g^2 = 0.88$ nm^{-2} > 0.25nm^{-2} and a polymer brush should be apparent.
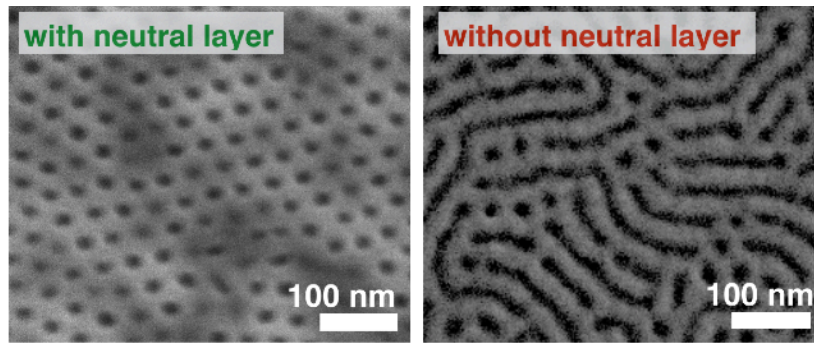
Fig. 4.14: Influence of polymer brush on cylinder orientation. Cylinders are parallel to substrate if no RCP is used on SiO$_2$ (right). With RCP brush cylinders are perpendicular to the substrate surface (left). 30 nm of BCP 67 were deposited and annealed at 180 °C for 4h.

Figure 4.14 demonstrates the influence of the neutralization of a Si/SiO$_2$ surface with a RCP on the microphase separation and the orientation of the formed patterns with respect to the surface. The bare Si/SiO$_2$ surface is not neutral for PS and PMMA. BCP lithography results in the formation of PMMA cylinders arranging themselves parallel to the substrate surface as shown in the SEM image in Figure 4.14 (right) forming a fingerprint-like pattern. Surface neutralization with the RCP, however, promotes perpendicular orientation of the PMMA cylinders as shown in Figure 4.14 (left).

4.2.5 Nanopores on various material surfaces

Very little work [51] has been reported about the investigation of the PS-b-PMMA BCP phase separation on surfaces other than Si/SiO$_2$ with or without RCP brushes or similar surface neutralization layers. However, as the interfacial energy between polymer and substrate affects the phase separation of the polymers crucially and seems to determine the orientation of PMMA cylinders in the PS matrix, experiments on different materials are discussed here.

Besides the SiO$_2$ surfaces with and without the neutralizing random copolymer brush as reference, TiO$_x$ with and without RCP and thin films of gold and platinum are used as substrates. These materials have been selected, since they are widely used in (semiconductor) devices and provide a chemical contrast to SiO$_2$. Thin films of Ti, Au and Pt (film thicknesses: 10-15 nm, for Au: 2 Ti nm as adhesive layer underneath) were deposited by electron beam evaporation onto plasma cleaned Si surfaces with native SiO$_2$. Au and Pt were also deposited by a sputter PVD process. In order to characterize the surfaces, surface energies and their polar fraction were determined by the OWRK method (App. A1) from contact angle measurements with water, diiodomethane and ethylene glycole. All results are compiled in Table 4.4.

The BCP lithography with BCP67 was examined on these surfaces at conditions optimized for neutralized SiO$_2$ surfaces as described before (polymer thickness: 30 nm, annealing temperature: 180 °C, annealing time: 24 h, chamber pressure: 1 x 10^{-3} mbar). The resulting nanoporous PS films are depicted in Figure 4.15.

Surprisingly, the non-neutralized SiO$_2$ surface is the only one evoking the PMMA cylinders to orient parallel to the substrate surface. All other surfaces seem to be neutral with respect to PS and PMMA resulting in nanopore formation perpendicular to the surface. This is in conflict with the theory explained before, that the interfacial energy $\gamma_{substrate-PS}$ between the surface and PS needs to be commensurate to the interfacial energy $\gamma_{substrate-PMMA}$ between the surface and PMMA, as all surface free energies (SFE) are quite similarly with approx. 42 mN/m. In particular, the SFE of SiO$_2$ and Au$_{evap}$ or Au$_{sput}$ are very similar, even though the pore orientation is completely different (Fig. 4.15).

Tab. 4.4: Measured contact angles (CA) with water, diiodomethane and ethylene glycol and surface free energies (SFE) determined by OWRK method of different surfaces: Silicon with native oxide with and without random copolymer, titanium (10 nm e-beam evaporated onto $Si/SiO_{2,nat}$) with native oxide with and without random copolymer, e-beam evaporated and sputter deposited gold and platinum (e-beam: 10 nm onto $Si/SiO_{2,nat}$, with 2 nm Ti adhesive promoter for Au; sputter dep.: 35 nm). Contact angles with styrene and methylmethacrylate (MMA) monomers and polymers. PS contact angles on RCP brush could not be measured due to RCP degradation at high PS melting temperatures.

		SiO_2 +RCP	SiO_2	$TiOx$ +RCP	$TiOx$	Au_{evap}	Au_{sput}	Pt_{evap}	Pt_{sput}
CA [°]	H_2O	80	54	78	75	92	95	68	109
	CH_2I_2	42	58	49	47	24	28	44	41
	EtGly	57	42	58	53	59	67	47	55
SFE [mN/m]		39	48	36	39	46	45	40	39
	polar	9 %	46 %	14 %	7 %	0.1 %	0.1 %	12 %	0.2 %
CA [°]	Styrene	0	18	3	16	2	3	4	3
	PS	-	19	-	3	2	18	12	5
	MMA	0	0	4	0	0	0	0	0
	PMMA	21	32	24	24	23	33	23	23

In order to understand the interactions between the individual polymer species of the BCP with the substrates, contact angles (CA) of the polymers PS and PMMA and their monomers styrene and MMA on the substrates were measured. CA with the monomers styrene and MMA are easily accessible as the monomers are liquid at room temperature. MMA wets all surfaces completely, while styrene shows exceptions on bare SiO_2 and TiO_x surfaces, which show a significant difference in their wettability with MMA. As the behavior of the monomers is not directly to be transferred to the polymers, contact angles of the polymers with the substrates were measured as well. As the polymers are solid at room temperature small amounts of the polymer powders were deposited onto the surfaces and annealed at temperatures above the polymer melting points for approx. 5 h (PS: 240 °C, PMMA: 160 °C) in air.

Contact angle measurements show the wettability of PMMA is quite similar for all surfaces, however PS, again, shows some deviations for SiO_2 and Au_{sput} surfaces. As a general trend, the contact angles of PMMA are always larger than the contact angles of PS on the same surface. Nevertheless, the measurements cannot explain the peculiar influence of SiO_2 surfaces on the orientation of cylinders (Fig. 4.15), since e.g. Au_{sput} shows almost the same contact angles as SiO_2 and also Pt_{evap} is very comparable to Au_{sput}. Thus in total, the results indicate that the total surface free energy SFE does not exclusively determine the cylinder orientation. However, the polarity of the surfaces, i.e. the polar contribution to the SFE, significantly differs for the SiO_2 surface from all other material surfaces. The bare SiO_2 shows a high polar fraction of 46 %, while all other surfaces are nearly completely disperse. This point indicates that the surface polarity has a major influence on the cylinder orientation. A study [52] using different neutralization layers on SiO_2 surfaces comes to a similar conclusion.

Figure 4.15 shows, that no neutralization layer is needed for the nanopore formation on TiO$_x$ surfaces or metal surfaces from gold and platinum. However, even though the cylinder orientation is perpendicular for these surfaces, the size of the nanopores differs on different substrate materials. The pore size distribution of the nanopores on the SiO$_2$ surface with RCP, on TiO$_x$, Au and Pt determined by numerical image evaluation are shown in Figure 4.16. The average pore diameters (with standard deviation) reach from (16.5 ± 3.9) nm for TiO$_x$, (16.8 ± 2.9) nm for SiO$_2$+RCP, (17.4 ± 3.2) nm for Pt to (18.0 ± 2.5) nm for Au. Such deviations are probably due to an adjustment of the polymer system to the surface energies [27]. As stated in Equation 4.9, the free energy of the polymer system during microphase separation can be understood as the sum of the PS-PMMA interactions F$_{mix}$, the interfacial energies F$_{interface}$ towards air/ vacuum and the substrate, respectively, and the elastic free energy of the chains F$_{elast}$. Here, F$_{mix}$ and interactions at the air interface are expected to be constant for all experiments on the different surfaces. The energy contribution of the interface with the substrate determines mainly the pattern orientation as discussed in detail at the beginning of Chapter 4.2. This energy, in addition to the elastic energy, probably results in deviations of the pattern shape and size. Is it discussed in [27] that in addition to F$_{interface}$ an adjustment of F$_{elast}$ can allow for a new equilibrium on surfaces with slightly varying surface energy or inhomogeneities. The adjustment can be understood as a flexible stretching of the polymer chains.
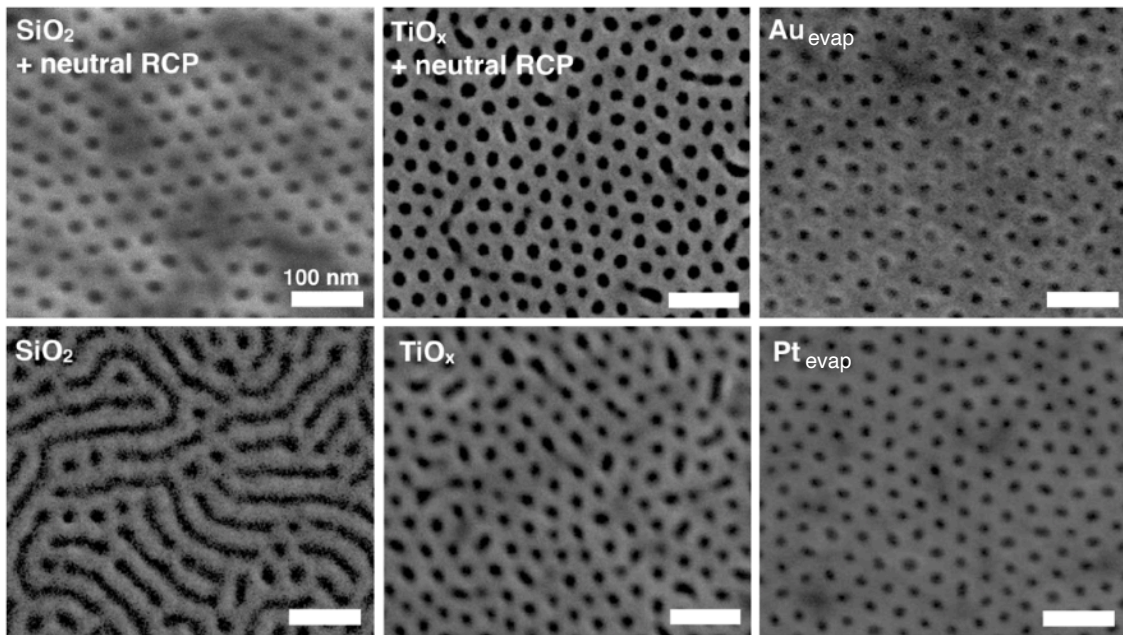
Fig. 4.15: SEM images of nanoporous PS matrices after BCP lithography on several material surfaces: Si with native SiO$_2$ with and without neutralizing RCP layer. TiOx (10 nm e-beam evaporated onto Si/SiO$_{2,nat}$), oxidized at ambient atmosphere with and without neutralizing RCP layer, Au (10 nm e-beam evaporated onto Si/SiO$_{2,nat}$) and Pt (10 nm e-beam evaporated onto Si/SiO$_{2,nat}$). Scale bars for all images are 100 nm.
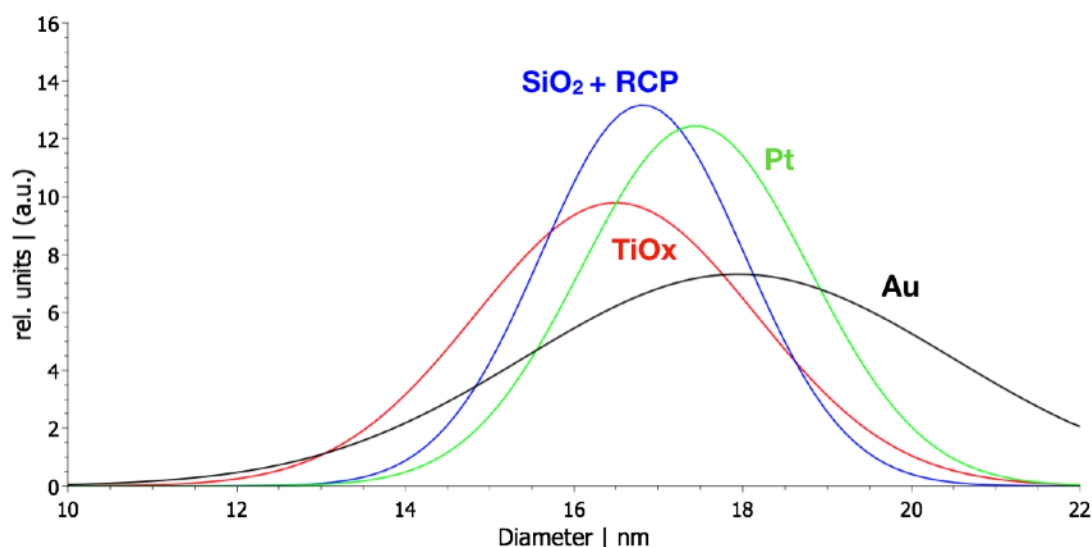
Fig. 4.16: Diameter distribution of nanopores after BCP lithography on different substrates (Au_{evap}, TiO_x, SiO_2 + RCP, Pt_{evap}). Diameters are analyzed by the image evaluation software described in Chapter 4.2.2 of corresponding SEM images from Figure 4.15. Size distribution on Au appears very broad as software analysis suffers from bright contrasts at pore rims due to charging in the SEM.
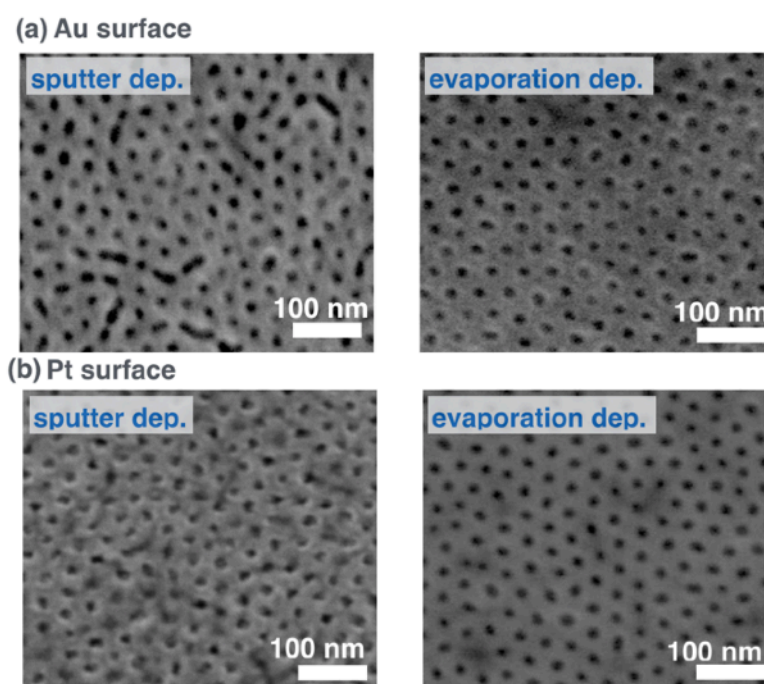
Fig. 4.17: SEM images of nanoporous PS matrices on gold (a) and platinum (b) surfaces prepared by different PVD techniques. Nanopores on rougher sputter-deposited films appear smaller and more irregular in shape than on smooth electron-beam evaporation deposited films. Sputter deposited films: 35 nm thickness, evaporated films: 10 nm thickness.

All metal thin films in Figure 4.15 are prepared by electron beam evaporation. Due to the choice of this deposition technique all films are very smooth. Sputter deposited films, in contrast, are usually rougher. Figure 4.17 shows that this also affects the nanopore formation.

The nanopores on e-beam deposited smooth surfaces appear very homogeneous and round-shaped. The pore diameters both on gold and platinum surfaces are with about 18 nm similar to the feature sizes on SiO_2 surfaces. The R_{rms} roughness of the electron beam evaporated metal surfaces was determined by AFM and is approx. 0.5 nm. On the rough sputter-deposited surfaces, however, nanopores are irregularly deformed. It should also be noticed that the average pore diameters are with approx. 15 nm smaller than on smooth surfaces (18 nm). Higher pore densities can be reached on the rougher surfaces with 8.8 x 10^{10} cm^{-2} in contrast to an average density of 8.4 x 10^{10} cm^{-2} on smooth surfaces. These results are summarized in Table 4.5. As a conformal coverage of a rough surface probably leads to stretched polymer chains, it is assumed again that F_{elast} is responsible for the smaller pore sizes on rough surfaces.

Tab. 4.5: Nanopore feature sizes after BCP lithography on metal surfaces. Root mean square (rms) roughnesses R_{rms} of sputter- and electron beam evaporation deposited gold and platinum films are measured by AFM.

	Au_{evap}	$Au_{sputtered}$	Pt_{evap}	$Pt_{sputtered}$
pore density [x10^{10} cm^{-2}]	7.1	8.8	8.4	8.8
pore size [nm]	18.0 ± 2.5	14.4 ±1.7	17.4 ± 3.2	15.7 ± 2.4
R_{rms} roughness [nm]	0.4	5.6	0.6	1.2

Section summary

The application of ordered nanopores in the PS thin films for lithographic surface modification requires an orientation of the PMMA cylinders perpendicular to the substrate surface. Here it is shown for the first time that surfaces of TiO_2/Ti, Au and Pt can be patterned with vertical nanopore arrays. Surprisingly, this works even without the need for a neutralizing surface layer, unlike for SiO_2/Si surfaces.

Surface free energies (SFE) of the substrate and interfacial energies with PMMA and PS are analyzed by contact angle measurements. The orientation of PMMA cylinders during microphase separation is observed to be mostly determined by the polar fraction of the SFE. Ordered nanoporous PS films are favorably created on unpolar surface, such as Au, Pt or TiO_x. The influence of surface roughness on the homogeneity of the nanopores shape and the pore density is discussed for these surface materials. For more polar surfaces such as SiO_2, the surface can be functionalized with a random copolymer brush forcing the BCP into perpendicular cylinder orientation.

4.2.6 Nanopores with home-made polymers

The phase separation of home-made PS-b-PMMA block copolymers is investigated in this section. The BCP lithography with these polymers is expected to show other microphase separation motives than cylinders, as the polymers are located in different regions in the phase diagram.

The block copolymers BCP20, BCP34 and BCP56 were synthesized at the Department of Chemistry at Paderborn University in the „Organic and Macromolecular Chemistry" group of Prof. Dr. Dirk Kuckling by Dr. Artjom Herberg and Tarik Rust.

The polymer synthesis was performed by means of a ‚reversible addition-fragmentation chain transfer (RAFT) polymerization' and polymers were analyzed by NMR, SEC and DSC (specifications App. A5). All investigated block copolymers are tagged in Figure 4.18 in the PS-b-PMMA phase diagram and polymer data are summarized in the table for better classification. BCP67, the commercially available polymer described before, is included as a reference. The home-made BCP20, BCP34 and BCP56 mainly differ in their block length ratios f_{PS} and their total molecular weight M_n. BCP20 and BCP34 are located in the disorder region of the phase diagram due to their low molecular weights. The BCP56 with higher molecular weight has a larger PS fraction, thus hits the phase of spherical polymer separation.

	●BCP20	●BCP34	●BCP56	●BCP67
M_n [kg/mol]	20.2	34.0	55.8	67.1
f(PS) [%]	57	74	79	69
PDI	1.38	1.31	1.21	1.09
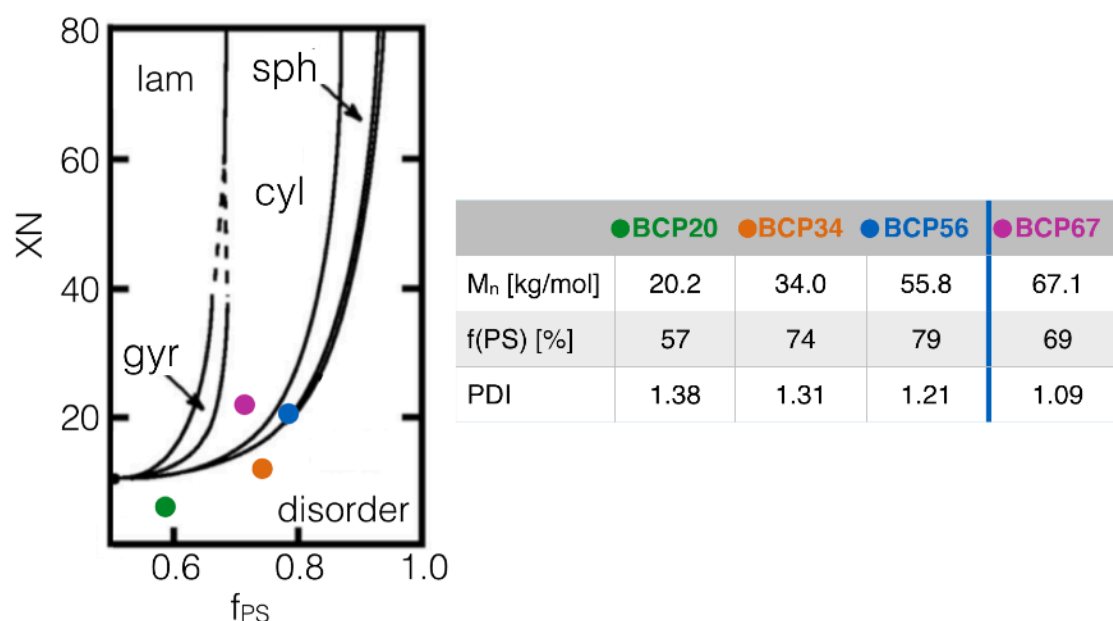
Fig. 4.18: Phase diagram of PS-b-PMMA (based on [26]). BCP67 is the commercially available polymer and marked as reference. Polymers BCP56, BCP34 and BCP20 are home-made by RAFT polymerization. Specifications are listed in the Table.

Synthesis of PS-b-PMMA by RAFT. The ‚reversible addition-fragmentation chain transfer polymerization' (RAFT) [53] allows for the synthesis of polymers with controlled molecular weight and low PDI. The chain growth is mediated by a chain transfer agent (CTA). The CTA forms a radical intermediate RAFT adduct, which rapidly interchanges growing polymer chains. A typical CTA, also used here, is 2-(2-Cyanopropyl)-dithiobenzoat (CPDB), which is suitable for the polymerization of both PMMA and PS (Fig. 4.19 (a)).

In the first step the PMMA block is synthesized. 1.064 ml (10 mmol) MMA, 2.46 mg (0.015 mmol) azobis(isobutyronitril) (AIBN) and 22.1 mg (0.1 mmol) CPDB are dissolved in 1.5 ml 1,4-Dioxane under argon

atmosphere. After flushing the reaction mixture for 15 min with argon, polymerization is started at a temperature of 70 °C. The reaction is stopped after 24 h by freezing in liquid nitrogen, solvents are removed by rotary evaporation. The polymer is redispersed in tetrahydrofurane and precipitated in diethylether in an aceton-freezer. The product (Fig. 4.19 (b)) is filtered and dried in vacuum.

In a second step, this synthesized PMMA from step one is used as a PMMA macro initiator for the subsequent growth of the PS block. 87.9 mg PMMA macro-CTA, 1.0 mg (6.1 µmol) AIBN and 0.6 ml (4.89 mmol) styrene are flushed with argon for 15 min and polymerized at 70 °C for 24 h. The reaction is stopped by freezing in liquid nitrogen. The pink, highly viscous product is dissolved in THF and precipitated in methanol at room temperature. The product (Fig. 4.19 (c)) is filtered and dried in vacuum.
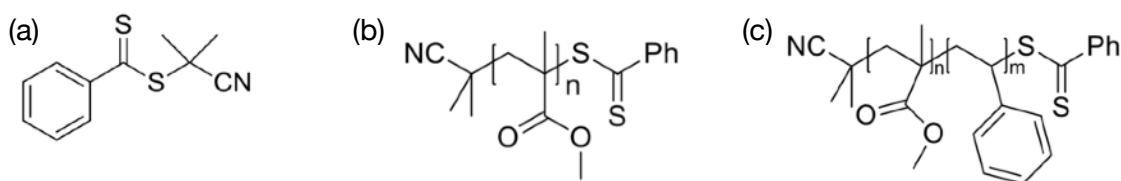
Fig. 4.19: (a) Chain transfer agent, (b) PMMA macro initiator, (c) PS-b-PMMA.

The synthesized BCPs are analyzed by NMR for determination of the block length ratio and molecular composition, by SEC for the molecular weight distribution and DSC for phase transition temperatures. Quantities are given for the synthesis of BCP56, all other PS-b-PMMA BCPs are synthesized in an analogous way.

BCP lithography with home-made BCPs. These block copolymers are treated for BCP lithography as described for the BCP67. The same RCP polymer brush is used, even though it is to note, that ideally the grafting layer should be adjusted to the polymers. Annealing temperature, annealing time and BCP film thickness are varied for parameter optimization as stated above for BCP67.

BCP20. The BCP20 is a PS-b-PMMA BCP with a polystyrene fraction of 57 %. The PDI is with 1.38 quite large. Due to the small molecular weight of 20.2 kg/mol, a proper phase separation cannot be predicted (see phase diagram Fig. 4.18).
The substrate is covered with the RCP grafting layer, as described above. The BCP20 is dissolved in toluene at 1 wt%. The film thickness was set to 36 nm and 51 nm, respectively. The sample was annealed for 7 h at 180 °C at a pressure of 1×10^{-3} mbar. The phase separated film was exposed to UV light for 20 min and afterwards, the PMMA was removed with acetic acid for 30 min at room temperature.
This procedure results in a phase separated sponge-like polystyrene matrix as shown in Figure 4.20 (a). Image analysis with the image analysis software of Chapter 4.2.2 determined the pore density to 6.1×10^{10} cm^{-2}. The pore size is broadly distributed around (19.4 ± 6.2) nm, with 28 % of pores having an elongated shape and being too large. The two different BCP film thicknesses show no significant difference in morphology. Increasing the annealing temperatures could improve the result, however, from its position in the phase diagram, no ordered formation of PMMA cylinders in a PS matrix can be expected. The results resemble a gyroidal-like material separation, however with varying PMMA diameter, most likely due to the large PDI. PMMA domains form a network within the PS matrix, as depicted in Fig. 4.20 (b). A cut through such a gyroidal pattern is expected to show a surface morphology as in Fig. 4.20 (a) with a broad size distribution of partially cut PMMA domains with irregular shape.

Such gyroidal networks create nanoporous PS films with large surface/volume ratio. The channels can be selectively filled acting as a template or be used for sensing applications.
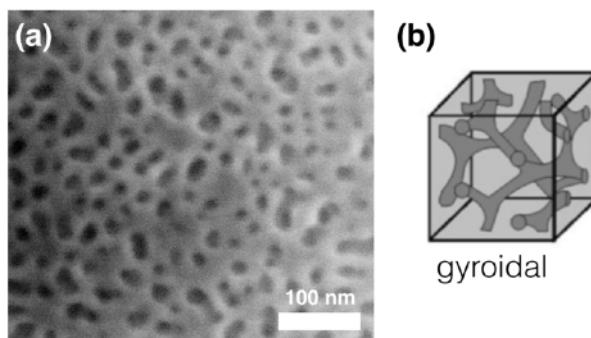
Fig. 4.20: (a) SEM image of BCP20 showing a gyroidal-like phase-separation behavior. A 36 nm thick polymer film was annealed at 180 °C for 7 h. PMMA was removed using acetic acid. (b) Sketch of a gyroidal phase separation [26].

BCP 34. The BCP34 is a PS-b-PMMA with a polystyrene fraction of 74 %. The PDI is with 1.31 still large, but with a higher molecular weight of 34 kg/mol, its position in the phase diagram is closer to the cylinder-in-matrix formation regime.

For parameter optimization in BCP lithography, samples with film thicknesses of 40 and 50 nm, annealing temperatures of 170 °C, 180 °C and 190 °C and times of 3 h and 19 h are prepared.

The variation of the film thicknesses does not show a crucial difference in the phase separated patterns. However with a thickness of 50 nm the pore densities are slightly higher and the pore shape is more distinct. The variation of annealing temperature shows highest pore densities at 170 °C. For 180 °C the pore shape and size is very inhomogeneous, possibly due to starting degradation. The degradation decreases the pore density drastically for 190 °C. Temperatures lower than 170 °C are not likely to improve the result as no starting degradation is visible at this temperature.
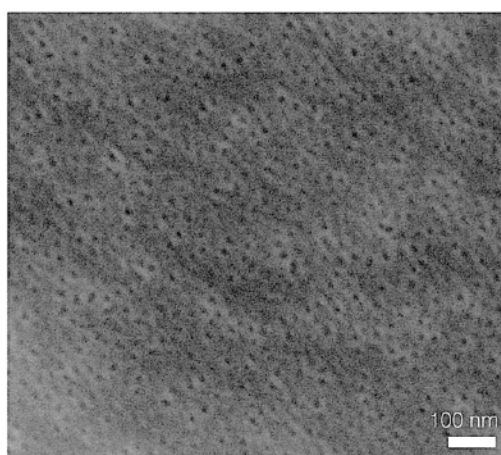
Fig. 4.21: SEM image of BCP34 prepared with best parameters. Polymer is deposited with a film thickness of 50 nm and annealed at a temperature of 170 °C for 3 h. PMMA was removed by acetic acid.

Best results for the BCP34 (Fig. 4.21) are achieved with a polymer thickness of 50 nm and an annealing temperature of 170°C. As expected the quality increases further with increasing annealing time. The maximum pore density reached is $9.0\text{x}10^{10}$ cm^{-2} , the mean pore diameter is measured to be (15 $\pm$ 5) nm, thus broadly distributed with 5% of pores being larger than the average. Besides, the pores are not regularly hexagonally arranged. However, as the phase diagram predicts a phase separation without order, the result is good and probably cannot further be improved.

BCP 56. With a small PDI of 1.2, a quite high molecular weight of 56 kg/mol and a PS fraction of 79 %, BCP56 is placed in the spherical phase region in the phase diagram (Fig. 4.18) and thus should result in a formation of bcc ordered PMMA spheres in a PS matrix.

For parameter optimization the polymer film thickness is set to either 25 nm or 30 nm. In all cases, spherical (or cylindrical) volumes are observed. No significant difference can be seen for different film thicknesses (Fig. 4.22 (a+d)). Pore densities are quite similar with $9.1\text{x}10^{10}$ cm^{-2} and $9.2\text{x}10^{10}$ cm^{-2}, respectively. However for a thickness of 30 nm, the pores are slightly more homogeneous in size and shape.

The annealing temperature is varied in Figure 4.22 (a-c) between 140 °C and 170 °C at a fixed film thickness of 30 nm. With increasing temperature the pore density decreases and the pores become more inhomogeneous. This is due to proceeding polymer degradation. For the lowest temperature of 140 °C, phase separation is most homogeneous. The pore density is $9.2\text{x}10^{10}$ cm^{-2} with only 5% of pores being significantly larger than (16 $\pm$ 5) nm. Whereas for 160 °C, the pore density already decreased to $5.0\text{x}10^{10}$ cm^{-2}. The mean diameter is (20 $\pm$ 6) nm with a broadly distributed pore size of 37 % of significantly larger pores. Some regions of the sample are free of pores as degradation destroyed all patterns. For 170°C (not shown here) only single pores can be found.
An increase of the annealing time from 4 to 6 h at optimum conditions (140 °C, 30 nm film thickness) increases the pore density slightly and less pores are significantly larger (Fig. 4.22 (e)).

The appearance of the nanopores after the phase-separation is quite similar to that of a BCP in the cylindrical regime. However, the evaluation of the coordination numbers indicates that no phase separation into hexagonal patterns occurred. The distribution of coordination numbers is uniform between 4 and 6. This is quite unlikely for a cylinder-like phase-separation which shows a favored 6-fold coordination even if BCP pore sizes and orientations are not optimal. The lack of hexagonal arrangement is in agreement with the BCPs placing in the phase diagram. The PMMA spheres in the PS matrix are supposed to arrange themselves in a body-centered cubic cell (Fig. 4.22 (f)). As PMMA spheres embedded in the PS can not be removed by UV exposure and development in acetic acid, these spheres are probably not visible, thus a more square-like arrangement is expected.
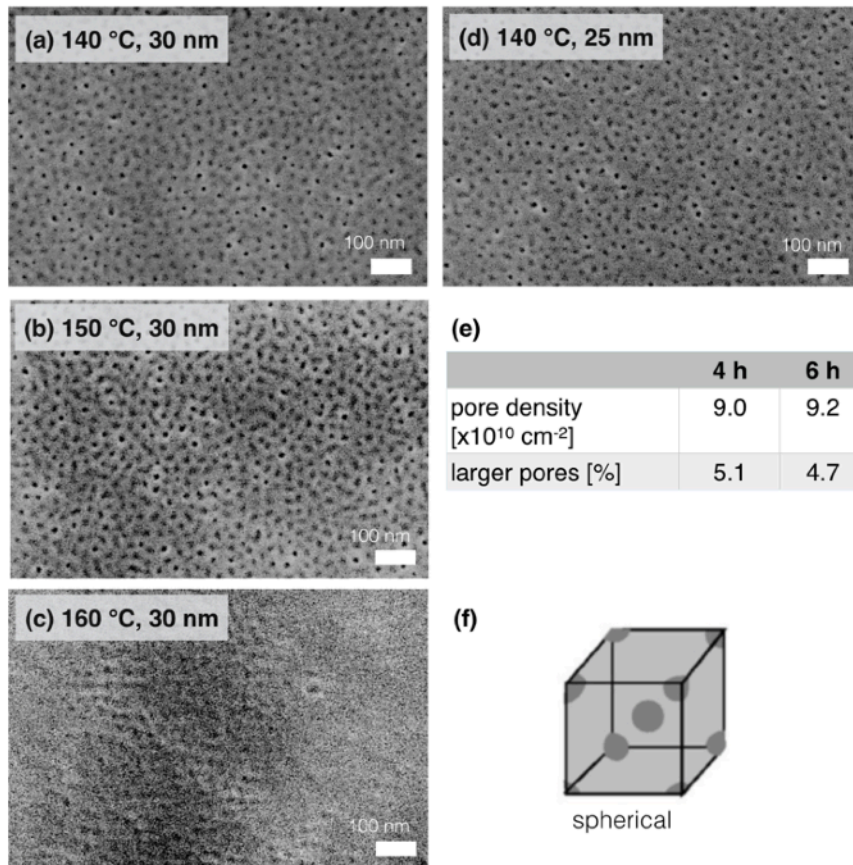
Fig. 4.22: (a-d) SEM images of BCP56 annealed at different temperatures and film thicknesses. In (a-c) annealing temperatures are varied between 140°C - 160°C, the film thickness is fixed to 30 nm, annealing time to 4 h. (d) Smaller film thickness of 25 nm, annealing temperature was 140 °C, annealing time 4 h. (e) Influence of increasing annealing time on pore density and size homogeneity for annealing at 140 °C and 30 nm film thickness. (f) Body-centred cubic unit cell of the expected PMMA spheres in PS matrix (from [26]).

4.3 Nanopore pattern transfer by reactive ion etching

Block copolymer thin films patterned by microphase separation and selective removal of one polymer species can be used as a lithography mask for the pattern transfer into a substrate. Here, the polystyrene mask with nanopores is used as an etching mask in a reactive ion etching process for the pattern transfer into a silicon substrate with native oxide. To this end, a plasma of 10 sccm CF_4 and 40 sccm N_2 is applied at room temperature in a ‚Plasma Sentech SI591'. This etching process is explained in detail in [54-57], the work was done in collaboration with Dr. Rosaria Puglisi and Dr. Cristina Garozzo from IMM-CNR in Catania, Italy.

To remove residuals of the polymers (BCP and RCP) from the surfaces, substrates are cleaned by a RCA process (see App. A2). This surface cleaning does not only result in a more homogeneous and smoother surface topography but also in a better wettability of the surface with water. This is shown in the SEM images in Figure 4.23 (a+c). Insets in (a+c) show contact angles with water. Schematics in (b+d) illustrate the layer system in cross-section with and without polymer residuals. Right after RIE the sample surface morphology is irregular (Fig. 4.23 (a)). Nanopores (dark spots) are barely visible, inhomogeneous polymer residuals cover the plane substrate surface. Contact angle measurements show that the surface is slightly hydrophobic with a contact angle of 84° (inset in (a)). After surface treatment with the RCA process the surface appears smoother, pores are clearly visible and the contact angle is decreased to 30° (inset in (c)).
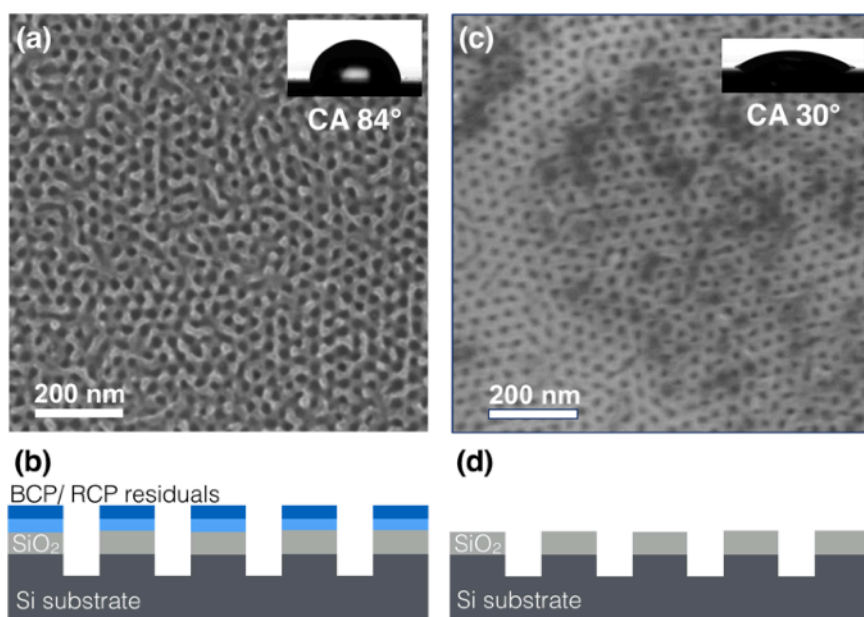
Fig. 4.23: Schematics (bottom) and SEM images (top) of the Si/SiO$_2$ surface patterned with nanopores formed by BCP lithography after pattern transfer into the substrate. (a+b) Right after the pattern transfer PS residuals cover the plane surface areas, leading to a contact angle with water of 84° (inset). (c+d) After cleaning the sample with an RCA process PS residuals are removed and the contact angle is decreased to 30°.

4.4 Placement of colloidal Au nanoparticles in nanopores

Gold nanoparticles (Au NPs) are important building blocks in nanotechnology as they can be used as catalyst for semiconductor nanowire growth or for plasmonic applications. For such experiments, the control of nanoparticle size, position and density is crucial. This chapter gives an example of how the nanopores created by block copolymer lithography and subsequent pattern transfer into SiO_2 by reactive ion etching can be used as topographic traps for the precise placement of nanoparticles on large-area surfaces at high particle densities.

Here, Au NPs with diameters of 5 nm or 10 nm, respectively, from colloidal suspensions are deposited site-selectively inside the nanopores. The use of colloidal NPs is interesting, as these suspensions can be easily produced e.g. by wet chemical Turkevich synthesis [58, 59] or laser ablation [60] in large amounts at low cost. Others show, how lift-off processes with nanopore masks and physical vapor deposited metal films can be used for nanoparticle positioning [49]. Processes involving high-temperature thermal thin film dewetting, however, are not well suited for the material combination of Au NPs on Si/ SiO_2 surfaces, as was shown in [56] that Au indiffusion into the Si is likely to occur, disabling the use of Au NPs as catalysts. However, the colloidal nanoparticles, if wet chemically synthesized, can be transported without the need of high temperatures and placed into sealed off SiO_2 pores, as will be shown here. Among the benefits of the technique proposed here is also that it does not need vacuum processing steps and that the colloids have a very narrow size and shape distribution, which is not easy to achieve in a PVD lift-off process.

Here, the doctor blade technique (Chap. 2.2) is used for the site-selective deposition of colloidal Au NPs into the SiO_2 nanopores. This is done in analogy to the creation of polymer sphere monolayers by convective self-assembly at a moving triple phase boundary (liquid, solid, gas), as explained in detail in Chapter 2. The influence of the NP concentration in the suspension, the deposition velocity and the substrate temperature are investigated in order to increase the fraction of nanopores filled with Au NPs. For better understanding of the deposition process of the NP into the nanopores, some thoughts on the wetting state of the nanopores are presented in the discussion of results.

4.4.1 Au nanoparticle deposition by doctor blade technique

Substrate patterning with nanopores. Silicon surfaces with 15 nm wet thermal SiO_2 are covered with a PS-co-PMMA random copolymer grafting layer and a PS-b-PMMA block copolymer thin film as stated above in Chapter 4.2. The BCP67 is used at a film thickness of 30 nm and microphase separated at 180 °C for 24 h at a pressure of 3 x 10^{-3} mbar, resulting in the formation of vertical PMMA cylinders in a PS matrix. Samples are then exposed to UV light for 20 min and developed in acetic acid for the selective removal of the PMMA cylinders. The nanostructured PS thin film acts as etching mask during a subsequent reactive ion etching process, by which the nanopores are transferred into the SiO_2 surface and etched down to the silicon. The PS residuals are removed by an RCA process which also results in a surface hydrophilization. Details can be found in Chapter 4.3 and Appendix A2.

Gold nanoparticles. A standard routine for the preparation of Au nanoparticles is the Turkevich approach [58, 59]. This process is based on the reduction of gold chloride with sodium citrate. Control over the concentration of chloroauric acid within the synthesis allows for a control over the particle diameter, ranging tyically between few and few ten nm [61]. The particles are surrounded by a citrate shell as residual from the synthesis, which also stabilises the particles in the suspension due to a negative surface charge [62].

Here, two aqueous monodisperse Au colloid suspensions (Tab. 4.6) are used: Au NPs with a diameter of 5 nm (CV < 15%) at a concentration of 5.0×10^{13} ml^{-1} and Au NPs with 10 nm diameter (CV < 10%) at a concentration of 5.7×10^{12} ml^{-1}, respectively. In both suspensions the Au NPs are citrate stabilized.

Tab. 4.6: Specifications of gold nanoparticle suspension. Material system, NP diameter, particle concentration, coefficient of variation (CV) of the size distribution and supplier are listed.

	Material solid/ liquid	Diameter [nm]	solid content [#/ml]	CV [%]	Supplier [Article number]
A	Au (citrate stab.) /water	5	5.0×10^{13}	< 15	Ted Pella [15702]
B	Au (citrate stab.) /water	10	5.7×10^{12}	< 10	Ted Pella [15703]

Au NP deposition by doctor blade technique. The general procedure of the doctor blade process is similar to that of the polystyrene sphere monolayer production in Chapter 2.2. A suspension droplet with a volume of (10-150) µl, depending on the sample size of typically (1-6) cm^2, is deposited onto the nanopore-patterned surface. Due to the good wettability of the sample surface (Chap. 4.3) the droplet spreads over the whole sample surface. The droplet is drawn over the surface with a velocity of the sample stage of 1 µm/s, 5 µm/s or 23 µm/s, respectively, the sample temperature is varied between room temperature (24 °C) and 43 °C, the relative humidity is kept constant at (45 ± 5) %. In a series of experiments particle concentration was systematically increased stepwise from the initial concentration by partial evaporation of the liquid medium on a hotplate at 40°C.

Data evaluation. High-resolution scanning electron microscopy (App. A3) images, are used to evaluate the Au NP deposition into the nanopores. A filling degree, i.e. the percentage of filled pores with respect to the total number of pores, is introduced for better comparability.

The total number of pores is determined numerically [37] as described above (Chap. 4.2.2). The number of pores filled with at least one Au nanoparticle is counted manually as the contrast in grey scale between Au NPs and plane surface areas is too low to be evaluated with the software. Exemplarily some Au NPs are marked by arrows in Fig. 4.24. For each determined value of pore filling degrees a sample area of approx. 3 µm^2 is analyzed.
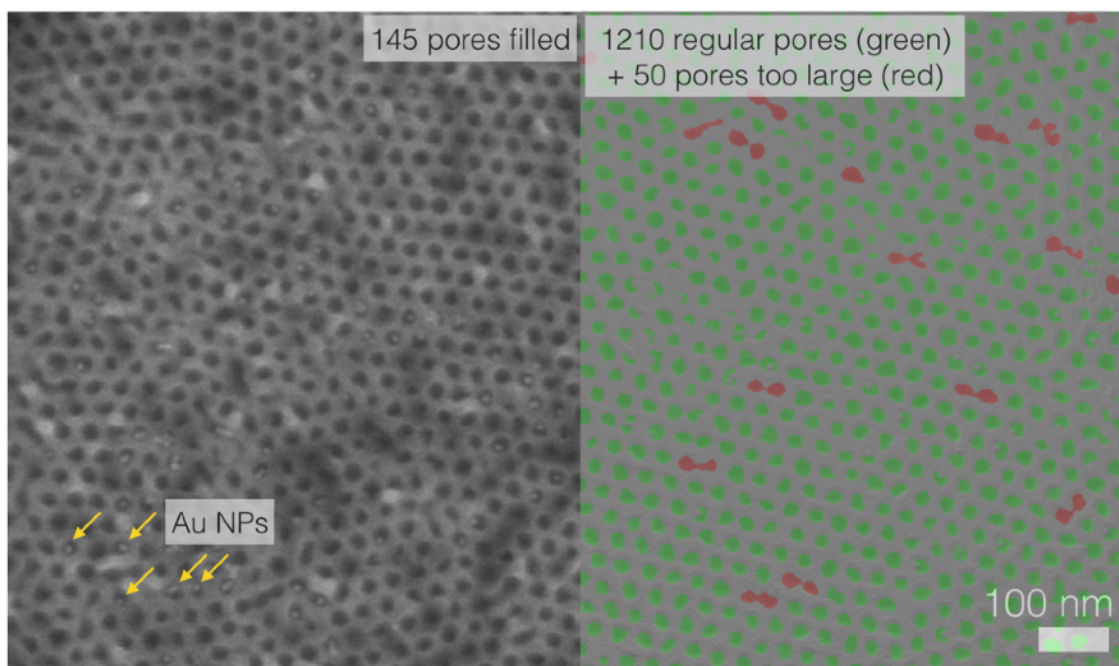
Fig. 4.24: SEM image of nanopores in SiO_2 created by BCP lithography with 11 % of nanopores selectively filled with 10 nm Au nanoparticles by convective self-assembly (24 °C substrate temperature, doctor blade velocity 5 µm/s, Au particle concentration 5.7×10^{12} ml^{-1}). Image overlay on the right showing numerically determined pores. 1210 regular sized pores are found and marked in green, 50 pores are too large and marked in red. 145 pores filled with at least one Au NP are counted manually.

4.4.2 Nanopore filling degree as a function of particle concentration and evaporation flux

The BCP lithography allows for the creation of high nanopore densities of up to 9.4×10^{10} cm^{-2} (specific to the BCP). In order to fill all of these nanopores with gold nanoparticles, a similarly large amount of nanoparticles is needed. Typical commercially available and stable Au NP suspensions are very dilute with concentrations of, in the present work, 5.7×10^{12} ml^{-1}. With a rough estimate for the pore volume a simple filling of pores with suspension would maximally result in the filling of 15 out of 10^6 nanopores with one Au NP. Thus, in order to fill high percentages of nanopores with NPs, a crucial increase of the NP concentration is necessary.

In the convective self-assembly of colloids described in Chapter 2.1, colloidal particles are transported from the bulk of a suspension droplet on a solid surface to the triple phase boundary due to evaporation fluxes. The particle concentration increases drastically at this triple phase boundary, where colloidal particles then form close-packed (mono-) layers. This effect of particle transport towards the substrate is exploited here.

A pore filling degree of 11 % as shown in Figure 4.24 is e.g. obtained after convective self-assembly of 10 nm Au NPs from the suspension with a particle concentration of 5.7×10^{12} ml^{-1}. In order to increase the filling degree further some assumptions can be made based on Equation 2.6 by Dimitrov et al. [63], discussed in Chapter 2.1.4, which describes the growth rate v of (2D-) colloidal crystals from suspensions at the triple phase boundary. According to this, one can either adjust the velocity of the doctor blade (i), enhance the particle volume fraction µ (ii) or increase the evaporation flux j_v (iii) in order to obtain enhanced pore filling.

(i) The adjustment of the velocity cannot be achieved here, as velocities as slow as needed for the deposition of the Au NPs, cannot be reached due to technical limitations. Thus, the velocity is kept constant during all following experiments at 5 µm/s. Experiments have shown, that at velocities of 23 µm/s basically all pores remain empty. At the minimum velocity for the present setup of 1 µm/s, the stage velocity was not sufficiently constant. The approaches (ii) and (iii) are investigated in the following. For (ii), the particle concentration in the suspension is increased by partial evaporation of the suspending medium prior to the experiment. For approach (iii), the evaporation flux is increased indirectly by increasing the sample temperature.

Influence of particle concentration. In order to investigate the influence of the particle concentration in the suspension all parameters of the doctor blade procedure are kept constant: the sample velocity is set to 5 µm/s, the sample temperature is held constant at room temperature (24 °C), the relative humidity is fixed at (45 ± 5) %. The particle concentrations however are varied as listed in Table 4.7.

Tab. 4.7: Concentrations of Au NP suspensions. Initial concentrations from supplier are marked in blue. Higher concentrations are obtained by partial evaporation of the liquid.

concentrations 5 nm Au NPs [ml^{-1}]	concentrations 10 nm Au NPs [ml^{-1}]
5.0×10^{13}	5.7×10^{12}
7.0×10^{13}	6.0×10^{12}
1.1×10^{14}	6.1×10^{12}
$> 5.0 \times 10^{14}$	1.0×10^{13}
	1.2×10^{13}
	$> 5.7 \times 10^{13}$

The initial concentrations (marked blue) are given by the manufacturer. From here, defined fractions of the liquid are evaporated to reach higher particle concentrations. The evaporation is performed at 40 °C on a hot plate for up to 24 hours. The highest concentrations are estimated, here 90 vol% of the liquid are evaporated.

The pore filling degrees resulting from particle deposition experiments with suspensions of these concentrations are plotted in Figure 4.25 (a+b) for the 5 and 10 nm Au NPs, respectively. For lowest particle concentrations of both NP sizes the pore filling is about 10 % as shown for the 10 nm NPs in the SEM image in Figure 4.25 (c). For the 10 nm Au NPs, a slight increase of the concentration to up to twice the initial concentration increases the achieved pore filling degree to up to 27% (Fig. 4.25 (b)).
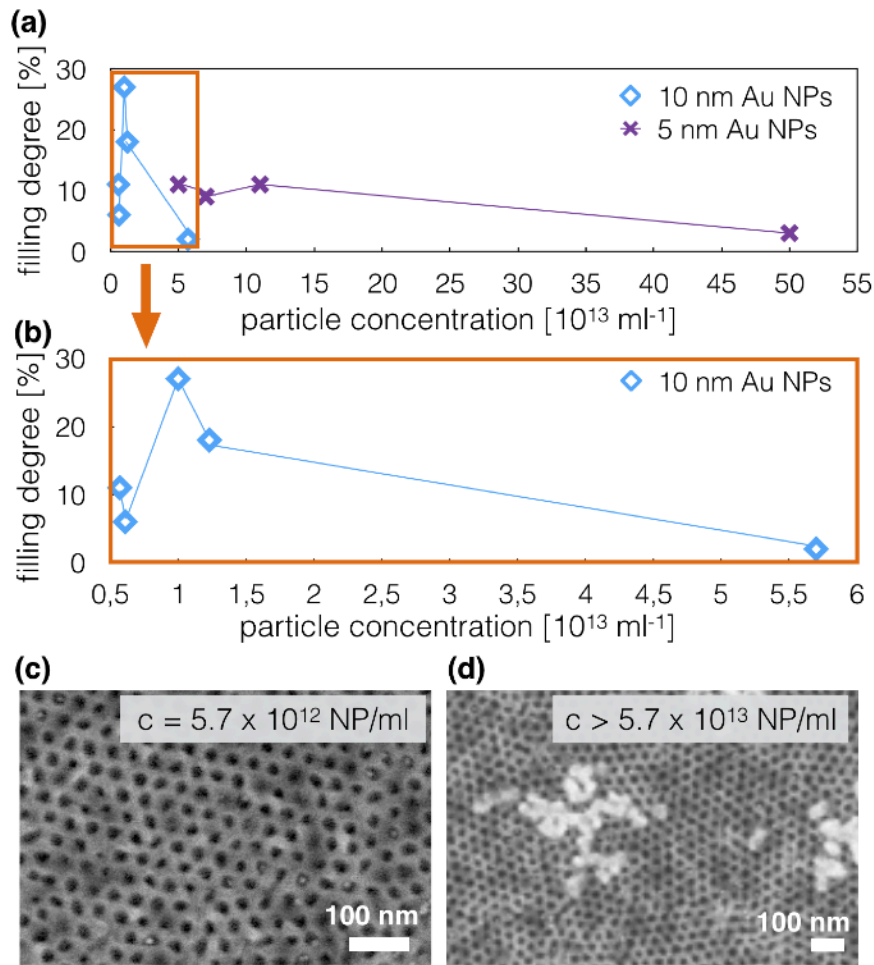
Fig. 4.25: (a) Filling degree of nanopores filled with at least one Au NP of 5 nm diameter (purple crosses) or 10 nm diameter (blue squares zoom-in (b)), respectively, obtained by doctor blade experiments with suspensions of different particle concentrations at otherwise same conditions. Filling degree increased slightly for concentrations 1-2x the initial concentration. SEM image in (c) shows a filling degree of 10 % with 10 nm Au particles at the initial concentration of 5.7×10^{12} ml^{-1}. The filling degree drops drastically for higher concentrations as NPs agglomerate forming flakes as shown in (d).

However, after further concentration increase, this trend cannot be continued. The filling degree drops rapidly. For the 5 nm Au NPs, filling does not exceed 10 %, even for double concentration, and also drops for higher concentrations. The pores remain empty, the filling degree decreases to 2%, with both suspensions in case of highest concentration after evaporation of 90 vol% of the liquid medium of the initial suspension. SEM investigations exhibit the formation of nanoparticle agglomerates as shown in Figure 4.25 (d) for 10 nm NPs at a concentration $> 5.7 \times 10^{13}$ ml^{-1}. This particle agglomeration does not allow for the selective concentration enhancement at the triple phase boundary and deposition of single NPs into the pores.

At high concentrations the Au NPs are no longer effectively stabilized by their citrate shell. It is shown in [64] that the particle stabilization by a citrate shell is only efficient at particle volume fractions < 0.001 vol%. This fraction is exceeded for 90 vol% evaporation of the liquid in the experiments shown here. This behavior can probably be explained by the DLVO theory (Chap. 2.1.2): the concentration of ions in the suspension probably exceeds the critical coagulation concentration (CCC), at which the energy barrier, preventing particles to enter the primary minimum, vanishes [46, 65]. Thus, the NPs coagulate irreversibly.

Influence of temperature on pore filling. By increasing the temperature of the sample, the evaporation flux at the triple phase boundary increases. This results in a faster particle transport from the bulk of the suspension droplet towards the triple phase boundary, where thus the particle concentration locally increases. This is realized experimentally by a variation of the sample holder temperature between room temperature (24 °C) and 43 °C. All other experimental parameters are kept constant as stated above. The initial Au NP concentrations of 5.7×10^{12} ml^{-1} in case of 10 nm Au NPs and 5.0×10^{13} ml^{-1} for the 5 nm Au NP suspension are used.
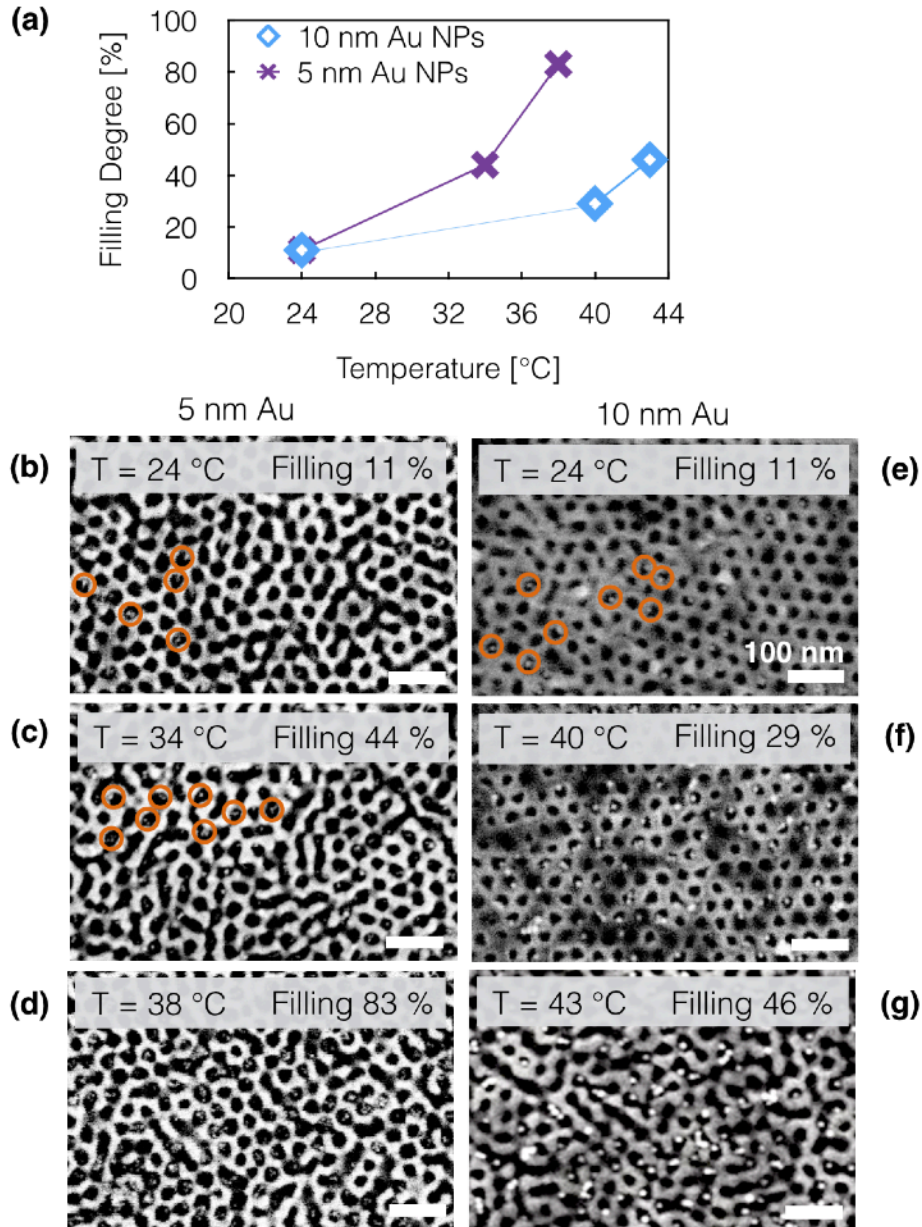
Fig. 4.26: (a) Temperature dependence of nanopore filling with 5 and 10 nm Au NPs. Filling degree increases constantly with increasing temperature for both suspensions. (b-d) corresponding SEM images of nanopores filled with 5 nm NPs at different substrate temperatures, (e-g) SEM images of temperature-dependent pore filling with 10 nm NPs. The scale bars for (b-g) are 100 nm. Some NPs are marked with a circle for better visibility.

The filling degree increases constantly with increasing substrate temperature for both particle suspensions as plotted in (a). SEM images of samples prepared at different temperatures are shown in Figure 4.26 using 5 nm NPs in (b-d) or 10 nm NPs in (e-g), respectively.

Within this temperature regime, the local particle concentration is large enough to fill the majority of the nanopores with Au NPs, while the particle deposition rates are high enough to avoid the formation of large agglomerates. Nanoparticles are selectively deposited into the pores before they can coagulate into large flakes which consume all NPs and suppress the deposition of single NPs.

Occasionally, small agglomerates of few (< 10) NPs are formed. These small agglomerates are then deposited into pores, as will be discussed later. This occurs mainly in experiments with the 5 nm Au NPs, probably as the initial concentration of this suspension is higher than for the 10 nm Au NPs.

At optimum conditions, i.e. a substrate temperature of 38 °C, a NP concentration of 5×10^{13} ml^{-1} at a doctor blade velocity of 5 μm/s, up to 83% of pores can be filled with at least one Au nanoparticle in case of 5 nm particle diameter as shown in the SEM image in Figure 4.27.

At higher temperatures (approx. > 40 °C for 5 nm NPs and > 45°C for 10 nm NPs), the evaporation of the suspensions liquid medium is too fast; the droplet can not be spread and moved over the surface properly, but evaporates completely within short time. Thus, pore filling is irregular: in areas of fast drying Au NPs can be found in pores but also on the plane substrate areas next to them; in other areas, again, the formation of large agglomerates occurs leaving the majority of pores empty.
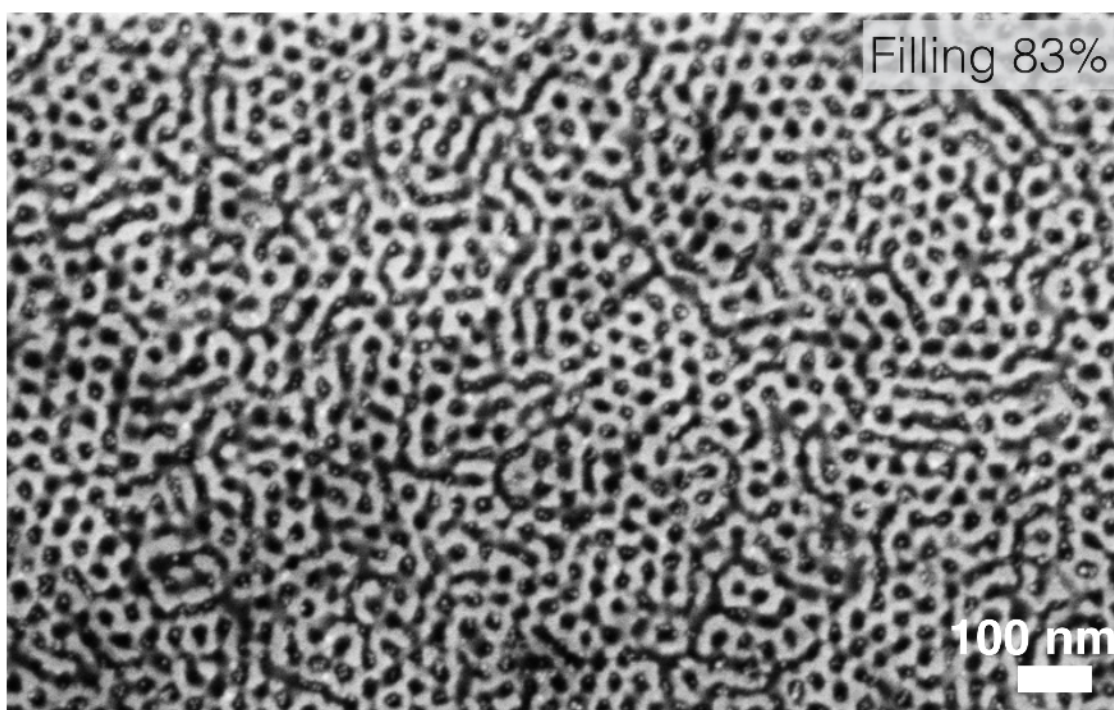
Fig. 4.27: Site-selective Au NP deposition into nanopores in SiO$_2$ prepared by BCP lithography with a pore filling of 83%. 5 nm Au NP with a suspension concentration of 5×10^{13} ml^{-1} are deposited using a doctor blade velocity of 5 μm/s at a substrate temperature of 38 °C.

Analysis of particle number per pore. For some applications of the arranged Au NPs, e.g. their use are catalysts for nanowire growth, the number of particles deposited into each pore needs to be controlled. The present experiments indicate, that by setting the ratio between particle size and pore size properly, the number of particles per pore can be tailored. The pore size is specific for the block copolymer used in BCP lithography.

Here, the BCP67 resulting in a nanopore diameter of 17 nm and a center-to-center distance between pores of 35 nm was used. The ratio between pore size and nanoparticle diameter is varied by using Au NP suspensions with different Au nanoparticle diameters of 5 nm and 10 nm, respectively.
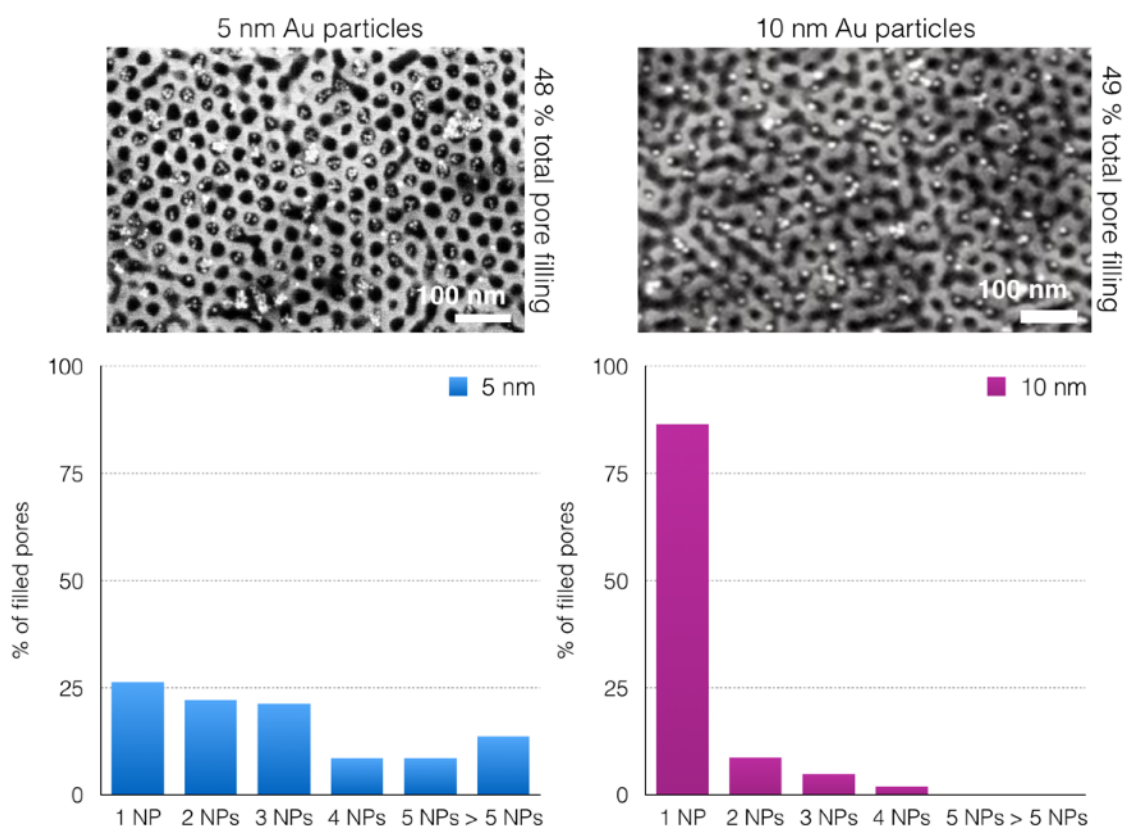
Fig. 4.28: Evaluation of number of particles deposited per pore for samples with almost equal pore filling degrees. For the 5 nm Au NPs (left) the distribution of particle number per pores is broad and agglomerates of 5 and more particles are found. For 10 nm Au NPs (right) 87% of filled pores contain one single particle.

SEM investigations show, that for 5 nm Au NPs it is more likely to obtain a deposition of several particles per pore, whereas for 10 nm particles most pores are filled with a single particle. This trend is quantified in Figure 4.28 where the number of particles per pore was counted, as visible in top-view SEM images. In both cases, the same pore filling degree of about 49 % is considered. In case of the smaller 5 nm Au NPs, the distribution of particles per pore is quite broad. Only 26 % of the total amount of filled pores contain exactly one Au NP while the other pores contain several particles or particle agglomerates. This is, however, probably not only a result of the geometrical commensurability between pore size and particle diameter, as 5 or more particles of a diameter of 5 nm are not likely to fit into a pore of 17 nm in diameter. The 5 nm Au NP suspension is used at a higher concentration. Thus, particle agglomeration could have started at the triple phase boundary prior to the particle deposition and already formed agglomerates of 5 or more particles are deposited from the suspension. This assumption is underlined by the fact that these agglomerates cannot only be found inside the pores but are also likely to be deposited on the plane surface areas.

For larger Au NPs with a diameter of 10 nm however 87 % of filled pores obtain only one Au particle. The deposition of 5 or more particles, which can be understood as an agglomerate, cannot be observed for the 10 nm suspension. Thus, by selecting the size of NPs fitting to the diameter of pores as well as the NP concentration, the selective filling of nanopores with single nanoparticles can be promoted.

Position of particles inside the pores. Cross-sectional transmission electron microscopy (TEM) images were taken in order to determine the position of the gold nanoparticles inside the nanopores and to assure the average number of trapped nanoparticles. A titanium layer was evaporated prior to TEM sample preparation to avoid a possible displacement of NPs. Figure 4.29 shows bright field TEM images, taken at 200 kV with a JEOL 2010F at the IMM-CNR in Catania, Italy. The pores are etched into the SiO_2 as well as into the silicon substrate, the gold nanoparticles with diameters of (4.5 - 6.7) nm are found inside the pores. It should be noted that the bottom of the pores and the pore sidewalls are amorphous, obviously due to native oxide formation after RIE pore transfer into the silicon. As a consequence, all Au NPs are located in pores sealed by SiO_2. The cross-sectional image exhibits information about the shape of the nanopores, which are approx. 19 nm in diameter with a center-center distance of 37 nm and a depth of approx. 19 nm. The pore shape is marked with a black dotted line for better visibility (Fig. 4.29 (a)). The gold nanoparticles are found to be positioned preferably at the pore side walls irrespective of the number of NPs in a pore, here varying from one (Fig. 4.29 (b)) to three (Fig. 4.29 (c)). This is possibly due to capillary forces drawing the particles towards the pore wall or interactions between the citrate shell covering the Au NPs and the pore walls.

In this case of the trapping of multiple particles inside one pore (Fig. 4.29 (c)), the nanoparticles are likely to be trapped as single particles and not as a formerly created agglomerate, as they are visible as single units.

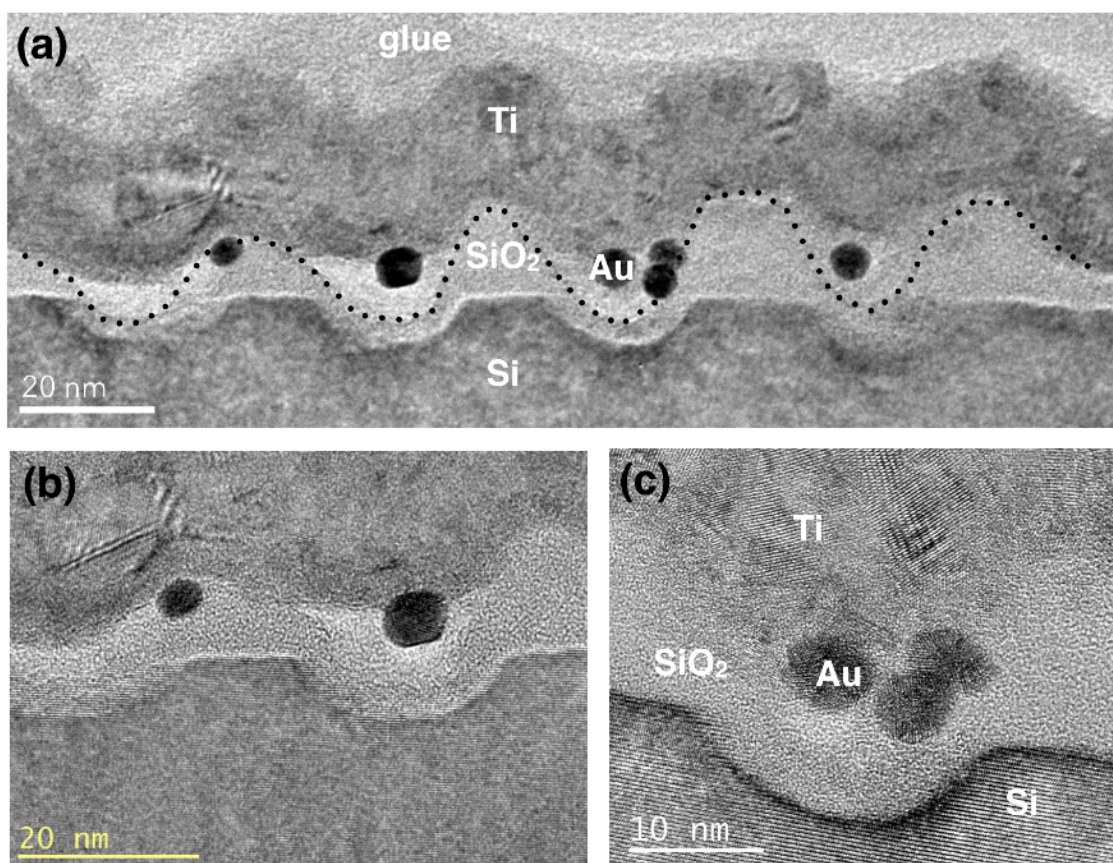Fig. 4.29: Cross-sectional TEM bright field images of nanopores in Si/SiO_2 with trapped Au NPs. Titanium was added as a protective layer during sample preparation. (a) Overview image with marked pore shape by black dotted line. (b+c) Detail images of single (b) or multiple (c) particles trapped in one pore.

4.4.3 Discussion of the nanoparticle deposition process

In order to increase the pore filling further and to optimize the positioning of nanoparticles inside the pores it is desirable to understand the mechanism of nanoparticle deposition. The principles of convective assembly and capillary assembly were explained in Chapter 3.1 for the deposition of µm-sized polymer spheres into trench structures. Both principles however can only be applied if the suspension enters into the topographic patterns, i.e. the structures are wetted with the suspension medium. This is however not trivial for nanometer-sized pores. In the following, some aspects are discussed which might help to understand the wetting state of the nanopores and the nanoparticle deposition.

Capillary condensation. Capillary condensation is the effect of condensation of a liquid in a capillary or small pore at vapor pressures below the saturation vapor pressure of the liquid above a plane surface. Strong van der Waals interactions between the vapor molecules in the limited space inside a capillary result in the formation of an equilibrium vapor-liquid interface [46]. The relation between the saturation vapor pressure and the equilibrium vapor pressure above this interface can be described by the Kelvin equation (Eqn. 4.14):

$$\ln \frac{P}{P_0} = \frac{-2\,\gamma}{rRT\rho} \cos \Theta \qquad (4.14)$$

with P the equilibrium pressure, P_0 the saturation pressure, γ the surface tension of the liquid, r the pore radius, R the universal gas constant, T the temperature, ρ the molar liquid density and Θ the contact angle [66].

For the characterization of porous materials, sorption isotherms of the absorbed volume of a species in dependence of the ratio P/P_0 are measured, giving a hysteresis curve of the sorption and desorption process. By this, pore filling mechanisms and pore characteristics, such as size and density, are investigated. Pressure ratios $0 < P/P_0 < 1$ are usually evaluated showing a steep increase of absorption above a characteristic P/P_0 ratio (for a hydrophilic material with nanopores of 7 nm width, measured at room temperature this ratio is about $P/P_0 = 0.6 - 0.9$ [66]) reaching a maximum surface loading with absorbent at $P/P_0 \approx 1$.

In order to estimate the loading with water in the nanopores created by BCP lithography and reactive ion etching in this work, the ratio P/P_0 is calculated with the Kelvin equation 4.14 at the given pore geometry. The pore radius of the created nanopores is 9 nm and the contact angle of water with the SiO_2 surface is assumed to 10°, which is a typical value of water on a planar, RCA cleaned SiO_2 surface (see App. A2). The surface tension of water is 70 mN/m and the molar density 55.4×10^3 mol/m^3. With this, the ratio P/P_0 can be determined to $P/P_0 = 0.894$ at room temperature. This large value allows for the assumption that capillary condensation occurs in the nanopores studied here, if stored in an atmosphere with a water pressure $\neq 0$. For an increased temperature of 40 °C (at which nanopore filling with Au NPs was most successful), the ratio P/P_0 increases slightly further to $P/P_0 = 0.899$. Assuming contact angles between 0° and 60° results in P/P_0 ratios of 0.893 to 0.945, respectively. Thus this factor does not change the general tendency of expected high water sorption. It should therefore be sure that nanopores contain water at ambient atmosphere.

Water sorption inside pores. The more detailed sorption behavior of water inside nanosized pores attracts much attention in current research. Up to now, compared to e.g. the N_2 sorption, the sorption mechanism is not completely understood. This is (i) because the water sorption does not follow the pore condensation model, valid for Ar or N_2 physisorption, of a homogeneous layer-by-layer adsorption, where reaching a critical film thickness results in capillary condensation and (ii) as physical/topographical as well as chemical surface characteristics of the pore walls influence the water sorption [66]. Models and simulations are being discussed,

which suggest the instant formation of a monolayer of water molecules at the walls of a hydrophilic pore. From here, additional water molecules adsorb at nucleation seeds, formed at e.g. chemical or topographical surface inhomogeneities, forming agglomerates at several points at the pore walls. At a critical water cluster size, which is dependent on the pore size, spontaneous capillary condensation occurs resulting in the filling of the pore with water [66, 67]. Densities, i.e. the aggregation state of water during this process, dependencies of surrounding conditions and the filling degree of the pore are topics of present research [66-68]. However, for hydrophilic pores at an atmosphere with a relative humidity > 0%, water sorption occurs [66]. The dependency on the temperature is studied in detail in [66], however no direct correlation between critical water cluster size and the temperature during the adsorption process was found. The desorption behavior shows capillary evaporation behavior similar to the well known Ar and N_2 desorption [66].

Wetting of nanopore-patterned surface. A full wetting of the nanoporous surface, as is indicated by the previous thoughts, is also indicated by sliding angle measurements. A water droplet with a volume of 2 µl is deposited onto the nanopore-patterned surface (15 min after RCA clean) and the sample is tilted from 0° starting position to 90°. The contact angles are measured for different tilting angles. Images of the droplet taken at some tilting angles are shown in Figure 4.30. The initial static contact angle of water on the patterned surface is 24.5°. During tilting, an advancing and receding contact angle at the opposing contact lines of the droplet on the surface are measured as the droplet deforms during tilting. In Figure 4.30 the advancing contact angle forms at the left side and increases with increasing tilting angle, while the receding contact angle at the right rim decreases (listed in Tab. 4.8).
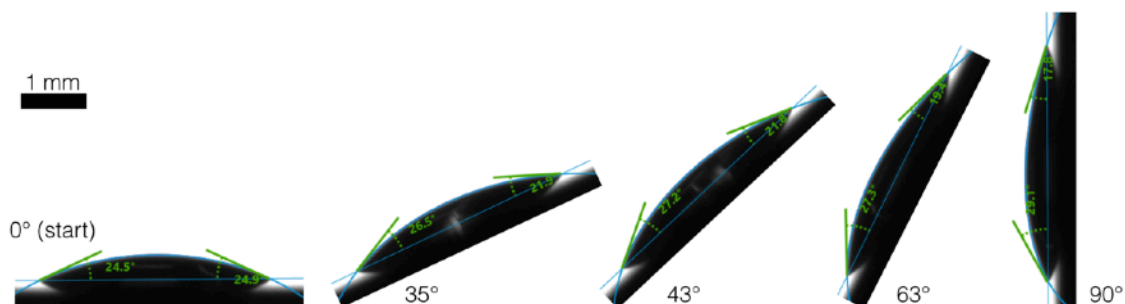
Fig. 4.30: Photographs of a water droplet deposited onto the nanoporous surface. The sample is tilted from 0° (starting position) to 90°, advancing and receding contact angles are measured (values listed in Table 4.8).

However up to a 90° tilting of the sample, the droplet does not roll off the substrate surface, i.e. no sliding angle occurs. This indicates a Wenzel wetting state with full wetting of the surface pattern with water. In contrast, if the droplet would sit on top of the pattern without wetting the whole surface as typical for Cassie-Baxter wetting, the droplet would roll off the surface for sample tilting angles of approx. 10-40°. Neither classical nor advanced models for the calculation of Cassie-Baxter, Wenzel or Laplace contact angles [69] expected for the given pore geometry are suitable for comparison with the experimental data. Only the expected contact angle for a Cassie-Baxter wetting can be calculated to 65°, thus a much larger contact angle than measured here (25° static CA). The Wenzel and the Laplace model are only valid for very deep pores, i.e. capillaries with an aspect ratio of pore depth/ pore width >> 10, typically >100 [69].

Tab. 4.8: Advancing and receding contact angles (CA) of water on the nanoporous substrate for different tilting angles. Static contact angle is given for plane (0° tilting) sample orientation.

tilting angle	advancing CA [°]	receding CA [°]	static CA [°]
0° (start)	-	-	24.7
35°	26.5	21.9	-
43°	27.2	21.8	-
63°	27.3	19.4	-
90°	29.1	17.8	-

In conclusion, it is likely that the nanopores contain water if stored at ambient atmosphere and get wetted if a water droplet is deposited on top of the surface. If this is the case capillary assembly as introduced in Chapter 3.1 could lead to the deposition of the gold nanoparticles inside the pores.

The experimental finding, that higher filling degrees, i.e. ratios of pores filled with NPs, can be achieved at higher substrate temperatures, results most likely from the enhanced evaporation flux at the triple phase boundary, at elevated temperatures. The higher evaporation flux leads to a higher particle flux towards triple phase boundary resulting in better pore filling. The Kelvin equation predicts a slight enhancement of the capillary condensation pressure of $P/P_0(298\,K) = 0.894$ to $P/P_0(313\,K) = 0.899$ if the temperature is increased from 298 K to 313 K, which can not be expected to influence the NP deposition crucially. The physisorption of water does not seem to be temperature dependent [66].

The favoured particle position at the pore walls, if once deposited inside the pore, could probably appear during drying of the surface. As water is adsorbed at pore walls, capillary forces are likely to draw the NPs towards the pore walls, as was also observed for polymer spheres inside trenches in Chapter 3.2 (however at a different size scale). Additionally, interactions of the pore walls and the adsorbed water with the citrate shell covering the Au NPs are likely to occur.

However, the exact mechanism of nanoparticle deposition inside the pores is not understood. Most assembly mechanisms are verified for the deposition of much larger particles onto substrate surfaces and most models investigated for porous surfaces and their wetting properties are valid for smaller pores with much higher aspect ratios.

Section summary

Nanopores in a PS matrix as created by BCP lithography are transferred into a SiO_2 substrate by reactive ion etching. These nanopores are then used as topographic traps for the site-selective deposition of Au nanoparticles with 5 nm or 10 nm diameter, respectively.

The doctor blade technique is used to deposit colloidal Au NPs into the nanopores: high NP concentrations lead to higher filling fractions, however, problems with the suspension stability occur; higher sample temperatures however lead indirectly to a locally increased concentration at the triple phase boundary resulting in filling fractions of up to 83 % of nanopores being selectively filled with Au NPs. For nanoparticles with diameters commensurate to the nanopores size, the number of deposited Au NPs per nanopore can be adjusted. Possible mechanisms of the Au NP deposition process are discussed.

Such precisely placed Au NPs can be used as catalysts for nanowire growth. However, the experimental procedure introduced here appears to be materials general and can also be transferred to other colloidal particles and substrate materials.

4.5 Hierarchical nanopores by combined nanosphere- and block copolymer lithography

For many applications of sub-20 nm patterns created by BCP lithography, e.g. for nanopattern integration in semiconductor devices, the control of pattern homogeneity, i.e. nanodomain orientation and pattern position with long-range order, is crucial. However, the self-organized microphase separation of BCP into the nanodomains lacks of long-range order, unless one gives the system time for interfacial energy optimization. Such time scales are however not applicable for industrial processing.

Directed self-assembly (DSA) offers the opportunity to guide the BCP nanodomains into well-defined long-range order. Most discussed advantages of the DSA approach are the so called pattern density multiplication along with improvement of the lateral order, improvement of the feature size uniformity and reduction of line edge roughness [70]. For DSA either external forces can be applied, such as temperature gradients [71], electric fields [72] or shear forces [73], or surfaces can be pre-patterned. Literature [70, 74] distinguishes between epitaxial DSA, where chemical surface modifications lead to orientational control due to tailored interfacial energies [75] and graphoepitaxial DSA, by which topographical patterns guide nanodomains into lateral order [76].

The most prominent example of DSA for long-range ordered BCP nanopatterns are parallel BCP lamella [77]. The parallel pattern arrangement can be achieved either by dense chemical pre-patterns of alternating preferential surface energies or by topographical pre-patterns with preferential wetting of polymers on trench-side walls.

Usually, DSA combines top-down pre patterning approaches, i.e. photo lithography, electron beam lithography or soft lithography with the bottom-up BCP lithography.

In this work however, a bottom-up pre-patterning along with the bottom-up BCP lithography is presented, which allows for a completely self-organized creation of hierarchical nanopatterns. The two self-assembly techniques introduced in the previous chapters - nanosphere lithography (NSL) and block copolymer (BCP) lithography - are shown to be suitable for the large-area patterning of surfaces with site-selective hierarchical nanopores (Chap. 4.5.1).

By means of NSL, antidot patterns, i. e. hexagonally arranged circular dots of free substrate within a thin film with diameters of few hundred nanometers are created. The preparation of these antidots by nanosphere lithography is explained in detail in Chapter 2.3.2. These patterns are then used as templates for block copolymer lithography. The influence of the pre-patterns on the self-organization of the BCP with respect to the material choice and antidot morphology are investigated. The created hierarchical nanopatterns allow for the better understanding of fundamental block copolymer interactions with the surface, regarding topography (Chap. 4.5.2) and material chemistry (Chap. 4.5.3) as the present approach offers both, graphoepitaxial and epitaxial DSA. This juxtaposed manipulation of the BCP behavior will lead to a discussion of the wetting state of the BCP on these surfaces with respect to the common theories of wetting on rough or patterned surfaces, i.e. in the Cassie-Baxter state and Wenzel state (Chap. 4.5.4).

Depending on these wetting states, the systems could be used as backside-supported nanomembranes for the size-exclusion of nanoparticles or as nanoscaffolds for pattern transfer onto e.g. curved surfaces, or due to their site-selective material contrasts and their porosity as nanochemistry batches.

4.5.1 Hierarchical nanopores

Figure 4.31 shows hierarchical nanopores created by nanosphere and BCP lithography: antidots in a gold thin film on a SiO_2 surface are filled with nanoporous polystyrene. The antidot-patterned thin film is prepared as explained in Chapter 2.3.2. Briefly, PS spheres were shrunk from a diameter of 618 nm to 415 nm. 2 nm Ti as adhesion promoter and 28 nm Au where then deposited by electron beam evaporation. Subsequently, spheres were removed. The block copolymer is then spin casted onto the antidot pre-patterned surface. It is important to note that no neutralization layer, such as a random copolymer brush, was added prior to BCP deposition. The amount of deposited polymer is corresponding to a 30 nm layer on a plane surface. The BCP phase separation was performed analogous to plane surfaces at 180 °C for 24 h at a pressure of $1x10^{-3}$ mbar as described above, the PMMA cylinders are removed selectively by UV exposure and development in acetic acid.

The quality of the phase separation and pore arrangement inside the antidots is remarkably good. The phase separation seems to be complete as the size distribution of pores is small and their shape is very homogeneous. SEM images were analyzed with the Delaunay triangulation based software explained in Chapter 4.2.2. The hexagonal arrangement is nearly defect-free with 83 % of pores being 6-fold coordinated (this number cannot reach 100 % as pores near the antidot rims cannot have 6 neighbours). All together, this results in very high pore densities of $9.4 x 10^{10}$ cm^{-2} inside the antidots, which is close to the geometric maximum ($9.43 x 10^{10}$ cm^{-2}) and higher than the typically reached pore densities of $< 9.0 x 10^{10}$ cm^{-2} on plane surfaces.
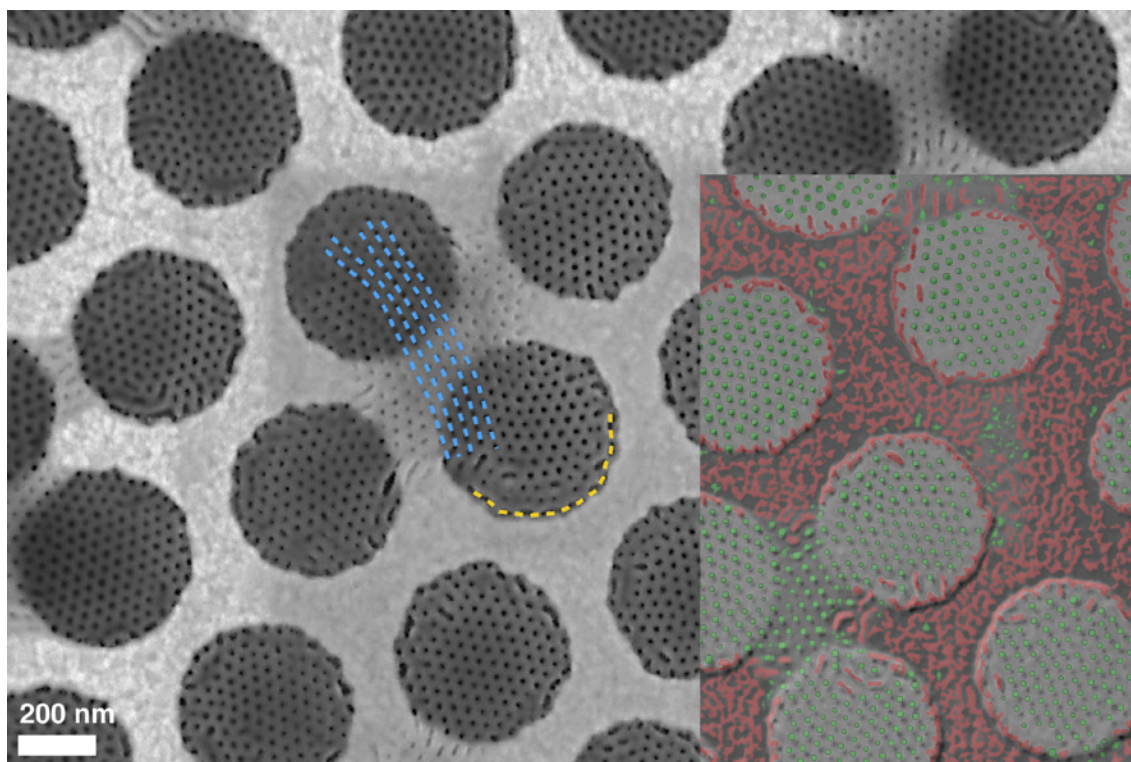
Fig. 4.31: Hierarchical nanopores in gold antidots. Delaunay triangulation results marking round-shaped nanopores with a diameter of (17.8 ± 2.1) nm green (larger pores and surfaces roughness are marked red) are added as overlay on the SEM image. Blue lines mark lattice planes reaching from one antidot to the other in areas, where microphase separation occurred on plane areas between antidots. Pores inside antidots arrange themselves along the antidot walls following pore wall roughnesses as marked with a yellow line.

The pore arrangement inside the antidots follows the shape of the rims. The roughness of the antidot walls and deviations from a perfect round shape are repeated by the pores, as e.g. marked yellow in Figure 4.31. However, these pores directly next to the rims show deviations in shape and diameter. This becomes visible by the numerical image analysis. Pore sizes are evaluated with this software and as a result pores with diameters from (9.4 - 21.7) nm are marked green, whereas larger pores are marked red (here areas with different contrasts on the plane metal film most likely resulting from surface roughness are marked red, too). The overlay in Figure 4.31 shows that the pores at the antidot rims are mostly too large.

Occasionally, nanopores were also formed on islands on the plane surfaces of the metal film between the antidots. This probably occurred due to surface roughness, which improved wettability with the polymer. Here, the polymer film thickness is higher and phase separation into ordered nanopores took place. These nanopore islands connect several antidots and nanopore arrangement is in registry with the orientation inside the nanopores within these areas. An example of a resumed domain orientation is marked by blue lines in Figure 4.31.

The vertical orientation of the nanopores inside the antidots is surprising, because the antidot bottoms consist of non-neutralized SiO_2. On plane SiO_2 surfaces without neutralization layer PMMA cylinders usually orient themselves parallel to the surface as explained in Chapter 4.2.4. The topography or material choice of the antidot thin films however seems to guide the PMMA cylinders into the perpendicular orientation without the use of a neutralization layer. For better understanding of the nanopore formation process inside the antidots and the guiding effect of the antidot pre-pattern on the nanopore orientation experiments with antidots of different morphology were performed. To this end, antidot pre-patterns are prepared by different material deposition techniques (sputter deposition and electron beam evaporation) resulting in different topographies. In order to change the interaction of the BCP with the substrate surface, antidots are also prepared in thin films from different materials.

4.5.2 Influence of antidot morphology

The creation of antidots with different morphology is realized by using either sputter deposition of the material thin film or electron beam evaporation during nanosphere lithography. The influence of the deposition technique on the side wall slope of antidots was discussed in detail in Chapter 2.3.2. Figure 4.32 shows antidots in platinum thin films on SiO_2 surfaces. PS spheres were shrunk from 618 nm in diameter to 415 nm. Platinum was then deposited by (a) sputter deposition (41 nm) or (b) electron beam evaporation (16 nm), respectively. BCP lithography was then performed on these substrates by the standard procedure without the RCP brush.

For both samples, nanopores were formed site-selectively inside the antidots and with vertical orientation. Due to the small slope of the antidot walls prepared by sputter deposition (Chap. 2.3.2), their rims are not clearly visible in Figure 4.32 (a) (the approximate position of one antidot is marked by a yellow dotted line). However it is striking that nanopores are confined into hexagonally arranged circular areas. The pores are very homogeneous in size and shape, thus high pore densities of 9.4×10^{10} cm^{-2} inside the antidots are obtained. The rims of the antidots in (b), prepared by e-beam evaporation, are clearly visible due to sharp material contrast at steep sidewall slopes. Here, nanopores are also preferentially formed inside the antidots. Besides, they occasionally form islands on the plane areas between antidots. The elongated nanopores in Figure 4.32 (b) most likely result from unfinished phase separation. The different slopes of the antidot walls do not seem to affect the microphase separation crucially, which is confirmed by determination of the pore densities being similarly 9.4×10^{10} cm^{-2} for both types of antidots (for optimum annealing parameters).

Again, it is striking that the nanopores, i.e. former PMMA cylinders, are oriented perpendicular to the non-neutralized substrate surface. This is the case for both samples, even though the freely accessible SiO_2 surface area is much smaller in the sputter deposited antidots.
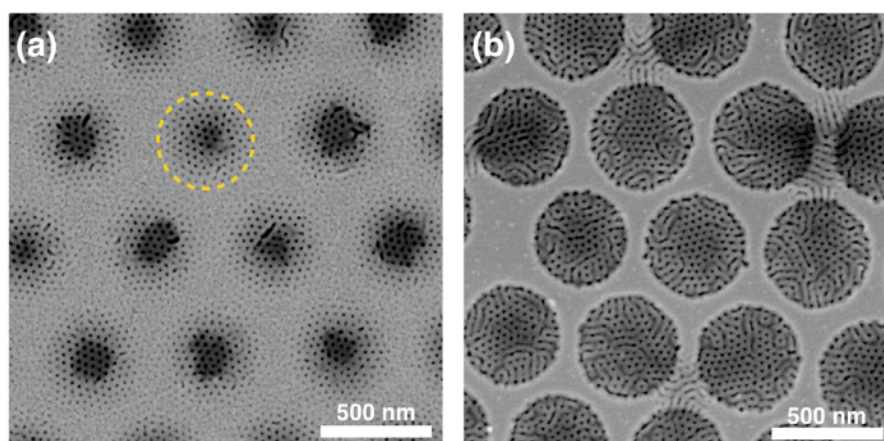
Fig. 4.32: SEM images of hierarchical nanopores in platinum antidots prepared by (a) sputter deposition (rim of one antidot marked in yellow) and (b) electron-beam evaporation on a Si/SiO$_2$ surface. For both samples, the BCP67 was annealed for 24 h at 180 °C at 1x10^{-3} mbar.

Thus, the morphology of the antidot patterns does not seem to determine the PMMA cylinder orientation exclusively, as no guiding by a perpendicular antidot wall slope is apparent in the case of the sputter deposited pre-patterns. However, since on plane platinum thin films BCP microphase separation was shown in Chapter 4.2.5 to result in a perpendicular PMMA cylinder orientation as well, the material influence is further investigated in the following.

4.5.3 Influence of antidot thin film material

Antidot-patterned thin films from different materials are prepared to investigate the material influence on the BCP lithography, as experiments on plane surfaces from different materials showed different behavior in the microphase separation due to different polarities of surfaces (Chap. 4.2.5).

Antidots were created in Pt, Au and TiO$_x$ thin films (all electron-beam evaporated), the results are summarized in Figure 4.33. Film thicknesses were 30 nm, 31 nm (including 2 nm Ti adhesion promoter) and 33 nm, respectively.

Gold and platinum antidots (Fig. 4.33 (a, c)) show similar results. Nanopores are site-selectively formed inside the antidots, while the plane metal film areas in between are predominantly free from polymer patterns. Nanopores are homogeneous in size and shape, as microphase separation of the BCP resulted in PMMA cylinder orientation perpendicular to the surface, even though the antidot bottoms consist of non-neutralized SiO$_2$. Performing the BCP lithography on an antidot-patterned TiO$_x$ surface results in a very different nanopore formation. Pores can be found all over the surface, i.e. inside the antidots but also on the plane TiO$_x$ thin films in between the antidots. These pores seem irregular - the size distribution is broad and the pores are not homogeneously round shaped, but more ellipsoidal. This could result form an oblique PMMA cylinder orientation with respect to the surface.

AFM measurements (Fig. 4.33 (b, d, f)) provide further insight into the polymer behavior. The nanoporous PS is found to form elevated globes on top of the antidots. In case of metal surfaces, these globes reach heights of about 50 nm above the plane metal surfaces between the antidots[1]. Such globes are also found on the antidots in TiO$_x$ thin films, however, they are much less distinct with heights of only about 5 nm.

---

[1] The plane areas in between the antidots are likely to be covered with a thin polymer film themselves, thus the actual height in unknown. This will be discussed later.
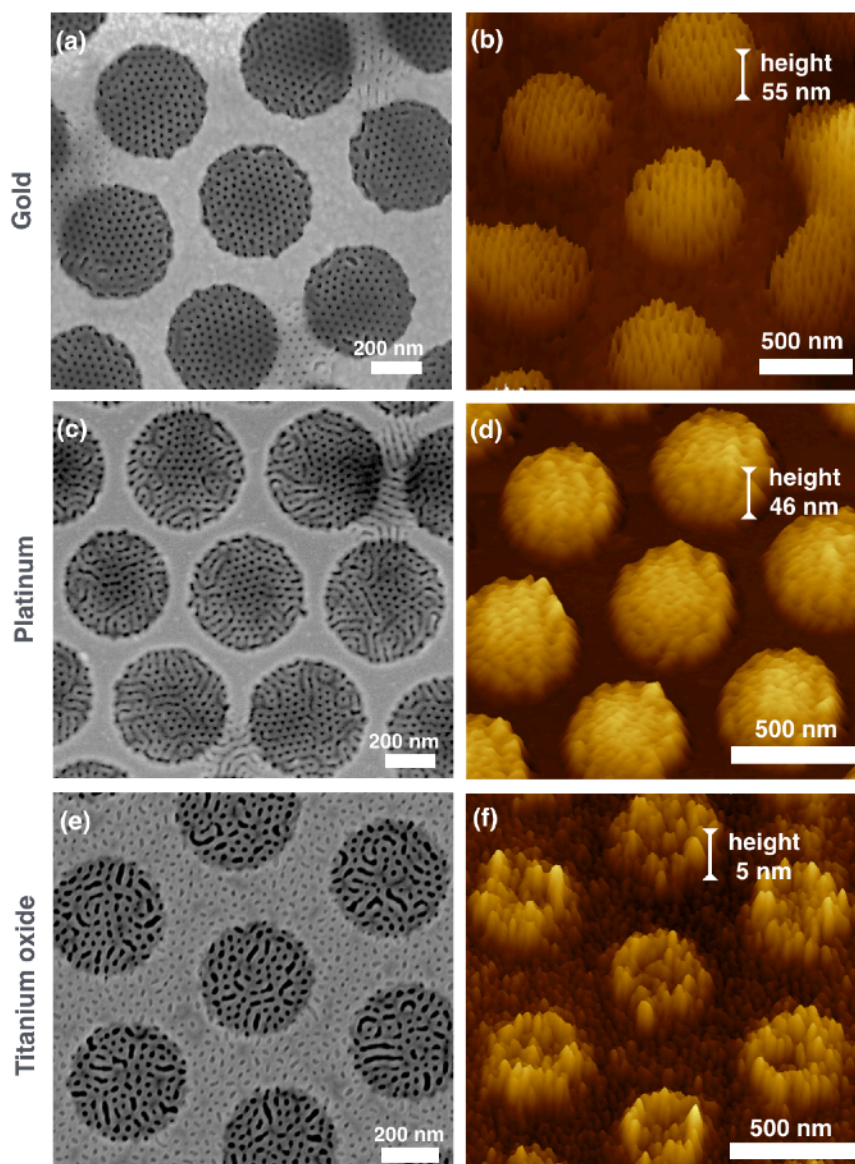
Fig. 4.33: SEM (a,c,e) and AFM (b,d,f) images of hierarchical nanopores in antidots from different materials (all electron-beam evaporated). Site-selective nanopore formation inside antidots occurs in Au (a,b) and Pt (c,d) antidots, while pores are formed all over the TiOx surface (e,f). AFM images show the formation of elevated PS globes on the antidots. This effect is more distinct on the metals (b,d).

To assure that this effect is caused by the thin film material characteristics, an antidot-patterned TiO_x thin film as used in Figure 4.33 (e,f) was covered with an additional 5 nm thin sputter-deposited film of platinum prior to polymer deposition. This resulted again in the site-selective nanopore formation, shown in Figure 4.34. Microphase separation into nanopores with defined shape is not completed, but the site-selectivity is obvious. Thus, the materials choice obviously affects the wetting of the polymer on these hierarchically patterned samples and influences the microphase separation crucially.
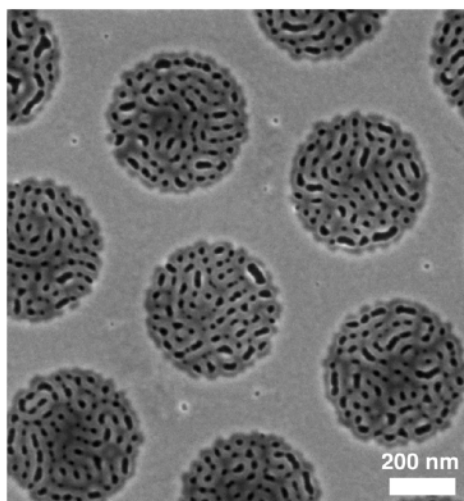
Fig. 4.34: SEM images of nanopores inside antidots that were prepared by e-beam evaporation of 33 nm Ti and subsequent sputter deposition of 5 nm Pt.

4.5.4 Discussion of wetting states

The investigations so far reveal that the combination of both topographic surface patterns and material influence the block copolymer phase separation allowing for the creation of hierarchical nanopores. In the following, the influence of the polymer film thickness (i), the wetting state of the polymer within the antidots (ii), the globe formation (iii) and the nanopore orientation (iv) are discussed.

(i) Film thickness. When depositing a thin film onto a patterned surface, wetting behavior is complex and can lead to local variations in film thicknesses. As stated above, the film thickness of the polymer determines the microphase separation into ordered patterns crucially. Such wetting dependent film thickness variations could lead to the result shown in Figures 4.31 - 34. In order to understand if the polymer film thickness is the determining factor for the site-selective nanopore formation found here, it is investigated if there is a very thin polymer film covering the metal surface between antidots where no nanopores are visible.

It was described above (Chap. 4.2.3) that there exists a minimum polymer film thickness for microphase separation into regular patterns, as shown for plane surfaces in Figure 4.10. Here, only very few pores were visible. Such single pores can also be occasionally found in between metal thin film antidots, as e.g. visible in Figure 4.34, indicating the presence of a thin film.

A better wettability of the TiO_x surface with the polymer might result in a larger film thickness on the elevated part next to the antidots resulting in large-area nanopore formation. A higher film thickness on the TiO_x film corresponds to a more homogeneous polymer spreading on the surface, which would be consistent with the observed weak globe formation.

In order to scrutinize these assumptions, cross-sectional bright-field TEM images are taken. Figure 4.35 shows the cross sections of antidots from gold (b), platinum (d) and titanium (f) on $Si/SiO_{2,nat}$ with BCPs film and corresponding SEM top-view images (from Figure 4.32 and 4.33). The antidot thin films were all prepared on silicon surfaces with the native oxide. As protective layer, 10 nm Ni was deposited onto all samples prior to TEM sample preparation. The cross-sectional TEM images show one antidot each with the nanoporous polystyrene inside. Ni nanoparticles are embedded inside the PS pores due to the deposition of the protective Ni film and allow for a better visualization of pores. The formation of a polymer globe on top of the antidot is only poorly visible in these images. The cutting plane through the samples does not hit

the antidot center, where the maximum globe height is expected, but cuts a segment of the circular antidot and thus the globe at a smaller height. Moreover, it cannot be excluded that the deposition of the metal film on top of the polymer deforms the PS membrane.

Figure 4.35 (a + b) show the selectively formed nanopores inside antidots in an electron beam evaporated gold thin film. Cross-sectional TEM images reveal that no polymer film at all is formed on top of the gold thin film. The platinum thin films in Figure 4.35 (c+d) were sputter deposited, thus the wall slopes are very flat. Again, nanopores are formed site-selectively inside the nanopores, however a very thin polymer film of approx. 6 nm is apparent on the Pt thin film between the antidots. At this thickness, no microphase separation of the BCP into ordered nanodomains occurs. For thicknesses > 14 nm, pore formation can be observed in the TEM images. For the TiO$_x$ thin films in Figure 4.35 (e+f), nanopores are formed all over the sample, inside and outside the antidots. This can be confirmed by the TEM image, revealing a thick polymer film being apparent on the TiO$_x$.
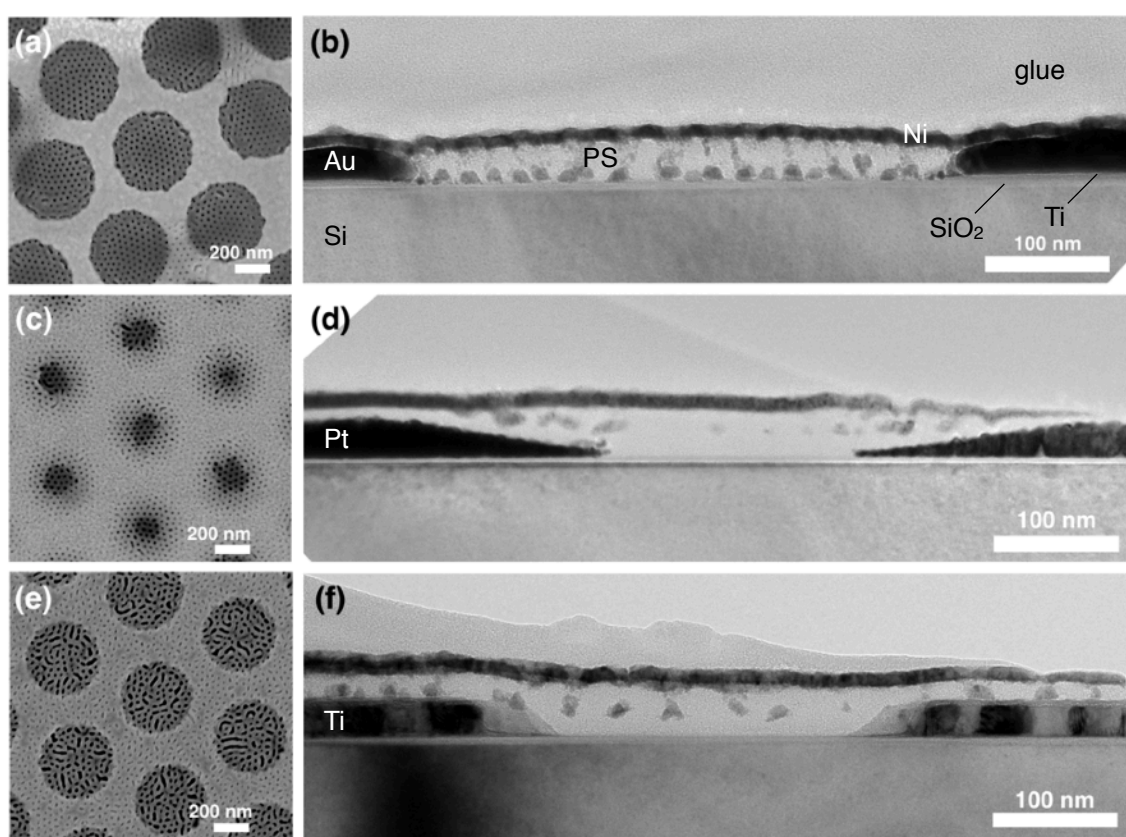
Fig. 4.35: Top-view SEM images (a, c, e) and cross-sectional bright-field TEM images (b, d, f) of nanopores inside Au (a, b), Pt (c, d) and TiO$_x$ (e, f) antidots. All patterned antidot thin films are prepared on a silicon surface with native oxide layer. Au und TiO$_x$ antidots are prepared by electron beam evaporation, while the Pt thin film is sputter deposited. A 10 nm Ni film is deposited onto all samples after BCP lithography as protective layer for the TEM sample preparation and to allow for an easy distinction between the PS from the BCP film and the glue used in TEM sample preparation.

(ii) Wetting state. In general, wetting of topographically patterned surfaces is not trivial [46]. The basic wetting theories in literature are the Cassie-Baxter and the Wenzel approach, which are briefly introduced in Appendix A1. Possible wetting states of the antidot patterns following these theories are depicted in Figure 4.36. In case of Wenzel state-like wetting (a) all the surface is wetted by the liquid, in this case the polymer, i.e. the liquid covers the whole surface and follows all topographies or roughnesses. In Cassie-Baxter state-

like wetting (c), in contrast, the liquid forms a layer on top of the topographic patterns or roughnesses and does not cover the complete surface but leaves air pockets underneath the polymer film. An intermediate state, with a partial penetration of the liquid into the pattern, is described by the Laplace wetting [46], comparable to (b).
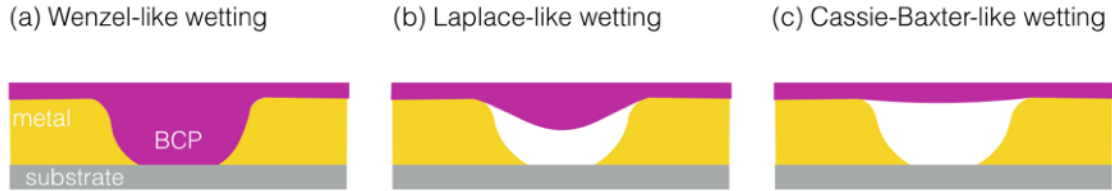
Fig. 4.36: Sketch depicting possible antidot filling situations by the BCP in a Wenzel state-like wetting (a), Cassie-Baxter state-like wetting (c), or an intermediate state comparable to a Laplace wetting (b).

In the present case, geometrical considerations allow for the estimation of possible wetting states by comparing the available amount of polymer and the volume of the observed polymer globes on the antidots. The volume of polymer deposited onto the samples is assumed to being commensurate to the amount of polymer spin-casted on a plane surface under the same experimental conditions (polymer suspension concentration, spin speed). This polymer volume is available for the surface and antidot-pattern coverage. For simplification, the shape of an antidot is assumed to be a cylindrical hole in the metal film. In case of Wenzel state-like wetting the antidot would be filled up with the polymer. Comparing the amount of polymer to the volume of the antidots, the polymer could fill up the antidot and then form an additional cylindrical globe on top of the antidots with a height of maximum 16 nm. The AFM images in Figure 4.33 however showed globes with a height of 50 nm. Thus, unless geometrical simplifications are applied within this estimation, a Wenzel state wetting would be unlikely, especially since not all deposited polymer is available to fill up the antidots but in particular in the case of the Pt antidot film a polymer thin film is present on the plane areas in between the antidots. Thus, the antidot patterns are more likely to be wetted in a Cassie-Baxter- or Laplace-like state.

(iii) Globe formation. In order to find out if one of these states is present it is helpful to determine why and when the polymer globes are formed. AFM measurements (Fig. 4.37 (c)) show, that directly after spin casting of the polymer onto the antidot thin film no globes can be found but troughs of approximately 16 nm depth are formed.
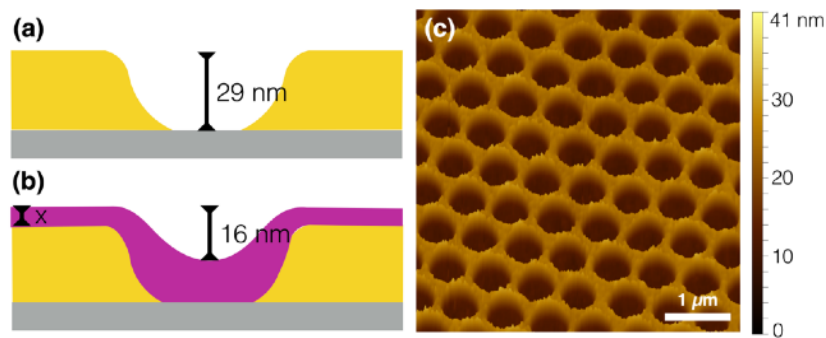
Fig. 4.37: (a) Sketch of the antidot height without polymer. (b) Sketch of height measured by AFM after polymer deposition. (c) AFM image of polymers on an evaporated Au antidot film.

Figure 4.37 (a, b) compares the measured antidot height before and after polymer deposition, where the BCP distribution in (b) is assumed on AFM images as in (c). The prepared antidots have a height difference of 29 nm between the antidot bottom and the plane surfaces in between antidots (a). This is in agreement with the amount of deposited metal during antidot preparation. After polymer deposition, this height difference is decreased to 16 nm. Thus more polymer is deposited into the antidots than onto the plane areas around, as shown in the schematics in (b). Figure 4.37 (c) shows an AFM image of the antidot pattern with polymer on- and inside the antidots prior to annealing.

Probably, the globe is formed during the annealing of the polymers for microphase separation. Residual solvent and gas could remain inside the antidots. During the annealing under vacuum conditions, these gas and solvent amounts would leak from the surface and could press the polymer upwards forming the polymer globe. This is, however, a speculation and needs to be further investigated.

(iv) Nanopore orientation. The observed formation of PMMA cylinders perpendicular to the surface can also be understood on the basis of wetting of the surface in a Cassie-Baxter- or Laplace-like state. The PMMA cylinder orientation would not be expected if the polymer would be in contact with the non-neutralized SiO_2 on the antidot bottom, where experiments on plane surfaces show parallel cylinder orientation (Fig. 4.14). In case of the Laplace- or Cassie-Baxter wetting (Fig. 4.36 (b+c)) the polymer film is free-standing with two interfaces towards air/vacuum, which are referred to as neutral, resulting in perpendicular cylinder orientation.

In total, the surface energy does not just directly influence the orientation of the nanopatterns forming during microphase separation. The experiments show that on topographically patterned surfaces the surface energy determines the wetting with the BCP film and thus the spatial thickness profile of the BCP film, which in turn governs the order in the microphase separated films.

Section summary

The combined nanosphere and block copolymer lithography is shown to allow for the creation of hierarchical nanopore arrays on large areas.

Antidot-patterned metal or semiconductor thin films are created by nanosphere lithography. The antidots then act as a template in the subsequently applied block copolymer lithography. Depending on the antidot material, site-selective nanoporous PS islands inside the antidots can be created. The influence of the antidot-pattern on the wetting of the BCP film, the resulting film thickness profile and the ordering upon microphase separation is discussed.

4.6 Conclusions

The principle and applications of block copolymer (BCP) lithography are discussed in this chapter. The microphase separation of copolymers consisting of two blocks of unlike polymer species was used to produce self-arranged nanoscale patterns on surfaces. The BCP lithography was performed with polystyrene-b-polymethylmethacrylate (PS-b-PMMA) of a total molecular weight of (50-67) kg/mol containing approximately 70% PS. With such polymers, PS matrices with embedded PMMA cylinders can be produced in approximately 30 nm thin films. The cylinders have diameters of (15-20) nm and are hexagonally arranged with a center-to-center distance of 38 nm. The microphase separation of commercially available BCP as well as RAFT polymerized home-made BCP was investigated.

A better understanding of the microphase separation enables the improvement of the pattern homogeneity. The interfacial energies between polymer species themselves, air or the substrate surface are discussed in literature to determine the orientation of nanopatterns. The widely investigated substrate for BCP lithography is SiO_2, which is known to allow for the formation of PS-embedded PMMA cylinders perpendicular to the substrate surface only if the surface is neutralized e.g. by a random copolymer (RCP) brush. If not neutralized, cylinders will orient themselves parallel to the substrate surface forming finger print like patterns.
The influence of surface free energies and the surface polarity on the phase separation of the polymers was further investigated in the present work by choosing different materials as substrate. Contact angle measurements on different surfaces indicate that the polarity of the surfaces determines the cylinder orientation. It was found that on surfaces with predominantly dispersive surface energy, such as Au, Pt or TiO_x, no neutralization layer is necessary. This is interesting as the formation of a RCP brush layer takes much time (three days), while on non-polar surfaces no addition layer needs to be deposited. In addition, BCP patterns are often used as shadow mask in a pattern transfer process and here an additional RCP layer can disturb the procedure.
Beside these technical advantages, the knowledge of microphase separation of the polymers on different materials enlarges the field of possible applications of BCP lithography nanopatterning. Semiconductor and metal surfaces, and in particular high-surface energy metals like Au can be nanopatterned on large areas, which is not easily feasible with most conventional thin film patterning techniques.

By means of selective PMMA removal and reactive ion etching, nanopores with sub-20 nm dimensions are created on large areas of SiO_2 surfaces. As one possible application, such nanopores in SiO_2 are used as topographic traps to direct the transport of colloidal Au nanoparticles with sizes of 5 nm and 10 nm, respectively, into these nanopores. To this end, a doctor blade technique was used and the influence of experimental parameters on the deposition of Au NPs was investigated. By adjusting parameters such as the sample temperature, 17 nm pores could be filled selectively with 5 nm or 10 nm diameter Au NPs to a percentage of up to 83%. By matching pore size and particle diameter up to 87% of filled pores contain one single Au particle. Such a precise particle placement can be useful for catalytic growth of ordered semiconductor nanowire arrays, which are under investigation for advanced solar cell concepts. The high Au NP densities of up to 9×10^{10} cm^{-2} can also be interesting for catalysis in chemical reactions on porous surfaces.

In the last part, the two large-area self-assembly nano-patterning techniques discussed within this work - nanosphere lithography and block copolymer lithography - were combined for the preparation of hierarchical nanopores.

Antidot patterned thin films from different materials are created by nanosphere lithography as described in detail in Chapter 2.3.2. These structures were used as topographical and chemical templates for the block copolymer lithography. The influence of the antidot morphology after sputter- or electron beam evaporation on the polymers phase separation as well as different material combinations were investigated. Results show, that on all pre-patterned samples PMMA cylinders oriented perpendicular to the substrate surface are formed without the use of surface neutralization. On metallic antidot surfaces from gold and platinum highly uniform nanopores were formed site-selectively inside the antidots, while on titanium oxide antidot films, nanopores form all over the sample.

For a better understanding of the directed microphase separation the wetting state of the polymer on the pre-patterned surfaces was investigated. The surface free energy of the interfaces between polymers and surfaces might on the one hand determine the general wetting states and thus film thicknesses and on the other hand the motive orientation. The perpendicular cylinder orientation could be explained by a Cassie-Baxter or Laplace like wetting state with a freestanding polymer film on the antidots. This is however still focus of ongoing research.

The novel approach presented here for the creation of hierarchical nanopores is solely based on self-assembly techniques and therefore is applicable to large areas. It should be easily transferable also to other material combinations. It is expected that the hierarchical nanopores might be used as back-side supported membranes with pore sizes of few nanometers and improved mechanical stability.

4.7 Bibliography

[1] R. A. Puglisi, J. Nanomat. 586458 (2015)

[2] J. Y. Cheng, C. A. Ross, V. Z. H. Chan, E. L. Thomas, R. G. H. Lammertink, G. J. Vancso, Adv. Mater.13, 1174 (2001)

[3] K. Naito, H. Hieda, M. Sakurai, Y. Kamata, K. Asakawa, IEEE Trans. Magn. 38 (5), 1949 (2002)

[4] H. Tsai, H. Miyazoe, A. Vora, T. Magbitang, N. Arellano, C. C. Liu, M. J. Maher, W. J. Durand, S. J. Dawes, J. J. Bucchignano, L. Gignac, D. P. Sanders, E.A. Joseph, M. E. Colburn, C. G. Willson, C. J. Ellison, M. A. Guillorn, Proc. of SPIE 9779, 977910 (2016)

[5] W. A. Lopes, H. M. Jaeger, Nature 414, 735 (2001)

[6] H. C. Kim, X. Jia, C. M. Stafford, D. H. Kim, T. J. McCarthy, M. Tuominen, C. J. Hawker, T. P. Russell, Adv. Mater. 13, 795 (2001)

[7] M. Park, C. Harrison, P. M. Chaikin, R. A. Register, D. H. Adamson, Science 276, 1401 (1997)

[8] R. R. Li, P. D. Dapkus, M. E. Thompson, W. G. Jeong, Appl. Phys. Lett. 76, 1689 (2000)

[9] H. Staudinger, Berichte der deutschen chemischen Gesellschaft 53(6), 1073 (1920)

[10] P. G. de Gennes, Introduction to polymer dynamics, Cambridge University Press (1990)

[11] L. H. Sperling, Introduction to polymer dynamics, New Jersey: Wiley (1992)

[12] G. Moad, D. H. Solomon, The Chemistry of Radical Polymerization, Elsevier (2006)

[13] P. Flory, J. Chem. Phys. 17(3), 303 (1949)

[14] P. J. Flory, Principles of Polymer Chemistry, Cornell Univ. Press (1953)

[15] K. Sparnacci, D. Antonioli, V. Gianotti, M. Laus, F. Ferrarese Lupi, T. J. Giammaria, G. Seguini, M. Perego, ACS Appl. Mater. Interfaces 7, 10944 (2015)

[16] J. Moul, B. G. Frushour, J. R. Kontoff, H. Eichenauer, K. H. Ott, L. Schade, Polystyrene and Styrene Copolymers, in: Ullmann's Encyclopedia of Industrial Chemistry, Weinheim: Wiley-VCH (2007)

[17] M. Guaita, British Polymer J. 18(4), 226 (1986)

[18] M. F. Ashby, Materials Selection in Mechanical Design, Elsevier (2005)

[19] M. Ferriol, A. Gentilhomme, M. Cochez, N. Oget, J. L. Micloszynski, Polym. Deg. Stab. 79(2), 271 (2003)

[20] P. J. Flory, J. Chem. Phys. 10, 51 (1942)

[21] M. L. Huggins, J. Chem. Phys. 9(5), 440 (1941)

[22] T. P. Russell, R. P. Hjelm, P. A. Seeger, Macromolecules 23, 890 (1990)

[23] P. W. Majewski, K. G. Yager, J. Phys. Condens. Matter 28, 403002 (2016)

[24] Y. S. Jung, Ph. D. Thesis, MIT (2009)

[25] A. Menshikov, A. V. Bolshakova, I. V. Yaminskii, Prot. Met. Phys. Chem. Surf. 45(3), 295 (2009)

[26] F. F. Lupi, T. J. Giammaria, G. Seguini, F. Vita, O. Francescangeli, K. Sparnacci, D. Antonioli, V. Gianotti, M. Laus, M. Perego, ACS Appl. Mater. Interfaces 6, 7180 (2014)

[27] A. Andreozzi, E. Poliani, G. Seguini, M. Perego, Nanotechnology 22, 185304 (2011)

[28] S. Ham, C. Shin, E. Kim, D. Y. Ryu, U. Jeong, T. P. Russell, C. J. Hawker, Macromolecules 41, 6431 (2008)

[29] D. M. Trombly, V. Pryamitsyn, V. Ganesan, Phys. Rev. Lett. 107, 148304 (2011)

[30] L. H. Radzilowski, B. Carvalho, E. L. Thomas, J. Polym. Sci. B 34, 3081 (1996)

[31] A. Knoll, A. Horvat, K. S. Lyakhoca, G. Krausch, G. J. A. Sevink, A. V. Zvelindovsky, R. Magerle, Phys. Rev. Lett. 89(03), 035501 (2002)

[32] I. A. Zucchi, E. Poliani, M. Perego, Nanotechnology 21, 185304 (2010)

[33] X. Zhang, B. C. Berry, K. G. Yager, S. Kim, R. L. Jones, S. Satija, D. L. Pickel, J. F. Douglas, A. Karim, ACS nano 2(11), 2331 (2008)

[34] Q. Wang, P. F. Nealey, J. J. Pablo, Macromolecules 34, 3458 (2001)

[35] H. P. Huinik, J. C. M. Brokken-Zijp, M. A. van Dijk, J. Chem. Phys. 112, 5 (2000)

[36] M. Ceresoli, F. F. Lupi, G. Seguini, K. Sparnacci, V. Gianotti, D. Antonioli, M. Laus, L. Boarino, M. Perego, Nanotechnology 25, 275601 (2014)

[37] D. Drude, B. Sc. Thesis, Quantitative Bestimmung von Defektdichten in kolloidalen Masken, Paderborn University (2015)

[38] T. M. Liebling, Documenta Mathematica 419 (2012)

[39] D. T. Lee, B. L. Schachter, Int. J. Computer and Information Sciences 9 (1980)

[40] P. Mansky, Y. Liu, E. Huang, T. P. Russell, J. C. Hawker, Science 275, 1458 (1997)

[41] K. W. Guarini, C. T. Black, S. H. I. Yeung, Adv. Matter 14(18), 1290 (2002)

[42] B. H. Sohn, S. H. Yun, Polymer 43, 2507 (2002)

[43] R. D. Peters, X. M. Yang, T. K. Kim, B. H. Sohn, P. F. Nealey, Langmuir 16, 4625 (2000)

[44] J. Bang, J. Bae, P. Löwenhielm, C. Spiessberger, S. A. Given-Beck, T. P. Russell, C. J. Hawker, Adv. Mater. 19, 4557 (2007)

[45] W. Senaratne, L. Andruzzi, C. K. Ober, Biomacromolecules 6, 2427 (2005)

[46] H.-J. Butt, K. Graf, M. Kappl, Physics and Chemistry of Interfaces, Weinheim: Wiley-VCH (2003)

[47] L. C. H. Moh, M. D. Losego, P. V. Braun, Langmuir 27, 3698 (2011)

[48] W. J. Brittain, S. Minko, J. Polym. Sci A 45, 3505 (2007)

[49] J. Frascaroli, G. Seguini, S. Spiga, M. Perego, L. Boarino, Nanotechnology 26, 215301 (2015)

[50] E. Han, K. O. Stuen, Y. H. La, P. F. Nealey, P. Gopalan, Macromolecules 41, 9090 (2008)

[51] B. H. Kim, D. H. Lee, J. Y. Kim, D. O. Shin, H. Y. Jeong, S. Hong, J. M. Yun, C. M. Koo, H. Lee, S. O. Kim, Adv. Mater. 23, 5618 (2011)

[52] C. K. Shelton, T. H. Epps, Macromolecules 48, 4572 (2015)

[53] J. M. G. Cowie, V. Arrighi, Polymers: Chemistry and Physics of Modern Materials, Boca Raton: CRC Press (2008)

[54] R. Puglisi, P. La Fata, S. Lombardo, APL 91, 053104 (2007)

[55] C. Garozzo, C. Bongiorno, A. La Magna, R. A. Puglisi, ECS J. Sol. State Sci. Tech.1(3), 52 (2012)

[56] C. Garozzo, R. A. Puglisi, C. Bongiorno, S. Scalese, J. Mater. Res. 26 2, 240 (2011)

[57] C. Garozzo, C. Bongiorno, S. Di Franco, M. Italia, A. La Magna, S. Scalese, P. M. Sberna, R. A. Puglisi, Phys. Stat. Sol. A 210(8), 1564 (2013)

[58] J. Turkevich, P. C. Stevenson, J. Hillier. J. Phys. Chem. 57(7), 670 (1953)

[59] J. Turkevich, Discuss. Faraday Soc. 11, 55 (1951)

[60] F. Correard, K. Maximova, M.-A. Esteve, C. Villard, M. Roy, A. Al-Kattan, M. Sentis, M. Gingras, A. V. Kabashin, D. Braguer, Int. J. Nanomedicine 9, 5415 (2014)

[61] S. K. Sivaraman, S. Kumar, V. Santhanam, J. Colloid and Interf. Sci. 361, 543 (2011)

[62] S. H. Brewer, W. R. Glomm, M. C. Johnson, M. K. Knag, S. Franzen, Langmuir 21, 9303 (2005)

[63] A. Dimitrov, K. Nagayama, Langmuir 12, 1303 (1996)

[64] N. Shalkevich, W. Escher, T. Bürgi, B. Michel, L. Si-Ahmed, D. Poulikakos, Langmuir 26(2), 663 (2010)

[65] W. B. Russel, D. A. Saville, W. R. Schowalter, Colloidal Dispersions, Cambridge University Press (1989)

[66] M. Thommes, J. Morell, K. A. Cychosz, M. Fröba, Langmuir 29, 14893 (2013)

[67] M. H. Factorovich, E. G. Solveyra, V. Molinero, D. A. Scherlis, J. Phys. Chem. C 118, 16290 (2014)

[68] K. Morishige, S. Kittaka, J. Phys. Chem. C 119, 18287 (2015)

[69] V. Raspal, K. O. Awitor, C. Massard, E. Feschet.Chassot, R. S. P. Bokalawela, M. B. Johnson, Langmuir 28, 11064 (2012)

[70] S- J. Jeong, J. Y. Kim, B. H. Kim, H. S. Moon, S. O. Kim, Materials Today 16(12), 468 (2013)

[71] J. Bodycomb, Macromolecules 32, 2075 (1999)

[72] P. Mansky, Macromolecules 31, 4399 (1998)

[73] Z. R. Chen, Science 277, 1248 (1997)

[74] M. Li, C. K. Ober, Materials today 9(9), 30 (2006)

[75] L. Rockford, Phys. Rev. Lett. 82, 2602 (1999)

[76] R. A. Segalman, H. Yokoyama, E. J. Kramer, Adv. Mater. 13(15), 1152 (2001)

[77] S. O. Kim, Nature 424, 411 (2003)

5 Conclusions and Outlook

5.1 Conclusions

In this thesis, self-assembly processes for the large-area surface patterning with tailored nanometric features are investigated. Nanosphere lithography and block copolymer lithography are shown to be suitable self-assembly techniques for the creation of hexagonally arranged surface patterns with feature sizes from the lower µm to the sub-20 nm regime. The influence of interactions within the self-assembling systems and their interfaces with solid surfaces are investigated. The fundamental understanding of the interactions allows for the addition of surface pre-patterns for directed self-assembly, by which more complex tailored nanopatterns are created. Such patterns are shown to be suitable for the site-selective arrangement of 1D- and 2D- arrays of nanoobjects, as well as for the creation of hierarchical nanopores.

Within the first part of this thesis, the basics of convective self-assembly for the formation of monolayers of colloidal polymer spheres are introduced. By moving the so-called triple phase boundary, at which particle self-arrangement into hexagonally close packed arrays occurs, over a substrate surface via the doctor blade technique, polymer sphere monolayers are deposited on large areas of several cm^2.
It is shown that self-arranged sphere layers can be used to pattern the elastomer polydimethylsiloxane (PDMS), which is commonly chosen as stamp material for microcontact printing in soft lithography. Sphere monolayers are shown to be suitable topographic templates during PDMS curing. After mold release, the elastomer is patterned with hexagonally arranged elevated nanotips.
The sphere assemblies formed by convective self-assembly are used as masks for the nanopatterning of surfaces by nanosphere lithography (NSL). In NSL, the spheres act as a shadow mask through which the surface can be site-selectively modified. A material deposition onto a close-packed sphere monolayer, for instance, and subsequent mask removal allows for the formation of triangular shaped material nanoparticles with hexagonal arrangement on the surface. The use of polymeric spheres as NSL masks facilitates an easy mask modification. It is shown that a reactive ion etching treatment of the polymer spheres results in sphere shrinkage. Such an arrangement of shrunk spheres as deposition mask during NSL was used to create antidot patterns. The freely accessible round-shaped substrate areas within the material thin film exhibit a regular topographical as well as a site-selective chemical contrast.

The second part of the thesis deals with the formation of self-assembled 1D patterns. Nanosphere lithography is applied on linear sphere chains in order to create rows of nanogap electrodes. To this end, the capillary assembly of colloidal polymer spheres on pre-patterned surfaces was investigated. Topographic pre-patterning of a silicon surface with trenches by optical lithography and chemical surface functionalization with a self-

assembled monolayer (SAM) of octadecyltrichlorosilane (OTS) allowed for the site-selective deposition of polymer spheres inside the trenches, whereas sphere deposition on the plane areas next to trenches is suppressed [1]. The chemical surface modification with the OTS-SAM is explained in detail.

The use of single sphere rows as shadow masks during NSL resultes in the formation of opposing metallic tip pairs [2] connected via macroscopic metal films next to the spheres. It is shown that the variation of the material deposition angle during nanosphere lithography can be used for the tailoring of the gap width between the tip pairs. Finite element simulations are performed in order to predict the electrical field distributions between such nanotips if used as nanogap electrodes, showing strong field enhancement at the tips. This results in the formation of an inhomogeneous electric field along a row of tip pairs, which can be easily produced by our self-assembly approach.

In the third part of the thesis, the block copolymer (BCP) lithography is introduced which is also based on self-organization and allows for the large-area nanopatterning of surfaces. This technique extends the feature size of patterns investigated here down to the sub-20 nanometer range.

The principle of BCP lithography is explained. This technique is based on the microphase separation of copolymers, consisting of two unlike polymer species, into regular nanoscale patterns. Nanoporous polystyrene thin films with pore diameters of 17 nm with 36 nm periodicity were created by using PS-b-PMMA block copolymers containing approx. 70% polystyrene. Commercially available polymers as well as home-made polymers synthesized by RAFT polymerization (in cooperation with macromolecular chemistry group) are used. The influence of the surface free energy and polarity of several material surfaces on the phase separation of the BCP are discussed. It is shown that the polar fraction of the surface free energy is of crucial importance for the ordering of PMMA cylinders upon microphase separation.

The arrays of nanopores is shown to be suitable topographic traps for the precise placement of gold nanoparticles. Here, BCP lithography patterned nanoporous polystyrene is used as an etching mask in a reactive ion etching process for the pattern transfer into Si/SiO$_2$ surfaces. It is shown that colloidal gold nanoparticles with diameters of 5 or 10 nm, respectively, can be selectively deposited into the nanopores in the SiO$_2$. This is realized by the doctor blade technique, as used before for the nanosphere lithography approaches. Up to 83 % of nanopore could be filled with Au nanoparticles.

In the last chapter, nanosphere lithography and block copolymer lithography surface patterning are combined for the creation of hierarchical nanopores. Antidot patterned thin films from several materials are prepared by NSL and used as topographical and chemical template for the microphase separation of block copolymers. The wetting states occurring in such systems are investigated in order to get insight into the influence of the material choice on the polymer behavior and thus nanopore formation.

With some materials, such as titaniumoxide, a homogeneous nanoporous polystyrene film spanning over the antidot-patterns was obtained, while with antidot-patterns in metallic thin films from gold and platinum, nanopores are site-selectively created inside the antidots forming hierarchical nanopores.

In this thesis, different surface nanopatterning self-assembly techniques are investigated, spanning a feature size range of few microns down to few nanometers. The investigation of interfacial effects on the self-assembled patterns gives insight into the fundamental processes leading to the ordering of single units into regular arrays. The improved understanding of self-assembly in colloidal and block copolymer systems allows for a better control of the nanopatterning of surfaces and allows to create tailored nanofeatures by controlled manipulation of the surfaces of different materials with pre-patterns for directed self-assembly.

5.2 Outlook

It is shown in this work that the presented self-assembly techniques are suitable for the large-area surface patterning with ordered nanoscale features and that directed self-assembly also allows for the creation of more complex nanoarchitectures. This outlook section offers an insight into current collaborations for possible applications of the self-assembled nanopatterns as building blocks for the modern design of functional material surfaces.

Nanosphere lithography (NSL), which is an established technique for the creation of nanoparticle arrays, is shown in this work to allow for the creation of antidot patterns, which exhibit both topographical and chemical contrast. These patterns are of particular interest for their application as templates in directed self-assembly, as they are highly adjustable to their purposed applications: Their topography can be tuned easily by the choice of initial sphere size, which defines the pattern pitch, the sphere shrinking, which determines the antidot diameter and the thin film thickness, which corresponds to the depth of the antidots. The chemical contrast can be tailored by choice of substrate material and thin film material. By this, reactive and inert sites can be distinguished, or areas with alternating physical properties, such as wettability or refractive index, can be defined. This offers huge flexibility in material surface design. Two applications, which benefit from this flexibility are briefly shown in this thesis: Antidots are used to define inert and reactive areas for the site-selective deposition of protein micelles [3, 4]; and electrically conductive thin films with antidot-patterns were used as patterned electrodes creating advanced electro-optic effects in liquid crystals [5].

In a current research project, the adsorption behavior of DNA origami [6] on the antidot-patterned surfaces is investigated. This combination of unconventional lithography methods which are based on self-assembly techniques could allow for the hierarchical arrangement of single molecules and pave the way towards molecular breadboards for bioelectronics. In another recent collaboration, the antidot patterned glass slides are tested for their use as (semi-) transparent electrodes for organic LEDs with liquid crystals [7]. The patterned metal thin film is expected to show a higher transmission compared to a solid metal thin film, while the pattern additionally shows diffraction, allowing for the patterned illumination of the active material layer of the OLED.

Self-assembled nanosphere monolayers are shown in Chapter 2.3.3 to be interesting not only in NSL, but also as a topographic mold for the patterning of elastomers for soft lithography. It is shown that regularly arranged nanotips can be created in PDMS surfaces. In cooperation with a sensor group in electrical engineering, these patterned flexible PDMS samples are used as sensitive pressure sensors. The easy large-area patterning of the non-toxic PDMS could allow for the integration of these pressure sensors into electronic textiles.

By directed self-assembly, NSL is also shown to not only be suitable for the 2D surface patterning with nanopatterns. Also tailored 1D patterns can be created. In an extended outlook, preliminary result on the use of the nanogap electrodes with tunable gap width, created by directed self-assembly of nanospheres and NSL [1, 2], in dielectrophoretic particle trapping experiments are presented (Chap. 3.5.2). Here, further optimization of nanogap electrode addressing, e.g. by change of trench geometries, should allow for the simultaneous trapping of thousands of single nanoobjects. Nanogap electrodes with tunable gap width are hardly accessible by conventional direct writing techniques, which allow for the preparation of typically < 10 NGE pairs [8]. Thus, the presented approach based on self-assembly of NGEs offers great advantages e.g. for sensing applications, as the high number of parallel NGEs allow for much better statistics and better signal-to-noise ratios.

For the creation of surface patterns in the sub-20 nm regime block copolymer lithography was introduced. By this self-assembly technique, nanopores are created on surfaces of different materials. Fundamental studies of the nanopore formation process in dependence on different surface characteristics are shown. This insight paves the way for the use of BCP lithography for the patterning of different materials on large surfaces. For example, the creation of nanoporous polystyrene films on titanium oxide surfaces, which was realized in this work, could allow for a the patterning of implant materials in biomedical research. Cell behavior on pre-patterned surfaces is attracting much interest in current research [9, 10]. 20 nm nanopores, as prepared here by BCP lithography, are expected to increase tissue-compatibility [11], extending the life-time of implants in the human body.

In the present work, it is shown that arrays of nanopores are suitable topographic traps for the precise placement of gold nanoparticles. By optimization of experimental parameters, 83% of nanopores could be filled. However, the actual mechanism of Au NP deposition into the nanopores is not understood. Few thoughts on the wetting of the nanopores are discussed in Chapter 4.4.1. However, the mechanism is not clear. A more fundamental insight into the directed self-assembly at the nanoscale could allow for a further increase of the pore filling. The 2D arrays of nanoscale catalysts could be used for the directed growth of parallel semiconductor nanowires [12]. The concept of selective deposition of colloidal nanoparticles into nanopores by the presented approach, consisting of BCP pre-patterning and doctor blade assembly, can be transferred to other material systems with different kinds of colloidal nanoparticles.

Finally, the creation of hierarchical nanopores by combination of NSL and BCP lithography is shown in Chapter 4.5. With some antidot thin film materials, such as titaniumoxide, a surface-covering nanoporous polystyrene film spanning over the antidot patterns is obtained. Such an architecture could be interesting in application as back-side supported nanomembranes with homogeneous pore sizes of few nanometers. In an ongoing research project, the release of this supported membrane from the substrate is investigated. The membrane could then be used for filtration of nanoparticles. With antidot patterns in metallic thin films from gold and platinum, it is shown, that nanopores form site-selectively inside the antidots. Such hierarchical nanopores could be used for tailored nanoparticle placement or could act as batches in nanochemistry. This architecture of hierarchical nanopores can also be found in nature on the frustule of diatoms [13]. The diatoms benefits from photonic properties of the hierarchical nanopatterns are currently discussed in research [14] and could probably be transferred to nanotechnology.

The more fundamental understanding of the self-assembly processes gained in this work allows for the transfer of concepts to different materials systems and the controlled manipulation of the self-assembly environment for the directed self-assembly. The new insight into the unconventional lithography techniques makes them suitable for nanofabrication, in particular as the self-assembly based processes are easily up-scalable and thus allow for their application in technological processing, paving the way for large-area single-digit nanometer surface patterning.

5.3 Bibliography

[1] K. Brassat, F. Assion, U. Hilleringmann, J. K. N. Lindner, Phys. Stat. Sol. A 8, 1485 (2013)
[2] K. Brassat, J. K. N. Lindner, MRS Proceedings 1663, mrsf13-1663-ww04-09 (2014)
[3] A. A. Rüdiger, W. Bremser, O. I. Strube, Macromol. Mater. Eng. 301, 1181 (2016)
[4] A. A. Rüdiger, K. Brassat, J. K. N. Lindner, W. Bremser, O. I. Strube, submitted (2017)

[5] M. Wahle, K. Brassat, J. Ebel, J. Bürger, J. K. N. Lindner, H.-S. Kitzerow, Optics Express 25(19), 22608 (2017)

[6] P. W. K. Rothemund, Nature 440, 297 (2006)

[7] J. Vollbrecht, S. Blazy, P. Dierks, S. Peurifoy, H. Bock, H. Kitzerow, ChemPhysChem 18 (2017)

[8] A. Kuzyk, Electrophoresis 32, 2307 (2011)

[9] D. G. Bello, A. Fouillen, A. Badia, A. Nanci, Acta biomaterialia (in press) (2017)

[10] K. Kang, Y. Park, M. Park, M. J. Jang, S. M. Kim, J. Lee, J. Y. Choi, D. H. Jung, Y. T. Chang, M. H. Yoon, J. S. Lee, Y. Nam, I. S. Choi, Nano Lett. 16, 675 (2016)

[11] U. Mittnacht, H. Hartmann, S. Hein, H. Oliveira, M. Dong, A. P. Pego, J. Kjems, K. A. Howard, B. Schlosshauer, Nano Lett. 10, 3933 (2010)

[12] J. K. N. Lindner, D. Bahloul-Hourlier, D. Kraus, M. Weinl, T. Mélin, B. Stritzker, Mater. Sci. Semicond. Proc. 11, 169 (2008)

[13] L. De Stefano, I. Rea, I. Rendina, M. De Stefano, L. Moretti, Optics express 15(26), 18082 (2007)

[14] M. Kucki, T. Fuhrmann-Lieker, J. R. Soc. Interface 9, 727 (2012)

Appendix

A1 Wettability of solid surfaces

Surface energies and contact angles

When depositing a small amount of a liquid onto a solid surface, the liquid will spread [1]. The extend of this spreading is determined by the wettability of the surface: the liquid can either spread over the whole surface and completely wet it or the surface can be wetted partially by the liquid forming a droplet. The spreading parameter S (Eqn. A2.1) differentiates between these two states, by comparing the surface energy of the dry surface with the surface and interface energy in the wet state:

$$S = \gamma_{sg} - (\gamma_{sl} + \gamma_{lg})$$

(A2.1)

with γ the interfacial energies between the liquid l, solid s and gas g, respectively. For S > 0 total wetting occurs, as the liquid lowers its surface energy. For S < 0 partial wetting occurs [2]. This means, that a droplet with a distinct contact angle (CA) Θ at its contact line between the solid and gas phase is formed (Fig. A1.1). The shape of the droplet is then determined by the surface energies of the three contacting components liquid, solid and gas. The Young equation (Eqn. A2.2) allows for a quantitative description of partial wetting [3, 4]:

$$\gamma_{lg} \cos \Theta_Y = \gamma_{sg} - \gamma_{sl}$$

(A2.2)

with Θ_Y Young's contact angle. Contact angles < 90° correspond to good wetting properties. Surfaces forming such small CA are referred to as hydrophilic (for wetting with water). CA > 90° are created on hydrophobic surfaces. Surfaces with contact angles > 140° are called super-hydrophobic (Fig. A1.1). The total wetting (S > 0) is not defined.
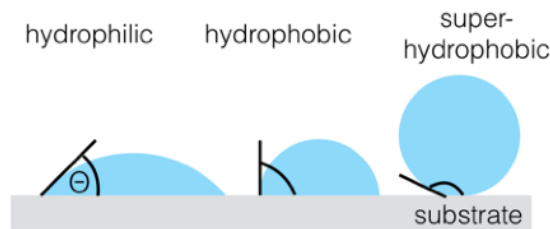
Fig. A1.1: Sketch of droplet shape on a hydrophilic, hydrophobic and super-hydrophobic surface.

Contact angle measurements and surface free energy determination

Contact angles can be measured by several methods, most of them based on optical evaluation of the drop shape or on force measurements. Commonly used techniques are the Wilhelmy plate, capillary rise, captive bubble or sessile drop technique [1]. The latter is used in this work and will be described in more detail.

For contact angle measurements with the sessile drop technique, a droplet of a liquid with defined volume is deposited onto a plane solid surface. A side-view photograph is then taken and the droplet geometry is evaluated. The contour of the droplet can be fitted by different methods, the most common of which are a Young-Laplace fit or an ellipse fit. The contact angle is then measured at the intersection between this fitted

droplet contour and the surface horizontal of the solid substrate. This angle is referred to as the static contact angle. This value is close to the Young CA, which is however defined for a perfect homogeneous smooth surface. As real surfaces are not perfectly homogeneous, neither chemically nor physically [1], dynamic contact angle measurements are performed by which the so-called advancing and receding contact angles are measured [2]. To this end, the volume of the sessile drop is continuously increased. Due to surface inhomogeneities, the wetted area of the droplet on the surface will stay constant for small volume increases, which leads to an increasing contact angle towards a maximum. Beyond this maximum contact angle, the contact line moves and the contact angle decreases again. This threshold angle Θ_{adv} is the advancing contact angle. The receding contact angle Θ_{rec} is analogously the smallest angle when decreasing the droplet volume, before the contact line moves [2]. The difference between these contact angles is the contact angle hysteresis $\Delta\Theta$:

$$\Delta\Theta = \Theta_{adv} - \Theta_{rec} \tag{A2.3}$$

This hysteresis can alternatively be determined by the so-called roll-off angle. The solid surface with the deposited liquid sessile drop is tilted towards the horizontal, which leads to an asymmetric deformation of the droplet. The tilting angle at which the drop starts to move is referred to as the roll-off angle. The advancing and receding contact angle can be determined from the droplet contour at this tilting angle. The contact angle hysteresis can be used as a measure for the wetting state of the liquid on textured surfaces, as explained below.

Measurement of the contact angles of different liquids on a solid also allows for the determination of the surface free energy (SFE) of the solid [5] by the OWRK method, named after Owens, Wendt, Rabel, Kaelble [6]. They found, that the interfacial energy between solid and liquid γ_{sl} can be written as (Eqn. A2.4)

$$\gamma_{sl} = \gamma_{sg} + \gamma_{lg} - 2\left(\sqrt{\gamma_{sg}^d \, \gamma_{lg}^d} + \sqrt{\gamma_{sg}^p \, \gamma_{lg}^p}\right) \tag{A2.4}$$

with $\gamma_{s, l, g}$ being the surface energies at the interfaces between the solid s, the liquid l and the gas g, respectively, and the superscripts d and p for the polar and dispersive energy contributions to the total surface energy. These contributions $\gamma^{p, d}$ sum up to the total surface energy γ:

$$\gamma = \gamma^d + \gamma^p \tag{A2.5}$$

With Young's equation (Eqn. A2.2), this gives:

$$\underbrace{\frac{(1+\cos\Theta_Y)\,\gamma_{lg}}{2\sqrt{\gamma_{lg}^d}}}_{y} = \underbrace{\sqrt{\gamma_{sg}^p}}_{m}\underbrace{\sqrt{\frac{\gamma_{lg}^p}{\gamma_{lg}^d}}}_{x} + \underbrace{\sqrt{\gamma_{sg}^d}}_{b} \tag{A2.6}$$

Plotting of the contact angles and liquid characteristics in form of of x and y following Equation A2.6, a linear fit can be drawn through the data, which then allows for the determination of the polar and disperse part of the interfacial energies between solid and liquid from the fit slope m and y-axis intercept b. Experimentally, contact angles of at least two liquids with known surface energy on a surface need to be measured. One of the liquids should have a predominantly polar character, the other liquid should be dispersive.

Wetting of textured surfaces

The Young contact angle Θ_Y is defined for plane, ideally homogeneous surfaces. Wetting of textured surfaces, however, cannot be described by the equilibrium of interfacial energies as in Young's equation (Eqn. A2.2). The texture of a surface, i.e. roughness or chemical and topographical patterns, induces changes in the wetting properties [1, 2]. The wetting of rough and chemically heterogeneous surfaces can be described by the Wenzel [7] and Cassie-Baxter [8] wetting models, respectively, and mixed cases between the extreme situations of Wenzel or Cassie-Baxter.
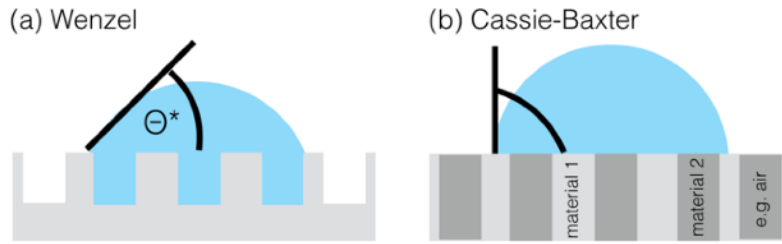

Fig. A1.2: Sketches of wetting of textured surfaces with apparent contact angles Θ^*. (a) Wetting of rough, topographically patterned surface assumed in Wenzel model with liquid penetrating all texture. (b) Wetting of a chemical inhomogeneous surface from materials 1 and 2 by Cassie-Baxter model. For the wetting of rough surfaces, this model assumes one of the materials being air, thus the droplet not penetrating the structure.

The Wenzel model describes the wetting of rough surfaces. The apparent contact angle Θ^* on topographically textured surface is correlated to the surface roughness r and the Young contact angle Θ_Y by the following expression [2]:

$$\cos \Theta^* = r \cos \Theta_Y \tag{A2.7}$$

The roughness r is defined as the ratio of the actual surface area and the projected area. As this ratio is always > 1, surface roughness decreases the contact angle on well-wettable surfaces (CA < 90° on smooth surface) and increases the contact angle on poorly wettable surfaces (CA > 90° on smooth surface) [1]. For hydrophilic rough surfaces, this wetting property-magnification results in a complete wetting of the surface with the liquid penetrating all surface patterns (Fig. A1.2 (a)).

Measurements of the roll-off angles and the contact angle hysteresis allow to distinguish between different wetting states. Surfaces wetted in a Wenzel state typically do not show a roll-off angle, i.e. the liquid droplet sticks to the rough surfaces even for tilting angles > 90°. This behavior correlates to a large contact angle hysteresis $\Delta\Theta$.

The Wenzel model only considers topographical surface textures. The influence of chemical inhomogeneities on the surface wetting are described by the Cassie-Baxter model.

The Cassie-Baxter model [2] relates the apparent contact angle Θ^* on a surface containing two different kinds of regions with different chemical properties by

$$\cos \Theta^* = f_1 \cos \Theta_1 + f_2 \cos \Theta_2 \tag{A2.8}$$

with the contact angles $\Theta_{1,2}$ on each of these region weighted by their surface fraction $f_{1,2}$ (with $f_1 + f_2 = 1$). For actual rough surfaces with hydrophobic properties, the chemical contrast is given by the surface material and

air as second material; the liquid droplet is assumed to not penetrate into the topographic texture leaving air pockets underneath the droplet (Fig. A1.2 (b)). Cassie-Baxter state wetted surfaces thus show a very small contact angle hysteresis and roll-off angle of 10-40°. Surfaces can be referred to as superhydrophobic for roll-off angles < 10°.

Most real surfaces however exhibit both, chemical and topographical contrast or exhibit hierarchical surface morphologies. On such surfaces, mixed states between Wenzel and Cassie-Baxter wetting can occur [2]. The description of the wetting properties of such more complex surfaces is topic of current research [9, 10].

Experimental details

In this work, the contact angle measurement are performed with a ‚Krüss Drop Shape Analyzer DSA 25 E'. Sessile droplets of the test liquid are deposited by automatic syringes or manually with an Eppendorf pipette onto the solid substrate. Typically, a droplet volume of 2-5 µl is deposited, as for the small volumina gravitational forces can be neglected. The droplet is illuminated from the back and a side-view image is taken. The analysis software ‚Advance' is used for the droplet contour fitting and the contact angle determination. Different contour fits (ellipse, circle, tangent, height-width, Young-Laplace) can be used, which are suitable for different contact angle regimes. For the contact angle measurements performed within this work, an ellipse fit is applied for contact angles between 10 - 140°, for contact angles < 10° a manual height-width fit is used. Typically, three droplets are deposited onto each surface and 10 measurements are taken for each droplet. Given contact angles are the mean value.

For the determination of the surface free energies of the surfaces, the OWRK method is applied. For this, contact angles with water, diiodo-methane and ethylene glycol are measured.

Dynamic contact angle measurements can be performed automatically. For this, a droplet with a typical starting volume of 5 µl is deposited on the surface with the automatic syringe. The syringe is then inserted into the droplet. The droplet volume is automatically increased and decreased, while contact angles are measured at small time intervals.

For the measurement of the roll-off angles, the complete contact angle measurement system is mounted onto a stepper-motor controlled tilting stage. The droplet is deposited onto the sample and the stage is then tilted stepwise, while the contact angles at both sides of the droplet are measured and the roll-off is observed. The sample can be tilted by 90° with respect to the horizontal sample orientation.

A2 Surface cleaning

Si (100) Wafer

Silicon (100) wafers with native oxide layer are used as substrate for all experiments. Wafers are Czochalski processed, have a thickness of (525 ± 20) µm, are p-doped with Boron and have a resistance of 14-24 Ω/cm. For the nanogap electrode fabrication in Chapter 3 Float Zone wafers are used.

The silicon surfaces are cleaned before further usage either wet-chemically by RCA process [11, 12] or in an oxygen-argon plasma. Both processes lead to an increase of the hydrophilicity of the silicon surfaces.

Wet chemical treatment: RCA process

The wet chemical RCA process [11] is commonly used in semiconductor industries. It consists of two steps:

Step 1: 50 ml H_2O, 15 ml H_2O_2 (35 %) and 10 ml NH_3 (25 %) are mixed in a teflon beaker. Samples are stored vertically and fully covered in the solution for 20 min at 80 °C. Particles and organic pollutants are removed. After the treatment the contact angle of water on the surface is decreased to 20° with respect to the typical contact angle of 30° - 40° of untreated wafers. Wafers are rinsed with H_2O, prior to the second RCA step.

Step 2: Samples are treated in a mixture of 50 ml H_2O, 15 ml H_2O_2 (35 %) and 15 ml HCl_{konz} at 80 °C for 20 min. Metallic residuals on the surfaces are removed. The contact angle with water is 10° after this treatment and homogeneous on the whole surface. After the complete RCA treatment, samples are stored in H_2O. Contact angles remain stable for 2 weeks. Before usage, samples are dried in a nitrogen flux.

Plasma treatment

The plasma surface cleaning is performed in the reactive ion etching plasma system „PlasmaLab System 80plus" by Oxford Instruments. Si/SiO$_{2, nat}$ samples are cleaned with 2 sccm O_2 and 8 sccm Ar at a pressure of 75 mTorr with a RF power of 50 W for 3 minutes on an Al transfer plate. This process is used as an alternative to the RCA wet chemical process. The contact angle of water on a plasma-cleaned silicon surface changes with storage time as shown in Figure A2.1. Immediately after plasma treatment, the contact angle is as small as 2°. It saturates towards the initial angle within 4-5 weeks of storage at ambient atmosphere and room temperature.
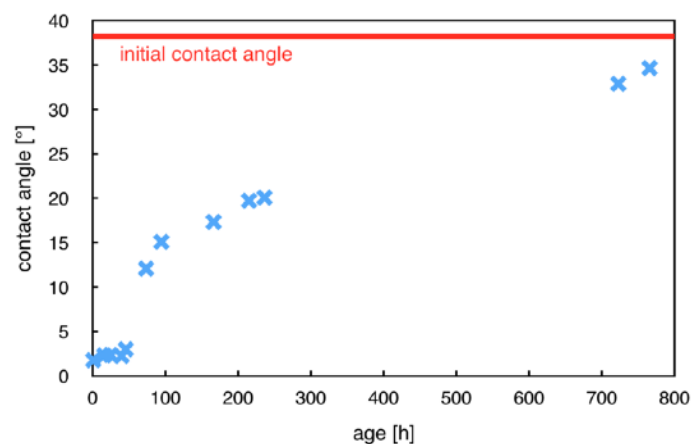

Fig. A2.1: Change of water contact angle on a plasma-cleaned Si/SiO$_2$ surface with sample age. Sample is stored at ambient atmosphere at RT. Initial contact angle prior to plasma-cleaning was 38°.

A3 Setups (alphabetic order)

This Appendix gives an overview of setups used for the investigations of samples prepared within the research projects of this thesis. Setups used by collaboration partners and other exceptional measurements are not listed here, but denoted at respective sites within the thesis.

Atomic force microscopy

Atomic force microscopy (AFM) is an imaging technique sensitive to height profiles. General information about the technique can be found in literature, e.g. [1, 13]. Here, AFM is used to determine surface roughnesses and pattern heights. Imaging is done in contact mode for the investigation of films. Tapping mode is used for the investigation of nanoparticles, e.g. Au nanoobjects or polymer spheres on silicon as particles with poor adhesion to the substrate can attach to the cantilever and thus be moved on the surface during measurement in contact mode. AFM measurements of PDMS elastomers or block copolymer films are also performed in tapping mode as the soft materials tend to stick to the cantilever, resulting in imaging artefacts.

Roughnesses are given either as peak-to-valley or root mean square (rms) values R_{rms}. Peak-to-valley roughnesses give the largest height difference between the lowest point on the investigated part of the sample to the highest elevation. Extrema, e.g. due to agglomerates on a sample, determine this value, thus outliers are taken into account drastically. This roughness value is typically much larger then the R_{rms} roughness, where outliers influence is diminished. The R_{rms} roughness R_{rms} is defined in Eqn. A3.1 with y as the deviation of datapoint n from the mean value.

$$R_{rms} = \sqrt{\frac{1}{n} \sum_n y_n^2} \qquad (A3.1)$$

Name	**Digital Instruments Dimension 3100 Series Scanning Probe Microscope**
Specs	Tapping mode, contact mode, MFM, used Cantilever: µmasch SPM tips HQ:CSC17/Al BS, 13 kHz, 0.18 N/m
used for	Topography of PDMS stamps, morphology of antidot patterns, wetting state of block copolymers inside antidots, roughness of sputter/ e-beam evaporation deposited thin films.

Name	**JPK Nanowizard (Group Prof. Grundmeier)**
used for	Homogeneity of SAMs: surface roughness, grain sizes

Confocal laser scanning microscopy

The confocal laser scanning microscopy (CLSM) is an optical imaging technique that allows for the profile visualization of microstructures on surfaces. By collection of imaging data from different focal planes within the sample, the 3D sample topography can be reconstructed. Extended literature can be found in [14].

In this work, CLSM is used for the measurement of depth, width and slope of edges of trench structures (Chap. 3.3) during all steps of substrate patterning by photolithography and reactive ion etching.

Name	**Olympus Lext OLS 4000**
Specs	Resolution: axial z = 10 nm, lateral x,y = 120 nm, laser wavelength λ = 405 nm
used for	Depth, width and slope of edges of trenches in silicon surfaces.

Contact angle measurements

Details on contact angle measurements are discussed in Appendix A1.

Name	**Krüss Drop Shape Analyzer DSA25E**
Specs	(Static and dynamic) sessile drop technique, pendant drop technique, measurements of sliding angles, test liquids: water (analytic quality), ethanol, ethylene glycole, diiodo methane
used for	Contact angle measurements, surface free energy (SFE) calculations

Ellipsometry

Ellipsometry is an optical thin film characterization technique [15]. Material properties such as the refractive index or the extinction coefficient can be determined. Thicknesses of thin films from 1 nm - several microns can be measured.

Name	**Nanofilm Technology, EP3-SW (Group Prof. Grundmeier)**
Specs	Resolution: lateral x,y = 1 µm, axial z = 0.1 nm, laser wavelength λ = 532 nm, angle of incidence 55° - 50° in 0.5° steps
used for	Thin film thickness of self-assembled monolayers (SAMs) and block copolymer thin films and random copolymer brushes. Refractive indices at 532 nm: Silicon: n = 4.152; siliconoxide: n = 1.461 [16] OTS: n = 1.50 [17] PS-PMMA (weighted mean value from PS and PMMA): n = 1.567 [18]

Light microscopy

Name	**Zeiss Axio Scope A1**
Specs	Bright field, dark field, differential interference contrast

Plasma cleaner

Name	**Harrick Plasma Cleaner/ Sterilizer PDC-32G (Group Prof. Kitzerow)**
Specs	used at: 10.5 W RF, approx. 0.1 mbar
used for	PDMS stamp treatment

Reactive ion etching

Name	**Plasma Technology PlasmaLab u80P**
Specs	process gases: O_2, Ar, SF_6, $SiCl_4$, CH_4, H_2, Cl_2, RF power max 400 W, inductively coupled plasma ICP65, ICP power max 300 W
used for	Sample surface cleaning, see App. A2, shrinking of polystyrene spheres
Recipe	2 sccm O_2, 8 sccm Ar, 75 mTorr, 50 W RF, no chiller, no ICP, different times

Scanning electron microscopy

Different scanning electron microscopes (SEMs) are used for sample imaging in this work. General information about SEM can be found in literature, e.g. [1, 19, 20].

Polymer spheres (Chap. 2+3) are predominantly investigated with the JEOL JSM-6060 and JSM-6300 F. In most cases, thin metal films are deposited onto the polymer sphere to reduce charging. As the spheres are used as shadow masks in nanosphere lithography, metal films were deposited onto the sample as part of the experiment. Material (most frequently Au, Ti or Pt) and film thicknesses (typically 10 - 50 nm) are mentioned individually within the text.

Structured PDMS stamps (Chap. 2.3.3) are investigated with the SEM Zeiss Ultra Plus in-lens detector. Acceleration voltage was 1.5-1.8 kV. For cross-sectional imaging, the PDMS stamp was frozen in liquid nitrogen and broken in frozen state.

The block copolymer samples (Chap. 4) are investigated with the scanning electron microscopy Zeiss Ultra Plus using an in-lens detector. As the polymer layers are non-conductive and no metal thin film deposition was desired, low acceleration voltages of 2 kV are used. The working distance was typically 3.5-4.5 mm.

Name	**JEOL JSM-6060**
Specs	W-Emitter, acc. voltage 0.2 to 30 kV, SE detector, EDAX-EDX system for element analysis
Figures	3.14, 3.17, 3.19

Name	**JEOL JSM-6300 F**
Specs	FEG Emitter, acc. voltage 0.2 to 30 kV, detector for SE and BSE
Figures	2.8, 2.9, 2.10(b), 2.11, 3.18, 3.20, 3.22, 3.23, 3.39

Name	**Zeiss Ultra Plus (Group Prof. Schaper)**
Specs	Acc. voltage 0.02 to 30 kV, beam current up to 100 nA, local charging compensation for imaging of non-conductive samples. In-Lens detector, SE detector, ESB detector. Combined EDX/ EBSD system for element analysis.
Figures	2.18, 2.19, all from Chapter 4

Name	**Raith PIONEER (Group Prof. Meier)**
Specs	SE detector, acc. voltage 2-30 kV, in-lens detector, electron beam lithography system
Figures	2.10(a, c, d, e), 3.21, 3.24, 3.33

Sputter coater

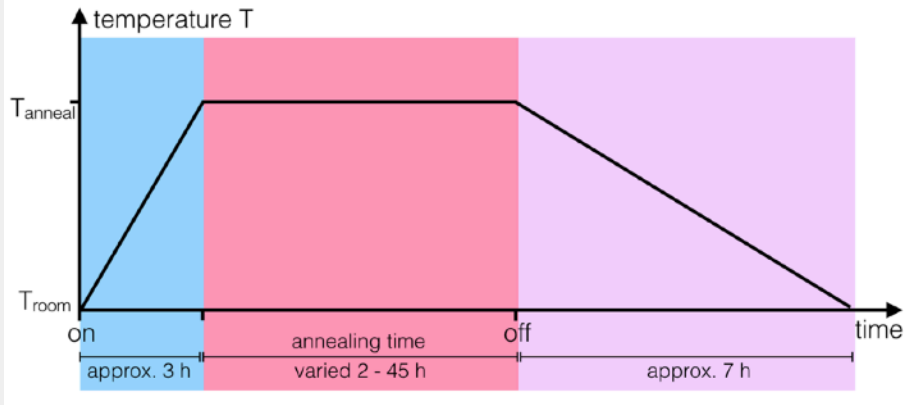| Name	**ISI PS-2 coating unit**
Specs	DC sputter system, gold and platinum targets (17.7 cm²), membrane pump, timer, Ar atmosphere, target-sample distance 12 mm
used for	Thin film + antidot preparation
Recipe	1.2 kV, 0.1 Torr, 20 µA, different times

Transmission electron microscopy

Transmission electron microscopy (TEM) is used for sample imaging and analysis. General information about TEM can be found in literature, e.g. [19, 21]. Nanopores, created by block copolymer lithography and subsequent reactive ion etching for the pattern transfer into a silicon substrate, are investigated by cross-sectional TEM at 200 kV (JEOL 2010F) regarding their shape, and the filling of the nanopores with gold nanoparticles in Chapter 4.4. In Chapter 4.5, hierarchical nanopore architectures from NSL and BCP lithography are investigated by cross-sectional TEM (JEOL JEM-ARM200F, 200 kV) in order to determine wetting states of the polymer on the pre-pattern and energy-filtered TEM (EFTEM) is applied for elemental analysis.

For the cross-sectional TEM sample preparation, samples are cut, sandwiched with a glue and conventionally prepared (dimple grinding + ion milling). Prior to the TEM sample preparation, 10-15 nm thick protective layers of either nickel or titanium (depending on the materials used on the actual sample) are deposited by PVD.

Name	**JEOL 2010F (IMM-CNR Catania, Italy)**
Figures	4.29

Name	**JEOL JEM-ARM200F**
Figures	4.35

Vacuum furnace

Name	**MMM Group VacuCell 22 (Group Prof. Kuckling)**
Specs	RT to 200 °C, pressure of 1×10^{-3} mbar, all block copolymer annealing times mean the dwell time of the sample at the targeted temperature.
used for	Block copolymer + random copolymer annealing

ζ-potential measurements

Name	**Malvern Zeta Sizer Nano-ZS (Group Prof. Bremser)**
Specs	Dynamic light scattering (detection angle 175°) for particle size distribution, surface ζ-potential, molecular weight
used for	ζ-potential measurements of aqueous polystyrene sphere suspensions, using Smoluchowski approximation

Home-built setups

Name	**Ultrafiltration**
Specs	track-etch filter (Whatman polycarbonate foil) with different pore size, inert gas, electrical conductivity measurement
used for	Exchange of liquid phase in colloidal suspensions

Name	**Electron beam evaporation system**
Specs	motorized 2-axis-sample holder tilting, 6 crucible electron beam evaporator, quartz scale for film thickness control, sample heating, turbo molecular pump system
used for	oblique and normal deposition of metals or insulators: Au (typ. deposition rates: 0.1-1.5 Å/s @ 5×10^{-6}-1×10^{-5} mbar), Ti (typ. 1 Å/s @ 5×10^{-7} mbar), SiO_2 (5-10 Å/s @ 5×10^{-6} mbar), Pt (0.1 Å/s @ 1×10^{-5} mbar)
	for further information see: C. Brodehl, Ph D Thesis, Paderborn University.

Name	**Doctor blade apparatus**
Specs	see Chapter 2.2, translational stage, Peltier heating/ cooling of sample holder, glove box for humidity regulation, camera
used for	Convective + capillary assembly of polymer (PS) or Au colloids from aqueous suspensions

A4 Photolithography mask

Photolithography was used for the topographic pre-patterning of silicon wafers with trenches in Chapter 3.2. The photolithography was performed by the group of Prof. U. Hilleringmann, electrical engineering at Paderborn University. Figures A4.1 shows the technical drawing of the lithography mask, Figure A4.2 shows sketches of the patterns with marked feature sizes. The mask is purchased from Toppan Photomask Inc. with the following specifications: 1X Master, 5'' x 0.090'', Quartz, Cr, minimum feature size $\geq$ 1.0 μm
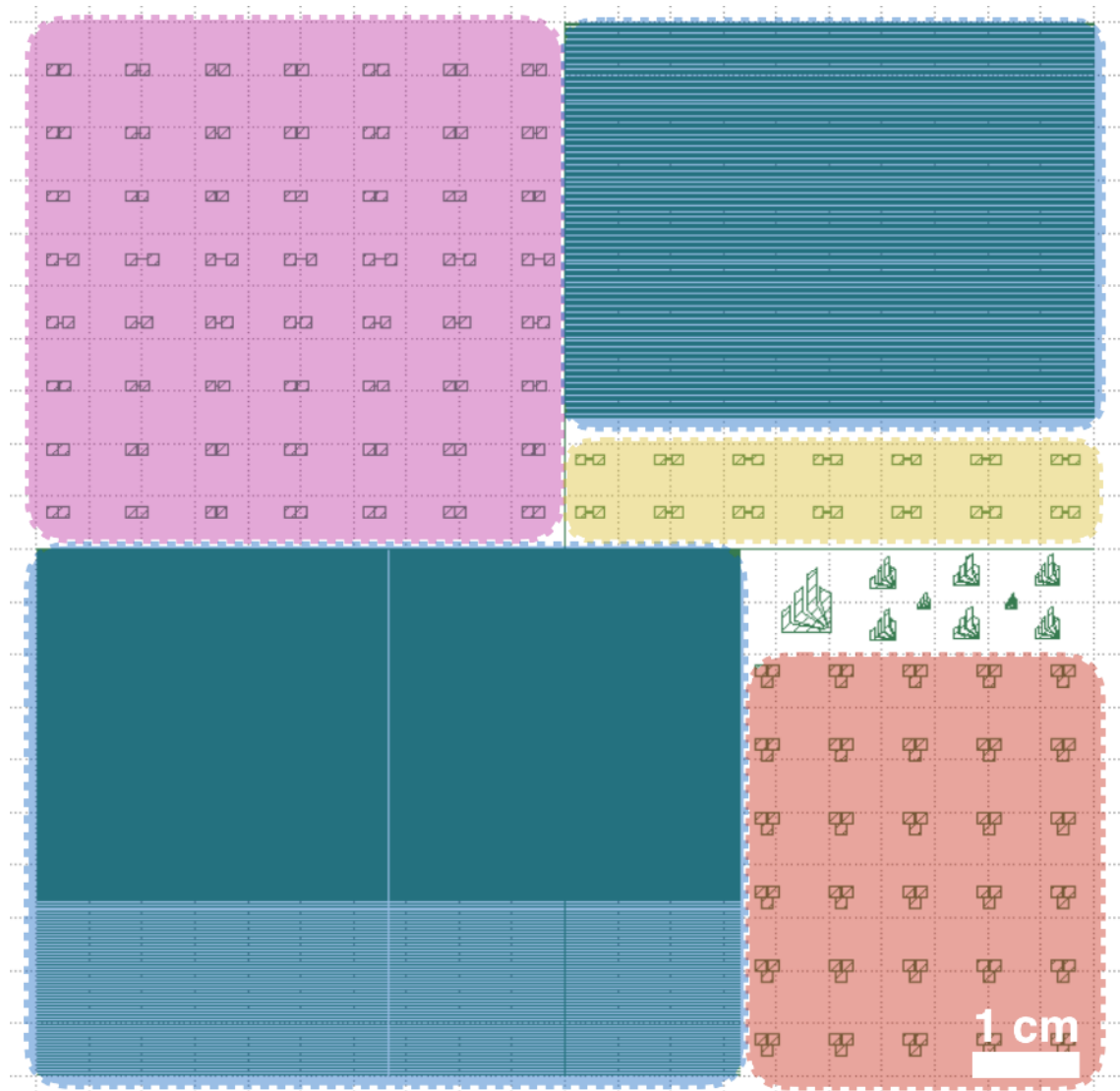

Fig. A4.1: Technical drawing of the photolithography mask with lines (blue), Lines ending in squares (pink), T-shaped lines ending in squares (red), zick-zack lines ending in squares (yellow) and the university logo (white). University Logo with edge length of 1 mm, 2 mm and 5 mm.
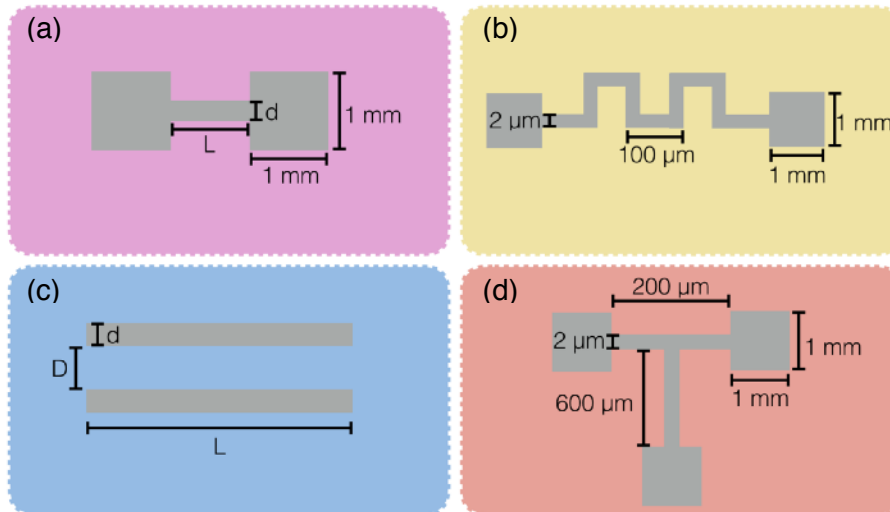
Fig. A4.2: Sketches of the patterns on the mask in Figure A4.1 with indicated feature sizes (color code corresponding to Fig. A4.1). (a) d = 1.8 - 2.2 μm, L = 50 - 1000 μm; (c) in the lower left of Fig. A4.1: d = 1 - 6 μm, D = 75 - 300 μm, L = 10000 μm and in the upper right: d = 0.9 - 2.1 μm, D = 200 μm, L = 50000 μm.

A5 Datasheets copolymers [22]

Sample Name: **Poly(styrene-b-methyl methacrylate)** *(polymethylmethacrylate rich in syndiotactic contents > 80%)*

Sample #: **P2400-SMMA**

Structure:
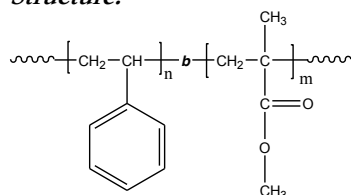
Composition:

Mn x 10³ S-b-MMA	PDI
46.1-b-21.0	1.09
T_g for PS block: 105°C	T_g for PMMA block: 128°C

Synthesis Procedure:

Poly(styrene-b-methyl methacrylate) is prepared by living anionic polymerization in THF at –78 °C using sec.BuLi initiator in the presence of LiCl. Polystyrene macroanions were end capped with a unit of diphenyl ethylene (DPE) before adding methylmethacrylate (MMA) monomer.
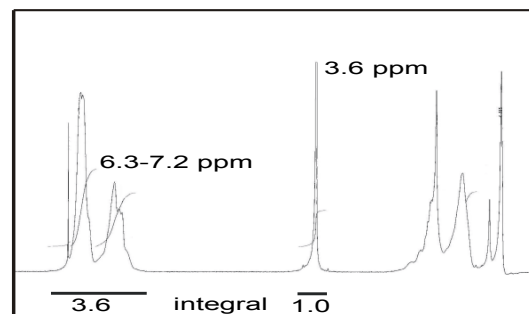
Characterization:

An aliquot of the anionic polystyrene block was terminated before addition of MMA and analyzed by size exclusion chromatography (SEC) to obtain the molecular weight and polydispersity index (PDI). The final block copolymer composition was calculated from ^{1}H-NMR spectroscopy by comparing the peak area of the poly(methyl methacrylate) protons (eg. –OCH₃ at 3.6ppm) with the of aromatic protons of polystyrene at 6.3-7.2 ppm. Copolymer PDI is determined by SEC.

Thermal analysis of the samples was carried out using a differential scanning calorimeter (TA Q100) at a heating rate of 15°C/min. The inflection glass transition temperature (T_g) of the sample has been considered.
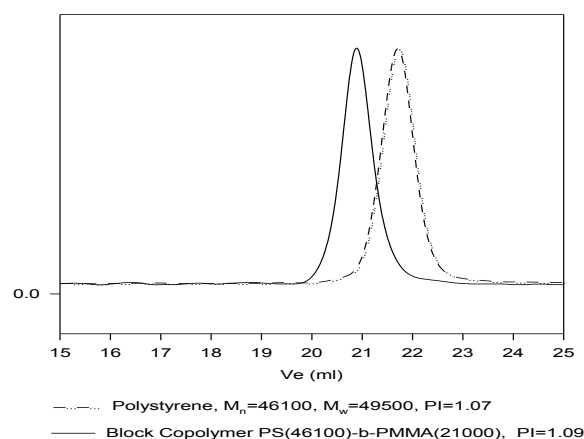
Solubility:

Poly(methyl methacrylate) is soluble in THF, CHCl₃, toluene and dioxane. The polymer precipitates from hexanes, methanol and ethanol.
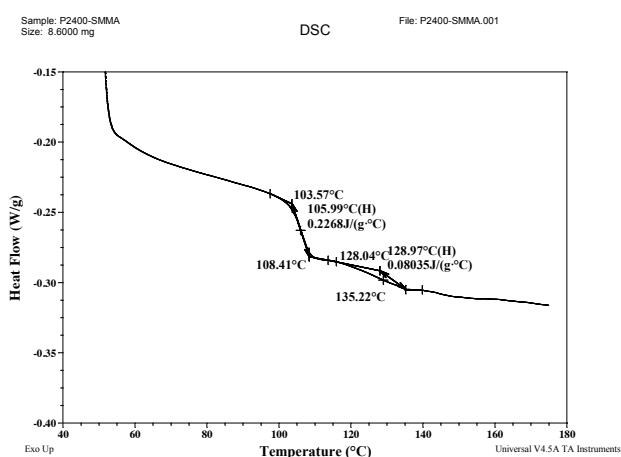
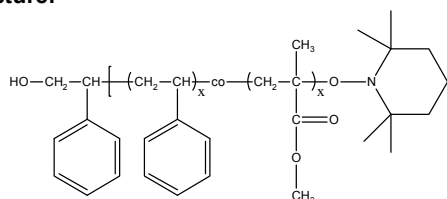**^{1}H-NMR Spectrum of P2400-SMMA:**

SEC of Sample P2400-SMMA:

Polystyrene, M_n=46100, M_w=49500, PI=1.07
Block Copolymer PS(46100)-b-PMMA(21000), PI=1.09

Thermograms of sample

Sample: **Poly(Styrene–*co*–Methyl Methacrylate), α-Hydroxy, ω-TEMPO-moiety terminated random copolymer**

Sample # **P19014D-SMMAranOHT**

Structure:

Composition:

Mn x 10^3 (g/mol)	M_w/M_n (PDI)
5.3	1.44

Polystyrene content: 74 mol %

¹H NMR spectrum (500 MHz, CDCl₃):

1H NMR (500 MHz, CDCl3): **P19014-D**

Synthesis:
Hydroxy-terminated poly(styrene-co-methyl methacrylate) was prepared by stable free radical polymerization at 135°C. The reaction scheme is shown below:
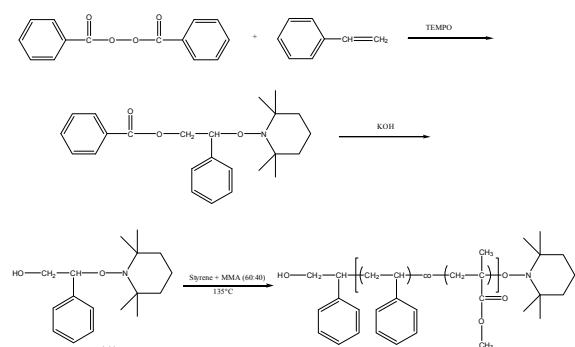
Characterization:
The molecular weight and polydispersity index (PDI) of the product was determined by size exclusion chromatography (SEC), using polystyrene as a standard. The ratio between polystyrene and poly(methyl methacrylate) in PS-PMMA copolymer was calculated from ¹H NMR spectroscopy by comparing the peak area of the PS phenyl protons at 6.5–7.3 ppm and the peak area of PMMA methyl protons at 3–3.6 ppm.

Solubility:
Poly(styrene–co–methyl methacrylate) is soluble in THF, DMF, toluene, and chloroform. It precipitates from methanol and hexanes.

(v. I-01)

Specifications home-made block copolymers

PS-b-PMMA block copolymers BCP56, BCP34 and BCP20 were synthesized by RAFT polymerization by Tarik Rust and Dr. Artjom Herberg from the Macromolecular Chemistry group of Prof. D. Kuckling in the Department of Chemistry at Paderborn University. Specifications of the polymer are listed in Table A5.1.

Tab. A5.1: Molar mass, polystyrene (PS) fraction, polydispersity index (PDI), degree of polymerization and Flory Huggins parameter $\mathcal{X}$ of RAFT-synthesized PS-b-PMMA block copolymers BCP56, BCP34 and BCP20 and the PMMA homopolymer used as macroinitiator ([M]:[CTA]:[I] = 70:1:0.15).

	BCP 56	BCP 34	BCP 20	p(MMA) homopolymer
Molar mass [kg/mol]	55.8	34.0	20.0	11.5
PS fraction [%]	79	74	57	-
PDI	1.21	1.31	1.38	1.07
Polymerization degree P_n	345	261	174	115
$\mathcal{X}$(450 K)	0.0365	0.0350	0.0300	

Block length ratios were determined by ^{1}H-NMR (exemplary spectrum for BCP56 in Fig. A5.1), polydispersities by size exclusion chromatography (SEC), polymerization degrees are calculated from blocklength ratios and P_n of p(MMA). Flory-Huggins parameters $\mathcal{X}$(450 K) at annealing temperatures are taken from [23].
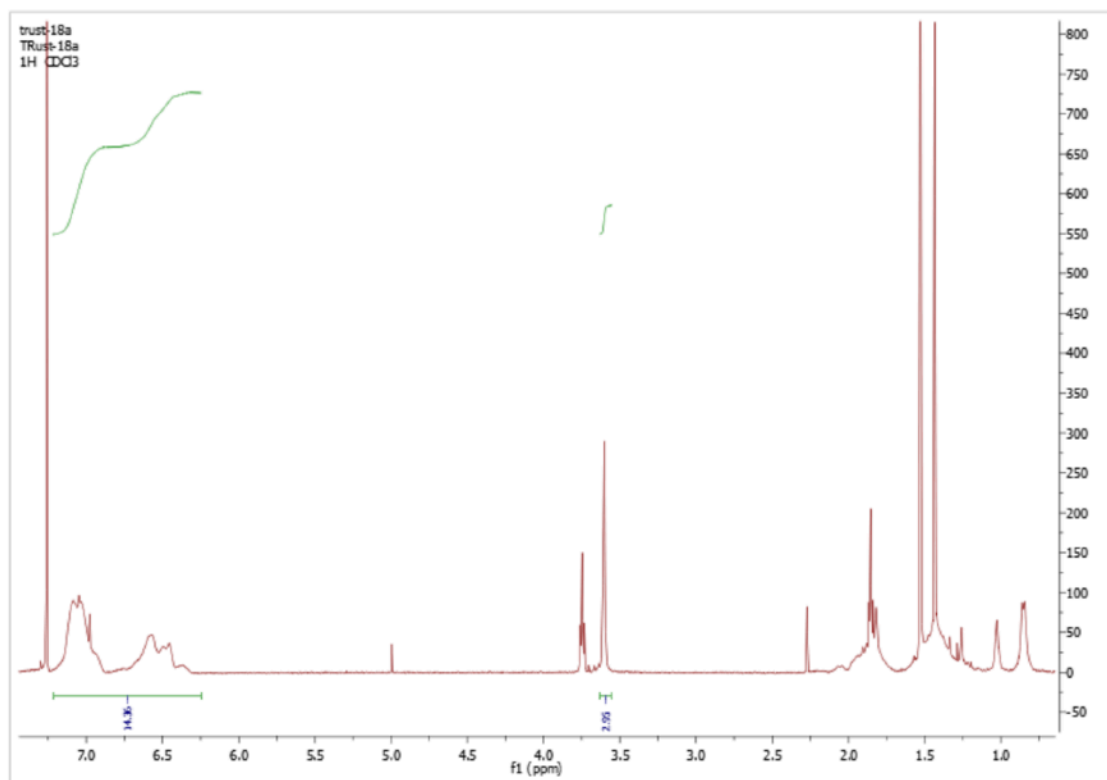

Fig. A5.1: ^{1}H-NMR spectrum of BCP56.

A6 Bibliography

[1] H.-J. Butt, Physics and Chemistry of Interfaces, Weinheim: Wiley-VCH-Verlag (2003)

[2] P. G. de Gennes, F. Brochard-Wyart, D. Quéré, Capillarity and Wetting Phenomena, New York: Springer (2004)

[3] T. Young, Phil. Trans. R. Soc. Lond. 95, 65 (1805)

[4] T. S. Chow, J. Phys.: Cond. Matter 10(27), 445 (1998)

[5] Y. Yuan, T. R. Lee, Contact angle and wetting properties, in: Surface science techniques, Springer (2013)

[6] D. K. Owens, R. C. Wendt, J. Appl. Polym. Sci. 13(8), 1741 (1969)

[7] R. N. Wenzel, Ind. Eng. Chem. 28, 988 (1936)

[8] A. B. D. Cassie, S. Baxter, Transact. Faraday Soc. 40, 546 (1944)

[9] A. J. B. Milne, A. Amirfazli, Adv. Coll. Interf. Sci. 170(1), 48 (2012)

[10] V. Raspal, K. O. Awitor, C. Massard, E. Feschet-Chassot, R. S. P. Bokalawela, M. B. Johnson, Langmuir 28, 11064 (2012)

[11] W. Kern, D. A. Puotinen, RCA Rev. 31, 187 (1970)

[12] K. Uemura, Y. Mori, T. Haibara, Nippon Steel Techn. Report 83, 61 (2001)

[13] G. Binnig, C. F. Quate, C. Gerber, Phys. Rev. Let. 56, 930 (1986)

[14] J. B. Pawley (Editor), Handbook of Biological Confocal Microscopy, Berlin: Springer (2006)

[15] E. A. I. Harland Tompkins, Handbook of Ellipsometry, Norwich: William Andrew (2005)

[16] I. H. Malitson. J. Opt. Soc. Am. 55, 1205 (1965)

[17] Y. Wang, M. Liebermann, Langmuir 19, 1159 (2003)

[18] N. Sultanova, S. Kasarova, I. Nikolov, Acta Physica Polonica A 116, 585 (2009)

[19] R. F. Egerton, Physical principles of electron microscopy, New York: Springer (2005)

[20] J. I. Goldstein, D. E. Newbury, P. Echlin, D. C. Joy, A. D. Romig, A. E. Lymann, C. Fiori, E. Lifshin, Scanning electron microscopy and x-ray microanalysis. New York: Plenum Press (1992)

[21] D. B. Williams, C. B. Carter, Transmission electron microscopy, New York: Springer (2009)

[22] Polymer Source Inc., https://polymersource.com/ (15.04.2015)

[23] Y. S. Jung, MIT, Ph. D. Thesis (2009)

B Contributions in peer reviewed journals & Conference contributions

Contributions in peer reviewed journals

- Hierarchical nanopores by block copolymer lithography on surfaces of different materials pre-patterned by nanosphere lithography
  K. Brassat, D. Kool, J. Bürger, J. K. N. Lindner (2018) (t.b. submitted)
- Directed adsorption of DNA origami nanostructures in nanohole arrays
  K. Brassat*, S. Ramakrishnan*, J. Bürger, M. Hanke, M. Doostdar, J. K. N. Lindner, G. Grundmeier, A. Keller (2018) (t.b. submitted)
- Easily accessible protein nanostructures via enzyme mediated addressing
  A. A. Rüdiger, K. Brassat, J. K. N. Lindner, W. Bremser, O. I. Strube, Langmuir (2018) (submitted)
- Functionalized graphene oxide quantum dots: synthesis, characterisation and application
  A. Wolk, M. Rosenthal, S. Neuhaus, K. Huber, K. Brassat, J. K. N. Lindner, R. Grothe, G. Grundmeier, W. Bremser, R. Wilhelm, Scientific reports (2018) (submitted)
- 2D switchable blue phase gratings manufactured by nanosphere lithography
  M. Wahle, K. Brassat, J. Ebel, J. Bürger, J. K. N. Lindner, H.-S. Kitzerow, Optics Express 25(19), 22608 (2017) DOI 10.1364/OE.25.022607
- Low-voltage DNTT-based thin-film transistors and inverters for flexible electronics
  T. Meyers, F. F. Vidor, K. Brassat, J. K. N. Lindner, U. Hilleringmann, Microelectronic Engineering 174, 35 (2017) DOI: 10.1016/j.mee.2016.12.018
- A template-assisted self-organization process for the formation of a linear arrangement of pairs of metallic tips
  K. Brassat, J. K. N. Lindner, MRS Proceedings 1663, mrsf13-1663-ww04-09 (2014)
- **Cover article:** Self-organization of nanospheres in trenches on silicon surfaces
  K. Brassat, F. Assion, U. Hilleringmann, J. K. N. Lindner, Physica Status Solidi A 210 (8), 1485-1489 (2013) DOI 10.1002/pssa.201200899

Conference contributions

(presenting author underlined)

Oral contributions

- Hierarchical nanopatterns by site-selective DNA origami adsorption on pre-patterned surfaces
  K. Brassat, S. Ramakrishnan, A. Keller, J. K. N. Lindner, MRS Spring Meeting 2018, Phoenix, Arizona, 02.-06.04.2018
- Micro- and nanopatterned surfaces with tailored chemical and topographical contrast by self-assembly techniques
  K. Brassat, D. Kool, J. Bürger, J. K. N. Lindner, EMRS Fall Meeting 2017, Warsaw, Poland, 18.-21.09.2017
- **Invited talk:** Bioinspired material design by hierarchical self-assembly on pre-patterned surfaces
  K. Brassat, A. Keller, G. Grundmeier, W. Bremser, O. Strube, J. K. N. Lindner, EMRS Spring Meeting 2017, Strasbourg, France, 22.-26.05.2017
- **Invited talk:** Regular surface nanopatterning with nanosphere lithography, block copolymer lithography and combinations of both
  K. Brassat, Ch. Brodehl, J. K. N. Lindner, BraMat 2017, Brasov, Romania, 9.-11.03.2017
- Hierarchically ordered nanopore structures formed by combined nanosphere and block copolymer lithography
  K. Brassat, D. Kool, J. K. N. Lindner, EMRS Fall Meeting 2016, Warsaw, Poland, 19.-22.09.2016
- **Plenary talk:** Nanopatterning of surfaces with nanosphere lithography, block copolymer lithography and combinations of both
  K. Brassat, Ch. Brodehl, J. K. N. Lindner, ICPAM-11, Cluj-Napoca, Romania, 8.-14.09.2016
- **Invited talk:** Hierarchical self-assembly by colloidal and block copolymer lithography
  K. Brassat, EMN Supramolecular Materials Meeting 2016, Berlin, Germany, 16.-20.08.2016
- Self-assembled nanogap electrodes in microfluidic channels
  K. Brassat, Ch. Brodehl, M. Wahle, J. K. N. Lindner, GRK Convention 2015, Paderborn, Germany, 24.-25.11.2015
- Self-assembled nanogap electrodes for the directed assembly of nanoparticles
  K. Brassat, Ch. Brodehl, J. K. N. Lindner, EMRS Fall Meeting 2015, Warsaw, Poland, 14.-19.09.2015
- Self-arrangement of colloidal Au Nanoparticles in SiO_2-Nanopores fabricated by Block-Copolymer Lithography
  C. Garozzo, K. Brassat, A. LaMagna, R. Puglisi, J. K. N. Lindner, EMRS Fall Meeting 2015, Warsaw, Poland, 14.-19.09.2015
- Tuning the distance between opposing metallic nanotips formed by a template-assisted self-assembly process
  K. Brassat, C. Brodehl, M. Wahle, J. K. N. Lindner, MRS Spring Meeting 2014, San Francisco, California, 21.-25.04.2014
- Selective deposition of nanospheres in trenches on silicon surfaces by self-organization
  K. Brassat, J. K. N. Lindner, Frühjahrstagung DPG 2013, Regensburg, Germany, 10.-15.03.2013
- Self-organization of nanospheres in trenches on silicon surfaces
  K. Brassat, F. Assion, U. Hilleringmann, J. K. N. Lindner, EMRS Fall Meeting 2012, Warsaw, Poland, 17.-21.09.2012

Poster contributions

- Tailored antidot patterns created by nanosphere lithography for bioapplications
  <u>K. Brassat</u>, A. Keller, G. Grundmeier, W. Bremser, O. Strube, J. K. N. Lindner, EMRS Spring Meeting 2017, Strasbourg, France, 22.-26.05.2017

- Joining self-assembly techniques: A route to hierarchical nanopores
  <u>K. Brassat</u>, J. K. N. Lindner, Europhotonics Spring School 2017, Barcelona, Spain, 21.-24.03.2017

- Enzyme mediated autodeposition of protein particles on nanosphere lithographically nanostructured surfaces
  <u>K. Brassat</u>, A. Rüdiger, J. Bürger, W. Bremser, O. Strube, J. K. N. Lindner, EMRS Fall Meeting 2016, Warsaw, Poland, 19.-22.09.2016

- Arrangement of perovskitic semiconductor nanoparticles using soft lithography
  <u>K. Brassat</u>, J. Bürger, M. Reineke, D. Briese, K. Duschik, M. Schaper, J. K. N. Lindner, EMRS Fall Meeting 2016, Warsaw, Poland, 19.-22.09.2016

- Site-selective protein immobilization on regular antidot patterns fabricated by nanosphere lithography
  <u>K. Brassat</u>, A. Rüdiger, J. Bürger, W. Bremser, O. Strube, J. K. N. Lindner, EMRS Fall Meeting 2016, Warsaw, Poland, 19.-22.09.2016

- High-resolution TEM and STEM-EELS studies of colloidal Au nanoparticles self-assembled in nanometric SiO_2 nanopore arrays fabricated by block-copolymer lithography
  R. A. Puglisi, C. Bongiorno, K. Brassat, C. Garozzo, A. La Magna, <u>J. K. N. Lindner</u>, EMRS Fall Meeting 2016, Warsaw, Poland, 19.-22.09.2016

- Sub-20 nm surface patterning by block copolymer lithography
  <u>K. Brassat</u>, J. K. N. Lindner, Europhotonics Spring School 2016, Porquerolles, France, 30.03.-01.04.2016

- Correlation between defect densities in colloidal nanosphere masks and experimental parameters
  D. Drude, <u>K. Brassat</u>, Ch. Brodehl, J. K. N. Lindner, EMRS Fall Meeting 2015, Warsaw, Poland, 14.-19.09.2015

- Variable-distance nanogap electrodes in a microfluidic channel
  <u>K. Brassat</u>, Ch. Brodehl, M. Wahle, J. K. N. Lindner, Europhot. Spring School 2015, Paderborn, Germany, 2015

- Variable-distance nanogap electrodes in a microfluidic channel
  <u>K. Brassat</u>, Ch. Brodehl, M. Wahle, J. K. N. Lindner, GRK Convention 2014, Paderborn, Germany, 8.-9.12.2014

- Self-assembly for the directed self-assembly of smaller objects in a microfluidic channel
  K. Brassat, <u>J. K. N. Lindner</u>, MRS Fall Meeting 2014, Boston, Massachusetts,30.11.-05.12.2014

- Numerical analysis of defects in colloidal nanosphere masks
  D. Drude, K. Brassat, Ch. Brodehl, T. Riedl, <u>J. K. N. Lindner</u>, EMRS Fall Meeting 2014, Warsaw, Poland, 15.-19.09.2014

- Surface patterning by nanosphere lithography
  <u>K. Brassat</u>, Ch. Brodehl, J. Pauly, D. Drude, J. Achtelik, T. Riedl, J. K. N. Lindner, Workshop Ionenstrahlen und Nanostrukturen 2014, Paderborn, Germany, 20.-22.07.2014

- Template-assisted self-assembly process for the formation of nanogap electrodes
  <u>K. Brassat</u>, M. Wahle, J. K. N. Lindner, Europhotonics Spring School 2014, Porquerolles, France, 31.03.-03.04.2014

- A template-assisted self-organization process for the formation of a linear arrangement of pairs of metallic tips
  K. Brassat, <u>J. K. N. Lindner</u>, MRS Fall Meeting 2013, Boston, Massachusetts,01.-06.12.2013

- Colloidal nano-lithography: state-of-the-art
  <u>K. Brassat</u>, J. Pauly, R. Kemper, M. Strake, C. Brodehl, W. Sievers, T. Riedl, J. K. N. Lindner, 46th Biennial Meeting of the Colloid Society, Paderborn, Germany, 23.-25.09.2013

C List of abbreviations

Abbreviation	Full name
AFM	Atomic force microscopy
ATRP	Atom transfer radical polymerization
BCP	Block copolymer
CA	Contact angle
CCC	Critical coagulation concentration
CLSM	Confocal laser scanning microscopy
CP	Copolymer
CTA	Chain transfer agent
CV	Coefficient of variation
DEP	Dielectrophoresis
DI	Deionized
DLVO	Derjaguin, Landau, Verwey, Overbeek
DSA	Directed self-assembly
DSC	Differential scanning calorimetry
EDL	Electric double layer
EMA	Enzyme mediated autodeposition
EtOH	Ethanol
FE	Field enhancement
FEM	Finite element method
FITC	Fluorescein isothiocyanate
ITO	Indium tin oxide
LC	Liquid crystal
MMA	Methylmethacrylate
MPTMS	3-Mercaptopropyltrimethoxysilane
NGE	Nanogap electrode
NMR	Nuclear magnetic resonance spectroscopy

Abbreviation	Full name
NP	Nanoparticle
NSL	Nanosphere lithography
OTS	Octadecyltrichlorosilane
OWRK	Owen, Wendt, Rabel, Kaelble
PDI	Polydispersity index
PDMS	Polydimethylsiloxane
PMMA	Polymethylmethacrylate
PS	Polystyrene
PS-b-PMMA	Polystyrene-block-polymethylmethacrylate
PS-co-PMMA	Polystyrene-co-polymethylmethacrylate
PVD	Physical vapor deposition
RAFT	Reversible addition-fragmentation chain-transfer polymerization
RCP	Random copolymer
RIE	Reactive ion etching
rms	Root mean square
RT	Room temperature
SA	Self-assembly
SAM	Self-assembled monolayer
SEC	Size exclusion chromatography
SEM	Scanning electron microscopy
SFE	Surface free energy
TASA	Template assisted self-assembly
TEM	Transmission electron microscopy
THF	Tetrahydrofurane
μCP	Micro contact printing